UNIVERSITY OF SOUTHAMPTON

Analysis of VRPM (Transverse-Flux) Machines for Renewable Energy Applications

by

Jaime Renedo Anglada

A thesis submitted for the degree of
Doctor of Philosophy

in the
Faculty of Engineering and the Environment
Engineering Sciences

November 2017

UNIVERSITY OF SOUTHAMPTON
ABSTRACT

FACULTY OF ENGINEERING AND THE ENVIRONMENT
ENGINEERING SCIENCES

Doctor of Philosophy

Analysis of VRPM (Transverse-Flux) Machines for Renewable Energy Applications

by Jaime Renedo Anglada

Rotor speeds of tidal and wind energy conversion systems (10/150 rpm) are lower than in traditional power plants such as gas or steam turbines (1500/3000 rpm). The low speed of the rotor makes it necessary to install a gearbox when conventional electric generators are used, which can reduce reliability and increase maintenance cost. Since transverse flux machines (TFMs) have a high specific torque, they are attractive as direct-drive generators for wind and tidal turbines. However, TFMs have complex three-dimensional geometries and structures, which complicates the task of modelling. Therefore, the aim of this Thesis is to develop intuitive fundamental theory particularly tailored for the modelling of permanent magnet transverse flux machines.

The Thesis makes several novel contributions in the field of electromagnetic modelling of TFMs. Firstly, it develops a complex permeance framework for the case of TFMs using a scalar potential formulation. The complex permeance function is used to obtain the homopolar magnetic field distribution in the air-gap taking into account curvature and slotting. Furthermore, an algorithm to quickly obtain the coefficients of the complex permeance function is presented.

The complex permeance function is then used to formulate a torque equation. A generalisation of Harris *et al.*'s torque equation for TFMs is derived for any mmf waveform and phase advance angle. The torque equation is based on Lorentz's BiL principle, where i is the equivalent current of the magnets and B is the magnetic field produced by the stator winding. The result is a fairly simple equation that relates torque to the electric and magnetic loadings of the machine and a flux factor that depends on the machine's geometrical parameters.

In addition, a virtual mutual inductance (VMI) approach to calculate the flux linkage in TFMs is proposed. The VMI between the stator windings and the magnets' equivalent currents is obtained by integrating the flux produced by the stator windings over the surface of the magnets. Based on the reciprocity theorem ($\mathfrak{M}_{12} = \mathfrak{M}_{21}$) it can be used to obtain the flux linkage in the stator windings. This methodology has been validated using experimental data and three-dimensional finite element analysis showing a reasonable level of accuracy. Key design parameters such as back emf and power factor are then readily calculated using the proposed methodology.

The well-known current sheet model has been adapted for the calculation of eddy current power losses, produced by asynchronous harmonics in the air-gap, in the outer rotor geometry of TFMs. Furthermore, the problem is formulated using transfer matrices, which reduces the complexity of the problem significantly. The transfer matrices are used to express the boundary conditions

sequentially; this simplifies the solution because instead of inverting a large matrix, as commonly done in the literature, it is only necessary to invert a matrix of order two.

These analytical techniques are applied to optimise the design of a tidal generator. The optimisation philosophy developed in this Thesis emphasises the fact that torque and power factor are closely interlinked. Furthermore, it is shown that the low power factor of TFMs is not produced by the leakage flux in the classical way but due to the *ineffective use of the magnetic flux*. Understanding the relationship between torque and power factor is a key step to unlock the full potential of TFMs.

Finally, all through this Thesis a particular single-sided TFM design case study is used. However, the background theory developed is completely general and it can be applied to any kind of permanent magnet machine. The proposed future work includes the application of the methodologies developed for the analysis and design of radial permanent magnet machines, magnetic gears, magnetic actuators and more complex flux-concentrating TFMs.

Contents

List of Figures **ix**

List of Tables **xiii**

Declaration of Authorship **xv**

List of Publications **xvii**

Acknowledgements **xix**

Preface **xxi**

1 Introduction **1**
- 1.1 Overview . . . 1
- 1.2 The Role of Renewable Energy . . . 1
  - 1.2.1 Wind Energy . . . 4
    - 1.2.1.1 Reliability, Gearboxes and Direct Drive Technology . . . 6
  - 1.2.2 Marine Energy . . . 9
    - 1.2.2.1 SeaGen . . . 10
    - 1.2.2.2 The OpenHydro Turbine . . . 10
- 1.3 Classification of Electric Machines . . . 11
  - 1.3.1 Description of the Transverse Flux Machine under Study . . . 12
  - 1.3.2 Modelling of Transverse Flux Machines . . . 16
- 1.4 Aims and Objectives . . . 17
- 1.5 Novel Contributions . . . 18
- 1.6 Outline of the Thesis . . . 18

2 Calculation of the Air-gap Magnetic Field Distribution in Electric Machines **21**
- 2.1 Introduction . . . 21
- 2.2 Reluctance Networks or Magnetic Circuits . . . 23
- 2.3 Finite Element Analysis . . . 29
  - 2.3.1 Calculation of Torque using FEA . . . 30
- 2.4 The Sub-domain Method . . . 32
- 2.5 Conformal Mapping . . . 34
  - 2.5.1 Background Theory . . . 35
  - 2.5.2 The Schwarz-Christoffel Transformation . . . 36
  - 2.5.3 Schwarz-Christoffel Toolbox for Matlab . . . 37
  - 2.5.4 Field Equations in Conformal Mapping . . . 38
- 2.6 Gibbs' Methodology . . . 39
  - 2.6.1 Single-Slot Model . . . 40
  - 2.6.2 Multiple-Slots Model . . . 41
  - 2.6.3 Limits of Application . . . 42
    - 2.6.3.1 Practical Limit . . . 43

2.6.3.2 Numerical Limit 43
2.6.3.3 Representation of the Limits 44
2.7 Summary 45

3 The Complex Permeance Framework 47
3.1 Introduction 47
3.2 Zarko's Complex Permeance 48
3.2.1 Limitations of Zarko's CP 49
3.3 Modified Complex Permeance 49
3.3.1 Proportional-Logarithmic Transformation (T_1) 50
3.3.2 Schwarz-Christoffel Transformation (T_2) 51
3.4 Effect of Curvature on the Magnetic Field 52
3.4.1 Curvature Coefficient 54
3.4.2 Magnetic Field Relations 56
3.4.3 Permanent Magnet Transformation 59
3.5 Properties of the CP Function 60
3.5.1 Analysis of $\overline{\lambda}_r$ 61
3.6 Estimation of the Coefficients of the CP Function 63
3.6.1 Analysis of the Matrix $\mathbf{X}$ 64
3.6.2 Random Sampling 69
3.7 Results 69
3.8 Conclusion 72

4 Analysis of Transverse-Flux Machines 73
4.1 Introduction 73
4.2 Torque Equation 74
4.2.1 Torque Produced by a Current Loop 75
4.2.2 Total Torque 76
4.3 Flux Factor 78
4.3.1 Flux Factor of a Single Current Loop 78
4.3.2 Total Flux Factor 79
4.4 Virtual Mutual Inductance Approach 79
4.4.1 Calculation of the Virtual Mutual Inductance 80
4.5 Circuit Parameters and Performance 82
4.5.1 Back EMF and Torque Constants 82
4.5.2 Phase Inductance 83
4.5.3 Power Factor 84
4.6 Case Study 86
4.6.1 Electrical Parameters of the Machine 88
4.6.2 Study of the current design 89
4.7 Conclusions 91

5 Calculation of Rotor Losses in Transverse-Flux Machines 93
5.1 Introduction 93
5.2 Calculation of Rotor Losses: the Traditional Approach 94
5.2.1 Solution without Eddy Currents 98
5.2.2 Calculation of Power using the Poynting Vector 98
5.2.3 The problem with the traditional approach 99
5.3 Calculation of Rotor Losses using Transfer Matrices 100
5.3.1 Transfer matrix for a conductive region 102
5.3.2 Transfer matrix for a non-conductive region 103
5.3.3 Calculation of losses 104
5.3.4 Reduction of the complexity of the problem 104

5.4 3D Effects . . . 106
5.4.1 2D Case . . . 107
5.4.2 3D Case . . . 108
5.4.3 Application to TFMs . . . 110
5.5 Asynchronous Harmonics . . . 112
5.5.1 No-Load Magnetic Field Distribution . . . 112
5.5.2 Stator's Magnetic Field Distribution . . . 113
5.6 Limitations of the complex permeance and current sheet model . . . 114
5.7 Results . . . 115
5.8 Summary . . . 118

6 Design and Optimisation of a TFM for Tidal Power Generation 121
6.1 Introduction . . . 121
6.2 Machine Topology . . . 122
6.3 Theory . . . 125
6.3.1 Torque . . . 126
6.3.2 Back emf . . . 126
6.3.3 Phase inductance . . . 126
6.3.4 Power factor . . . 127
6.4 Optimisation Philosophy . . . 128
6.4.1 Optimisation of the C-core shape . . . 130
6.4.1.1 Some remarks about the C-core shape . . . 131
6.4.2 Losses . . . 132
6.5 Work-flow of the Process . . . 132
6.6 Case Study . . . 134
6.7 Summary . . . 137

7 Conclusions and Future Work 143
7.1 Conclusions . . . 143
7.2 Future Work . . . 145

A Rotor Losses in High Speed PM Machines 161
A.1 Analysis of Slotting Models for the Calculation of No-Load Rotor Losses in PM Machines . . . 161
A.1.1 Conclusion . . . 165
A.2 Effect of Curvature on Rotor Losses . . . 165
A.2.1 Transient FEA . . . 167
A.2.2 Results and Discussion . . . 167
A.2.3 Conclusions . . . 171

B Simulation of Electro-mechanical Systems 173

C Software Developed in Matlab 175
C.1 Complex permeance function . . . 175
C.2 Calculation of the no-load asynchronous harmonics . . . 176
C.3 Class that defines a TFM . . . 181
C.4 Example of the modelling of a TFM . . . 188
C.5 Calculation of the rotor losses in a TFM . . . 190
C.6 Optimisation of a tidal turbine . . . 196

List of Figures

1.1 Four commonly used wind generator systems. 5
1.2 Nacelle of a constant speed wind turbine, specifically the NEG Micon. Source: Bundesverband Wind Energie (BWE: German Wind Energy Association, 2014). . . 7
1.3 Nacelle of a direct drive wind turbine, specifically the Enercon E-66 DD. Source: Bundesverband Wind Energie (BWE: German Wind Energy Association, 2014). . . 7
1.4 Schematic view of the SeaGen, ©2011 IEEE. 10
1.5 The 16 m prototype during construction, ©2014 IEEE. 11
1.6 Classification of electric machines. 13
1.7 Front view and cross-section of a single sided TFM. 13
1.8 Picture of the stator and the rotor of the TFM under study. 14
1.9 Dimensions of the TFM explained schematically. 15
1.10 Dimensions of the C-core in detail. 15
1.11 Path of the magnetic field depending on the current. 15
1.12 Developed model of the TFM. The positive force is shown in red and the negative one in green in two rotor positions. 16

2.1 A schematic view of a magnetic circuit. 24
2.2 Electrical analogy to the magnetic circuit shown in Figure 2.1. 24
2.3 A schematic view of a magnetic circuit with an air-gap. 25
2.4 Electrical analogy to the magnetic circuit shown in Figure 2.3. 25
2.5 A simplified synchronous machine. 26
2.6 Flux lines of the fringing magnetic field in a tooth-to-tooth configuration. 26
2.7 Magnetic equivalent circuit of an induction motor, from (Ostovic, 1986), ©1986 IEEE. 27
2.8 A node with the reluctance branches and fluxes, from (Amrhein and Krein, 2009a), ©2009 IEEE. 28
2.9 Model of the induction motor considered in (Amrhein and Krein, 2009a), ©2009 IEEE. 28
2.10 The process of finite elements, based on (Bathe, 1996). 29
2.11 Example of a PM motor divided in sub-domains, from (Zhu et al., 2010), ©2010 IEEE. 33
2.12 z-plane. 35
2.13 w-plane. 36
2.14 Example of a polygon in the z-plane transformed into the upper half plane of the w-plane. 36
2.15 Flux lines and equipotential lines obtained using the SC toolbox. 37
2.16 Developed geometry considered by Gibbs. 40
2.17 Geometry of a single slot and the corresponding air-gap magnetic flux density waveform. 40
2.18 Geometry of a machine with multiple slots and the corresponding magnetic flux density waveform. 41
2.19 Numerical and practical limits of the two methodologies as a function of the geometric variables. Also, representation of Freeman's limit. 44

3.1 Zarko's geometry, from (Zarko et al., 2006), ©2006 IEEE. 48
3.2 Conformal transformations required to obtain the magnetic field distribution in the air-gap. 49
3.3 Cylindrical geometry studied showing only one slot in the z-plane. 53
3.4 Rectangular developed model obtained after the proposed transformation in the w-plane. 54
3.5 The curvature coefficient, K_J, as a function of the ratio between the air-gap radius and the air-gap length. 56
3.6 $M(r_z) = \frac{R_g}{r_z}$ 58
3.7 Permanent magnet in the cylindrical geometry, the z-plane. 59
3.8 Permanent magnet in the rectangular developed geometry, the w-plane. 59
3.9 Geometry considered to apply the Gauss Law. 61
3.10 Points chosen to estimate the parameters of the permeance function. 65
3.11 The amplitude of the first four harmonics of the radial component of the magnetic field with $N_h = 10$ and $N_p = 5$. 66
3.12 Magnetic field distribution obtained using FEA with a scalar potential formulation. 66
3.13 The amplitude of the first four harmonics of the radial component of the magnetic field $N_h = 11$ and $N_p = 5$. 67
3.14 Function and harmonics of the example function $f(x) = a\sin(x) + b\sin(2x)$. . . . 68
3.15 The set of random points, S. In this case it consists 250 random points.. 70
3.16 $\lambda_r(\theta, r)$ in the middle of the air-gap, $r = R_g$. 70
3.17 The amplitude of the first four harmonics of the radial component of the magnetic field $N_h = 11$ and $N_p = 5$, with a set of 500 random points. 71
3.18 Radial component of the magnetic field distribution in the air-gap obtained using the CP function, quarter of the model only. 71

4.1 Developed model of the TFM. 75
4.2 Forces applied to the equivalent current loop at a distance δ. 75
4.3 Fringing around the C-core head, axial geometry considered to obtain the equivalent length. 77
4.4 Schematic view of the air-gap of the TFM under study with the equivalent current loops at a particular position of the rotor, β. 80
4.5 Schematic view of a single coil in the air-gap at the position β. 81
4.6 Phasor diagram with current only in the quadrature axis. 85
4.7 Average torque of the TFM obtained with the torque equation presented this chapter, Harris *et al.* torque equation, the value measured in the lab and 3D FEA (Harris and Mecrow, 1993; Harris and Pajooman, 1995). 87
4.8 Real part of the CP function associated to the SC transformation, $\mathrm{Re}\{\lambda_{SC}\}$, as a function of the position, θ, for three different lengths, δ. 87
4.9 Magnetic field passing through a C-core, 3D FEA model. 88
4.10 The measured flux linkage and the one obtained with the flux linkage equation proposed using the virtual mutual inductance (VMI) approach. 89
4.11 Average torque per phase and power factor as a function of the number of C-cores. 90
4.12 Air-gap inductance, L_g, and leakage inductance, L_l, as a function of the number of C-cores with the axis on the left hand side of the graph. Flux factor, K_B, with the axis in per unit on the right hand side of the graph. 90

5.1 Cylindrical current sheet model of an outer rotor PM machine with the corresponding current sheet at the stator slotless surface. 95
5.2 General model with current sheet on boundary the h. 100
5.3 Simplified representation of a given region, n. 102
5.4 Region n is divided into N_t sub-regions. 105
5.5 Paths of the eddy currents for the 2D and 3D cases. 106

5.6 Schematic representation of the developed model of the thin can with the appropriate axes. This is the geometry considered for the 2D case. 107
5.7 Schematic representation of the developed model of the thin can with the appropriate axes. This is the geometry considered for the 3D case with end effects and overhang. 108
5.8 Rotor losses in the TFM obtained using FEA at 50 Hz, $\hat{B}_{qk} = 1$ T. 115
5.9 No-load asynchronous harmonics of the TFM. 116
5.10 Stator's asynchronous harmonics of the TFM. 117
5.11 Rotor losses as a function of the mechanical speed of the rotor. 119

6.1 Picture of the tidal turbine developed at the University of Southampton. 122
6.2 3D model of the TFM topology considered for this chapter. 123
6.3 Dimensions of the C-core in detail. 124
6.4 Topology of the tidal generation system. 125
6.5 Phasor diagram with current only in the quadrature axis. 127
6.6 The flux factor, K_B, as a function of the number of C-cores for four values of d_m/g. 128
6.7 The torque optimisation function, f_{opt}, as a function of the number of C-cores for four values of d_m/g. 130
6.8 Simplified work-flow of the design optimisation process proposed. 133
6.9 Flux factor, K_B, and optimisation function, f_{opt}, for the tidal turbine under study. 134
6.10 The flux factor, K_B, and the torque optimisation function as a function of the number of C-cores for four values of d_m/g for $t/\tau = 0.25$. 138
6.11 The flux factor, K_B, and the torque optimisation function as a function of the number of C-cores for four values of d_m/g for $t/\tau = 0.3$. 139
6.12 The flux factor, K_B, and the torque optimisation function as a function of the number of C-cores for four values of d_m/g for $t/\tau = 0.35$. 140
6.13 The flux factor, K_B, and the torque optimisation function as a function of the number of C-cores for four values of d_m/g for $t/\tau = 0.4$. 141

A.1 Quarter model of the PM synchronous generator under study. 162
A.2 Complex permeance function obtained with the multiple-slots and single-slot models; radial and tangential components. 163
A.3 Magnetic field distribution in the air-gap obtained using two-dimensional static FEA and the CP function. 164
A.4 No-load amplitude of the significant magnetic induction space harmonics of time order 12 at 90 000 rpm. 164
A.5 Quarter model of the PM synchronous machines under study. 165
A.6 Complex permeance function obtained with and without curvature; radial and tangential components. 168
A.7 Eddy current density at a particular instant of time obtained using transient FEA, Machine A shown as an example. 168
A.8 Magnetic field distribution in the air-gap obtained using two-dimensional static FEA and the CP function with and without curvature. 169
A.9 Amplitudes of significant magnetic induction space harmonics, Machine A is running at 65 000 rpm and Machine B is running at 32 500 rpm. 170
A.10 No-load rotor power loss at rated speeds calculated using transient FEA. 170

B.1 Schematic electromechanical energy conversion system. 173
B.2 Schematic representation of the simulation philosophy. 174
B.3 One phase of the machine implemented in Simulink SimPowerSystems. 174

List of Tables

1.1 Renewable electricity generation in Europe, 2012. 3
1.2 Important companies in the marine energy sector (Marine Current Turbines LTD, 2017; OpenHydro Group Limited, 2017; Magallanes Renovables, S.L. , 2017; Wello OY, 2017; Andritz Hydro Hammerfest , 2017; Pelamis Wave Power, 2015; Aquamarine Power, 2015; Alstom, 2017). 9
1.3 Parameters of the TFM 14

4.1 Electrical parameters of the TFM 88

5.1 Value of K_S for the TFM 111
5.2 Rotor losses in the TFM for a field of 1 T 115
5.3 No-load rotor losses in the TFM under study 118
5.4 On load rotor losses in the TFM under study 118

6.1 Symbols of the TFM 124
6.2 Design specifications 134
6.3 Parameters of the Machines 135
6.4 Performance Comparison 136
6.5 Some examples from the automotive industry, data from (Popescu et al., 2015) . 136

A.1 Parameters of the Machine 162
A.2 No-load rotor power loss 164
A.3 Parameters of the Machines 166
A.4 No-load rotor power loss 169

Declaration of Authorship

I, Jaime Renedo Anglada, declare that this thesis entitled *Analysis of VRPM (Transverse-Flux) Machines for Renewable Energy Applications* and the work presented in it are my own and has been generated by me as the result of my own original research.

I confirm that:

1. This work was done wholly or mainly while in candidature for a research degree at this University;
2. Where any part of this thesis has previously been submitted for a degree or any other qualification at this University or any other institution, this has been clearly stated;
3. Where I have consulted the published work of others, this is always clearly attributed;
4. Where I have quoted from the work of others, the source is always given. With the exception of such quotations, this thesis is entirely my own work;
5. I have acknowledged all main sources of help;
6. Where the thesis is based on work done by myself jointly with others, I have made clear exactly what was done by others and what I have contributed myself;
7. Either none of this work has been published before submission, or parts of this work have been published as shown in the list of publications.

Jaime Renedo Anglada

Signed:

Date:

List of Publications

- J. R. Anglada and S. M. Sharkh, "Analytical calculation of air-gap magnetic field distribution in transverse-flux machines," *2016 IEEE 25th International Symposium on Industrial Electronics (ISIE)*, Santa Clara, CA, 2016, pp. 141-146. doi: 10.1109/ISIE.2016.7744880
- J. R. Anglada and S. M. Sharkh, "Modelling of Non-traditional Permanent Magnet Machines for Direct Drive Applications," *2016 CIGRE Session*, Paris (oral presentation).
- J. R. Anglada and S. M. Sharkh, "An insight into torque production and power factor in transverse-flux machines," *2016 XXII International Conference on Electrical Machines (ICEM)*, Lausanne, 2016, pp. 120-125. doi: 10.1109/ICELMACH.2016.7732515
- J. R. Anglada, S. M. Sharkh and A. A. Qazalbash, "Analysis of slotting models for the calculation of no-load rotor losses in PM machines," *2016 XXII International Conference on Electrical Machines (ICEM)*, Lausanne, 2016, pp. 1325-1331. doi: 10.1109/ICELMACH.2016.7732696
- J. Renedo Anglada; S. Sharkh, "An Insight into Torque Production and Power Factor in Transverse-Flux Machines," in *IEEE Transactions on Industry Applications*, 2017, vol.53, no.3, pp.1971-1977. doi: 10.1109/TIA.2017.2665344
- J. R. Anglada, S. M. Sharkh and A. A. Qazalbash, "Influence of Curvature on Air-Gap Magnetic Field Distribution and Rotor Losses in PM Electric Machines," in *COMPEL - The international journal for computation and mathematics in electrical and electronic engineering*, 2017. doi: 10.1108/COMPEL-05-2016-0200
- J. R. Anglada; S. Sharkh, "Analytical Calculation of the Torque Produced by Transverse Flux Machines," in *IET Electric Power Applications*, 2017, vol.11, no.7, pp.1298-1305 doi: 10.1049/iet-epa.2016.0759.
- S. M. Sharkh and J. R. Anglada, "Rotor losses in PM Synchronous Machines," *Losses in Electrical Machines and Associated Thermal Management*, UK Magnetics Society Meeting, Nottingham, 2017.
- J. R. Anglada; S. Sharkh, "Analysis of Transverse Flux Machines using a Virtual Mutual Inductance Approach," in *IEEE Transactions on Energy Conversion*, vol.PP, no.99, pp.1-1 10.1109/TEC.2017.2768298.

Acknowledgements

Firstly, I would like to express my gratitude to my supervisor, Prof. Suleiman M. Sharkh. He has guided me and kept me on track all through this long process of the PhD. Also, he encouraged me to keep on going in the moments of doubt. The outcome of this Thesis would have been very different without his support. Also, I am very grateful to my second supervisor Prof. John Atkinson, and my internal examiner, Prof. Andrew Cruden for their useful comments. I am also very grateful to my external examiner, Prof. Martyn R. Harris, for his constructive and illustrative comments during the viva; his broad experience and knowledge about this topic made me really enjoy the exam.

This work was supported by TSL Technology Ltd. and EPSRC (grant number 1426759). In particular I am very grateful to the team at TSL Technology Ltd., including Dr. Mike Yuratich and Dr. Aleks Dubas.

I would like to thank the people from the Mechatronics Group in general and in particular my office mates: Jorge, Lijun, Robert, Xingda, Mutaz, Adam, Giuseppe, Ahmed, Joe and Vorrapath. Also, I thank Ali for all the useful discussions on the topic of eddy currents.

I have to thank Iole for all her support and positive vibes during this process. I will always remember all the good moments that we lived together in Southampton, special mention to our squash and tennis matches. This stage of my life would have been very difficult without the support from my parents, Maite y Javier; and my brother Javier. I have to thank my friends from Chile, Spain and Southampton who helped me to enjoy life. Special mention to my teammates of Hong Kong Chef FC, the *Mewers*, the *Office Dudes* lunch club, *las sopas* and the Crew from Omdurman.

Finally, if you are not in a rush you might find your name here:

C	L	E	S	R	U	N	G	T	V	R	U	B	E	N	X
L	T	O	M	A	S	Q	P	R	K	W	F	G	O	P	T
E	Y	P	J	F	W	M	A	I	T	E	D	P	Z	U	K
M	G	E	U	A	S	U	C	J	P	N	T	E	X	G	I
E	Q	J	R	U	C	H	O	M	S	K	Y	P	T	Y	R
N	M	A	N	A	N	M	B	T	I	P	D	O	Z	B	S
S	R	V	S	U	L	E	I	M	A	N	P	C	F	O	T
U	R	I	H	G	I	O	L	E	R	Y	M	A	R	K	E
S	A	R	A	H	U	N	G	S	T	H	G	O	T	C	N
X	D	T	L	A	E	T	I	D	R	F	E	R	S	E	Y
S	Q	V	H	J	L	O	J	E	D	U	R	T	U	B	M
A	Z	I	M	B	G	L	O	H	K	L	T	H	O	P	E
B	F	K	Y	G	I	O	R	G	I	A	3	S	T	A	N
A	O	A	F	R	T	E	G	M	N	B	T	O	P	E	X
Z	T	H	M	T	I	T	E	Z	D	N	I	C	O	T	L

Preface

The original title of this Thesis when it was presented for the viva examination was *Analysis of Transverse Flux Machines for Renewable Energy Applications*. The author of this Thesis always preferred the name *variable-reluctance permanent-magnet* (VRPM) machine, which was coined by Prof. Martyn R. Harris, but it was decided to use the term *transverse-flux machine* because it is the term more widespread today (even we were criticised for using the term VRPM machine by some of our peers).

During the viva examination it was pointed out by the external examiner, Prof. Martyn R. Harris, that the term *transverse-flux machine* is not the best to refer to this kind of machines. This is because it is possible to design a machine with a *transverse-flux* that in reality operates (from the magnetic point of view) like a normal radial permanent magnet machine. Therefore, the term *transverse-flux machine* does not provide any information about the behaviour of the device. On the other hand, the term *variable-reluctance permanent-magnet machine* is directly linked to the electromagnetic interaction that takes place. This is because the torque is actually produced by the fact that the C-cores modulate the homopolar field (by a variation of the reluctance) to produce a heteropolar field that interacts with the magnets from the rotor.

The purpose of changing the title of this Thesis is twofold: to use the most suitable name for this kind of machines based on the underlying principle of torque production and secondly to acknowledge the contributions of Prof. Harris in this topic by using the name he prefers.

Jaime Renedo Anglada

Geneva, Switzerland

November 2017

Chapter 1

Introduction

1.1 Overview

There is great interest in electric machines with high specific torque for low speed renewable energy applications such as wind and tidal turbines. Recently, that interest has been intensified by the need of high torque machines for direct drive wind or tidal turbines.

This Thesis deals with transverse flux machines, which is a type of electric machine capable of achieving a high specific torque, as an alternative for direct drive systems. This is based on the fact that it is possible to *get rid of the gearbox* in the drive train. However, these devices present a challenge from the analysis and design point of view because their topology is very different to that of the *traditional machines*. This is because the torque production is based on the interaction of a homopolar flux with a heteropolar flux rather than two heteropolar fluxes rotating at the same speed.

Therefore, this Thesis develops background theory suitable for the analysis, modelling and design of transverse flux machines. The theory developed here is meant to be used as a *first design step* providing an insight into the system to the machine designer, which later can be refined using numerical methods such as finite element analysis.

It is worth mentioning that all through the document a particular single-sided transverse flux machine is used as a case study. However, the theory developed is completely general and could be used to study other machines.

1.2 The Role of Renewable Energy

The debate on climate change has evolved significantly in the last decades, some time ago certain sectors of society still denied the effect of greenhouse gas emissions over the environment but now their impact is broadly accepted and the discussion is focused in how to take action (Jeffrey et al., 2013; Stern, 2007; U.K. Government, 2008). The Paris Agreement (PA) is the latest example of the global scale of this problem[1]. The PA is an agreement between 193 countries dealing with the reduction of greenhouse gases emissions; this agreement is an example of the international efforts to stop climate change. The agreement was reached under the United Nations Framework Convention on Climate Change (UNFCCC) and it should start in 2020. The aims of the Paris Agreement are (United Nations Framework Convention on Climate Change, 2016):

- *Holding the increase in the global average temperature to well below 2 ^oC above pre-industrial levels and to pursue efforts to limit the temperature increase to 1.5 ^oC above pre-industrial levels, recognizing that this would significantly reduce the risks and impacts of climate change;*
- *Increasing the ability to adapt to the adverse impacts of climate change and foster climate resilience and low greenhouse gas emissions development, in a manner that does not threaten food production;*
- *Making finance flows consistent with a pathway towards low greenhouse gas emissions and climate-resilient development.*

Traditionally, the energy sector has been one of the highest producer of CO_2 in the world because of the dependency on fossil fuels. Based on the International Energy Agency (IEA) the energy sector is still very dependent on fossil fuels (coal, oil and natural gas) (International Energy Agency, 2014). In fact, a comparison of the energy mix of the world in 1973 and 2012 shows that the energy consumption went from 6106 Mtoe (mega tons of oil equivalent) to 13371 Mtoe, which is an increment of almost 120%. It is important to highlight that coal, oil and natural gas accounted for 86.7 % of the total in 1973 and 81.7 % in 2012. The dependency on these three sources decreased only by 5 % in 39 years.

If we now focus on the electricity sector we can do a similar analysis. In the electricity sector the dependency on fossil fuels in 2012 is *only* 67.9 % instead of 81.7 % in 1973 (International Energy Agency, 2014). In this context we can infer that the problem of dependency on fossil fuels is not only present in the primary energy supply but also in electricity generation. It is important to mention that besides the hydroelectric energy that accounts for 16.2 % of the total generated in 2012 all other renewable energy sources contribute less than 5 % of the total electricity generation.

The concerns over the impact of climate change due to CO_2 emissions in society has made de-carbonisation of the energy sector a priority to regulators in the European Union (EU) and internationally (Jeffrey et al., 2013). To achieve a reduction of CO_2 the EU has set ambitious goals for 2020 (Comission to the European Parliament, 2013) in what is called *The 2020 Climate and Energy Package* (European Comission, 2015), that is a set of binding legislation which aims to ensure the European Union meets its climate and energy targets for 2020. These targets, known as "20-20-20", set three key objectives for 2020:

- A 20% reduction in EU greenhouse gas emissions from 1990 levels;
- Raising the share of EU energy consumption produced from renewable resources to 20%;

[1]It seems that Trump's administration is committed to leave the accord but it is not clear to what extent this is going to impact the energy markets.

- A 20% improvement in the EU's energy efficiency.

Achieving these goals will require a significant change in the current regulation to make renewable energies competitive in the electricity market in particular. The substantial growth of renewable energy generation in recent years has relied on subsidies that reached $101 billion globally in 2012 with almost 60% of these paid in the European Union (International Energy Agency, 2013c). The risk of the energy subsidies is that they represent a high economic burden for a country and the efficiency of this inversion is not always guaranteed. For this reason the International Monetary Fund started a challenging campaign to reformulate the energy subsidy policy in all the world (Clements et al., 2013). The subsidies and the public policy in general have proven to be effective because in the last 30 years the development of the renewable energies has been very high; in 2014 renewables accounted for almost 25% of the electricity generation in the EU (European Comission, 2014).

The sources of the renewable energy in 2012 are shown in table 1.1. We can classify hydro as a *traditional* renewable energy and the rest as *non-traditional*. This classification is useful because, as it will be shown later, the increment of big scale hydroelectric energy is expected to be low in Europe.

TABLE 1.1: Renewable electricity generation in Europe, 2012.

	Hydro	Wind	Biomass	Solar	Geothermal	Marine
EU-28 [TWh]	366.4	205.8	149.4	71.0	5.8	0.5
Share (%)	45.9	25.8	18.7	8.9	0.7	0.1

In 1990 hydro was practically the only renewable energy source but by the year 2000 there was a *boom* of wind energy generation that continued until today. The influence of solar energy remains low but it is expected to increase both in the residential and the industrial context (International Energy Agency, 2013a,b,c). The total amount of hydroelectric energy has remained almost constant because in the EU countries in general suitable locations for dams are already used and normally the environmental and social impact is high due to the size of these power plants. For these reasons the amount of energy from big hydro power plants is expected to remain almost constant (U.S. Department of Energy, 2013). However, there are some interesting projects about upgrading conventional hydro power plants into variable speed and/or pumped storage hydro power plants (Janning and Schwery, 2009; Schmidt et al., 2011; Pannatier et al., 2010). Many renewable energy sources such as wind and solar can't be produced on demand. Therefore, storage capacity is needed and variable speed pumped storage power plants can be useful in that respect.

To achieve the ambitious goals proposed such as the 20-20-20 it is necessary to boost the deployment of all types of renewable energy sources. The problem is doing this without having to rely on expensive subsidies that can deteriorate the competitiveness and economic efficiency of countries. A possible solution to this problem is that the regulation instead of giving subsidies to the generation should help to make the renewables competitive and in this context the market will pull instead of being pushed by the public organisations (Jeffrey et al., 2013; Allan et al., 2014; Lawrence et al., 2013).

Wind and marine energy technologies are based on the principle that a flow of air or water moves a turbine at low speed (5-25 rpm for wind turbines and 5-150 rpm tidal turbines). Since traditional generators rotate at much higher speeds (3000-1500 rpm) it is necessary to install a gearbox in the drive train. These gearboxes are expensive, not fully reliable and the maintenance costs are high; which makes the price of the energy go up.

1.2.1 Wind Energy

In the context of renewable power generation wind energy has been the fastest growing energy technology in the world because it is one of the most cost-effective renewable source of electricity (Hansen and Hansen, 2007; Bull, 2001). Since 1995 the average growth has been almost 25 % per year and it is expected to keep growing (International Energy Agency, 2013b; U.S. Department of Energy, 2013).

Most of the installed systems at utility scale have a standard three-blade rotor (Hansen and Hansen, 2007). In terms of the electric generator there are two main concepts: geared and direct-drive (McMillan and Ault, 2010). As the name suggests the geared system has a gearbox (normally a three-stage gearbox (Hansen and Hansen, 2007)) to transform the low speed rotation (around 5-25 rpm (Semken et al., 2012)) into the high speed required by traditional generators. On the other hand, the direct-drive has a special type of generator that is designed specifically to operate at low speeds. Normally direct-drive electric generators are larger than geared ones because the size of the machine is proportional to the torque produced.

Polinder et al. (2013) did an extensive review of the current trends in the wind energy industry. The four most commonly used configurations are shown in Figure 1.1. This list is almost the same list as the one presented by Hansen and Hansen (2007) except for the system called *Type B* that is the same as the second one of Polinder's list but instead of using a power electronics converter it has a variable resistance connected to the rotor windings. This configuration is almost extinct because it is considerably more inefficient than the second one in the list presented here. A brief description of each of these technologies is shown below, based on (Polinder et al., 2013; Hansen and Hansen, 2007; Zhu and Hu, 2012a,b).

A. Constant Speed Squirrel-Cage Induction Generator

This was the most common technology in the early days of wind turbines, sometimes this system is called the Danish Concept. It consists simply in a three-stage gearbox and a squirrel-cage induction generator directly connected to the grid. In this system there is no control of the speed therefore variations in the wind speed can make it inefficient. The main strength of this design is that all the components are standard making it very cheap. Other strength is that the squirrel-cage induction generator is very robust and reliable because of its simplicity.

B. Doubly Fed Induction Generator

This system became very popular after 1996 when many manufacturers moved from the constant speed squirrel-cage to this configuration. This system consists of a multi-stage gearbox, a doubly fed induction generator and a power electronic converter to feed the rotor winding. The converter has a rated power of about 25 % of the rated power of the generator, enabling to operate in speeds from 60 % to 110 % of the rated speed of the machine with the consequent improvement of efficiency. An important disadvantage of this

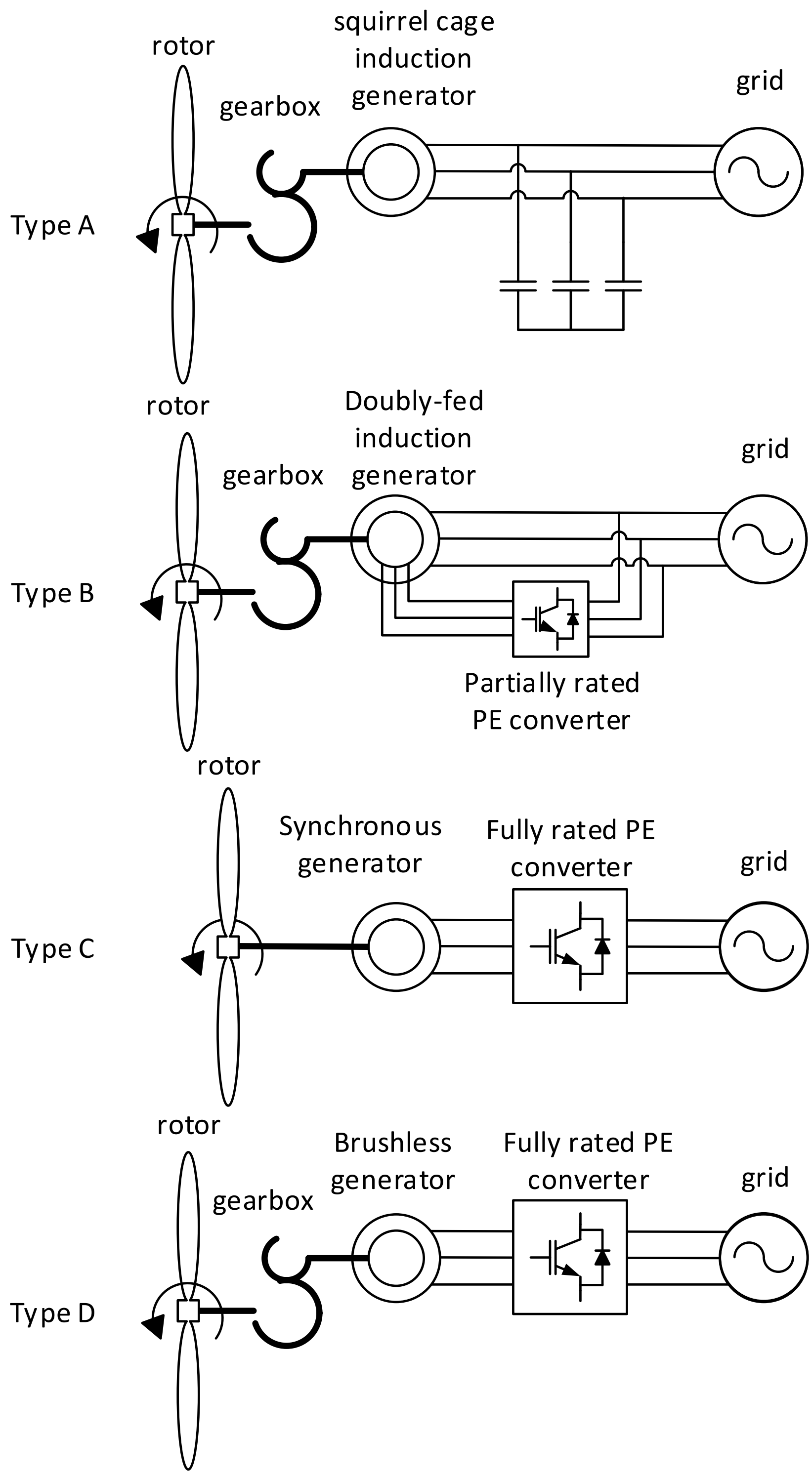

FIGURE 1.1: Four commonly used wind generator systems.

system was noticed when the operators of the power system imposed voltage-ride through requirements on wind farms[2].

C. Direct Drive Generator System

Since 1992 there have been manufacturers using gearless generator systems. The generator itself is a synchronous machine and it is necessary to have a fully rated power electronic converter for the grid connection. In the past most of the direct-drive generators were electrically excited but now there are several designs using permanent magnets. The main advantage of the direct drive generator systems is that by getting rid of the gearbox the system is more reliable (in theory) and the maintenance costs are lower, however this needs to be studied in more detail. Section 1.2.1.1 analyses the problem of gearboxes and direct drive generators extensively.

D. Brushless Generator with Gearbox and Full Power Converter

This system is an evolution of B that improves the voltage-ride through capability of wind farms. The system is made of a gearbox, a brushless generator and a fully rated power converter. The main disadvantage of this configuration is that the power converter is more expensive that the one required in B and decreases the overall efficiency.

Choosing between these systems for a particular project is a very important step in the design and still there is not a clear winner (Polinder et al., 2013; McMillan and Ault, 2010; Hansen and Hansen, 2007). The next section presents an analysis of the problems of gearboxes and the advantages of a direct drive configuration.

1.2.1.1 Reliability, Gearboxes and Direct Drive Technology

Reliability is one of the key issues for wind turbines, particularly in off-shore power plants (Polinder et al., 2013; McMillan and Ault, 2010; Tavner et al., 2006). Gearboxes are one of the most expensive components of the generator system and several failures in this component have generated uncertainty in the industry (Echavarria et al., 2008; Spinato et al., 2009; Arabian-Hoseynabadi et al., 2009). The typical configuration of a geared wind turbine is presented in Figure 1.2. It can be appreciated that it has a low speed shaft connected to the rotor spinner and the gearbox to increase the rotation speed of the shaft of the traditional generator.

The alternative to the geared drive train is the direct drive configuration shown in Figure 1.3. The generator in this case is directly connected to the low speed shaft; it can be appreciated that the generator is considerably bigger in diameter than in Figure 1.2. Also the direct drive electric generator can be more complicated and more expensive than in the geared one.

In the literature there is a very high number of publications suggesting that direct drive generators specifically designed for wind turbines (Grauers, 1996; Semken et al., 2012; Ran et al., 2011; Zavvos et al., 2013; Polinder et al., 2006; Spooner et al., 2005; National Renewable Energy Laboratory, 2010; Bang and Polinder, 2008; Bang et al., 2008; Polinder et al., 2007). Almost every one of these publications states that a direct drive system is inherently more reliable than

[2]The author believes that the name “Doubly Fed Induction Generator” is an inaccurate and misleading name because there is nothing being induced since the frequency of the rotor currents is actively controlled. A more accurate name would be simply doubly fed asynchronous generator.

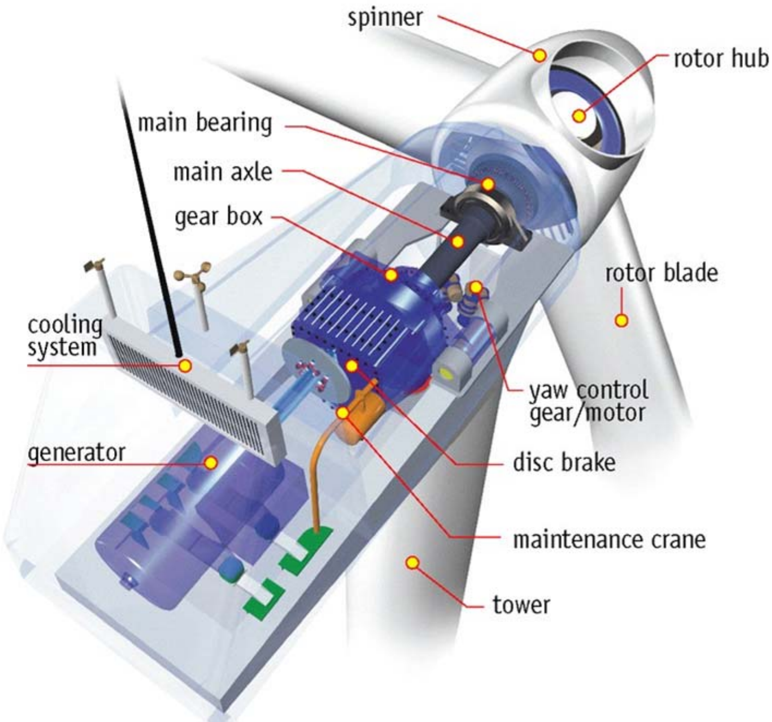

Figure 1.2: Nacelle of a constant speed wind turbine, specifically the NEG Micon. Source: Bundesverband Wind Energie (BWE: German Wind Energy Association, 2014).

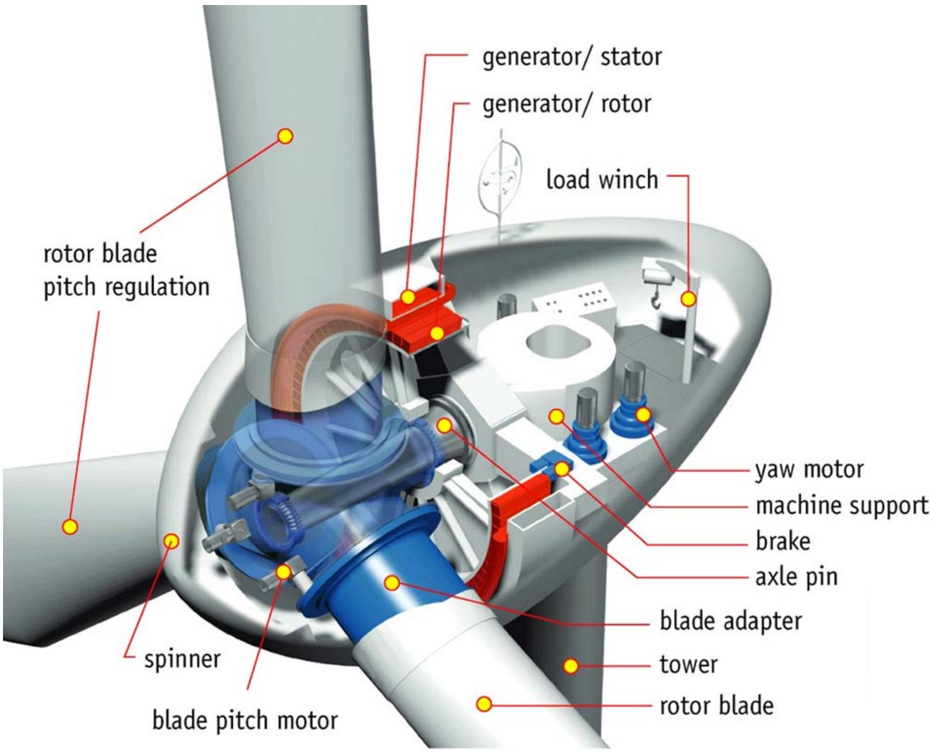

Figure 1.3: Nacelle of a direct drive wind turbine, specifically the Enercon E-66 DD. Source: Bundesverband Wind Energie (BWE: German Wind Energy Association, 2014).

a geared one because of the long history of failures in the gearbox (Echavarria et al., 2008; Windpower Monthly, 2005; Rasmussen et al., 2004). However, in the literature there is no conclusive scientific proof of this assertion. Furthermore, there are some articles that suggest that reliability of direct drive wind turbines is almost the same as geared turbines or even worse (McMillan and Ault, 2010; Echavarria et al., 2008; Spinato et al., 2009; Arabian-Hoseynabadi et al., 2009).

To understand the widespread belief that gearboxes are diminishing the overall reliability of wind turbines we need to move to the late 1990's when massive series of failures in the gearboxes of the NEG Micon brought the company close to bankruptcy (Windpower Monthly, 2005). The causes of these failures are still not clear even though wide ranging research has been carried out (Rasmussen et al., 2004; Spinato et al., 2009). Rasmussen *et al.* suggested that the failure was probably caused by the misalignment of the bearings. On the other hand, it was suggested that the problem of gearboxes was partly due to the fast development of the industry when in reality suitable gearboxes for the bigger turbines simply did not exist before (Windpower Monthly, 2005); this idea is consistent with Rasmussen's claim. A study of the different gearboxes of wind turbines was reported in (National Renewable Energy Laboratory, 2004, 2003).

Despite all these problems some studies state that geared machines are still more reliable than direct drive machines (Echavarria et al., 2008; Arabian-Hoseynabadi et al., 2009; McMillan and Ault, 2010). Then why is there such an interest in the development of direct drive systems? The answer to this question can be found in (Spinato et al., 2009). Spinato *et al.* postulate that direct drive systems are not necessarily more reliable. However, the gearbox technology is mature and substantial improvements are not expected. On the other hand, there is not a standard solution for the direct drive generators, which implies that the industry is not mature yet and revolutionary concepts are expected to appear over time. The following is a summary of the reasons why direct drive technology will remain of interest in the future (Spinato et al., 2009):

- Direct drive systems are not necessarily more reliable than geared systems. However, the failures in the gearbox can be considered *catastrophic* and the operation hours lost for repair/replacement are very high.
- The gearbox industry is mature and substantial improvements are not expected in the future.
- The failure rates in direct drive generators is higher than in traditional generators. However, the industry is not mature (there is not a single technology that stands out amongst the rest) therefore revolutionary concepts are expected to appear.
- The hours of operation lost by a failure in the generator are lower than in a gearbox failure because the repair is simpler. Therefore the total downtime hours produced by a failure in the generator are lower.
- In direct drive systems a full scale power converter is required and the failure rate of this device is high. Currently the development of power electronics is extremely high therefore we expect an improvement of the reliability of these devices.

This section has given a very brief overview of the wind energy industry, including the history and the challenges for the future. The main idea is that if we want to keep increasing the presence of the wind in the energy mix we need to make it more competitive from the economic point of view. In this context the direct drive concepts are very promising because even though they have not proven yet that they are more reliable the technology is moving very fast and year after year many new concepts will appear (Grauers, 1996; Semken et al., 2012; Ran et al., 2011; Zavvos et al., 2013; Polinder et al., 2006; Spooner et al., 2005; National Renewable Energy Laboratory, 2010; Bang and Polinder, 2008; Bang et al., 2008; Polinder et al., 2007).

1.2.2 Marine Energy

The marine energy sector is still at a very early stage and besides the case of Scotland the share of the energy mix is almost insignificant in the rest of the world (International Energy Agency, 2013c, 2014; Jeffrey et al., 2013; Lawrence et al., 2013). But there is a strong effort both from governments and the industry to develop this technology because it has several positive aspects like high predictability, higher power density and therefore smaller turbines than those of wind generators. In addition, it can be implemented in places where there is no social impact. One of the most important research centres in the world is the European Marine Energy Centre in Orkney, Scotland (European Marine Energy Centre (EMEC) Ltd, 2017), where both industry and academia can test prototypes in real conditions. Some of the most relevant companies in the marine energy sector are shown in table 1.2.

Table 1.2: Important companies in the marine energy sector (Marine Current Turbines LTD, 2017; OpenHydro Group Limited, 2017; Magallanes Renovables, S.L. , 2017; Wello OY, 2017; Andritz Hydro Hammerfest , 2017; Pelamis Wave Power, 2015; Aquamarine Power, 2015; Alstom, 2017).

	Location	Technology
Aquamarine Power	Edinburgh, UK	Wave energy
Pelamis Wave Power	Edinburgh, UK	Wave energy
ScottishPower Renewables	Glasgow, UK	Wave energy
Wello Oy	Finland	Wave energy
Openhydro	Ireland	Tidal energy
Magallanes Renovables	Spain	Tidal Energy
Alstom (now GE)	USA	Tidal energy
Andritz Hydro Hammerfest	Norway	Tidal energy

Pelamis Wave Power went into bankruptcy in December 2014 and Aquamarine Power did the same in October 2015. Alstom was acquired by GE and its cooperation with EMEC ceased. Also, Openhydro was acquired by DCNS in 2013. All these rapid changes in the market show that the marine energy sector is a *hot topic*.

The marine energy industry has similarities with the wind energy industry, in particular the tidal energy devices. Most tidal energy devices are made of a turbine connected to a generator directly or through a gearbox. As in the case of the wind, the tides flow very slowly (around 1 m/s) and hence the ration speed of the turbines is low (from 10 to 150 rpm normally). Therefore, either a gearbox to increase the rotation speed of the shaft or special direct drive generators are needed. The problems of reliability in this case are critical because a repair requires very complicated operations underwater in places with strong currents. For these reasons the direct drive systems are even more interesting in this case than in wind turbines.

The following sections show two devices for harvesting energy from the sea to give the reader a general idea about what is happening in the industry and academia.

1.2.2.1 SeaGen

The SeaGen was the first commercial scale tidal generator in the world connected to the grid (Marine Current Turbines LTD, 2017); it is installed in Strangford Lough, Northern Ireland. It has a rated power of 1.2 MW using two turbines with a diameter of 16 m each. There are plans to scale-up this project to 20 m turbines and 2 MW of rated power. Figure 1.4 shows a general view of the turbines and the generator system.

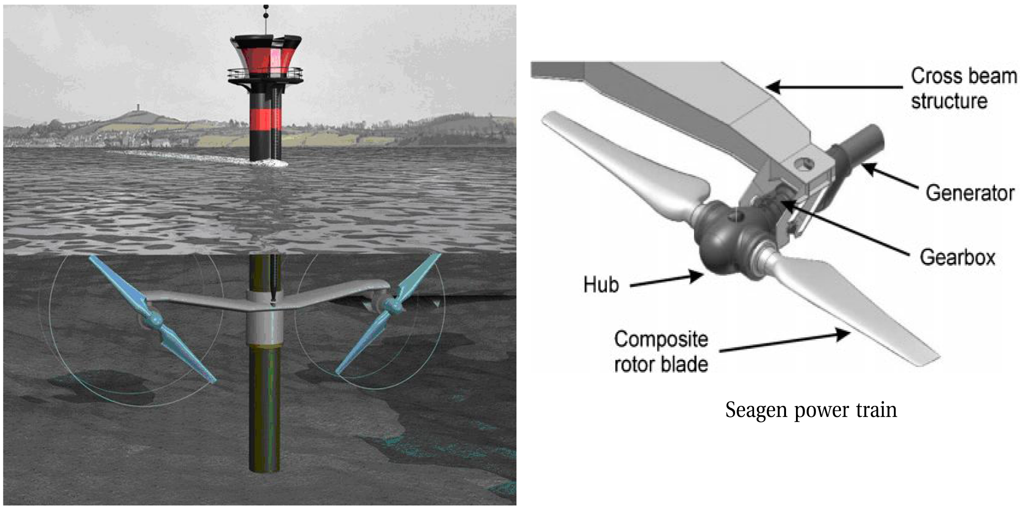

Figure 1.4: Schematic view of the SeaGen, ©2011 IEEE.

The drive train has a very similar topology to the wind turbine system. One of the *advantages* of this particular design is that the turbines can be lifted to the top of the tower for maintenance or repair. According to the manufacturer each six months a group of people need to bring a hydraulic system for lifting the two turbines for maintenance and every 5 years an industrial vessel with a crank has to come to replace the complete drive train (Marine Current Turbines LTD, 2017; Keysan et al., 2011; Douglas et al., 2008).

One very interesting project carried out in the University of Edinburgh aims to replace the geared generator with a direct drive machine. Muller *et al.* developed what is called the C-GEN that is a novel permanent magnet generator to reduce the overall mass of the system, in which the electromagnetic and structural design are integrated (Hodgins et al., 2009; Keysan et al., 2012; Mueller et al., 2007; Ran et al., 2011; Subiabre and Mueller, 2011).

1.2.2.2 The OpenHydro Turbine

OpenHydro is a company based in Dublin that has been in the industry since 2005. The OpenHydro concept is very interesting because the electric machine and the turbine are one integrated design (OpenHydro Group Limited, 2017). The electric machine is in the outside ring and not in the axis of rotation in a similar way as the marine thrusters developed by Sharkh *et al.* (Sharkh et al., 2004).

Figure 1.5: The 16 m prototype during construction, ©2014 IEEE.

The generator itself has been designed specifically for this application and it is direct drive, that aims to improve reliability and avoid the problems of short life-cycle and high maintenance costs of the SeaGen. The large diameter and the non-traditional topology produce a high torque machine suitable for direct drive (Baker et al., 2014; Villegas and Cawthorne, 2013).

It is important to mention that in the design process it was considered *impractical* to fit water seals so the generator operates with a water-gap instead of an air-gap (Baker et al., 2014). To hold the turbine in place with the water-gap the systems has magnetic bearings (Spooner and Dunne, 2011). This is an interesting solution but of course requires a high amount of magnetic material that increases the overall cost of the system. There are almost no scientific publications about this system and for this reason it is not possible to assess its performance. However, it is one of the most successful marine turbine in the market.

1.3 Classification of Electric Machines

Figure 1.6 displays graphically a classification of electric machines. In grey we have the traditional machines: DC machines, induction machines and electrically excited (EE) synchronous machines; these devices are analysed extensively in (Kundur, 1993; Fitzgerald et al., 2003; Matsch, 1972; Say, 1965; Hendershot and Miller, 2010) and a detailed description of them is outside the scope of this document. The reluctance machines are shown in light orange, the characteristics of them can be found in (Lovatt, 2005). In green we have the permanent magnet (PM) machines that are the main topic of this Thesis. We can define three sub-classes of PM machines depending on the flux path:

- **Radial flux**: They are probably the most common type of PM machine. The concept is very similar to the synchronous machines but instead of having an electrical excitation there are permanent magnets (Hendershot and Miller, 2010).
- **Axial flux**: As the name suggests, the magnetic flux is parallel to the axis and in some cases it has a toroidal slotless stator, some examples of these machines are described in (Polinder et al., 2013).
- **3D flux**: In the literature this kind of machines is referred as *Transverse Flux Machines* (Harris and Pajooman, 1995; Harris et al., 1996, 1997a; Pajooman, 1997; Zhang et al., 2014; Kastinger, 2002; Blissenbach and Viorel, 2003; Kang et al., 2003; Ibala et al., 2011; Bang et al., 2008; Yang et al., 2012; Kang and Weh, 2008; French et al., 2002; Polinder et al., 2005; Ueda et al., 2013; Polinder et al., 2003). We included as 3D flux machines because there is not a single standard characteristic that these machines share except that the magnetic field follows a path that is 3-dimensional (not like in the previous two sub-classes). Inside this category there are machines that have a high torque capability like the variable-reluctance permanent-magnet (VRPM) machine. For air-cooled TFMs, like the one described in (Pajooman, 1997), the torque density[3] is between 30 to 50 kNm/m^3 when for a traditional machine with the same type of cooling this value is between 10 17 kNm/m^3.

1.3.1 Description of the Transverse Flux Machine under Study

This section shows a particular VRPM or transverse flux machine (TFM) built at the University of Southampton that will be used all through the document as a case study. This machine has a very simple structure which makes it robust, easy to construct and reliable but on the other hand it has some issues regarding its low power factor. Furthermore, it has been studied in detail in the past, which makes it the ideal candidate to apply the theory developed in this Thesis.

The magnetic topology of this machine is similar to that of claw-pole machines. Fig. 1.7 shows the radial and axial cross-sections of the machine built at the University of Southampton (Harris and Mecrow, 1993; Harris and Pajooman, 1995; Harris et al., 1996, 1997a; Pajooman, 1997). The stator has two phases comprising a circular coil each, linking and magnetising 20 laminated C-cores which modulate the armature's magnetic field to produce a fundamental heteropolar (40 poles) harmonic in the radial direction. The number and width of the C-cores has been carefully selected to maximise the flux utilisation factor and the torque produced by the machine.

The outer rotor comprises a cylindrical yoke with 4 arrays of 40 heteropolar magnets each, glued to the inside surface. Each phase is associated with two arrays of magnets: one array positioned over the left-hand C-core legs and the other array, which is spatially anti-phase with the first, is positioned over the right-hand C-core legs. The two sets of magnet arrays corresponding to the

[3]The torque density defined as torque per volume.

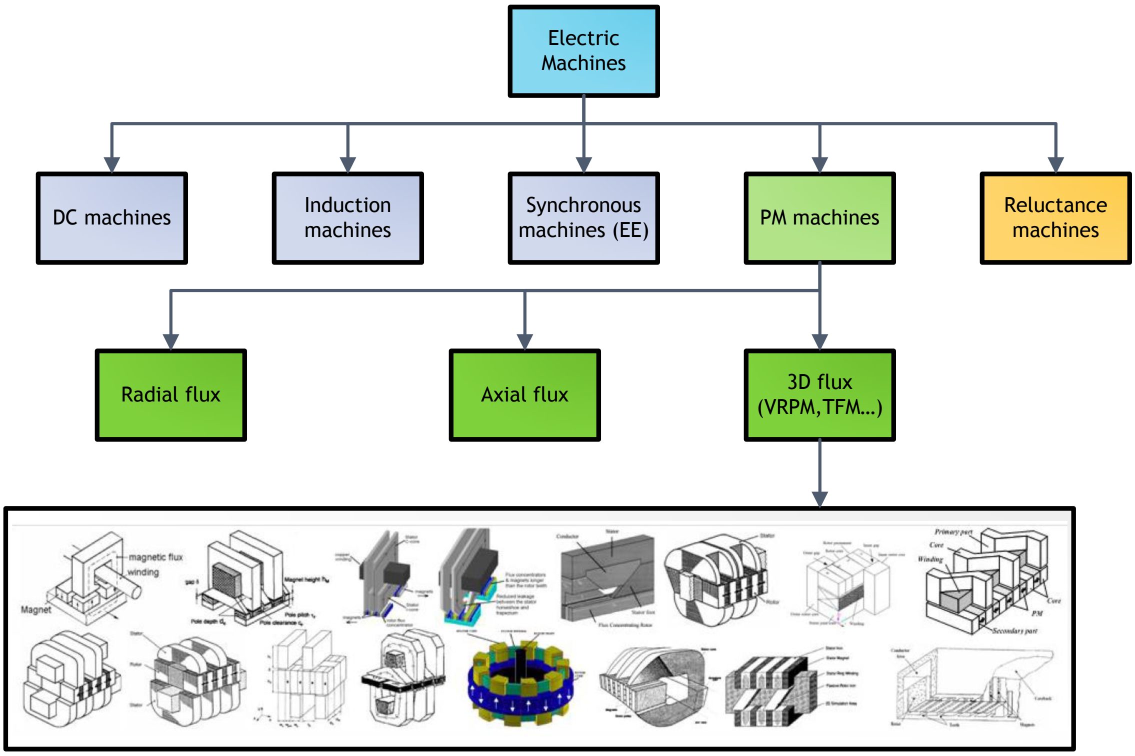

Figure 1.6: Classification of electric machines.

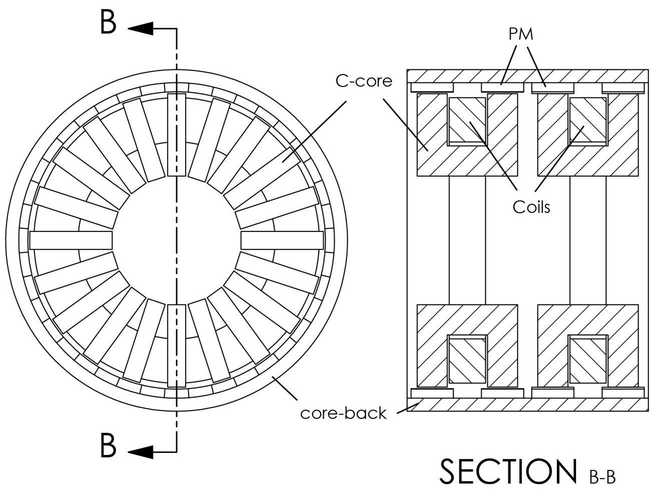

Figure 1.7: Front view and cross-section of a single sided TFM.

two phases are spatially shifted by 90 electrical degrees (alternatively, the two sets of C-cores could be spatially shifted by 90 electrical degrees). The radial heteropolar flux harmonic interact with the magnets to produce useful torque. The aligned position is defined as the position of the rotor in which the flux passing through the C-cores is maximum.

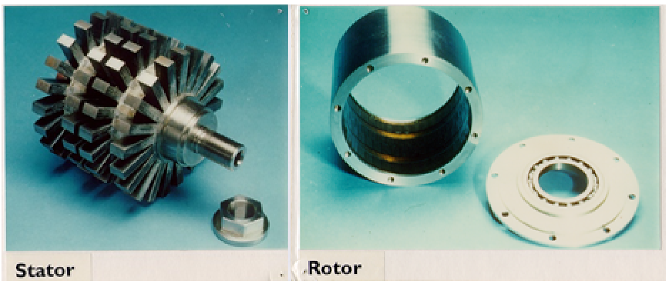

FIGURE 1.8: Picture of the stator and the rotor of the TFM under study.

Figure 1.8 shows a picture of the prototype machine. The key geometrical parameters of this device are shown in table 1.3, which also defines the symbols used. The value of the magnetic gap, g_z, is calculated as

$$g_z = d_m + c_g. \tag{1.1}$$

TABLE 1.3: Parameters of the TFM

Quantity	Symbol	Value
Stator radius	R_s	73 mm
Rotor radius	R_r	78.5 mm
Clearance gap	c_g	1 mm
Magnet thickness	d_m	4.5 mm
Magnet axial length	L_{mag}	21 mm
C-core head width	l_{core}	15 mm
C-core axial length	w_s	50 mm
C-core height	h_s	41 mm
C-core slot width	w_c	20 mm
C-core slot height	h_c	24 mm
Winding clearance	h_{co}	2 mm
Pole pitch	θ_λ	18^o
Tooth pitch	θ_t	7.02^o
Slot pitch	θ_s	10.98^o
Number of C-cores	N_c	20
Number of turns	N_w	230
Number of phases	q	2
Magnetisation	$\mathcal{M}$	$\sim$ 835 kA/m

The principle of operation is based on the variation of the reluctance with the position, seen from the rotor side, because of the C-cores. Figure 1.11 shows schematically the path of the magnetic field in two different positions. If there is a current that goes out of the paper (dot in the figure) because of the *right hand rule* the magnetic field will be counter-clockwise and there will be an electromagnetic force that will try to move the rotor towards the magnets that create a magnetic field in the same direction.

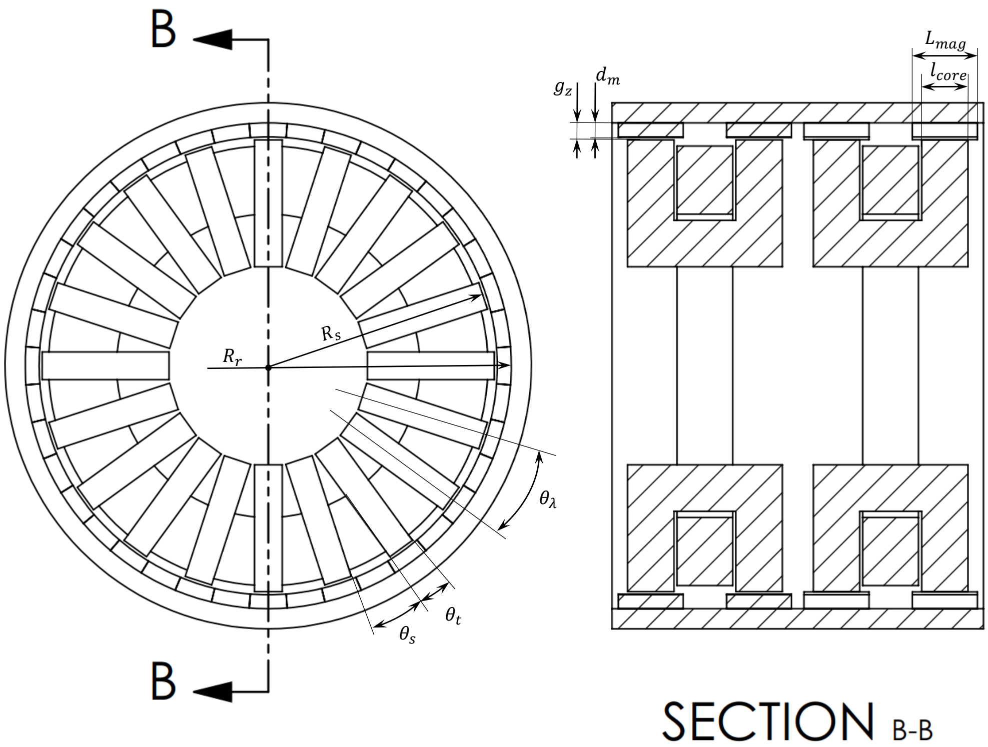

FIGURE 1.9: Dimensions of the TFM explained schematically.

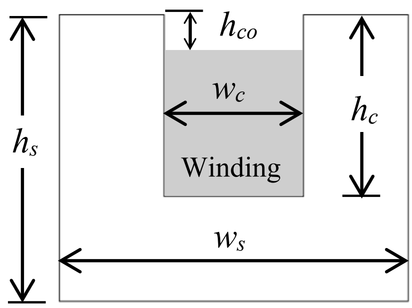

FIGURE 1.10: Dimensions of the C-core in detail.

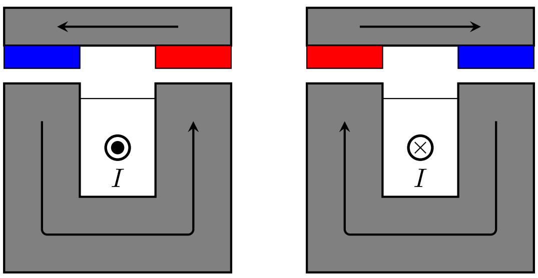

FIGURE 1.11: Path of the magnetic field depending on the current.

When the current goes *into the paper* the magnetic field produced will be clockwise and the electromagnetic force will try to align with the magnets on the opposite way than the previous case.

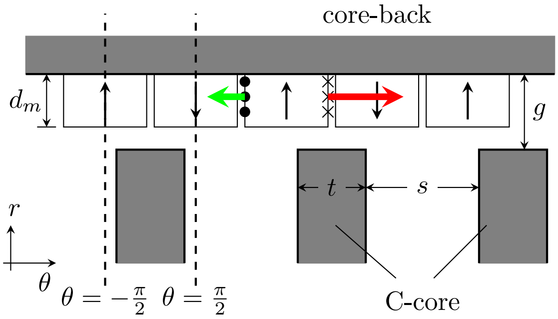

(a) Maximum torque position with a positive current.

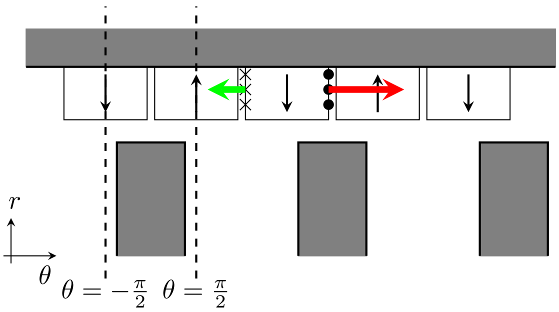

(b) Maximum torque position with a negative current.

FIGURE 1.12: Developed model of the TFM. The positive force is shown in red and the negative one in green in two rotor positions.

Figure 1.12 shows the developed model of the air-gap of the TFM with the equivalent currents shown as dots and crosses (shown only for one PM). Figure 1.12 shows the maximum torque position for a positive current (flux going up in subfigure a) and the maximum torque position for a negative current (flux going down in subfigure b).

With the appropriate current waveform with more than one phase this machine can produce a net positive torque. The machine built in Southampton has two phases with 90 electric degrees of difference and 20 C-cores per phase, in each phase there are two rows of 40 magnets with alternating polarity.

1.3.2 Modelling of Transverse Flux Machines

The modern trend to study machines with complicated geometries such as TFMs (Gieras, 2005; Keysan et al., 2012; Kang and Weh, 2008; Yang et al., 2012; Baker et al., 2014; Zhang et al., 2014; Doering et al., 2015; Liu et al., 2015; Wan et al., 2015; Dobzhanskyi and Gouws, 2016) and claw pole machines (Washington et al., 2012; Baker et al., 2012; Ahmed et al., 2014; Deodhar et al., 2015; Washington et al., 2016) is to use 3D CAD modelling and numerical methods like finite element analysis (FEA). This approach can be conveniently complemented with optimisation algorithms, particularly evolutionary genetic algorithms, which have been used widely in this area (Pompermaier et al., 2012; Zhang et al., 2016; Oh and Kwon, 2016). However, the insight provided by numerical methods is not as deep as that provided by analytical methods and the combination of 3D CAD modelling and 3D FEA tends to be more time consuming. Therefore, there remains significant interest in analytical methods that can be used at the initial design optimisation stage to produce nearly optimal models that can be refined further using FEA, which significantly reduces time and effort.

The computational capability of computers has improved (and keeps on improving) at a fast pace. Consequently, the simulation time keeps reducing accordingly. However, when we state that 3D FEA combined with 3D CAD modelling is time consuming we are talking about the total time of the process. Two-dimensional geometries can be easily parametrised but 3D geometries (such as the topologies of TFMs) have many geometrical parameters; which complicates the geometrical modelling significantly. Therefore, the overall time of the process is high.

The design of brushless permanent magnet (PM) machines is a complex iterative process in which many factors have to be taken into account. However, when designing traditional PM machines there are several analytical expressions to obtain a quick estimation of the performance of these devices before refining the final design with more complicated methods such as FEA (Hendershot and Miller, 2010; Tapia et al., 2013). Because of the three-dimensional nature of TFMs the number of free geometrical parameters is high; which means that the approach that uses genetic algorithms combined with 3D FEA may not be feasible (Zhang et al., 2016; Oh and Kwon, 2016). Furthermore, the simple analytical expressions derived for traditional PM machines are not always suitable for the analysis of TFMs because of their different topology and principle of operation.

1.4 Aims and Objectives

In general terms, this Thesis deals with the analysis, modelling and design of transverse flux machines suitable for renewable energy applications. In particular, the TFM developed at the University of Southampton and described in section 1.3.1 will be used as a case study throughout the document.

The specific objectives of the research presented in this Thesis are:

- Develop an analytical framework based on the complex permeance function to obtain the magnetic field distribution in the air-gap of homopolar transverse flux machines.
- Implement the complex permeance function in a toolbox based on Matlab.
- Investigate in depth the parameters, such as the slotting model and curvature, that influence the accuracy of the complex permeance framework developed.
- Generalise the torque equation proposed by (Harris and Mecrow, 1993; Harris and Pajooman, 1995; Harris et al., 1996; Pajooman, 1997) and combine it with the complex permeance framework.
- Develop a methodology to calculate the flux linkage and back emf in transverse flux machines.
- Study the relationship between torque and power factor, which tends to be low, in transverse flux machines.

- Study the application of the current sheet model for the calculation of rotor losses in transverse flux machines. In particular, investigate the usage of transfer matrices to reduce the complexity of the problem.

- Establish some *design guidelines* for transverse flux machines based on the background theory developed and provide an insight into the optimisation process of these devices.

1.5 Novel Contributions

The following novel contributions are presented in this Thesis:

- A functional Matlab-based framework using the complex permeance function has been successfully developed (Anglada and Sharkh, 2016a). This toolbox has been used to study the effect of curvature (Anglada et al., 2017) and the slotting model considered (Anglada et al., 2016) for the calculation of rotor eddy-current losses in high speed PM machines.

- A generalization of Harris *et al.*'s torque equation has been developed, validated and implemented in a Matlab-based toolbox (Anglada and Sharkh, 2017b).

- A virtual mutual inductance approach has been proposed for the calculation of the flux linkage. This approach has been validated using 3D FEA and experimental data (Anglada and Sharkh, 2017a).

- Using the torque equation and the virtual mutual inductance approach it has been proven that the low power factor of transverse flux machines is not due to leakage in the classical way, as many authors sustain, but due to the *ineffective use of the magnetic flux* (Anglada and Sharkh, 2016b, 2017c).

- The cylindrical multilayer current sheet model has been reformulated using transfer matrices. The approach using transfer matrices allow us to study geometries with any number of layers without increasing the complexity of the problem significantly.

- An optimisation methodology based on a trade-off between torque density and power factor has been proposed. Several generic curves for single-sided TFMs are shown in this Thesis but the principle is completely general and can be applied to other topologies.

- All the methodologies described in the previous bullet points have been implemented in a *transverse flux machine* optimisation software based on Matlab. The case study is a tidal generator.

1.6 Outline of the Thesis

The first part of this Thesis is an introduction to the broad field of electric machines for renewable energy applications. Chapter 1 includes an overview of the scope of this document, the context of the energy sector with particular emphasis on wind and tidal energy, an introduction to transverse flux machines, and the aims and objectives. Chapter 2 shows the most commonly used methods for the calculation of the magnetic field distribution in the air-gap of electric machines.

Chapter 3 shows the implementation of the complex permeance function for the homopolar field distribution of transverse flux machines. The expressions obtained here for the magnetic field distribution in the air-gap are used in the following chapters for the calculation of torque, back emf, power factor and rotor losses.

Chapter 4 describes a generalisation of Harris *et al.*'s torque equation (Harris and Mecrow, 1993; Harris and Pajooman, 1995; Harris et al., 1996; Pajooman, 1997) and a novel equation for the calculation of flux linkage (and back emf) of transverse flux machines. These two expressions are then used to illustrate the problem of the low power factor of these machines.

Chapter 5 deals with the calculation of eddy current losses in general but applied to transverse flux machines. The most important part of this chapter is the usage of transfer matrices in the formulation of the problem to reduce the complexity.

Chapter 6 puts together the methodologies presented in chapters 3, 4 and 5 to design a transverse flux machine for tidal power generation. This chapter illustrates how to use the methodologies developed in previous chapters for the preliminary design of transverse flux machines.

Chapter 7 shows the conclusions and future work.

Chapter 2

Calculation of the Air-gap Magnetic Field Distribution in Electric Machines

2.1 Introduction

The magnetic flux-density distribution in the air-gap of an electric machine determines performance parameters like torque, induced electromotive force and eddy current losses. If the magnetic field distribution in the air-gap is fully known, then all the performance parameters can be readily obtained. Obtaining the magnetic field distribution in the air-gap is basically achieved by solving Maxwell's equations with some particular boundary conditions. However, the complex topologies of rotating electric machines mean that the boundary conditions are not *easy to handle*. Therefore, there are several methods, both analytical and numerical, for calculating the magnetic field distribution. The aim of this chapter is to review the most relevant methodologies to provide theoretical foundations for the following chapters.

In the early days of the electric machines as we know them today (the transformer, the induction machine, the DC machine and the synchronous machine) the design was almost based on the *intuition* of the engineer. Most of the documents written by Nikola Tesla contain very little quantitative analysis about the performance of such devices (Tesla, 1888a,c,b, 1896). Almost ten years later, Charles Proteus Steinmetz developed the fundamental theory of AC phenomena and rotating machines using complex numbers (Steinmetz, 1894, 1897; Alger and Arnold, 1976)[1]. However, most of Steinmetz's work on magnetic fields was based on empirical formulae that relied on direct observation and he did not attempt to calculate analytically the electromagnetic field distribution.

Carter was one of the first to analyse quantitatively the problem of the electromagnetic fields in rotating electric machines; he suggested a method based on conformal mapping that transformed the slotted geometry of the air-gap into a slotless one in which the field could be calculated. He

[1] Evidence suggests that Steinmetz was the first one to use the letter j to represent the 90^o shift.

defined a coefficient to quantify the effect of slotting on the mean value of the magnetic field waveform (Carter, 1900, 1926). However, the transformation from the slotted geometry into the slotless one is a Schwarz-Christoffel (SC) transformation that does not have an explicit expression for complicated domains (Driscoll and Trefethen, 2002) which makes the practical application of this method difficult. Until 1929 the analysis of electric machines was mainly based on empirical and equivalent circuit methods when Hague (1917) presented several methods to analyse the magnetic field distribution produced by currents with different boundary conditions (O'Connell and Krein, 2009). The main disadvantage of this method was that the field was expressed as infinite series, which are more complicated to handle. Gibbs (1958) presented two different methods to account for slotting based on conformal mapping, one method was a simplification considering infinitely wide teeth and the other one takes into account the neighbouring slots. Freeman (1962) applied Gibbs' methods to a range of practical geometries and expressed the distribution as a Fourier series showing the coefficients in graphs as a function of the normalised parameters of the air-gap. The main disadvantage of Gibbs' methods is that to calculate the conformal map it is necessary to do a Schwarz-Christoffel (SC) transformation like in Carter's method.

The appearance of numerical methods like finite element analysis (FEA) allowed machine designers to have very accurate solutions for the air-gap magnetic field even considering the non-linear behaviour of materials. However, the process involved in such numerical methods tends to be time consuming and in general it is difficult to gain an insight into the system under study unless several geometries are analysed; some numerical solvers provide tools for parametric analysis for this purpose. Numerical methods are very useful tools for the validation and the refinement of the final design. But, analytical methods remain very useful procedures for an initial design combined with an optimisation based on the insight provided.

Recently two analytical methods have been suggested in order to obtain an accurate solution of the magnetic field in the air-gap: the sub-domain method and the complex permeance method. In the sub-domain method the air-gap geometry is separated into simpler sub-domains; the expression of the field for each of them and the field distribution is obtained by applying the appropriate boundary conditions at the interface (Liu and Li, 2007; Liu et al., 2008; Dubas and Espanet, 2009; Wu et al., 2010a; Zhu et al., 2010; Wu et al., 2010b, 2011, 2012b,a; Lubin et al., 2013), see section 2.4. This method provides an accurate solution for the magnetic field but the computation time is long because the problem has to be solved in each position of the rotor. Also, the qualitative interpretation of the results of the sub-domain method is not easy due to the inherent mathematical complexity of the formulation.

The complex permeance method proposed by Zarko *et al.* (Zarko et al., 2006; Boughrara et al., 2009a,b, 2013) uses conformal mapping to obtain a function that modulates the magnetic field distribution from the slotless configuration that was previously obtained by Zhu *et al.* (Zhu et al., 1993; Zhu and Howe, 1993a,b,c; Zhu et al., 2002). One of the main disadvantages of the complex permeance method proposed by Zarko is that the computation time is relatively high because of the necessity of evaluating the permeance function at a great number of points to generate the whole waveform. This method is described in detail in chapter 3 where we show just a particular application of the CP method to TFMs.

The aim of this chapter is to review the most relevant methods used to calculate the magnetic field distribution in the air-gap of electric machines. Section 2.2 shows the most simplified method and probably the most common as well; it is based on a 1-dimensional reluctance network. Section 2.3 discusses the basis for FEA applied to the field of rotating electric machines. Section 2.4 presents the sub-domain method briefly; a simple example is given. Section 2.5 describes the use of conformal mapping to solve Maxwell's equations. This section is particularly important because the theory developed in the following chapters is based on conformal mapping. Section 2.6.3 is a natural extension to the previous section that gives a clear criterion to choose between single-slot and multiple-slots methods. It is important to point out that this is the first time that a clear criterion is expressed based on a theoretical background; this is an original contribution by the author of this Thesis (Anglada et al., 2016). Finally, section 2.7 summarises the chapter.

2.2 Reluctance Networks or Magnetic Circuits

To obtain the magnetic field distribution in the air-gap of an electric machine Maxwell's equations with very complicated boundary conditions need to be solved. In most of the cases this solution is impossible to obtain but with some simplifying assumptions we can construct a model that calculates the magnetic field using an analogy to Ohm's Law (Laithwaite, 1967; Carpenter, 1968; Fitzgerald et al., 2003; Kirtley, 2003). If we consider that the frequencies involved are low (the displacement current can be neglected (Stoll, 2011)) and we can ignore the effect of radiation then the system is magneto-quasistatic (Fitzgerald et al., 2003). Under these assumptions the relevant Maxwell equations are the following:

$$\oint_C \vec{H} \cdot d\vec{l} = \iint_S \vec{J} \cdot d\vec{a} \tag{2.1}$$

$$\oiint_S \vec{B} \cdot d\vec{a} = 0. \tag{2.2}$$

Equation (2.1) is the integral form of Ampere's Law where $\vec{J}$ is the current density expressed as a vector, it means that the integral of the tangential component of the field intensity $\vec{H}$ around a closed contour C is equal to the total current passing through any surface S surrounded by this contour (Fitzgerald et al., 2003). The second one is expressing in a mathematical way that there are no magnetic monopoles[2], or what is the same that the magnetic flux density $\vec{B}$ is conserved. We can apply this to a simple magnetic circuit like the one shown in Figure 2.1 to calculate the magnetic field.

To calculate the magnetic flux in the metal core we can assume that the permeability of the iron is much higher than the one of the air and that *almost* all the flux is confined inside the metal. Considering that the magnetic flux density is uniform across the cross-section of the metal:

$$\Phi = \iint_S \vec{B} \cdot d\vec{a} \rightarrow \Phi = B_c \cdot A_c. \tag{2.3}$$

[2]Dirac developed a theory about the existence of magnetic monopoles (Dirac, 1931). However, the only documented detection of a magnetic monopole is the so-called "Valentine's Day Monopole" detected by Blas Cabrera (Cabrera, 1982); which has been widely disputed. This topic is still controversial (Rajantie, 2016).

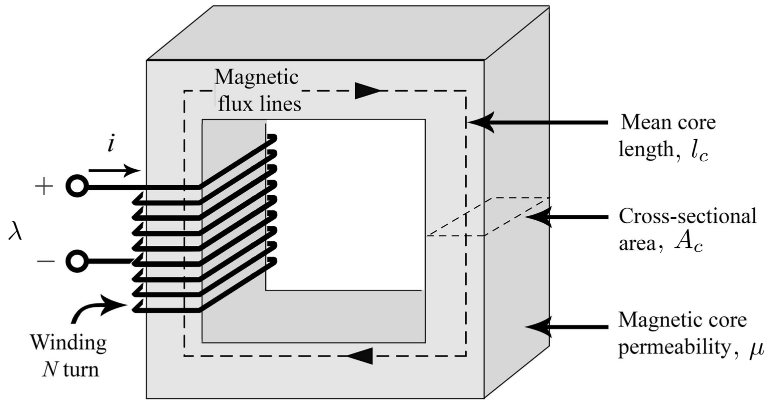

FIGURE 2.1: A schematic view of a magnetic circuit.

We can use (2.1) to calculate the magnetic field intensity:

$$\mathcal{F} = Ni = \oint \vec{H} \cdot d\vec{l}, \tag{2.4}$$

where i is the current, N the number of turns and $\mathcal{F}$ the total magnetomotive force.

If the core is not very wide we can assume that all the paths are close to the mean core length, l_c. So we have the following relationship:

$$\mathcal{F} = Ni = H_c \cdot l_c. \tag{2.5}$$

To calculate the magnetic flux density and the total flux:

$$\vec{B} = \mu \vec{H} \rightarrow \Phi = \mu H_c A_c. \tag{2.6}$$

After these manipulations we can express what in the literature is sometimes called *Ohm's Magnetic Law*, that is simply making an analogy to an electric circuit:

$$\mathcal{F} = \Phi \Big(\frac{l_c}{\mu A_c} \Big) = \Phi \cdot \mathcal{R} \rightarrow \mathcal{R} = \frac{l_c}{\mu A_c}, \tag{2.7}$$

where the magnetomotive force $\mathcal{F}$ is analogous to voltage, the total flux Φ to current and $\mathcal{R}$, that is called reluctance, is analogous to the resistance. This *magnetic circuit* is shown in Figure 2.2.

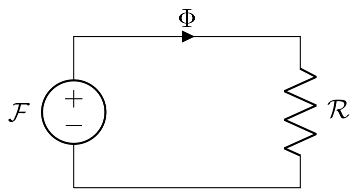

FIGURE 2.2: Electrical analogy to the magnetic circuit shown in Figure 2.1.

We can apply the same idea to more complicated geometries, like the one shown in Figure 2.3 that is exactly the same case as the previous one but with an air-gap in the core.

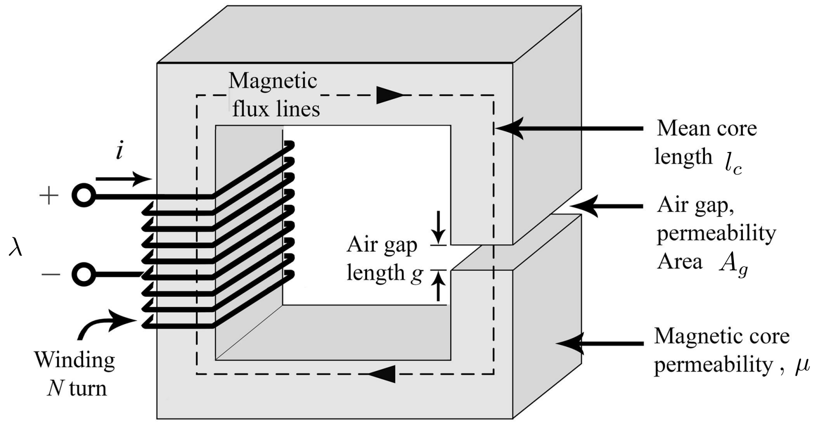

FIGURE 2.3: A schematic view of a magnetic circuit with an air-gap.

The magnetic circuit in this case has two reluctances, one for the core ($\mathcal{R}_c$) and other one for the air-gap ($\mathcal{R}_g$). The analogue electrical circuit is shown in Figure 2.4, in which the two series reluctances are calculated as follows:

$$\mathcal{R}_c = \frac{l_c}{\mu A_c}, \tag{2.8}$$

$$\mathcal{R}_g = \frac{g}{\mu_0 A_g}, \tag{2.9}$$

and the total flux:

$$\Phi = \frac{\mathcal{F}}{\mathcal{R}_{tot}} = \frac{\mathcal{F}}{\mathcal{R}_c + \mathcal{R}_g} = \frac{Ni}{\frac{l_c}{\mu A_c} + \frac{g}{\mu_0 A_g}}. \tag{2.10}$$

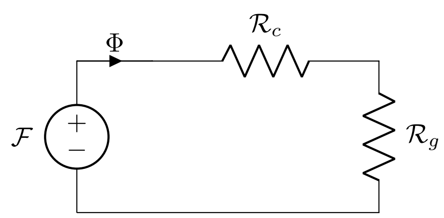

FIGURE 2.4: Electrical analogy to the magnetic circuit shown in Figure 2.3.

This procedure can be applied to estimate the flux in electric machines. Let us consider the simplified synchronous machine shown in Figure 2.5, taken from an example in (Fitzgerald et al., 2003). The examples shown previously are extremely simple but this methodology can be applied to more complicated geometries and it also allows to quantify the magnetic coupling of several electric circuits as it is shown in (Laithwaite, 1967; Carpenter, 1968).

To obtain the magnetic field in the air-gap for design purposes we can use the equivalent magnetic circuit. This approach is valid for obtaining an approximate result that is in the same order of

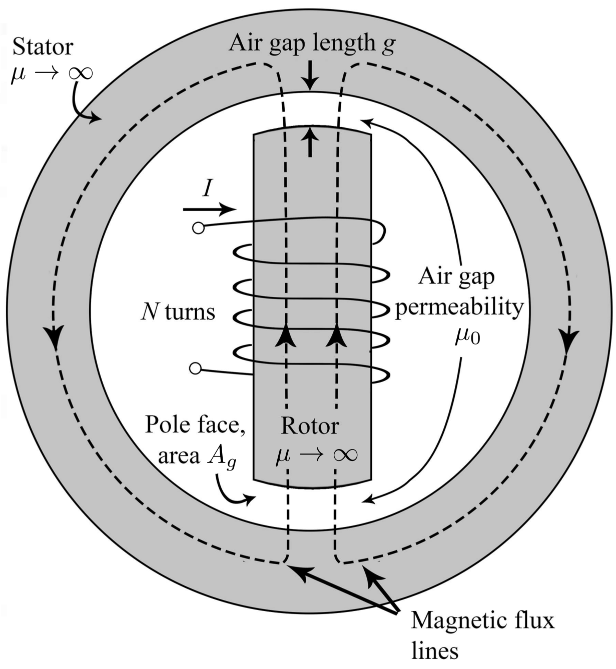

FIGURE 2.5: A simplified synchronous machine.

magnitude as the real solution but is not completely accurate because in practice we do not know the path of the magnetic field. In the presence of air-gaps that have a *toothed member* the magnetic field tends to fringe as it is shown in Figure 2.6 and therefore the simplistic methodology presented previously is not completely accurate nor reliable for a detailed analysis.

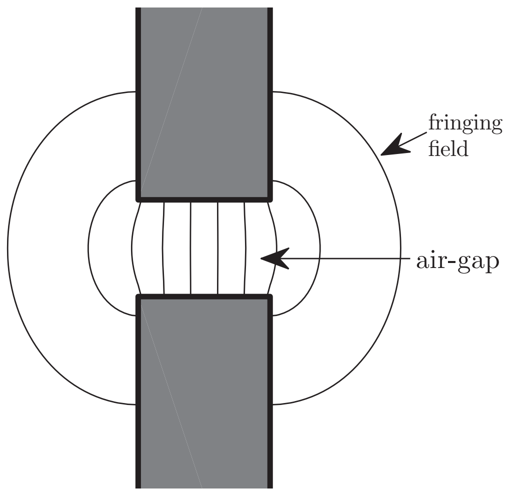

FIGURE 2.6: Flux lines of the fringing magnetic field in a tooth-to-tooth configuration.

Probably the most important feature of the magnetic equivalent circuit methodology is that because of its simple formulation, even if the results are approximated, it provides a very significant insight into the system. Once the method is fully understood, the designer has the intuition to know in which direction the magnetic flux *will tend to go* even if the exact value is not known. For this reason several researchers have tried to generalise this methodology to make it suitable for applications that require a better accuracy.

One of the most significant contributions in this sense was done by Ostovic (1986, 1987, 1988, 1989). In these papers the magnetic equivalent circuits have several reluctances to model each of the different flux paths. Ostovic suggested constructing an equivalent magnetic circuit in the air-gap to take into account fringing, interpolar flux and leakage; then the problem is formulated as a system of matrix equations. Figure 2.7 shows the magnetic equivalent circuit of the air-gap of an induction machine. It can be appreciated that the complexity of this circuit is very high. The increased complexity of these reluctance networks provides more accurate results but on the other hand it makes the physical interpretation more difficult and therefore the insight provided (that is probably the most important part of this method) into the system less straightforward.

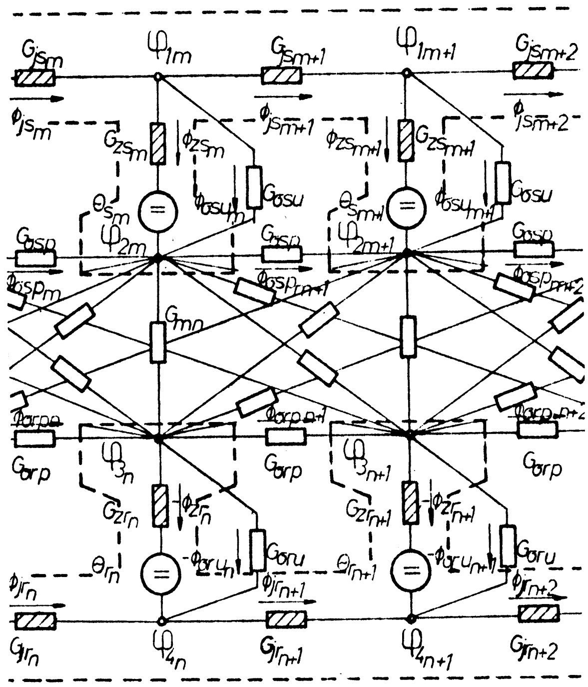

Figure 2.7: Magnetic equivalent circuit of an induction motor, from (Ostovic, 1986), ©1986 IEEE.

In summary, Ostovic's formulation applies the idea of the magnetic equivalent circuit taking into account several effects that the simplistic approach was ignoring. However, because of the complexity of the equivalent circuits and the matrices involved the insight provided is low.

Several papers have reported successful results in the application of this methodology to electric machines (Lovatt, 2005; Blissenbach and Viorel, 2003; Dogan et al., 2013; Hodgins et al., 2009; Kang et al., 2003; Polinder et al., 2005; Yang et al., 2012), particularly in the academic environment. However, each of these papers shows an implementation in a particular application that could not be easily generalised. In this context, Amrhein and Krein postulated a general framework that uses the magnetic equivalent circuit idea to model electromechanical devices (Amrhein and Krein, 2009a,b, 2010). The most important idea of this framework is that it *puts together* all the magnetic equivalent circuit theory in a rigorous way analogous to the typical matrix structural analysis (or the so-called direct stiffness method) so that it can be used for any 3D geometry. Also, with this formulation the computational implementation should be straightforward.

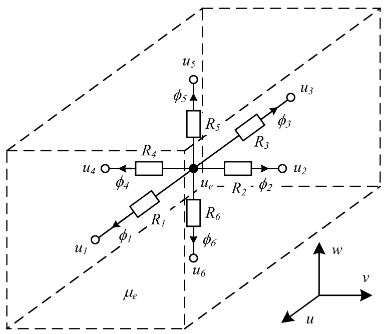

FIGURE 2.8: A node with the reluctance branches and fluxes, from (Amrhein and Krein, 2009a), ©2009 IEEE.

The mathematical formulation is analogous to the typical matrix structural analysis, that is: define the nodes that are connected by the components of the circuit (reluctances or magnetic sources), express this information as a matrix equation and solve it (Amrhein and Krein, 2009a). Figure 2.8 shows an arbitrary 3D node with six branch reluctances, from (Amrhein and Krein, 2009a).

In (Amrhein and Krein, 2009a) there is an example of this method applied to study the performance of an induction motor, a cross-section of the model considered is shown in Figure 2.9.

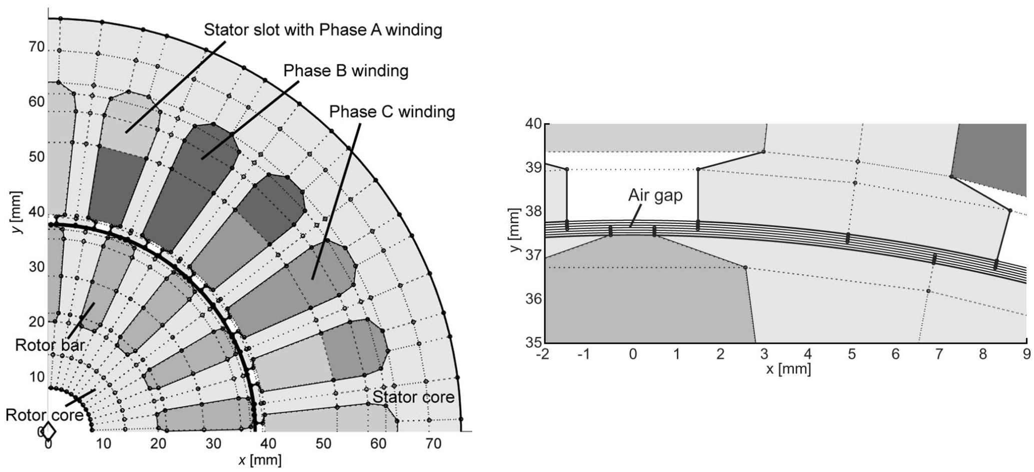

FIGURE 2.9: Model of the induction motor considered in (Amrhein and Krein, 2009a), ©2009 IEEE.

Amrhein and Krein's framework (Amrhein and Krein, 2009a) has several advantages like the simple formulation and the compatibility with computational implementation, but because the sizes of the matrices due to the high number of nodes the solution requires high computational capability (compared to the traditional analytical methods). Therefore, this method can be considered a hybrid between analytical and numerical methods. In fact, this particular formulation presents great similarities with finite element analysis, that is described in the next section, and even though there are not commercial software that provide solutions based on this methodology it can be an interesting idea for the future. The main advantage of this method compared with

FEA is that it obtains a reasonable accuracy using a *coarser* grid than FEA, which reduces the computational time.

2.3 Finite Element Analysis

The finite element analysis (FEA) is an extremely useful numerical tool that is very widely spread in engineering in general. This method gained major importance with the development of digital computers in the 60s due to its easy computational implementation. Typically FEA has been used for the analysis of solids, fluid dynamics and structures but it is applicable to almost every field of engineering like heat transfer, fluids and electromagnetism. Figure 2.10 shows the general process of finite element analysis, from (Bathe, 1996). In this section neither the theoretical derivation nor the application of FEA to a particular case are shown, for a detailed explanation see reference (Bathe, 1996), which shows the mathematical background in depth.

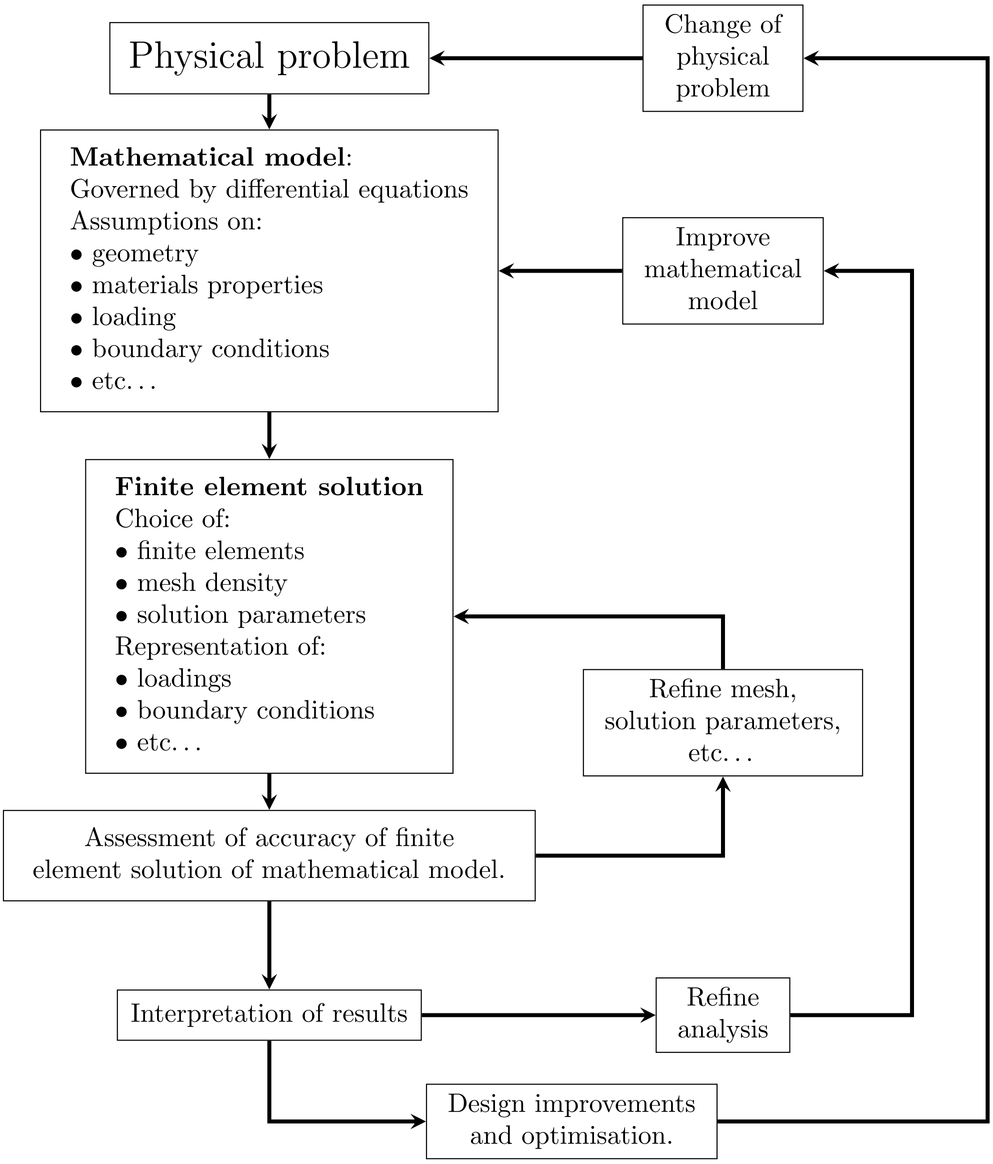

FIGURE 2.10: The process of finite elements, based on (Bathe, 1996).

In the context of electromagnetism this method was first presented in the 70s by Chari and Silvester (Silvester and Chari, 1970; Chari and Silvester, 1971; Chari et al., 1981), since then it has become the most widely used computational method for electromagnetic field analysis for electric machines (Pajooman, 1997). Because of the compatibility with the computational implementation several commercial software (like Ansys and Opera for example) and open-source software (like OpenFOAM and FEM) have been developed. These software use very refined algorithms for the meshing and solving, and they are compatible with other CAD software for the design process making FEA a very powerful tool for the industry and academia.

2.3.1 Calculation of Torque using FEA

Once the magnetic field distribution is obtained the next step is to use this information to calculate the performance of the machine under study. The calculation of torque has a particular importance in this project because one of the objectives is to design machines with high torque capability. Almost every FEA software uses the Maxwell Stress Tensor (MST) to calculate torque (or force). In practical terms we can state that the MST is a tool to calculate forces once the total magnetic field is obtained. An example of the derivation of the MST can be found in (Kirtley, 2003).

The Lorentz Force can be calculated as the cross product of the current (as a vector in 3D) and the flux density at any point. But there is other component of the traction that comes from the variation of the permeability. An empirical expression for the force density using this idea according to Kirtley is the following:

$$\vec{f} = \vec{J} \times \vec{B} - \frac{1}{2}\left(\vec{H} \cdot \vec{H}\right)\nabla\mu,$$

where $\vec{H}$ is the magnetic field intensity and μ is the permeability of the material at each point. We know that the current density is the curl of the magnetic field intensity so we can rewrite the previous expression as:

$$\vec{f} = \left(\nabla \times \vec{H}\right) \times \mu\vec{H} - \frac{1}{2}\left(\vec{H} \cdot \vec{H}\right)\nabla\mu,$$

$$\vec{f} = \mu\left(\nabla \times \vec{H}\right) \times \vec{H} - \frac{1}{2}\left(\vec{H} \cdot \vec{H}\right)\nabla\mu,$$

since

$$\left(\nabla \times \vec{H}\right) \times \vec{H} = \left(\vec{H} \cdot \nabla\right)\vec{H} - \frac{1}{2}\nabla\left(\vec{H} \cdot \vec{H}\right),$$

then, the force density can be written as:

$$\vec{f} = \mu\left(\vec{H} \cdot \nabla\right)\vec{H} - \frac{1}{2}\mu\nabla\left(\vec{H} \cdot \vec{H}\right) - \frac{1}{2}\left(\vec{H} \cdot \vec{H}\right)\nabla\mu,$$

in a more compact way:

$$\vec{f} = \mu\left(\vec{H} \cdot \nabla\right)\vec{H} - \nabla\left(\frac{1}{2}\mu\left(\vec{H} \cdot \vec{H}\right)\right). \tag{2.11}$$

Working with this vector equation it can be proved that for k'th component of the force density:

$$f_k = \frac{\partial}{\partial x_i}\Big(\mu H_i H_k - \frac{\mu}{2}\delta_{ik}\sum_n H_n^2\Big), \tag{2.12}$$

where δ_{ik} is Kronecker's delta defined as $\delta_{ik} = 1$ if $i = k$ and 0 otherwise. Instead of working with sums we can define the tensor T and define the express density as the divergence of the tensor:

$$f_k = \frac{\partial}{\partial x_i} T_{ik},$$

for the three components we can use the vector operator:

$$\vec{f} = \nabla \cdot T. \tag{2.13}$$

This deduction is valid in the context of electric machines (low frequency electromagnetics). For a complete formulation it is necessary to include the Poynting vector. A more detailed analysis is given in (Woodson and Melcher, 1968).

Now let us apply this to the particular case we are interested in, an electric machine in a Cartesian coordinate system. Using the coordinate system x, y and z, for an arbitrary point $\vec{r} = (x, y, z)$ at the instant of time t the MST, T, is given by:

$$\begin{aligned} T(\vec{r}, t) &= \begin{bmatrix} T_{xx} & T_{xy} & T_{xz} \\ T_{yx} & T_{yy} & T_{yz} \\ T_{zx} & T_{zy} & T_{zz} \end{bmatrix} \\ &= \begin{bmatrix} \frac{\mu_0}{2}\Big(H_x^2 - H_y^2 - H_z^2\Big) & \mu_0 H_x H_y & \mu_0 H_x H_z \\ \mu_0 H_y H_x & \frac{\mu_0}{2}\Big(H_y^2 - H_x^2 - H_z^2\Big) & \mu_0 H_y H_z \\ \mu_0 H_z H_x & \mu_0 H_z H_y & \frac{\mu_0}{2}\Big(H_z^2 - H_x^2 - H_y^2\Big) \end{bmatrix}, \end{aligned} \tag{2.14}$$

where $\vec{H}(\vec{r}, t)$ is a function of space and time, which are not shown in the matrix for simplicity.

For example, if we want to calculate the force density in the x-component:

$$f_x(\vec{r}, t) = \frac{\partial T_{xx}(\vec{r}, t)}{\partial x} + \frac{\partial T_{xy}(\vec{r}, t)}{\partial y} + \frac{\partial T_{xz}(\vec{r}, t)}{\partial z}.$$

To obtain the total force that a solid object feels, we can integrate this expression over a volume V:

$$\vec{F} = \iiint_V \vec{f} \cdot dv = \iiint_V \nabla \cdot T dv. \tag{2.15}$$

If S is a closed surface that surrounds V we can apply the divergence theorem and then we obtain:

$$\vec{F} = \iiint_V \vec{f} \cdot dv = \oiint_S T \cdot d\vec{a}. \tag{2.16}$$

The most important concept of (2.16) is that to obtain the total force that a body is *feeling* we do not need to calculate the force density in all the volume, but it is only necessary to know the MST, or what is the same, the field intensity, over a surface that surrounds this body.

If we apply it to a 2-dimensional model of a rotating electric machine we can calculate the torque produced using the MST. The traction in the tangential direction τ_θ is obtained as follows:

$$\tau_\theta = \mu_0 H_r H_\theta \tag{2.17}$$

If the length of the machine is L and Γ is a closed path in the air-gap, then the total tangential force is the following:

$$F_\theta = \oint_\Gamma \tau_\theta L d\ell = \oint_\Gamma \mu_0 H_r H_\theta L \, d\ell, \tag{2.18}$$

hence the torque:

$$T = F_\theta \cdot r = Lr \oint_\Gamma \mu_0 H_r H_\theta \, d\ell. \tag{2.19}$$

FEA is a powerful tool for studying the electromagnetic behaviour of rotating electric machines. The application of refinement algorithms for meshing and solution has increased the speed and the accuracy significantly. Also, the MST combined with FEA enables the calculation of the torques and forces readily. However, when looking at (2.14) we see a complicated 3 by 3 matrix that is difficult to assimilate. Intuitively it is very difficult to understand the meaning of each of these terms and for this reason this method does not provide a good insight into the system. Here is the main weakness of FEA: analytical methods can provide information to the designer so she/he can use the intuition to improve the design but with FEA the calculation starts and you have the final result.

The current trend in the design of novel electric motors and generators is dominated by FEA. The typical procedure is: an idea of a concept machine, parametrisation of the geometry, FEA calculation of the field and optimisation using techniques like genetic algorithms (Keysan et al., 2012; Ueda et al., 2013; Henneberger and Bork, 1997; Baker et al., 2014; Colli et al., 2005; Guo et al., 2006; Ifedi et al., 2013; Kang and Weh, 2008; Kastinger, 2002; Lewis, 2002; Pompermaier et al., 2012; Potgieter and Kamper, 2012; Rahman et al., 2006; Subiabre and Mueller, 2011; Yan et al., 2009). This approach implies the simulation of hundreds or thousands of different scenarios and use an algorithm to *pick the best*. After analysing a great number of scenarios it is possible to have an intuition of which parameters are affecting the design, but it is not straightforward.

2.4 The Sub-domain Method

The sub-domain method was originally proposed by Liu *et al.* (Liu and Li, 2007; Liu et al., 2008). Zhu *et al.* from the University of Sheffield generalised it and applied to a great number of practical cases (Wu et al., 2010a; Zhu et al., 2010; Wu et al., 2010b, 2011, 2012b,a). Simultaneously, at the University Henri Poincaré, Lubin *et al.* also analysed several motors and also applied it to magnetic gears (Dubas and Espanet, 2009; Lubin et al., 2013) with satisfactory results.

The procedure of the sub-domain method aims to directly solve the partial differential equations in each of the sub-domains to obtain the unknown coefficients by applying the boundary conditions on the interfaces between sub-domains. Figure 2.11 shows the geometry of an electric motor divided in sub-domains.

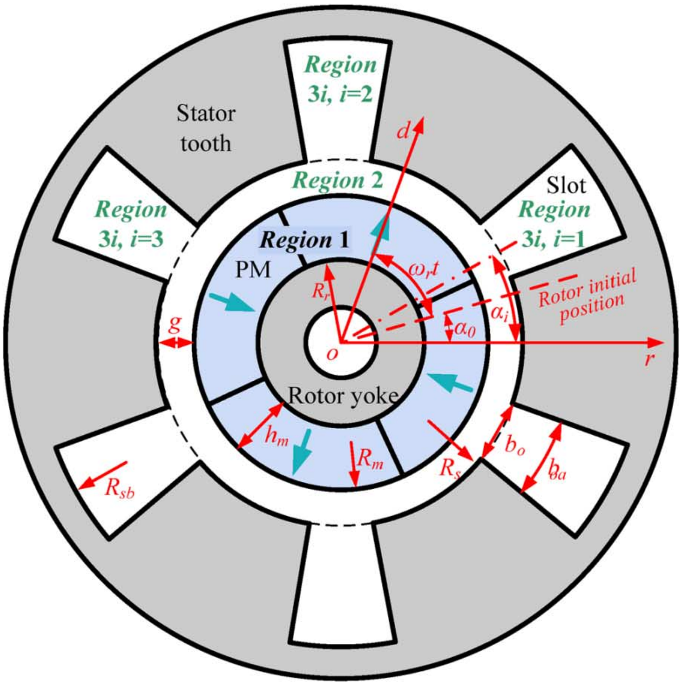

FIGURE 2.11: Example of a PM motor divided in sub-domains, from (Zhu et al., 2010), ©2010 IEEE.

For the particular geometry shown in Figure 2.11 the general expressions of the scalar potential functions are as follows (example from (Zhu et al., 2010)):

$$\phi_1(k \neq 1) = \sum_k \left[A_1(k)r^k + B_1(k)r^{-k} + \frac{M_{ck}r}{\mu_r(1-k^2)}\right]\cos(k\alpha) + \sum_k \left[C_1(k)r^k + D_1(k)r^{-k} + \frac{M_{sk}r}{\mu_r(1-k^2)}\right]\sin(k\alpha), \quad (2.20)$$

$$\phi_1(k = 1) = \left[A_1(1)r + B_1(1)r^{-1} + \frac{M_{c1}r\log(r)}{\mu_r}\right]\cos(\alpha) + \left[C_1(1)r + D_1(1)r^{-1} + \frac{M_{s1}r\log(r)}{\mu_r}\right]\sin(\alpha), \quad (2.21)$$

for region 1,

$$\phi_2 = \sum_k \left[A_2(k)r^k + B_2(k)r^{-k}\right]\cos(k\alpha) + \sum_k \left[C_2(k)r^k + D_2(k)r^{-k}\right]\sin(k\alpha), \quad (2.22)$$

for region 2 and

$$\phi_{3i} = \sum_{m} C_{3i}(m) \left[\left(\frac{r}{R_{sb}} \right)^{F_m} - \left(\frac{r}{R_{sb}} \right)^{-F_m} \right] \cdot \sin \left[F_m \left(\alpha + \frac{b_{oa}}{2} - \alpha_i \right) \right], \tag{2.23}$$

for each of the slots of region 3. Where μ_r is the relative permeability of magnets, k and m are the harmonic orders, R_{sb} is the radius of the slot bottom, $A_1(k) \to D_1(k)$, $A_2(k) \to D_2(k)$ and $C_{3i}(m)$ are the coefficients determined by the boundary conditions. For a more detailed explanation see the references (Wu et al., 2010a; Zhu et al., 2010) that have the same notation shown here.

Once all the coefficients are obtained from the scalar potential function, the magnetic field can be obtained. The main problem is that each of the coefficients $A_1 \to D_1$, $A_2 \to D_2$ and C_{3i} in reality is a sum of terms so when the interface boundary conditions are applied this becomes a system of equations with a high number of variables. Furthermore, this procedure has to be done in each position of the rotor making the computation time of this method high.

There is ongoing research in this topic. A recent paper by Pfister et al. (2016) shows a general methodology based on the sub-domain method including the diffusion effects, which models eddy currents. This methodology has not been implemented by the author of this Thesis but if the numerical complexity is not high it could be an interesting option for the future.

In summary the sub-domain method is a very interesting way of obtaining the magnetic field in the air-gap because it is analytical and the accuracy is high. However, the large matrices involved in the solution process diminish the insight provided to the machine designer. Also, the computation time is high due to the complexity of the methodology if high order harmonics are considered.

2.5 Conformal Mapping

Conformal mapping is a standard method for solving boundary value problems in two-dimensional potential theory. In simple terms, the idea is to use conformal mapping to *map* the given domain into a simpler one in which the solution of the Laplace's equation is known. The solution obtained is then *mapped back* onto the original domain (Kreyszig, 2011). This technique has been successfully used for the calculation of the magnetic field distribution in the electromagnets for particle accelerators (Halbach, 1968, 1990).

The main problem is that when the given geometry is a polygon, which is commonly the case in the context of electric machines, the conformal transformation needed is a Schwarz-Christoffel Transformation. In many cases there is not an explicit expression for the Schwarz-Christoffel Transformation, which makes the solution difficult.

Conformal mapping, combined with the complex permeance method described in the following chapter, has been successfully used for the calculation of the magnetic field distribution in electric machines (Markovic et al., 2004, 2005; Zarko et al., 2006; Boughrara et al., 2009a,b, 2013). The PhD Thesis developed at the Ecole Polytechnique Federale de Lausanne, EPFL, by Dr Miroslav

Markovic provides a very comprehensive analysis of conformal mapping and provides several examples of the application of this methodology (Markovic, 2004).

This section is particularly important because the complex permeance framework described in the following chapter is based on conformal mapping.

2.5.1 Background Theory

Let us study a complex function $w = f(z)$ defined in a domain $\mathcal{D}$ of the z-plane. For each point in $\mathcal{D}$ there corresponds a point in the w-plane. If the function $f(z)$ is analytic in $\mathcal{D}$ then the mapping given by $w = f(z)$ is conformal, this means that the angles are preserved (for example if two curves cross in a right angle on the z-plane they should cross at 90^o in the w-plane), except at points where the derivative $f'(z)$ is zero.

The great importance of conformal mapping theory is based on the fact that it can be readily used to solve the Laplace and Poisson equations in 2-D. In particular, conformal mapping yields a standard method to solve two-dimensional boundary value problems.

The most important step of this method to solve magnetic or electrostatic potential problems is the choice of the functions that transform the geometry (the maps). Depending on the properties of the function applied the new domain will have particular features. Several transformations can be applied in a sequence to *reach* a certain desired geometry.

As an example the function $w = f(z) = z^2$ will be analysed to demonstrate the fundamentals of the theory. Considering the polar form $z = r_z e^{j\theta}$ and $w = r_w e^{j\phi}$, from this expression $w = z^2 = r_z^2 e^{2j\theta}$. So $r_w = r_z^2$ and $\phi = 2\theta$. In figure 2.12 the z-plane is shown with a region $\mathcal{D}$ defined as $1 \leq |z| \leq 2$ and $\pi/6 \leq \theta \leq \pi/3$.

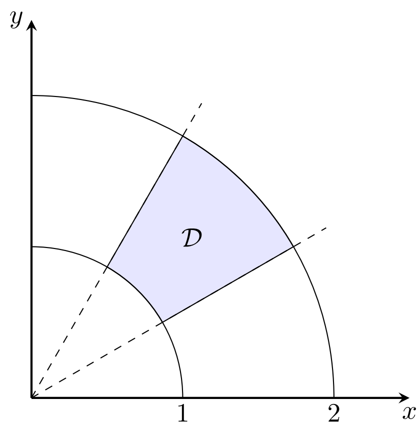

FIGURE 2.12: z-plane.

In the w plane the domain $\mathcal{D}$ is defined as $1 \leq |w| \leq 4$ and $\pi/3 \leq \phi \leq 2\pi/3$, this is shown in figure 2.13.

This example shows how a region is modified by a conformal transformation ($f(z) = z^2$ in this case) and it can be appreciated that the angles are preserved. This property is extremely

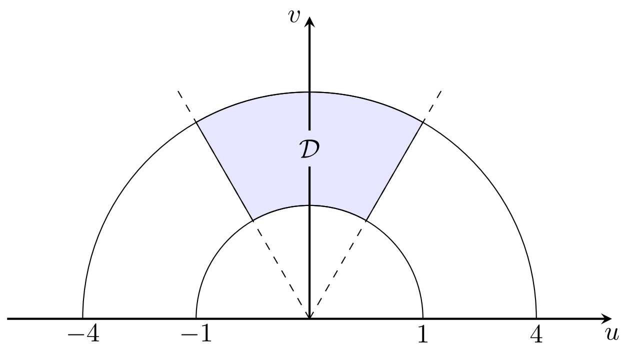

FIGURE 2.13: w-plane.

important because it is the definition of conformal transformation and it is valid if the complex function $f(z)$ is analytic and the derivative $f'(z)$ is not zero.

2.5.2 The Schwarz-Christoffel Transformation

The Schwarz-Christoffel conformal transformation is a particular conformal map that has very useful properties to solve two-dimensional magnetic or electrostatic potential problems.

The general formula is a standard procedure to obtain a conformal map f from the upper half of a certain complex plane w that is usually called the *canonical domain* into the interior of a polygon on the z-plane that is called the *physical domain* in the literature (Gibbs, 1958; Driscoll, 2005).

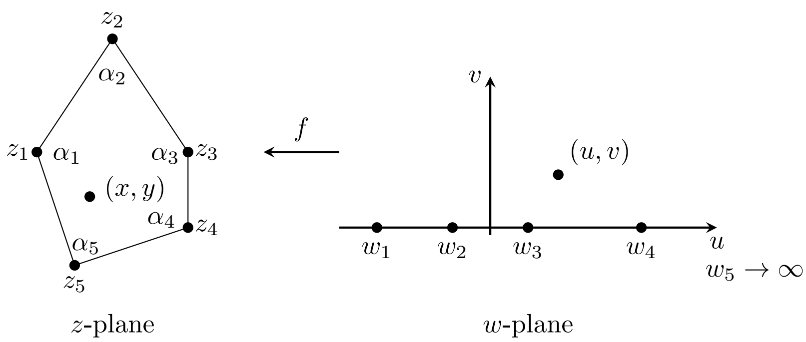

FIGURE 2.14: Example of a polygon in the z-plane transformed into the upper half plane of the w-plane.

Figure 2.14 shows a certain polygon on the z-plane and the corresponding transformation into the w-plane. The general mathematical relationship between the z-plane and the w-plane is equation (2.24) expressed in an integral form. In the equation w_k represents the point k in the w-plane and α_k is the internal angle of the vertex k on the polygon of the z-plane, of course $1 \leq k \leq N$.

$$z = f(w) = A \int \prod_{k=1}^{N} (w - w_k)^{\frac{\alpha_k}{\pi} - 1} dw + B, \tag{2.24}$$

with N being the number of sides of the polygon. A and B are integration constants that have to be determined from the geometry.

An equivalent expression to equation (2.24) is:

$$\frac{dz}{dw} = A \prod_{k=1}^{N} (w - w_k)^{\frac{\alpha_k}{\pi} - 1}. \tag{2.25}$$

The Schwarz-Christoffel mapping derivative is important for potential problems as it will be explained in the following sections.

The main practical difficulty is that for many cases equation (2.24) cannot be obtained analytically so it has to be determined numerically by solving a system of non-linear equations. This approach is often called the *Numerical Schwarz-Christoffel Transformation.*

2.5.3 Schwarz-Christoffel Toolbox for Matlab

Driscoll *et al.* have developed a Matlab-based toolbox based on Schwarz-Christoffel transformations (Driscoll, 2005; Driscoll and Trefethen, 2002). The advantage of this toolbox is that the algorithms used to solve complicated polygons are very efficient and the fact that it is based on Matlab facilitates the usage. It has been successfully used in several scientific publications in the field of rotating electric machines such as (O'Connell and Krein, 2009).

The toolbox has many features but the most important ones are that it can *solve* the map, evaluate the positions in the canonical domain and evaluate the derivative of the map.

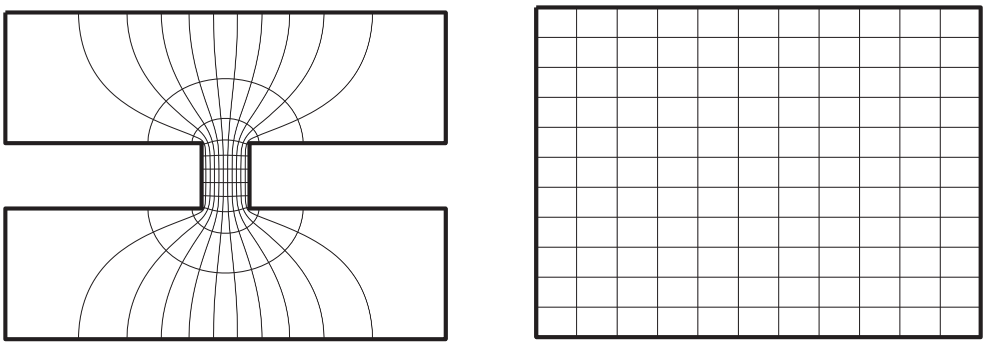

(a) Original domain. (b) Canonical domain.

FIGURE 2.15: Flux lines and equipotential lines obtained using the SC toolbox.

Figure 2.15(a) shows an arbitrary domain that can be considered the z-plane[3]. Using the appropriate function f, making sure that it is a conformal transformation[4], we can transform the original domain into a rectangle (or canonical domain) as shown in Figure 2.15(b). The magnetic field distribution in the canonical domain is very easy to obtain and this solution can be *brought back* to the z-plane using the properties of the function f.

[3]This particular example can be used to calculate the tooth-to-tooth permeance.

[4]In simple terms it means that the angles are preserved. Or what it is the same: making sure that the flux lines and equipotential lines cross with right angles.

2.5.4 Field Equations in Conformal Mapping

The previous sections introduced the concept of Conformal Mapping and described a particular case of conformal map that is extremely useful for the solution of electromagnetic fields. In this section the mathematical background of these methods is presented.

A conformal map is a one to one analytic function f of the complex variable z such that $w = f(z)$. This means that it *transforms* each point in z into a new point in w, consequently every $z_o = x_o + jy_o$ has an unique image $f(z_o) = w_o = u_o + jv_o$.

Considering the potential and flux functions, if each point is uniquely defined it also means that the potential and flux function will have the same value in z_o and w_o. As a consequence the equipotential and flux lines in z will be mapped into the corresponding lines in w.

In this section a generic field F is considered. In the case of electrostatics it would be the electrostatic field E and in magnetostatic analysis it would be the magnetic field intensity H.

Considering a generic potential function φ in the z plane we can define a field function F that represents any scalar field that satisfies Laplace's equation:

$$F(x, y) = F_x + jF_y = -\frac{\partial \varphi}{\partial x} - j\frac{\partial \varphi}{\partial y}.$$

In order to deduce the relationship between the field in the z-plane and the w-plane, the following scalar potential functions are defined:

- $\varphi(x, y) \equiv$ scalar potential in the z-plane.
- $\psi(u, v) \equiv$ scalar potential in the w-plane.

Considering that each point (u, v) in w is at the same potential than the corresponding point (x, y) in z the following equation must be satisfied in all the region:

$$\varphi(x, y) = \psi\Big(u(x, y), v(x, y)\Big). \tag{2.26}$$

The field in the z-plane:

$$F_z = F_x + jF_y = -\frac{\partial \varphi}{\partial x} - j\frac{\partial \varphi}{\partial y}. \tag{2.27}$$

The field in the w-plane:

$$F_w = F_u + jF_v = -\frac{\partial \psi}{\partial u} - j\frac{\partial \psi}{\partial v}. \tag{2.28}$$

From equation (2.26) we have:

$$\frac{\partial \varphi}{\partial x} = \frac{\partial \psi}{\partial u}\frac{\partial u}{\partial x} + \frac{\partial \psi}{\partial v}\frac{\partial v}{\partial x}, \tag{2.29}$$

$$\frac{\partial \varphi}{\partial y} = \frac{\partial \psi}{\partial u}\frac{\partial u}{\partial y} + \frac{\partial \psi}{\partial v}\frac{\partial v}{\partial y}. \tag{2.30}$$

Combining equations (2.29) and (2.30):

$$F_z = F_u \frac{\partial u}{\partial x} + F_v \frac{\partial v}{\partial x} + j\Big(F_u \frac{\partial u}{\partial y} + F_v \frac{\partial v}{\partial y}\Big). \tag{2.31}$$

As the potential functions are analytic they satisfy the Cauchy-Riemann conditions[5], hence equation (2.31) can be written as:

$$F_z = (F_u + jF_v)\Big(\frac{\partial u}{\partial x} - j\frac{\partial v}{\partial x}\Big), \tag{2.32}$$

$$F_z = F_w\Big(\frac{\partial u}{\partial x} - j\frac{\partial v}{\partial x}\Big). \tag{2.33}$$

Considering that $w = u(x,y) + jv(x,y)$, then

$$\frac{\partial w}{\partial x} = \frac{\partial u}{\partial x} + j\frac{\partial v}{\partial x} = \frac{\partial w}{\partial z}\frac{\partial z}{\partial x} = \frac{dw}{dz}. \tag{2.34}$$

The complex conjugate is given by:

$$\Big(\frac{dw}{dz}\Big)^* = \Big(\frac{\partial u}{\partial x} + j\frac{\partial v}{\partial y}\Big)^* = \frac{\partial u}{\partial x} - j\frac{\partial v}{\partial y}. \tag{2.35}$$

If equation (2.35) is substituted in equation (2.31), the relationship of the field in the w-plane with the z-plane is the following:

$$F_z = F_w\Big(\frac{dw}{dz}\Big)^*. \tag{2.36}$$

Equation (2.36) shows the explicit relationship between a vector field in the z-plane and the w-plane defined by the same potential function. With this relationship if the field on the w-plane is known (because it is a simple geometry for example) then the problem reduces to calculating the derivative, which is not trivial but is possible to do analytically.

2.6 Gibbs' Methodology

The first one to apply Conformal Mapping to the analysis of the magnetic field distribution in electric machines was Carter (Carter, 1900, 1926) who proposed the so-called *Carter coefficient* (Krause et al., 2013; Neville, 1967) to quantify the effect of slotting over the mean value of the magnetic field. Since Carter's coefficient considers only the effect of slotting over the mean value of the magnetic field, the details of the effect over the space harmonics is ignored. These

[5] The general expression of the Cauchy-Riemann conditions:

$$\frac{\partial u}{\partial x} = \frac{\partial v}{\partial y}$$

$$\frac{\partial u}{\partial y} = -\frac{\partial v}{\partial x}$$

harmonics are particularly important for the calculation of torque in transverse flux machines and no-load rotor losses.

Gibbs (Gibbs, 1958) postulated two methods to obtain the magnetic field distribution in the simplified geometry shown in figure 2.16. One method considers a single-slot surrounded by infinitely wide teeth, section 2.6.1, and the other one considers the multiple slots and teeth, section 2.6.2. The most important contribution of Gibbs compared with Carter was that the former obtains the magnetic field distribution (including the space harmonics) instead of only considering the mean value.

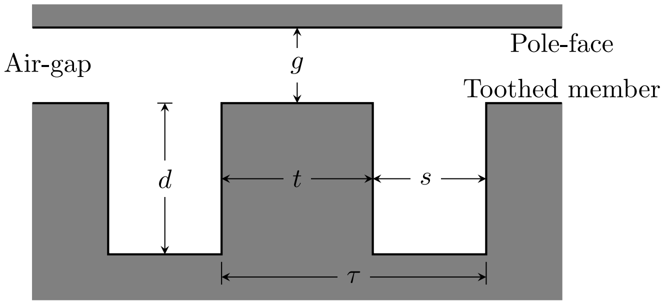

FIGURE 2.16: Developed geometry considered by Gibbs.

2.6.1 Single-Slot Model

Figure 2.17 shows the geometry considered for a single slot surrounded by infinitely wide teeth that we will call the z-plane. The field is produced by a magneto-motive force of V between the toothed member and the pole-face.

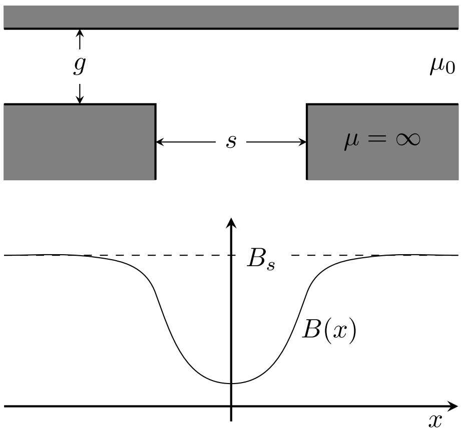

FIGURE 2.17: Geometry of a single slot and the corresponding air-gap magnetic flux density waveform.

The magnetic flux density B on the pole-face as a function of the intermediate variable w can be shown to be given by

$$B(w) = \frac{w-1}{(w-a)^{\frac{1}{2}}(w-b)^{\frac{1}{2}}} B_s, \tag{2.37}$$

with $a = 1/b$ and b is obtained from the equation:

$$\frac{b-1}{\sqrt{b}} = \frac{s}{g}. \tag{2.38}$$

B_s is the value of the magnetic flux density if there were no slots:

$$B_s = \frac{\mu_0 V}{g}. \tag{2.39}$$

The distance along the pole-face,

$$x = \frac{g}{\pi}\left\{ -\log\left|\frac{1+p}{1-p}\right| + \log\left|\frac{b+p}{b-p}\right| + \frac{2(b-1)}{\sqrt{b}}\tan^{-1}\frac{p}{\sqrt{b}}\right\} - \frac{s}{2}, \tag{2.40}$$

with the parameter p given by the intermediate variable w:

$$p^2 = \frac{b-w}{a-w}. \tag{2.41}$$

To obtain the magnetic field distribution B and x are evaluated as a function of w for values from -1 to 0.

2.6.2 Multiple-Slots Model

The objective is to transform the geometry shown in Figure 2.18 into a rectangle to solve the Laplace equation with the same assumptions as in the previous section. The main difference between this method and the one that considers a single-slot is that there is not an explicit equation for the transformation. This is why it is necessary to operate with the intermediate variables α and k. The parameters α and k are obtained by solving the following system of

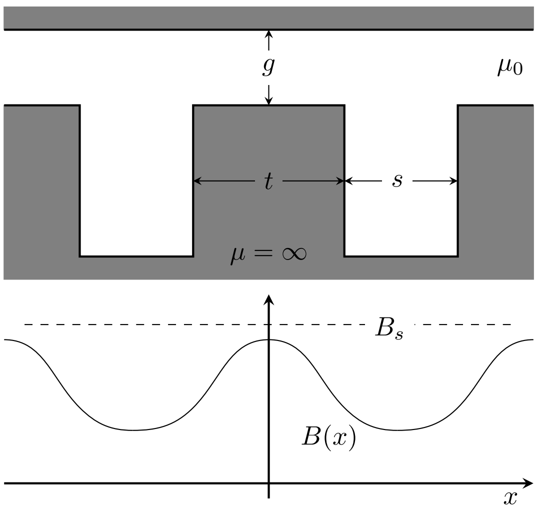

FIGURE 2.18: Geometry of a machine with multiple slots and the corresponding magnetic flux density waveform.

non-linear equations:

$$\frac{g}{s} = \frac{\mathrm{K}(k)}{\pi}\left\{\frac{\mathrm{sn}(\alpha,k)\ \mathrm{dn}(\alpha,k)}{\mathrm{cn}(\alpha,k)} - \mathrm{Z}(\alpha,k)\right\}, \tag{2.42}$$

$$\frac{t}{s} = \frac{2\,\mathrm{K}(k')}{\pi}\left\{\frac{\mathrm{sn}(\alpha,k)\ \mathrm{dn}(\alpha,k)}{\mathrm{cn}(\alpha,k)} - \mathrm{Z}(\alpha,k)\right\} - \frac{\alpha}{\mathrm{K}(k)}, \tag{2.43}$$

with

$$k' = \sqrt{1-k^2}, \tag{2.44}$$

where $\mathrm{K}(k)$ is the complete elliptic integral of the first kind. The functions $\mathrm{sn}(\alpha,k)$, $\mathrm{cn}(\alpha,k)$ and $\mathrm{dn}(\alpha,k)$ are the Jacobi trigonometric functions defined as inverse elliptic integrals. Finally, $\mathrm{Z}(\alpha,k)$ is the Jacobi Zeta function defined as a function of the elliptic integrals (Dwight, 1947).

The expression for the magnetic flux density as a function of the intermediate variable v is:

$$B(v) = \frac{(1+k_1^2v^2)^{\frac{1}{2}}}{(1+k^2v^2)^{\frac{1}{2}}}B_{max}, \tag{2.45}$$

where

$$B_{max} = \frac{\pi g}{s\,\mathrm{K}(k_1)}\frac{\mathrm{cn}(\alpha,k)}{\mathrm{sn}(\alpha,k)\ \mathrm{dn}(\alpha,k)}B_s, \tag{2.46}$$

with $k_1 = k\,\mathrm{sn}(\alpha,k)$.

The distance along the pole-face,

$$x(v) = \frac{s}{\pi}\left[\left\{\frac{\mathrm{sn}(\alpha,k)\ \mathrm{dn}(\alpha,k)}{\mathrm{cn}(\alpha,k)} - \mathrm{Z}(\alpha,k)\right\}\beta + \tan^{-1}\frac{-2\sum_1^\infty(-1)^m q^{m^2}\sin\frac{\pi m\alpha}{\mathrm{K}(k)}\sinh\frac{\pi m\beta}{\mathrm{K}(k)}}{1+2\sum_1^\infty(-1)^m q^{m^2}\cos\frac{\pi m\alpha}{\mathrm{K}(k)}\cosh\frac{\pi m\beta}{\mathrm{K}(k)}}\right], \tag{2.47}$$

with

$$\beta = \mathrm{F}\left(\frac{v}{(1+v^2)^{\frac{1}{2}}}, k'\right), \tag{2.48}$$

where $\mathrm{F}(\phi,k)$ is the incomplete elliptic integral of the first kind and q is called the nome, $q = e^{-\frac{\pi\,\mathrm{K}(k')}{\mathrm{K}(k)}}$.

To obtain the flux density distribution B and x are evaluated as a function of v for values from 0 to ∞ in a similar way as in the previous method.

2.6.3 Limits of Application

How to choose between these two models is an important matter. The single-slot model is simpler but it may not be suitable for some geometries. On the other hand, the multiple-slots model is more accurate but it is more complex and in some cases there might be numerical issues. Freeman proposed a criterion to choose between the two methods but he did not provide any justification for it (Freeman, 1962).

This topic was addressed by the author of this Thesis in (Anglada et al., 2016) and this section is based on that paper. Section A.1 illustrates the importance of choosing the appropriate slotting model for the calculation of rotor losses. The following sections present an original contribution.

2.6.3.1 Practical Limit

When the teeth are wide enough it was noted by Gibbs and Freeman that the maximum value of the flux density, B_{max}, is almost equal to B_s. This suggests that the effect of neighbouring slots on the field distribution in the vicinity of a slot is negligible.

We can define the following indicator to study if the single-slot model is going to give almost the same answer as the multiple-slots model for a particular geometry:

$$r_p = \frac{B_{max}}{B_s} = \frac{\pi g}{s\,\mathrm{K}(k_1)} \frac{\mathrm{cn}(\alpha, k)}{\mathrm{sn}(\alpha, k)\ \mathrm{dn}(\alpha, k)}, \tag{2.49}$$

where B_{max} is obtained from (2.46). With this indicator for any geometry (a given t/s and g/s) we can estimate immediately if both models give a similar answer. If the value of r_p is close to 1 it means that the interaction between adjacent slots is negligible and a single-slot model can be used. If it is significantly smaller than 1 then a multiple-slot model is needed.

2.6.3.2 Numerical Limit

This section shows the range of the geometrical variables within which the multiple-slots model is valid. Theoretically, according to the definition of the Schwarz-Christoffel transformation the geometry of Figure 2.18 can always be mapped into a rectangle. However, in practice when the ratio of the tooth width t and the air-gap length g is large, i.e., the teeth are very wide, the numerical solution of (2.42) and (2.43) becomes impossible.

Let us define the right hand side of (2.42) as $\mathrm{F_g}(\alpha, k)$ and the right hand side of (2.43) as $\mathrm{F_t}(\alpha, k)$:

$$\frac{g}{s} = \mathrm{F_g}(\alpha, k), \tag{2.50}$$

$$\frac{t}{s} = \mathrm{F_t}(\alpha, k). \tag{2.51}$$

Considering a particular value of $\frac{g}{s} = K$, a curve Γ_K of all the points (α, k) that satisfy this equation can be defined as the following:

$$(\alpha_i, k_i) \in \Gamma_K \Leftrightarrow \mathrm{F_g}(\alpha_i, k_i) = K. \tag{2.52}$$

Of all the points in Γ_K there is only one point (α_{opt}, k_{opt}) that satisfies:

$$\mathrm{F_t}(\alpha_{opt}, k_{opt}) = \frac{t}{s}. \tag{2.53}$$

To know the limits of application of the multiple-slots methodology we need to find the maximum tooth width within which the numerical solver can provide a solution. To find the maximum value of $\frac{t}{s}$ for a particular value of $\frac{g}{s}$ an algorithm was implemented in Matlab. The algorithm is divided in three stages:

(a) Choose a value of $\frac{g}{s} = \mathrm{F_g}(\alpha, k) = K$.

(b) Obtain the curve (*family of points*) Γ_K.

(c) Calculate the point (α_{opt}, k_{opt}) that maximizes the function $\mathrm{F_t}(\alpha, k)$ and evaluate $\frac{t}{s}|_{max}$.

The value of $\frac{t}{s}|_{max}$ will depend on the numerical precision of the software.

For this case as the value of $\frac{t}{s}$ increases k' —see equation (2.44)— tends to be close to zero. This results in k being close to 1 and the elliptic integral of the first kind has the following property:

$$\lim_{k' \to 0} \mathrm{K}(k') = \infty \Rightarrow \lim_{k \to 1} \mathrm{F_t}(\alpha, k) = \infty. \tag{2.54}$$

For this reason the numerical limit in which the multiple slots method *has* a solution will depend on the numerical precision of the software; for the case of Matlab the minimum value of k' in which $\mathrm{K}(k')$ is not infinite is $k' = 10^{-8}$.

2.6.3.3 Representation of the Limits

This section presents the results obtained using Matlab after implementing the algorithms to calculate the practical and numerical limits. To obtain the limits the previous methodology was applied for a range of values of $\frac{g}{s}$ to calculate the corresponding $\frac{t}{s}|_{max}$.

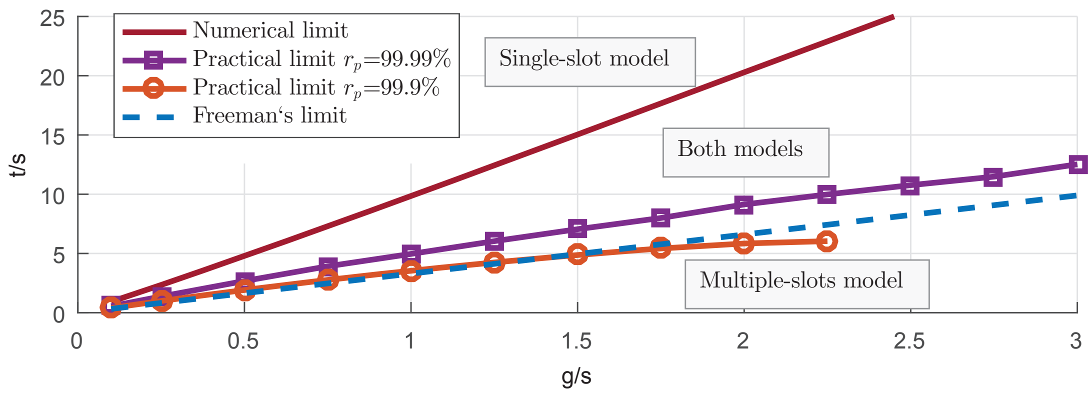

FIGURE 2.19: Numerical and practical limits of the two methodologies as a function of the geometric variables. Also, representation of Freeman's limit.

Freeman (1962) proposed the following criterion: if $t/g > 3.3$ the single-slot model should be used and if $t/g < 3.3$ the multiple-slots model should be used. This condition can also be expressed using the normalised parameters $\frac{t}{s}$ and $\frac{g}{s}$:

$$\text{if } \frac{t}{s} > 3.3\,\frac{g}{s};\ \text{single-slot model}, \tag{2.55}$$

$$\text{if } \frac{t}{s} < 3.3\,\frac{g}{s};\ \text{multiple-slots model}. \tag{2.56}$$

Figure 2.19 shows the limit proposed by Freeman, the numerical limit and the practical limit for 3 different values of r_p as a function of the normalised variables $\frac{t}{s}$ and $\frac{g}{s}$. The figure can be divided in three different regions. In the region above the solid red line the single-slot model should always be used because the multiple-slots model will fail as it was noted in section 2.6.3.2. Below the orange line with the circular markers ignoring the effect of the neighbouring slots can produce significant errors because the magnetic field in the middle of the teeth does not reach

B_s as it was described in section 2.6.3.1 (here the minimum value of r_p was considered to be the 99.9 %). Between these two lines *both* models can be used in the sense that they will give similar answers. However, above the magenta line with square markers that is r_p of 99.99 % the solution of both methods will be almost identical and $k' \to 0$. Freeman's limit in Figure 2.19 is the dashed blue line. It is almost the same as the practical limit with r_p of 99.9 %.

2.7 Summary

The aim of this chapter is to build the background in electromagnetic field theory required for the proper understanding of this Thesis. There is a particular emphasis on conformal mapping because this is the methodology that will be used in subsequent chapters.

A summary of these methods:

Reluctance Networks : The method itself is very simple and intuitive providing good insights. The typical formulation has very strong simplifications (neglecting fringing for example) and in an effort to make it accurate the reluctance networks become very complicated making the method itself similar to FEA. It can be a good alternative to FEA if it has lower computation time.

FEA : This method is very accurate and with the current CAD software it can be easily implemented in the design process. However, it is a numerical method and the insight provided is low unless several geometries are analysed. In this project we will use FEA for validation for these reasons.

Sub-domain : It is completely analytical but the mathematical formulation and solution is extremely complicated making very difficult to get an intuition about the system.

Conformal Mapping : This method does some simplifications but the insight provided is high. Furthermore, the Schwarz-Christoffel Toolbox for Matlab facilitates the usage and it can be readily implemented for the modelling of rotating machines.

The following chapters use conformal mapping to study transverse flux machines. This technique was chosen because it provides a deep insight into the system combined with reasonable accuracy and a low computational time. Furthermore, the Schwarz-Christoffel Toolbox can be used as the foundations of our own simulation codes.

Chapter 3

The Complex Permeance Framework

3.1 Introduction

In chapter 2 several methodologies to calculate the magnetic field in the air-gap of electric machines were presented with particular emphasis on conformal mapping. The complex permeance method proposed by Zarko *et al.* (Zarko et al., 2006, 2009; Boughrara et al., 2009a,b) uses conformal mapping to obtain a function that modulates the magnetic field distribution from the slotless configuration that was previously obtained by Zhu *et al.* (Zhu et al., 1993; Zhu and Howe, 1993a,b,c; Zhu et al., 2002).

This chapter presents a different approach to the complex permeance (CP) method using a scalar potential formulation (Hammond, 1982) to obtain the complex permeance function making the interpretation of the solution simpler and particularly suited for machines with a homopolar excitation (Anglada and Sharkh, 2016a). The methodology proposed to estimate the parameters of the permeance function reduces the computation time significantly because the number of points in which the function has to be evaluated is very low (enough to estimate the coefficients instead of evaluating the whole waveform in all the domain). The significant reduction in the computation time presents a major improvement in the context of the design and optimisation of electric machines.

This chapter is based on the work published by the author in (Anglada and Sharkh, 2016a; Anglada et al., 2017) and there are several novel contributions. First, it shows how to apply the CP function for the analysis of TFMs. In addition, the effect of curvature is effectively modelled using a proportional-logarithmic transformation that provides a deep insight as it does not modify the scale length. Finally, a novel algorithm for estimating the coefficients of the CP function based on random sampling, which can help to reduce the computation time significantly is described.

The chapter starts with a description of the complex permeance method considered and the difference between this method and Zarko's one. The following two sections show the complex transformations required to obtain the permeance function. Later, the mathematical model of the permeance function is shown and in the next section an algorithm to identify the parameters of the model is proposed. In the following section this method is applied to a real geometry, the TFM described in section 1.3.1 but the method can be generalised for any case that can be represented with a scalar potential formulation, and the results are validated with FEA. Finally the conclusions of this chapter are presented in section 3.8.

3.2 Zarko's Complex Permeance

The CP method was presented by Zarko *et al.* in (Zarko et al., 2006) as a natural generalisation of Zhu's relative permeance shown in (Zhu and Howe, 1993c). Zhu's relative permeance is a real function that modulates the radial component of the magnetic field to account for the slotting effect. The main contribution presented in (Zarko et al., 2006) is that considering the permeance function as a complex number can also modulate the tangential component of the magnetic field, not just the radial one. Furthermore, it is natural to consider the permeance function as a complex number because the Schwarz-Christoffel transformation is by definition a complex function. In (Zarko et al., 2006) the CP function is applied only to the magnetic field produced by the magnets in the rotor and in (Zarko et al., 2009) the armature windings magnetic field is considered.

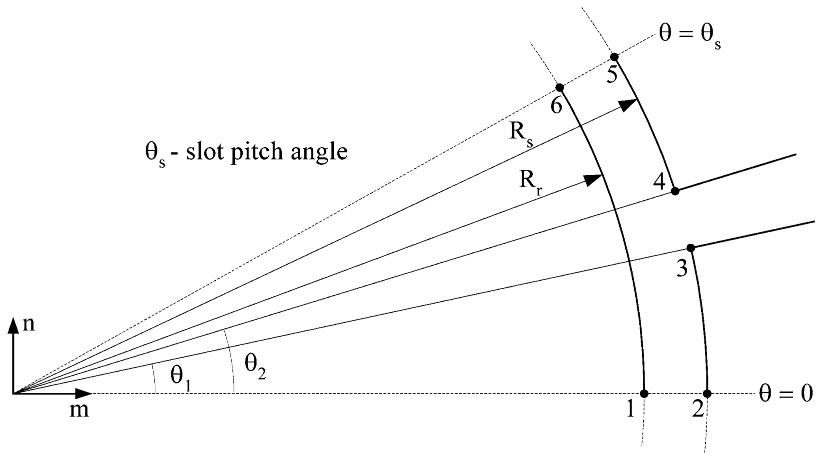

FIGURE 3.1: Zarko's geometry, from (Zarko et al., 2006), ©2006 IEEE.

Figure 3.1 shows the geometry considered by Zarko et al. (2006, 2009). It is important to point out that this transformation considers the effect of curvature with Rabinovici's transformation (Rabinovici, 1996) with the consequent change of scale described in section 3.4. Also, the methodology described in (Zarko et al., 2006, 2009) considers a single slot geometry (Gibbs, 1958) that in some cases may be inaccurate as described in chapter 2. The articles by Boughrara et al. (2009a,b) consider the effect of multiple slots using the SC Toolbox developed by Driscoll (Driscoll, 2005).

3.2.1 Limitations of Zarko's CP

- To obtain the coefficients of the permeance function it is necessary to do an iterative process to determine the coordinates of each point and later use a discrete Fourier transform, making the computation time very high.
- The implementation of the transformation itself is complicated and therefore the understanding of the system is more difficult.
- The torque is calculated using the Maxwell Stress Tensor making the interpretation difficult.
- To calculate the magnetic field produced by the permanent magnets in (Zarko et al., 2006) the deformation of the domain of the magnets is neglected (Krop et al., 2008).

3.3 Modified Complex Permeance

The air-gap of the machine under study has a toothed member (each C-core can be considered a tooth) and a smooth coreback. Figure 3.2 shows the z-plane, which is the real geometry, and the transformed domains (w and χ planes), which are described later in the chapter. The magnetic field distribution is obtained using a complex permeance (CP) function (Anglada and Sharkh, 2016a; Zarko et al., 2006; Boughrara et al., 2009a,b) adapted for a homopolar field distribution. We are assuming that the permeability of the iron is infinite and the effect of saturation is negligible.

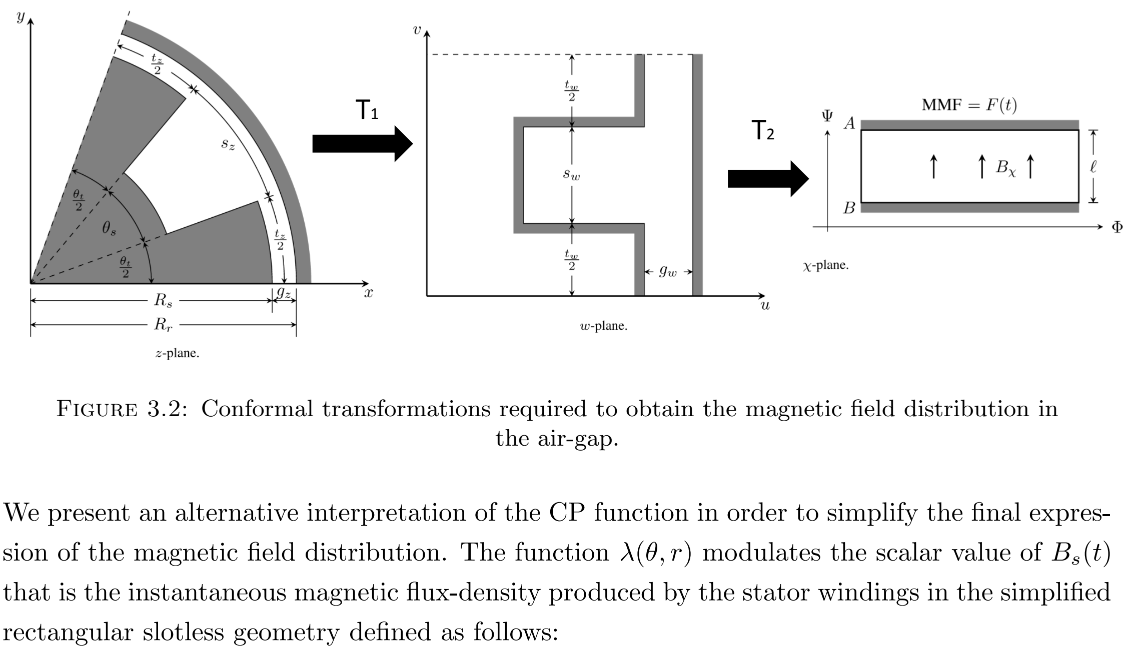

FIGURE 3.2: Conformal transformations required to obtain the magnetic field distribution in the air-gap.

We present an alternative interpretation of the CP function in order to simplify the final expression of the magnetic field distribution. The function $\lambda(\theta, r)$ modulates the scalar value of $B_s(t)$ that is the instantaneous magnetic flux-density produced by the stator windings in the simplified rectangular slotless geometry defined as follows:

$$B_s(t) = \frac{\mu_0 F(t)}{g_z}, \tag{3.1}$$

where $F(t)$ is the instantaneous magneto-motive force (MMF) produced by the stator windings and g is the effective air-gap length. The function $\lambda(\theta, r)$ depends only on the geometric properties of the air-gap that give the *shape*. The scalar value of $B_s(t)$ gives the *magnitude* to the function of the magnetic field distribution $\vec{B}_{stator}(t, \theta, r)$.

The function $\lambda(\theta, r)$ is calculated in such a way that the real part corresponds to the radial component and the imaginary to the tangential one. In this chapter the variable θ is expressed in electrical radians, such that a pole pitch is 2π; to change to mechanical radians it is necessary to divide by the number of pairs of poles. Accordingly, the expression of the stator's magnetic field distribution in the air-gap expressed as a vector is:

$$\vec{B}_{stator}(t, \theta, r) = B_s(t)\Big[\mathrm{Re}\left\{\lambda(\theta, r)\right\}\vec{u}_r + \mathrm{Im}\left\{\lambda(\theta, r)\right\}\vec{u}_\theta\Big]. \tag{3.2}$$

On the other hand, the rotor's magnetic field distribution is produced by the permanent magnets (PMs). The no-load magnetic field distribution in the air-gap of the slotless configuration can be expressed using complex number notation as

$$B_{sl}(\theta, r) = \sum_{n=1,3,5}^{\infty} K_n(r)\cos\big(n(\theta + \omega t)\big) + j\sum_{n=1,3,5}^{\infty} D_n(r)\sin\big(n(\theta + \omega t)\big), \tag{3.3}$$

where ω is the electrical frequency and the coefficients $K_n(r)$ and $D_n(r)$ are calculated according to (Zhu et al., 2002) and $j = \sqrt{-1}$ is the imaginary unit. Therefore, the magnetic field distribution produced by the rotor of the slotted geometry is

$$B_{rotor}(\theta, r, t) = B_{sl}(\theta, r) \cdot \lambda^*(\theta, r, t). \tag{3.4}$$

The value of $\lambda(\theta, r)$ is obtained using conformal mapping theory by transforming the original domain (z-plane) into a new one in which we know the solution, in this case the new domain is a rectangle (χ-plane) where the magnetic field is constant (Gibbs, 1958). To achieve this there are two conformal transformations to be done: a proportional-logarithmic transformation (Rabinovici, 1996) that transforms the circular geometry into a rectangular developed model and a Schwarz-Christoffel transformation that maps the developed model into a rectangle (Gibbs, 1958; Freeman, 1962; Zarko et al., 2006; Boughrara et al., 2009a,b).

3.3.1 Proportional-Logarithmic Transformation (T_1)

The first conformal transformation (T_1 in Figure 3.2) maps the circular geometry of the z-plane into a rectangular geometry in the w-plane. To achieve this T_1 has to be a proportional-logarithmic transformation (Rabinovici, 1996). This transformation is described in detail in section 3.4 and in (Anglada et al., 2017). The proportionality constant R_g chosen is the radius of the middle of the air-gap in this case. The transformation to obtain the w-plane is the following:

$$w = R_g \ln(z). \tag{3.5}$$

According to the theory of conformal mapping (Gibbs, 1958; Freeman, 1962; Driscoll and Trefethen, 2002) the relationship between the magnetic field in the z and w-planes expressed as complex numbers:

$$B_z = B_w \left(\frac{dw}{dz} \right)^* = B_w \left(\frac{R_g}{r_z} e^{j\theta_z} \right) \tag{3.6}$$

The term that multiplies B_w in (3.6) has a term that is a scale factor ($\frac{R_g}{r}$) and a second term ($e^{j\theta_z}$) that transforms the real component into radial and the imaginary one into tangential. To obtain the magnetic field at a particular point of the z-plane it is sufficient to know the value of the field on the w-plane and the derivative of the transformation evaluated in that point. If we define the relative permeance associated to the proportional-logarithmic transformation as

$$\lambda_{\log}(r) = \frac{R_g}{r}, \tag{3.7}$$

then, the expression of the magnetic field in the z-plane as a vector $\vec{B}_z$ in radial and tangential components is as follows

$$\vec{B}_z = \Big[\mathrm{Re}\left\{ B_w \right\} \vec{u}_r + \mathrm{Im}\left\{ B_w \right\} \vec{u}_\theta \Big] \lambda_{\log}(r). \tag{3.8}$$

3.3.2 Schwarz-Christoffel Transformation (T_2)

The details of Schwarz-Christoffel transformations and their application to solve this problem are given in (Gibbs, 1958; Freeman, 1962; Driscoll and Trefethen, 2002). According to the literature this transformation is sometimes called *Numerical Schwarz-Christoffel Transformation* because the equation of the transformation is not explicit, in this chapter the solution is obtained with the SC Toolbox developed by Driscoll (Driscoll, 2005).

The starting point is the polygon in the w-plane that needs to be transformed into a rectangle that is the χ-plane, shown schematically in Figure 3.2, in which the magnetic field distribution is known. The general equation of the SC transformation is as follows (Driscoll and Trefethen, 2002):

$$w = f(\chi) = K_1 \int \prod_{k=1}^{N} (\chi - \chi_k)^{\frac{\alpha_k}{\pi} - 1} d\chi + K_2, \tag{3.9}$$

where K_1 and K_2 are integration constants and α_k are the interior angles of the polygon. The function $\hat{f}(w)$ is defined as the inverse of $f(\chi)$:

$$\chi = \hat{f}(w). \tag{3.10}$$

Even though there is not an analytical expression of $\hat{f}(w)$ the derivative of the transformation of the w-plane into the χ-plane is defined as follows (taking into account that χ is a function of w)

$$\frac{d\chi}{dw} = \hat{f}'(w). \tag{3.11}$$

The relationship between the magnetic fields is given by

$$B_w = B_\chi\Big(\frac{d\chi}{dw}\Big)^* = B_\chi\Big\{\hat{f}'(w)\Big\}^*. \tag{3.12}$$

The functions $\hat{f}(w)$ and $\hat{f}'(w)$ can be evaluated in each point with the SC Toolbox once the map is created.

The SC transformation is such that the domain in the χ-plane is the rectangle shown in Figure 3.2. The solution to the Laplace equation considering an MMF $F(t)$ is the following:

$$B_\chi(t) = \frac{\mu_0 F(t)}{\ell}, \tag{3.13}$$

where the length ℓ can be calculated as the following:

$$\ell = |\chi_A - \chi_B|.$$

The SC Toolbox gives the option of obtaining $\chi_i = \hat{f}(w_i)$ making the calculation of ℓ trivial because is just the length of the side of the rectangle on the canonical domain. The field in the w-plane can be expressed as

$$B_w = B_\chi\Big\{\hat{f}'(w)\Big\}^* = B_s(t)\frac{g_z}{\ell}\Big\{\hat{f}'(w)\Big\}^*. \tag{3.14}$$

The term that multiplies $B_s(t)$ is the relative complex permeance associated with the SC transformation taking into account that w is a function of θ and r:

$$\lambda_{SC}(\theta, r) = \frac{g_z}{\ell}\Big\{\hat{f}'\big(w(\theta, r)\big)\Big\}^*. \tag{3.15}$$

For the polygon considered here there is not an explicit expression $\hat{f}$ but with the SC Toolbox (Driscoll, 2005) it can be evaluated at any point and also the derivative can be evaluated. Consequently, the function $\lambda_{SC}(\theta, r)$ cannot be obtained directly but can be evaluated at every point of the domain.

3.4 Effect of Curvature on the Magnetic Field

The problem of modelling the effect of curvature analytically was addressed by Rabinovici (1996) using a pure logarithmic transformation that maps the circular geometry into a rectangular one, which can be solved using conformal mapping techniques like those developed by Gibbs (1958) and Freeman (1962) based on the Schwarz-Christoffel transformation. However, a pure logarithmic transformation makes the length of the new geometry completely different from the real one thus making it difficult to assess how strong the effect of curvature is or what would happen if it is ignored. Similar methods were also used in (Zarko et al., 2006; Boughrara et al., 2009a; Markovic et al., 2004); although these produce a solution to the problem, they do not provide a direct insight into the effect of curvature partly due to the change in the length scale.

This section presents some original contributions about the influence of curvature on the magnetic field distribution and how the proportional-logarithmic transformation proposed by the author of this Thesis provides a deeper insight.

Figure 3.3 shows a generic cross-section of a rotating electric machine with a toothed stator and a smooth exterior rotor. One tooth-pitch is $\tau_z = s_z + t_z$. In Figure 3.3 s_z is the slot pitch, t_z the tooth pitch, g_z the effective air-gap length, R_r the rotor radius and R_s the stator bore radius. The effective air-gap length is defined as the magnet thickness plus the clearance gap plus the sleeve thickness.

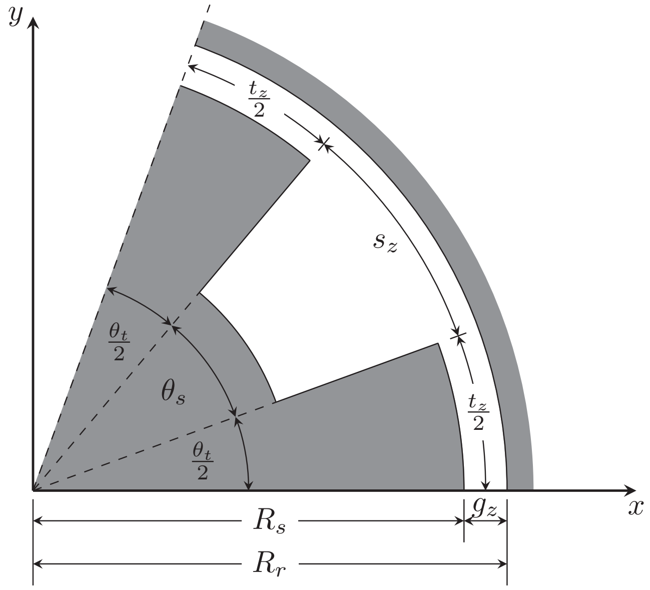

FIGURE 3.3: Cylindrical geometry studied showing only one slot in the z-plane.

The geometry in the z-plane in Figure 3.3 can be transformed into that shown in the w-plane in Figure 3.4 using a logarithmic transformation, as proposed by Rabinovici (Rabinovici, 1996):

$$w = R\ln(z) = R\ln(r_z) + jR\theta_z, \tag{3.16}$$

where R is a proportionality constant, $z = r_z e^{j\theta_z}$ is the complex variable in the z-plane and w the complex variable in the w-plane.

Rabinovici implicitly sets $R = 1$ in the above equation. However, this makes the w-plane geometry in Figure 3.4 very different in its scale from that in Figure 3.3. The vertical length of the geometry in the w-plane is equal to the angle of one tooth pitch, i. e. $\tau_w = \theta_\tau$, where θ_τ is the tooth pitch angle.

In this section we propose to set R to be the radius in the middle of the air-gap, $R_g = R_s + \frac{g_z}{2}$. This results in

$$t_w = R_g\theta_t = t_z, \tag{3.17}$$

$$s_w = R_g\theta_s = s_z, \tag{3.18}$$

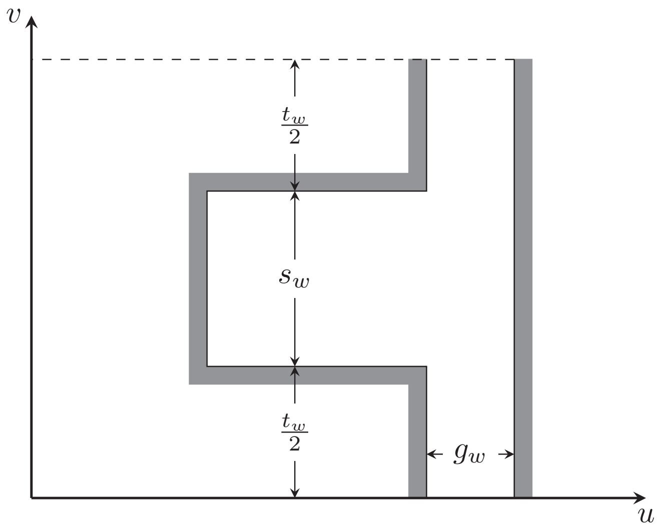

FIGURE 3.4: Rectangular developed model obtained after the proposed transformation in the w-plane.

$$\tau_w = R_g \theta_\tau = \tau_z, \tag{3.19}$$

$$g_w = R_g \Big[\ln(R_r) - \ln(R_s) \Big] = R_g \ln\left(\frac{R_r}{R_s}\right), \tag{3.20}$$

where θ_t and θ_s are the tooth and slot angles, respectively. From these equations it can be easily appreciated that all the geometrical length parameters are exactly the same as in Figure 3.3 with the exception of g_w.

It can be readily shown that g_w can be expressed in terms of g_z and R_g as follows:

$$g_w = R_g \ln\left(\frac{R_g + \frac{g_z}{2}}{R_g - \frac{g_z}{2}}\right). \tag{3.21}$$

After these first manipulations comes the first intuitive interpretation of this transformation. The geometry obtained from the proposed conformal transformation is exactly the same as the conventional developed model that is obtained simply by *cutting* and *opening* the machine. The only difference is in the parameter g_w whose value is given by (3.21).

3.4.1 Curvature Coefficient

Carter (Carter, 1900, 1926) proposed that the effect of slotting can be represented as a modification of the air-gap length of an equivalent slotless model. The effect of slotting on the mean air-gap flux density can be accounted by multiplying the air-gap length, g, by Carter's coefficient, K_c, (Krause et al., 2013) to obtain:

$$g' = gK_c, \tag{3.22}$$

which is set to be the gap of an equivalent slotless model. The mean value of the magnetic field in the slotted machine is then calculated as

$$B_{s-slotted} = \frac{\mu_0 F}{g'}. \tag{3.23}$$

where F is the mmf drop across the gap, g, of the slotless model. If we define $B_{s-slotless}$ as the mean value of the magnetic field of a slotless machine with a gap then

$$B_{s-slotless} = \frac{\mu_0 F}{g}. \tag{3.24}$$

Hence

$$B_{s-slotted} = \frac{B_{s-slotless}}{K_c}. \tag{3.25}$$

It was deduced previously, from (3.17)-(3.21), that using the proposed transformation the rectangular geometry obtained has the same basic dimensions as the original cylindrical geometry except for the air-gap length g_w. Following the same logic as that used when defining Carter's coefficient we define a curvature coefficient K_J such that

$$g_w = g_z K_J \,\rightarrow\, K_J = \frac{g_w}{g_z}. \tag{3.26}$$

Applying (3.26) to the mean value of the magnetic field:

$$B_{s-curv} = \frac{\mu_0 F}{g_z} = \frac{B_{s-rect}}{K_J}, \tag{3.27}$$

with

$$B_{s-rect} = \frac{\mu_0 F}{g_w}. \tag{3.28}$$

Substituting (3.21) into (3.26) we obtain the following expression for K_J as a function of the ratio between the radius of the machine and the air-gap length, R_g/g_z:

$$K_J = \frac{R_g}{g_z} \ln\left(\frac{\frac{R_g}{g_z} + \frac{1}{2}}{\frac{R_g}{g_z} - \frac{1}{2}}\right). \tag{3.29}$$

With this function a direct estimation of the influence of curvature on the mean value of the flux density can be obtained without any other calculation; the effect will depend on the ratio of g_z and R_g. Qualitatively this means that if the air-gap length is large compared to the radius of the machine the effect of curvature is significant and when the radius is considerably larger than the air-gap length this effect is negligible.

Like Carter's coefficient, the value of K_J is close 1; it equals 1 for a rectangular geometry and it becomes slightly grater than one as the curvature increases. The difference between the value of K_J and 1, i.e., $K_J - 1$, would therefore provide a measure of the effect of curvature on the magnetic field. Figure 3.5 shows a graph of $(K_J - 1)$ in percentage versus the ratio of the radius in the middle of the gap to the air-gap length. As expected, the influence of curvature reduces as the radius increases for a given air-gap length. Below a ratio of about 6 the effect of curvature is expected to be significant.

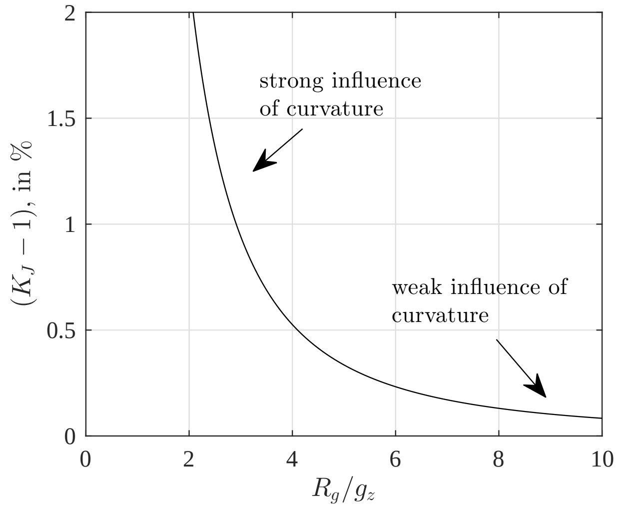

FIGURE 3.5: The curvature coefficient, K_J, as a function of the ratio between the air-gap radius and the air-gap length.

3.4.2 Magnetic Field Relations

Using the conformal transformation we can obtain the relationship between the magnetic field in the z-plane and the w-plane. With this relationship the solution of the rectilinear geometry in the w-plane can be transformed into a solution for the real cylindrical geometry in the z-plane. To deduce these equations, the magnetic scalar potential functions in both planes are considered (Hammond, 1999; Zarko et al., 2006; Boughrara et al., 2009a; Markovic et al., 2004, 2005; Anglada and Sharkh, 2016a; Anglada et al., 2017):

- $\varphi(x, y) \equiv$ scalar potential in the z-plane.
- $\psi(u, v) \equiv$ scalar potential in the w-plane.

Each point (u, v) in w is at the same potential as the corresponding point (x, y) in z and hence the following equation must be satisfied in all the domain:

$$\varphi(x, y) = \psi\Big(u(x, y), v(x, y)\Big). \tag{3.30}$$

The field intensity in the z-plane is obtained from the potential function in the z-plane, $\varphi(x, y)$, as follows:

$$H_z = H_x + jH_y = -\frac{\partial \varphi}{\partial x} - j\frac{\partial \varphi}{\partial y}. \tag{3.31}$$

The field intensity in the w-plane is obtained from the potential function in the w-plane, $\psi(u,v)$, as follows:

$$H_w = H_u + jH_v = -\frac{\partial \psi}{\partial u} - j\frac{\partial \psi}{\partial v}. \tag{3.32}$$

Applying the rule of an implicit derivative to the scalar potential we obtain:

$$\frac{\partial \varphi}{\partial x} = \frac{\partial \psi}{\partial u}\frac{\partial u}{\partial x} + \frac{\partial \psi}{\partial v}\frac{\partial v}{\partial x}, \tag{3.33}$$

$$\frac{\partial \varphi}{\partial y} = \frac{\partial \psi}{\partial u}\frac{\partial u}{\partial y} + \frac{\partial \psi}{\partial v}\frac{\partial v}{\partial y}. \tag{3.34}$$

Combining (3.31), (3.33) and (3.34) it can be shown that:

$$H_z = H_u\frac{\partial u}{\partial x} + H_v\frac{\partial v}{\partial x} + j\Big(H_u\frac{\partial u}{\partial y} + H_v\frac{\partial v}{\partial y}\Big). \tag{3.35}$$

As potential functions are analytic they satisfy the Cauchy-Riemann conditions (Hammond, 1999; Zarko et al., 2006; Anglada and Sharkh, 2016a; Anglada et al., 2017) and hence (3.35) they can be rewritten as

$$H_z = (H_u + jH_v)\Big(\frac{\partial u}{\partial x} - j\frac{\partial v}{\partial x}\Big), \tag{3.36}$$

or

$$H_z = H_w\Big(\frac{\partial u}{\partial x} - j\frac{\partial v}{\partial x}\Big). \tag{3.37}$$

Considering that $w = u(x,y) + jv(x,y)$, then

$$\frac{\partial w}{\partial x} = \frac{\partial u}{\partial x} + j\frac{\partial v}{\partial x} = \frac{\partial w}{\partial z}\frac{\partial z}{\partial x} = \frac{dw}{dz}. \tag{3.38}$$

The complex conjugate

$$\Big(\frac{dw}{dz}\Big)^* = \Big(\frac{\partial u}{\partial x} + j\frac{\partial v}{\partial x}\Big)^* = \frac{\partial u}{\partial x} - j\frac{\partial v}{\partial x}. \tag{3.39}$$

If (3.39) is substituted in (3.37), the relationship of the field intensity in the w-plane with the z-plane is then given by

$$H_z = H_w\Big(\frac{dw}{dz}\Big)^*. \tag{3.40}$$

Since $B = \mu_0 H$ in the air-gap, then

$$B_z = B_w\Big(\frac{dw}{dz}\Big)^*. \tag{3.41}$$

From (3.16):

$$\frac{dw}{dz} = \frac{R_g}{z} = \frac{R_g}{r_z} e^{-j\theta_z}. \tag{3.42}$$

Substituting (3.42) in (3.41) yields

$$B_z = B_w \left\{ \frac{R_g}{r_z} e^{j\theta_z} \right\} = B_w \left\{ M(r_z) e^{j\theta_z} \right\}. \tag{3.43}$$

The second term of (3.43), $e^{-j\theta_z}$, simply rotates and aligns the radial direction in the z-plane with the horizontal axis in the w-plane. It does not affect the value of the field and therefore it will not be analysed further.

The term $M = R_g/r_z$ can be interpreted as a scale factor, related with the flux focusing effect of curvature. Because of the nature of the transformation the region $r_z < R_g$ is *contracted*, which intensifies the field. In the region $r_z > R_g$, which is expanded compared to the rectangular model, the field's intensity is reduced. When $r_z = R_g$ the magnitude of the magnetic field is not altered.

The value of the scale factor in the z-plane therefore defines the influence of curvature on the magnitude of the magnetic field density at a particular point. Figure 3.6 shows a 2D representation of M in a certain region of the z-plane. The value of $M(r_z)$ was restricted to values between 0.5 and 1.5 because usually the value of M in the air-gap (the region of interest in this case) is within these limits.

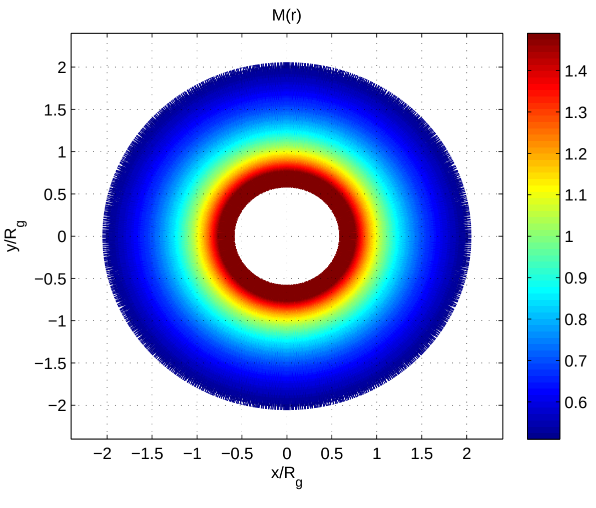

FIGURE 3.6: $M(r_z) = \frac{R_g}{r_z}$.

This representation of the scale factor $M(r_z)$ shows how the magnetic field is intensified in some regions and debilitated in others. As the radius reduces, the field lines are bunched closer together, thus intensifying the magnetic field, and vice versa. If the air-gap length is small and it is contained within the light green region the effect of curvature will be small. However, if this is not the case the effect of the scale factor will be important – neglecting the curvature gives inaccurate results. The proportionality constant R_g will determine the radius at which the scale factor is unity, the radius where distances are not distorted.

3.4.3 Permanent Magnet Transformation

In this section the transformation equations for a radially magnetised permanent magnet are deduced based on the assumption that these permanent magnets can be represented by two current sheets on the edges of each magnet (Boules, 1985; Rabinovici, 1996), with a current density J (A/m) equal to the magnetisation of the material, $J = \mathcal{M}$. A permanent magnet in the z-plane is represented in Figure 3.7 with the equivalent current sheets as dots and crosses.

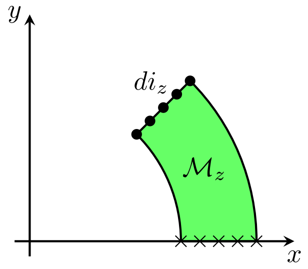

FIGURE 3.7: Permanent magnet in the cylindrical geometry, the z-plane.

Rabinovici (Rabinovici, 1996) proposes that a cylindrical permanent magnet in the z-plane is transformed into a rectangular one in the w-plane such that the magnetisation $\mathcal{M}_w$ in the w-plane is set in such a way that the total equivalent current is the same in both planes. The new permanent magnet in the w-plane is shown in Figure 3.8. The implicit assumption in this procedure is that the current density is constant along the edge of the magnets in the w-plane, i.e., that $\mathcal{M}_w$ is constant. In the following paragraphs it is shown that such assumption is not correct.

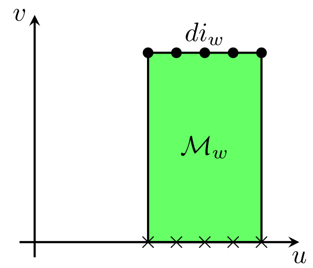

FIGURE 3.8: Permanent magnet in the rectangular developed geometry, the w-plane.

For the deduction of the transformation equations let us consider the permanent magnet in the z-plane shown in Figure 3.7 and the transformed magnet in the w-plane, Figure 3.8. The equivalent current sheets of the magnet in the z-plane have a constant current density J_z. To represent these two current sheets in the w-plane each differential current point, di_z, is mapped on the w-plane in the corresponding position (Rabinovici, 1996; Boughrara et al., 2009a). The magnitude of the current should be same in both planes, this is

$$di_z = di_w. \tag{3.44}$$

Each of these differential currents can be expressed in terms of the corresponding current density

$$di_z = J_z dr_z, \tag{3.45}$$

$$di_w = J_w du. \tag{3.46}$$

Combining (3.44), (3.45) and (3.46) yields

$$J_z dr_z = J_w du \Rightarrow J_w = J_z\Big(\frac{du}{dr_z}\Big). \tag{3.47}$$

The derivative can be obtained from (3.16). The final expression of the new current density is the following:

$$J_w(r_z) = J_z\Big(\frac{r_z}{R_g}\Big) = \frac{J_z}{M(r_z)}. \tag{3.48}$$

The current density of the equivalent current sheet is therefore not constant in the w-plane; it is modified by the scale factor, $M(r_z)$.

3.5 Properties of the CP Function

The function $\lambda_{\log}(r)$ associated to the logarithmic transformation is a real number and the function $\lambda_{SC}(\theta, r)$ associated to the SC transformation can be separated into real and imaginary parts that correspond to the radial and tangential components respectively. The permeance function can be expressed as the product of these two functions as follows:

$$\lambda(\theta, r) = \lambda_{\log}(r)\Big[\lambda_r(\theta, r) + j\lambda_\theta(\theta, r)\Big], \tag{3.49}$$

where

$$\lambda_{SC}(\theta, r) = \lambda_r(\theta, r) + j\lambda_\theta(\theta, r). \tag{3.50}$$

The function $\lambda_{SC}(\theta, r)$ has the same shape as the magnetic field distribution of the rectangular geometry (w-plane in this chapter, Figure 3.2) therefore for each r the real and imaginary parts can be expressed as Fourier series according to (Freeman, 1962) because of the symmetry of the boundary conditions the radial component has to be an even function (which can be approximated as a Fourier cosine series) and the tangential component has to be an odd function (which can be approximated as a Fourier sine series):

$$\lambda_r(\theta, r) = \overline{\lambda}_r\Big[1 + \sum_{n=1}^{\infty} \gamma_n(r)\cos(n\,\theta)\Big], \tag{3.51}$$

$$\lambda_\theta(\theta, r) = \sum_{n=1}^{\infty} \lambda_{\theta n}(r)\sin(n\,\theta), \tag{3.52}$$

with the coefficients calculated accordingly:

$$\overline{\lambda}_r = \frac{1}{\pi}\int_0^{\pi} \mathrm{Re}\Big\{\lambda_{SC}(\theta, r)\Big\}d\theta, \tag{3.53}$$

$$\gamma_n(r) = \frac{2}{\pi \overline{\lambda}_r} \int_0^{\pi} \mathrm{Re}\left\{\lambda_{SC}(\theta, r)\right\} \cos(n\theta) d\theta, \tag{3.54}$$

$$\lambda_{\theta n}(r) = \frac{2}{\pi} \int_0^{\pi} \mathrm{Im}\left\{\lambda_{SC}(\theta, r)\right\} \sin(n\theta) d\theta. \tag{3.55}$$

3.5.1 Analysis of $\overline{\lambda}_r$

From the strictly mathematical point of view the permeance function associated with the SC transformation is fully defined if the functions $\overline{\lambda}_r(r)$, $\gamma_n(r)$ and $\lambda_{\theta n}(r)$ are known in all the air-gap. The function $\overline{\lambda}_r(r)$ is the mean value of the radial magnetic field in the air-gap in the rectangular geometry that is the w-plane. To gain an insight about this function let us define a closed rectangular surface (a box) S of depth h as shown by a dashed line in Figure 3.9 in the rectangular developed model of the machine, this would be a projection of the w-plane. From Gauss' Law we know that the total flux through a closed surface is 0 and that there is only normal flux in the *top* A and *bottom* B of S:

$$\iint_A \vec{B}_w(u, v) \cdot d\vec{s} = - \iint_B \vec{B}_w(u, v) \cdot d\vec{s}. \tag{3.56}$$

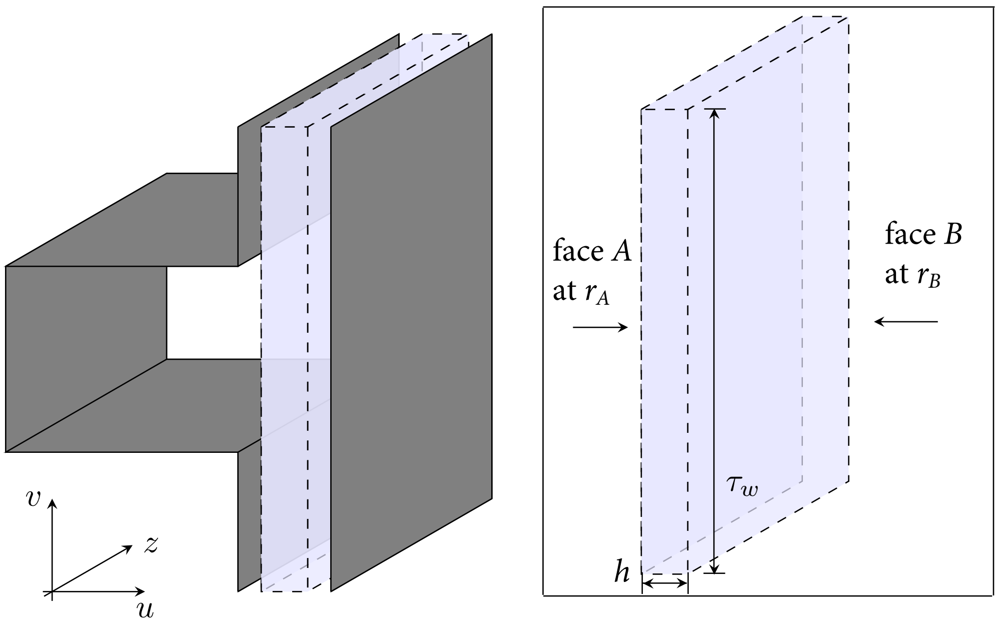

FIGURE 3.9: Geometry considered to apply the Gauss Law.

Only the real component of B_w is contributing to the flux so the total flux entering A:

$$\Phi_A = \iint_A \vec{B}_w(u, v) \cdot d\vec{s} = \iint_A B_{sw} \overline{\lambda}_r(r_A) \Big[1 + \sum_{n=1}^{\infty} \gamma_n(r_A) \cos(n\,\theta)\Big] \cdot ds, \tag{3.57}$$

where τ_w is the pole pitch and θ can be expressed:

$$\theta = \frac{2\pi}{\tau_w} v, \tag{3.58}$$

where v is the vertical coordinate as shown in Figure 3.9. The differential area can be expressed as:

$$ds = h \cdot dv. \tag{3.59}$$

(3.57) can be rewritten as:

$$\Phi_A = \int_0^{\tau_w} B_{sw} \overline{\lambda}_r(r_A) \Big[1 + \sum_{n=1}^{\infty} \gamma_n(r_A) \cos\Big(\frac{2\pi n}{\tau_w} v\Big)\Big] h \cdot dv \tag{3.60}$$

The total flux in A:

$$\Phi_A = B_{sw} \tau_w h \overline{\lambda}_r(r_A). \tag{3.61}$$

Similarly we can calculate the flux in B:

$$\Phi_B = -B_{sw} \tau_w h \overline{\lambda}_r(r_B). \tag{3.62}$$

Substituting (3.61) and (3.62) into (3.56):

$$B_{sw} \tau_w h \overline{\lambda}_r(r_A) = B_{sw} \tau_w h \overline{\lambda}_r(r_B), \tag{3.63}$$

All the terms are exactly the same by definition except the mean value of the permeance function so it was proven that

$$\overline{\lambda}_r(r_A) = \overline{\lambda}_r(r_B) = \overline{\lambda}_r, \tag{3.64}$$

for any value of r. The mean value of the permeance function, $\overline{\lambda}_r$, does not depend on the radius; it is constant in all the air-gap necessarily because of the conservation of flux. On the other hand the functions $\gamma_n(r)$ and $\lambda_{\theta n}(r)$ have an unknown shape but they can be approximated as polynomials. For the polynomial approximation, instead of using the variable r the distance to the coreback δ is used to simplify the subsequent expressions:

$$\delta = R_g + \frac{g}{2} - r. \tag{3.65}$$

The functions of the Fourier coefficients expressed as polynomials of δ are as follows

$$\gamma_n(\delta) = \gamma_n^0 + \gamma_n^1 \delta + \gamma_n^2 \delta^2 + \cdots, \tag{3.66}$$

$$\lambda_{\theta n}(\delta) = \lambda_{\theta n}^1 \delta + \lambda_{\theta n}^2 \delta^2 + \lambda_{\theta n}^3 \delta^3 + \cdots, \tag{3.67}$$

where γ_n^0, γ_n^1, γ_n^2, ..., are the Taylor coefficients for the radial component and $\lambda_{\theta n}^1$, $\lambda_{\theta n}^2$, $\lambda_{\theta n}^3$, ..., the corresponding ones for the tangential component[1].

3.6 Estimation of the Coefficients of the CP Function

One of the main disadvantages of the CP method implemented in (Zarko et al., 2006; Boughrara et al., 2009a,b) is that the computation time is high because the CP function needs to be evaluated at each point to obtain the waveform. However, with the proposed methodology for an arbitrary geometry the machine designer can decide the harmonic order, N_h, and the order of the polynomial of the Taylor series, N_p, and after that estimate the number of points that have to be evaluated in order to obtain the coefficients. For the radial component there are N_c coefficients ($\overline{\lambda}_r$, γ_n^0, γ_n^1, γ_n^2, ...) and for the tangential component there are $N_{c\theta} < N_c$ coefficients ($\lambda_{\theta n}^1$, $\lambda_{\theta n}^2$, $\lambda_{\theta n}^3$, ...). Under these conditions the model can be fully defined by evaluating at least N_c independent points. If N_h is the higher order harmonic and N_p the power of the last term of the Fourier series (which are defined by the the user), N_c is calculated as follows:

$$N_c = N_h(N_p + 1) + 1. \tag{3.68}$$

To describe the following algorithm to identify the parameters of the permeance function instead of directly calculating $\gamma_n(\delta)$ we will first calculate $a_n(\delta)$ that is the harmonic amplitude before normalisation:

$$a_n(\delta) = \overline{\lambda}_r \gamma_n(\delta). \tag{3.69}$$

For an arbitrary point (θ_i, r_i) the value of the permeance function:

$$\mathrm{Re}\Big\{\lambda_{SC}(\theta_i, r_i)\Big\} = \overline{\lambda}_r + \sum_{n=1}^{N_h}\sum_{m=0}^{N_p} a_n^m \delta_i^m \cos(n\,\theta_i), \tag{3.70}$$

where $\lambda_{SC}(\theta_i, r_i)$ is calculated as follows:

$$\lambda_{SC}(\theta_i, r_i) = \lambda(\theta_i, r_i)\frac{r_i}{R_g}. \tag{3.71}$$

If we consider K independent points, with $K > N_c$, we have an over determined linear system with K equations and N_c unknowns that are the coefficients. (3.70) can be written in a matrix form as follows:

$$\mathbf{XC} = \mathbf{\Lambda}, \tag{3.72}$$

[1] The tangential component does not have the $\lambda_{\theta n}^0$ term because there is not tangential component at $\delta = 0$ in this geometry.

where $[\mathbf{X}]_{K\times N_c}$ is the matrix with the points in which the permeance function is evaluated, organised to be consistent with (3.70) as follows:

$$\Big[\mathbf{X}\Big]_{K\times N_c} =$$
$$\begin{bmatrix} 1 & \cos(\theta_1) & \delta_1\cos(\theta_1) & \dots & \delta_1^{N_p}\cos(\theta_1) & \dots & \cos(N_h\,\theta_1) & \delta_1\cos(N_h\,\theta_1) & \dots & \delta_1^{N_p}\cos(N_h\,\theta_1) \\ 1 & \cos(\theta_2) & \delta_2\cos(\theta_2) & \dots & \delta_2^{N_p}\cos(\theta_2) & \dots & \cos(N_h\,\theta_2) & \delta_2\cos(N_h\,\theta_2) & \dots & \delta_2^{N_p}\cos(N_h\,\theta_2) \\ \vdots & \vdots & \vdots & \ddots & \vdots & \ddots & \vdots & \vdots & \ddots & \vdots \\ 1 & \cos(\theta_K) & \delta_K\cos(\theta_K) & \dots & \delta_K^{N_p}\cos(\theta_K) & \dots & \cos(N_h\,\theta_K) & \delta_K\cos(N_h\,\theta_K) & \dots & \delta_K^{N_p}\cos(N_h\,\theta_K) \end{bmatrix} \tag{3.73}$$

C is the matrix with the coefficients that we want to estimate:

$$\Big[\mathbf{C}\Big]_{N_c\times 1} = \begin{bmatrix} \overline{\lambda}_r \\ a_1^0 \\ a_1^1 \\ \vdots \\ a_1^{N_p} \\ a_2^0 \\ \vdots \\ a_{N_h}^{N_p} \end{bmatrix}. \tag{3.74}$$

Λ is the solution vector

$$\Big[\mathbf{\Lambda}\Big]_{K\times 1} = \begin{bmatrix} \mathrm{Re}\Big\{\lambda_{SC}(\theta_1, r_1)\Big\} \\ \mathrm{Re}\Big\{\lambda_{SC}(\theta_2, r_2)\Big\} \\ \vdots \\ \mathrm{Re}\Big\{\lambda_{SC}(\theta_K, r_K)\Big\} \end{bmatrix}. \tag{3.75}$$

The coefficients can be estimated using the following linear least squares algorithm:

$$\mathbf{C} = \Big[\Big(\mathbf{X}^t\mathbf{X}\Big)^{-1}\mathbf{X}^t\Big]\mathbf{\Lambda}, \tag{3.76}$$

where t denotes the transposed matrix.

Once the vector **C** is known the real part of the complex permeance function is fully defined. The procedure for the imaginary part is completely analogous. Once the real and the imaginary parts are obtained the magnetic field distribution is known as a vector in all the air-gap.

3.6.1 Analysis of the Matrix X

The algorithm described in the previous section enables the estimation of the parameters of the permeance function if we have the value of it in at least N_c *independent* points. But what is the meaning of independent points in this context? From the point of view of linear algebra we have

N_c independent points if and only if:

$$\text{rank}\left\{\mathbf{X}\right\} = N_c \tag{3.77}$$

This condition is equivalent to saying that we have N_c independent points if and only if the matrix $[\mathbf{X}^t\mathbf{X}]$ is not singular (all the eigenvalues are not zero).

To illustrate the problems that can bring the fact that the points are not independent let us consider the geometry of the TFM built at the University of Southampton. The first step if we want to estimate the parameters of the permeance function is to choose the number of harmonics considered and the order of the polynomial. For this example let us consider $N_h = 10$ and $N_p = 5$. The second step is to choose enough points in the domain to apply the algorithm described in the previous section, a logical approach is to apply a grid to the air-gap, we will call this set of points S_1. The 273 (which is a number grater than N_c so it is an overdetermined system) points chosen are shown in Figure 3.10.

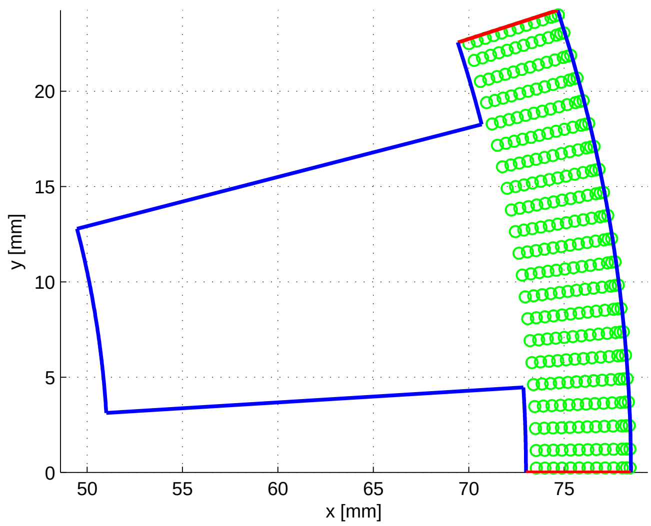

FIGURE 3.10: Points chosen to estimate the parameters of the permeance function.

Under these assumptions the parameters can be estimated and the values obtained for the harmonics are shown in Figure 3.11.

It can be appreciated in Figure 3.11 that the approximation is very accurate compared with the results obtained by evaluating the permeance function in thousands of points for each δ and later calculate the coefficients of the Fourier series by definition. Also the values obtained are consistent with the ones obtained with 2D FEA. Figure 3.12 shows the magnetic field distribution in the air-gap that was used to obtain the coefficients of the permeance function. The software used was Ansys Maxwell and for the calculation of the permeance function the analogy between electrostatic and magnetostatic was considered (the field expressed using the scalar potential formulation).

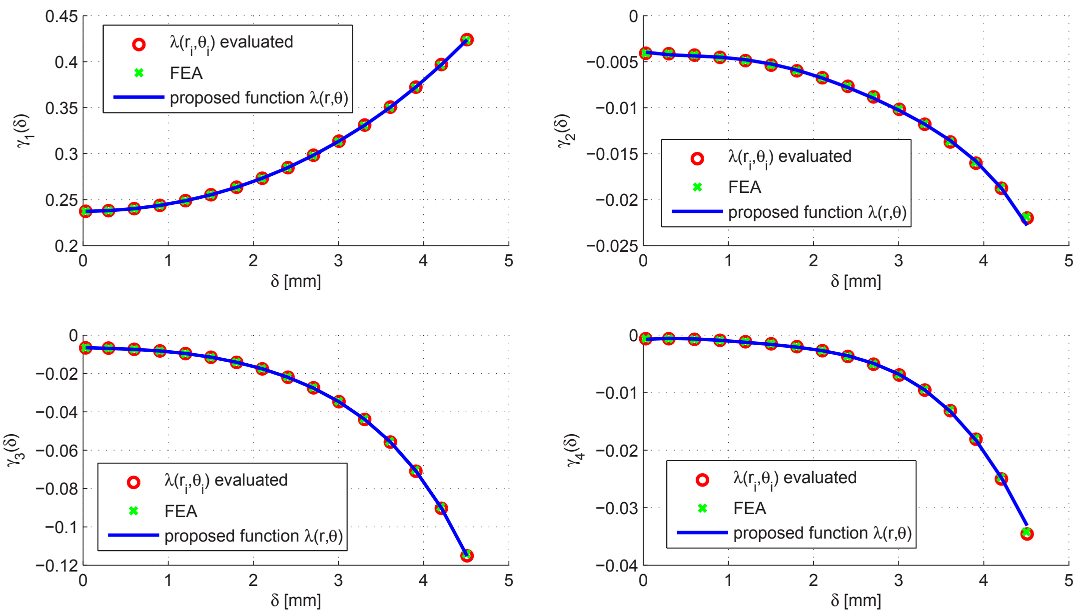

FIGURE 3.11: The amplitude of the first four harmonics of the radial component of the magnetic field with $N_h = 10$ and $N_p = 5$.

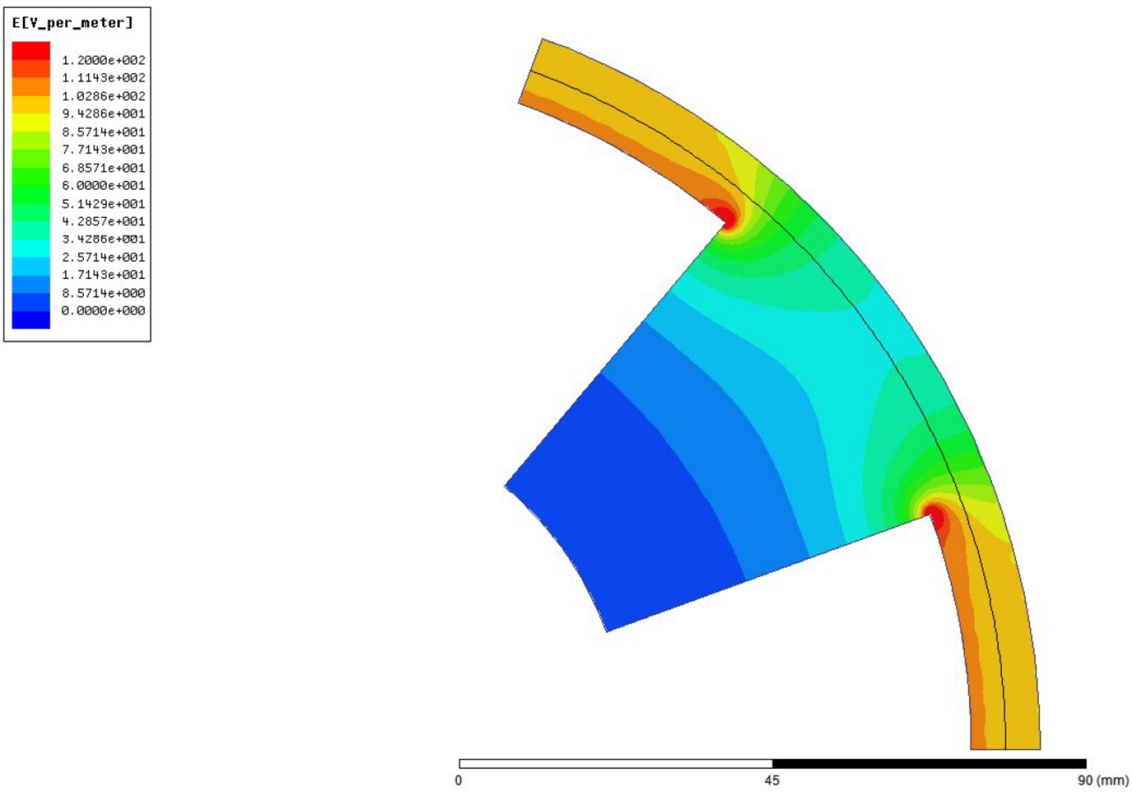

FIGURE 3.12: Magnetic field distribution obtained using FEA with a scalar potential formulation.

Let us assume that we want to use the same algorithm but now we consider $N_h = 11$ instead of $N_h = 10$ because for some reason we want to make sure that the 11th harmonic is not significant. Considering the same set of points S_1 the first four harmonics are shown in Figure 3.13.

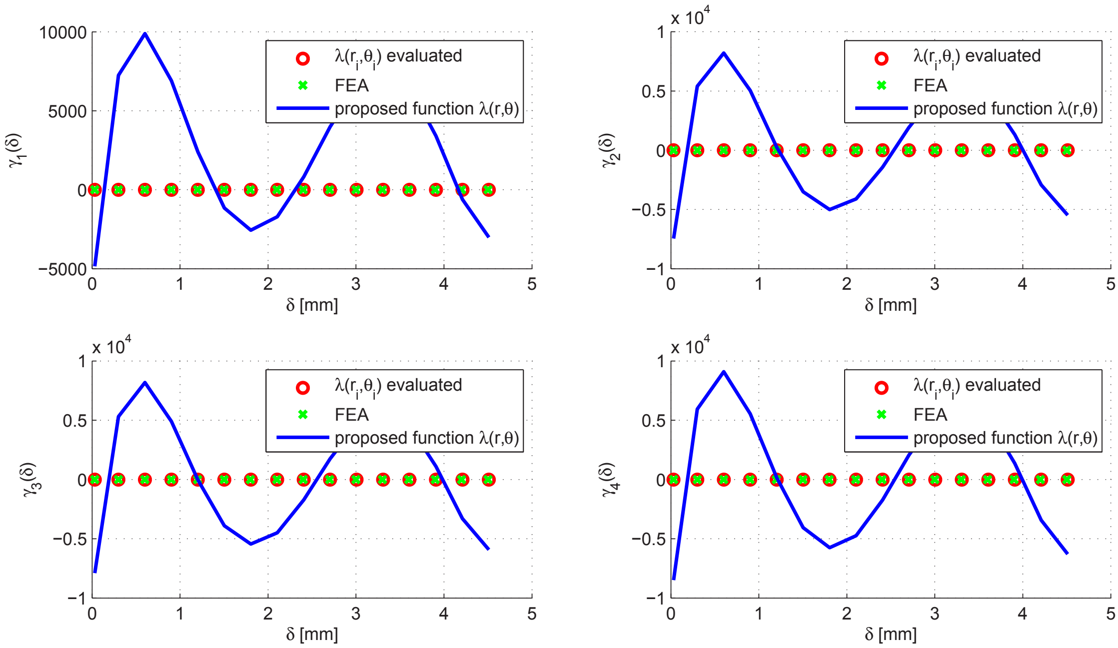

Figure 3.13: The amplitude of the first four harmonics of the radial component of the magnetic field $N_h = 11$ and $N_p = 5$.

We can see clearly in Figure 3.13 that the solution obtained is not consistent with the results obtained by direct evaluation and FEA. Even more, these results are not correct and the error in the calculation of the harmonics is very significant.

As an example to illustrate a similar situation let us assume that we have the following function:

$$f(x) = a\sin(x) + b\sin(2x) \tag{3.78}$$

and we want to estimate the value of the coefficients a and b. Using the same idea of creating a grid that was applied in the air-gap we will evaluate the function in 3 points:

$$x_1 = 0 \tag{3.79}$$
$$x_2 = \frac{\pi}{2} \tag{3.80}$$
$$x_3 = \pi \tag{3.81}$$

If we want to formulate this problem with the proposed algorithm we have the following matrix equation:

$$\begin{bmatrix} \sin(x_1) & \sin(2x_1) \\ \sin(x_2) & \sin(2x_2) \\ \sin(x_3) & \sin(2x_3) \end{bmatrix} \begin{bmatrix} a \\ b \end{bmatrix} = \begin{bmatrix} f(x_1) \\ f(x_2) \\ f(x_3) \end{bmatrix} \tag{3.82}$$

In this case we have that:

$$\mathbf{X} = \begin{bmatrix} 0 & 0 \\ 1 & 0 \\ 0 & 0 \end{bmatrix} \Rightarrow [\mathbf{X}^t\mathbf{X}] = \begin{bmatrix} 1 & 0 \\ 0 & 0 \end{bmatrix} \tag{3.83}$$

So the matrix that we want to invert, $[\mathbf{X}^t\mathbf{X}]$, is singular and the algorithm fails in giving a solution. We would have the same problem if we considered a grid of 5 points from 0 to 2π. Figure 3.14 shows the function $f(x) = a\sin(x) + b\sin(2x)$ with $a = 1$ and $b = 0.5$ in the range 0-2π in colour blue. The red and green curves are the first and second harmonics respectively. The dashed black lines are the grid we proposed, we can see that in all our *measurements* we see the green function vanish so the amplitude can't be estimated.

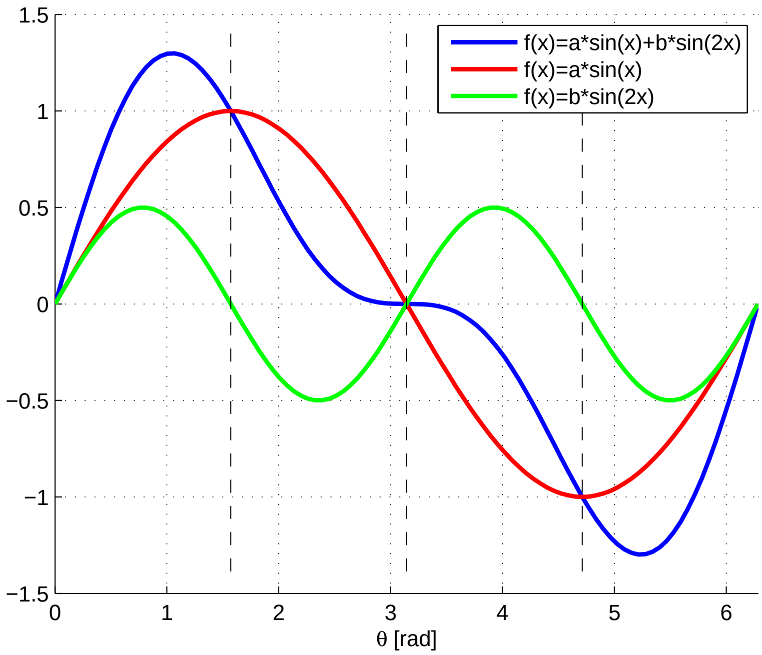

FIGURE 3.14: Function and harmonics of the example function $f(x) = a\sin(x) + b\sin(2x)$.

The same problem appears if we are trying to calculate the harmonic amplitude of a signal $f(t) = K + h\sin(2\pi f \cdot t)$ and we have a sampling frequency of the same value f. Each period we would measure the same value of $f(t) = f(t+T)$ so we could not estimate the value of K and h.

Now let us do something different, to avoid this problem we decide to pick the 3 points randomly. If we consider $\mathbf{R}(0,1)$ a random variable between 0 and 1 with constant probability density function we can express the problem as the following:

$$x_n = \pi \cdot \mathbf{R}(0,1) \tag{3.84}$$

Generating 3 random numbers in MATLAB we obtain by chance the following:

$$x_1 = 1.1962 \tag{3.85}$$

$$x_2 = 0.9505 \tag{3.86}$$

$$x_3 = 0.9266 \tag{3.87}$$

so the matrices:

$$\mathbf{X} = \begin{bmatrix} 0.9307 & 0.6810 \\ 0.8137 & 0.9460 \\ 0.7996 & 0.9604 \end{bmatrix} \Rightarrow [\mathbf{X}^t\mathbf{X}] = \begin{bmatrix} 2.1676 & 2.1715 \\ 2.1715 & 2.2810 \end{bmatrix} \tag{3.88}$$

hence, now the matrix can be inverted without any problem.

3.6.2 Random Sampling

To improve the reliability of this algorithm we want to make sure that we avoid having any problem in inverting the the matrix $[\mathbf{X}^t\mathbf{X}]$, or what is the same: that we have at least N_c independent points. To achieve this we propose to generate a set of random points. It was observed that if we have a given number of points distributed uniformly as a grid and we are trying to *detect* a high frequency space harmonic whose period is of a similar order of magnitude as the separation of the points; then the matrix $[\mathbf{X}^t\mathbf{X}]$ may produce problems in the inversion. Because of the nature of random sampling this problem does not appear because the points are not equally spaced. Each point is calculated as follows:

$$\delta_i = d_m \cdot \mathbf{R}(0,1), \tag{3.89}$$

$$\theta_i = 2\pi \cdot \mathbf{R}(0,1), \tag{3.90}$$

where $\mathbf{R}(0,1)$ denotes a random variable between 0 and 1 with constant probability density function.

Figure 3.15 shows the set of points S, which consists in 250 points generated randomly. The improvement in the stability of the algorithm is due to the fact that the points are not equally spaced and therefore the high frequency harmonics can be detected.

3.7 Results

This section illustrates the proposed methodology by its application to the transverse-flux (or VRPM) machine described in chapter 1.

The windings of the machine have $N_t = 230$ turns in the configuration analysed in this chapter and the rated current I is 10 A. The MMF in each C-core head is calculated as follows

$$F = \frac{1}{2}N_t I = 1150\,\mathrm{A}, \tag{3.91}$$

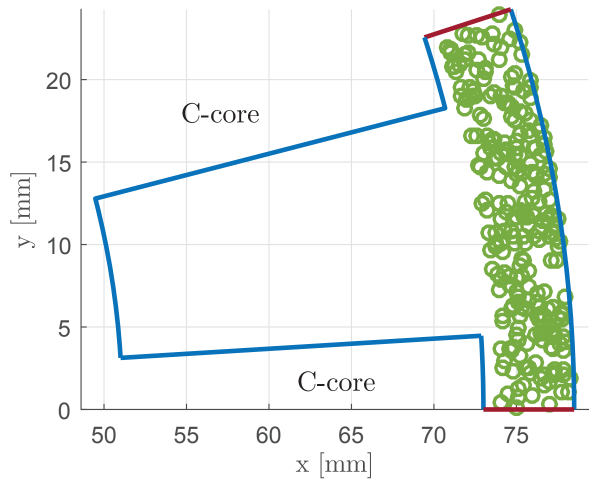

FIGURE 3.15: The set of random points, S. In this case it consists 250 random points..

therefore the magnetic field of the slotless configuration is

$$B_s = \frac{\mu_0 F}{g} = \frac{4\pi \cdot 10^{-7} \cdot 1150}{5.5 \cdot 10^{-3}} \approx 0.263\,\mathrm{T}. \tag{3.92}$$

If the current was a sinusoidal the value of B_s would not be constant but a sinusoidal function as well, the analysis here considering a constant current is the case of a square waveform.

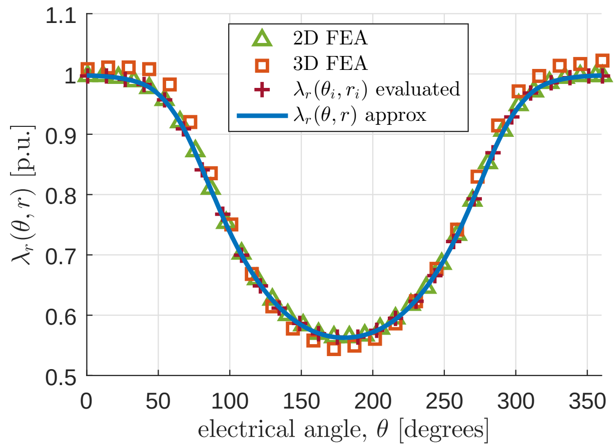

FIGURE 3.16: $\lambda_r(\theta, r)$ in the middle of the air-gap, $r = R_g$.

Figure 3.16 shows the real part of the permeance function at the middle of the air-gap ($r = R_g$). The green triangles were obtained using 2D FEA with a scalar potential formulation, the orange squares were obtained using 3D magnetostatic FEA, the red crosses are the value of $\lambda_r(\theta_i, r_i)$ evaluated using the SC Toolbox and the blue line is the approximated model considering 500 random points (which is a number much greater than N_c to make sure that it is an overdetermined system), the harmonic order $N_h = 11$ and the polynomial order $N_p = 5$. The value of $\overline{\lambda}_r$ obtained by evaluating the function, 2D FEA and the proposed model has less than 0.01 % error in this case.

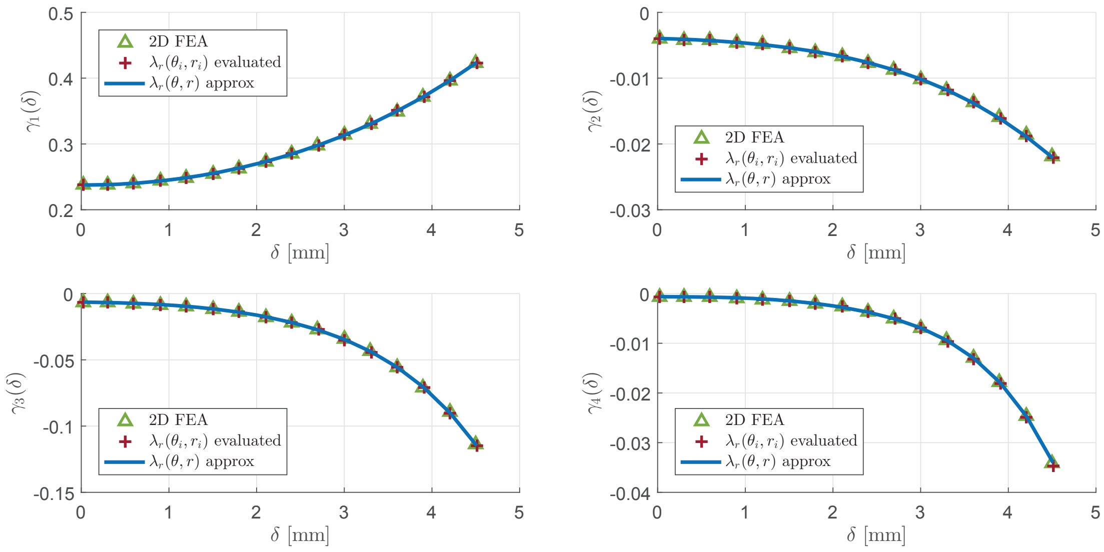

FIGURE 3.17: The amplitude of the first four harmonics of the radial component of the magnetic field $N_h = 11$ and $N_p = 5$, with a set of 500 random points.

To study the accuracy of the method in the entire domain and not only in the air-gap, Figure 3.17 shows the harmonic amplitude of the first four harmonics obtained by evaluating the permeance function, 2D FEA and the proposed method. The coefficients of the Fourier series for the comparison were calculated by evaluating (3.53) and (3.54) after obtaining the waveform with FEA or by evaluating points with the SC Toolbox. The software developed for this chapter is shown in Appendix C at the end of this Thesis.

As an example, one of the possible outcomes of the code developed in this Thesis is shown in Figure 3.18. The radial component of the magnetic field distribution is shown in the air-gap in a similar way as the typical FEA package would.

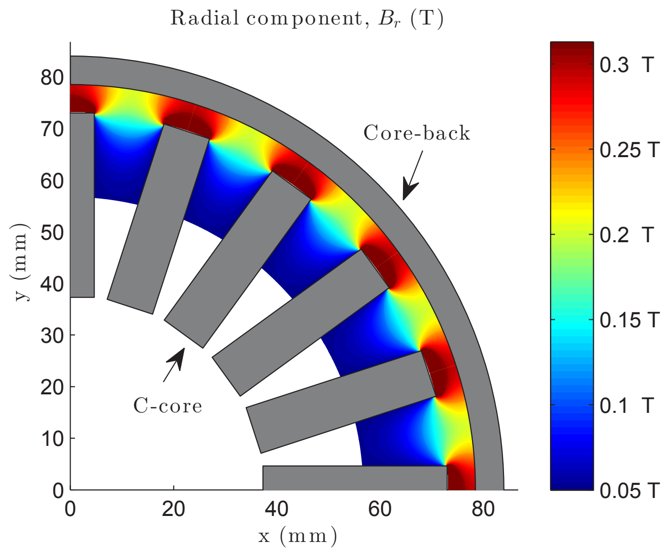

FIGURE 3.18: Radial component of the magnetic field distribution in the air-gap obtained using the CP function, quarter of the model only.

3.8 Conclusion

This chapter illustrates how to obtain the magnetic field distribution in the air-gap of electric machines using the CP method combined with random sampling. The case study is a TFM but it can be applied to other machines that have a slotted topology. The results obtained with the methodology presented here are consistent with FEA and with the traditional CP method.

In this chapter the influence of curvature on the magnetic field distribution in slotted rotating PM electric machines has been investigated. The proposed proportional logarithmic transformation provides an insight into the effect of curvature because it preserves the length scale. The curvature coefficient, K_J, indicates when the effect of curvature is going to be important. The value of the curvature coefficient, K_J which is the ratio of the air-gaps in the rectangular and cylindrical models in the w and z-planes, respectively, tends to be small. However, this small change of the air-gap length in the w-plane has a significant influence in the amplitude of the asynchronous harmonics of the magnetic field distribution (Anglada et al., 2017). The effect of curvature on rotor losses is discussed in section A.2.

Random sampling can effectively improve the computation time by reducing the number of points at which the CP function has to be evaluated. To generate the whole waveform of the CP function at a particular radius, r, it is necessary to evaluate a large number of points depending on the accuracy required. With a small set of randomly generated points we can accurately estimate the CP function coefficients in all the air-gap. Random sampling was preferred to uniform sampling because of the improvement of the stability of the algorithm.

The formulation of the problem is such that the *shape* of the CP function is deduced from conformal mapping theory and we only have to calculate the coefficients of the polynomials. This allows us to directly estimate the amplitude of the harmonics, which facilitates subsequent analysis of performance.

Chapter 4

Analysis of Transverse-Flux Machines

4.1 Introduction

Traditionally, the renewable energy industry has been dominated by induction machines, electrically excited synchronous machines and conventional radial or axial permanent magnet (PM) machines, which normally operate at high speed (1500-3000 rpm) and low torque. Wind and marine turbines normally operate at low speed, around 5 to 25 rpm, making it necessary to install a gearbox in the drive-train to enable the use of a conventional generator (Sopanen et al., 2011; Polinder et al., 2006; Spooner et al., 2005; Mueller et al., 2007; Semken et al., 2012). Several novel machines have been designed to operate as direct-drive generators in renewable energy sources but they are not widespread across the industry (Polinder et al., 2013; National Renewable Energy Laboratory, 2014, 2015; Carroll et al., 2015). Transverse flux machines (TFMs), which sometimes are called variable-reluctance permanent-magnet (VRPM) machines, can achieve a high torque density which makes them an interesting option for direct-drive operation (Weh and Mayer, 1984; Weh and May, 1986; Harris and Mecrow, 1993; Harris and Pajooman, 1995; Harris et al., 1996, 1997a; Pajooman, 1997; Henneberger and Bork, 1997). However, TFMs tend to have a complicated topology with a three-dimensional path of the magnetic field which makes the task of modelling and understanding the behaviour of these devices difficult. Additionally, TFMs tend to have a low power factor which has hindered their acceptance (Harris et al., 1997b; Anglada and Sharkh, 2016b).

The current trend to study machines with complicated geometries such as TFMs (Gieras, 2005; Keysan et al., 2012; Kang and Weh, 2008; Yang et al., 2012; Baker et al., 2014; Zhang et al., 2014; Doering et al., 2015; Liu et al., 2015; Wan et al., 2015; Dobzhanskyi and Gouws, 2016) and claw pole machines (Washington et al., 2012; Baker et al., 2012; Ahmed et al., 2014; Deodhar et al., 2015; Washington et al., 2016) is to use 3D CAD modelling and numerical methods like finite element analysis (FEA). This approach produce accurate results but does not provide an insight as deep as that provided by analytical methods.

The aim of this chapter is to develop the background theory for the analytical modelling of TFMs. Even though the methods were developed for the study of TFMs they are completely general and can be used for the analysis of radial PM machines, magnetic actuators, magnetic gears, etc... Both methods are based on the fact that PMs can be replaced with equivalent current sheets (Boules, 1985).

The calculation of torque is based on the Lorentz force equation, i.e. the BiL principle. However, in this case B is the stator's magnetic field, i the equivalent current of the PMs and L the axial length. This allows us to calculate the torque using a compact equation, which relates torque to the electric and magnetic loadings of the machine and a flux factor (Anglada and Sharkh, 2017b).

In addition, this chapter presents an alternative novel analytical methodology for TFMs based on a virtual mutual inductance, $\mathfrak{M}$ which is measured in [H], between the equivalent current loops of PMs and the stator windings (Anglada and Sharkh, 2017a). This virtual mutual inductance, $\mathfrak{M}$, can be used to calculate the flux linkage, back EMF and power factor of the machine using only the stator's magnetic field distribution.

The virtual mutual inductance approach presented in this chapter provides a very deep insight into the behaviour of TFMs because the path of the stator's magnetic field is simpler than that of the PMs. Therefore, the calculation of the flux linkage using the virtual mutual inductance, $\mathfrak{M}$, is more intuitive and the relationship between torque and power factor can be readily understood. Understanding this relationship can be the key to unlocking the full potential of TFMs through a trade-off between torque density and power factor.

The chapter starts with the formal derivation of the torque equation in section 4.2 followed by the calculation of the flux factor in section 4.3. The virtual mutual inductance approach is explained in section 4.4. Next, section 4.5 presents the calculation of the circuit parameters and performance of the machine using the torque equation and the virtual mutual inductance approach. Appendix B illustrates how to use the proposed methodologies for the simulation of electromechanical systems, emphasising its compatibility with Simulink/SimPowerSystems. Section 4.6 then concludes with a case study and the validation of the methodologies.

4.2 Torque Equation

Figure 4.1 shows a developed model of the TFM with dots and crosses representing the equivalent currents placed along the edges (equivalent currents are shown for one magnet only).

The basic approach is to firstly calculate the average torque of a single current loop at an arbitrary distance from the core-back and then calculate the total torque by integrating the resulting expression over the length of the magnets' equivalent current sheets. The linear current density, J, is equal to the magnetisation of the material $\mathcal{M}$ as described in (Boules, 1985).

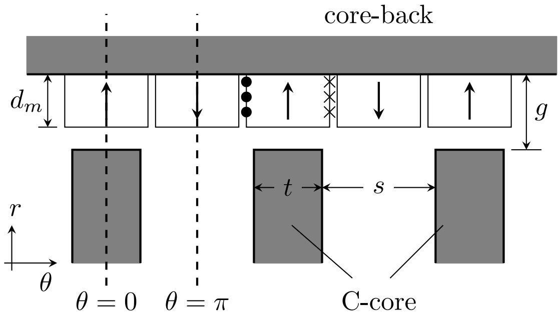

FIGURE 4.1: Developed model of the TFM.

4.2.1 Torque Produced by a Current Loop

If we consider a current loop that represents a layer of the magnet and one C-core head, this is the same as saying that we will calculate the force along the line $r = r_\delta$ as shown in Figure 4.2. The average tangential force of half of a fundamental electrical period can be calculated using the BiL principle. The radial magnetic field $B_r(t, \theta, r)$ is produced by the current in the winding, L is the active C-core length and i_δ is the equivalent current of the magnets at r_δ.

The tangential force can be divided in two components: the positive force of the currents going out of the paper (dots) and the negative force that comes from the opposite currents (crosses) as it is shown in Figure 4.2. Because the positive currents, i_δ, (dots in the figure) are located under the teeth and the negative currents, $-i_\delta$, (crosses) are located in the slot regions, the total force is positive because the magnetic field is stronger under a tooth than that in the slot regions.

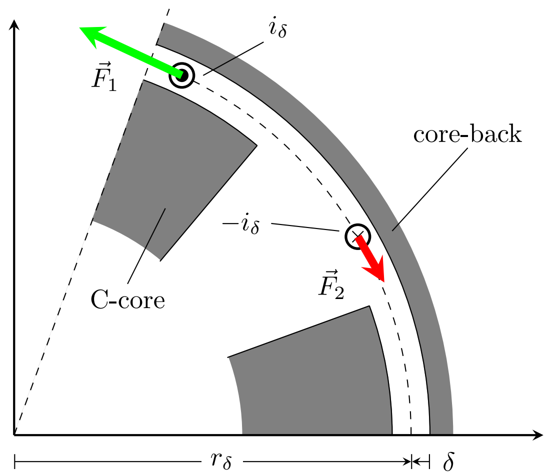

FIGURE 4.2: Forces applied to the equivalent current loop at a distance δ.

The average force experienced by i_δ and $-i_\delta$ in Figure 4.2 over half of an electrical cycle can be calculated as

$$F_\delta = \frac{1}{\pi}\Big\{ \int_{-\frac{\pi}{2}}^{\frac{\pi}{2}} B_r(t, \theta, r_\delta) i_\delta L \, d\theta - \int_{\frac{\pi}{2}}^{\frac{3\pi}{2}} B_r(t, \theta, r_\delta) i_\delta L \, d\theta \Big\}. \tag{4.1}$$

We can define $B_{sc}(\delta)$ as the magnetic field of the slotless geometry corrected for the curvature at a distance δ as follows

$$B_{sc}(\delta) = \frac{\mu_0 F}{g}\frac{R_g}{r_\delta} = B_s \frac{R_g}{r_\delta}. \tag{4.2}$$

Using $B_{sc}(\delta)$ and considering that ϕ is the phase advance angle of the current (angle between the emf, E, and the current, I) we can express the force as follows

$$F_\delta = i_\delta L B_{sc}(\delta)\cos(\phi) K_B(\delta), \tag{4.3}$$

where $K_B(\delta)$ is called the flux factor for the loop at distance δ and it only depends on the geometry. From (4.1), (4.2) and (4.3) the general expression of the flux factor is as follows

$$K_B(\delta) = \frac{1}{B_s(\delta)\pi\cos(\phi)} \int_{-\frac{\pi}{2}}^{\frac{\pi}{2}} \Big\{ B_r(t,\theta,r_\delta) - B_r(t,\theta+\pi,r_\delta) \Big\} d\theta. \tag{4.4}$$

Considering that N_c is the number of C-cores (also the number of pole pairs) and that each C-core has two heads the total torque per phase can be expressed as

$$T_\delta = N_c L D_g B_s i_\delta K_B(\delta)\cos(\phi). \tag{4.5}$$

It is important to note that in (4.5) N_c, L, D_g and $\cos(\phi)$ are known parameters of the machine and do not depend on r_δ.

4.2.2 Total Torque

The total torque produced by one phase can be obtained by integrating (4.3) along the magnet width, d_m. If we consider δ as the distance from the equivalent current loop to the core-back, the total torque can be expressed as the following

$$T = \int_0^{d_m} dT_\delta = \int_0^{d_m} N_c L D_g B_s K_B(\delta)\cos(\phi)\, di_\delta. \tag{4.6}$$

The differential current at the edge of the magnet can be expressed in terms of the magnetisation, $\mathcal{M}$, taking into account that there are two adjacent magnets, as

$$di_\delta = 2\mathcal{M}\, d\delta. \tag{4.7}$$

Therefore the total torque can be expressed as follows

$$T = 2N_c L D_g B_s \mathcal{M} d_m \cos(\phi)\Big[\frac{1}{d_m}\int_0^{d_m} K_B(\delta)\, d\delta\Big], \tag{4.8}$$

where $\mathcal{M}d_m = F_m$ is the total MMF of one permanent magnet and the term inside the brackets can be defined as the total flux factor:

$$K_B^{Total} = \frac{1}{d_m}\int_0^{d_m} K_B(\delta)\, d\delta. \tag{4.9}$$

The expression of the torque produced by a machine with q phases is then

$$T = 2qK_B^{Total} B_s F_m L N_c D_g \cos(\phi). \tag{4.10}$$

This expression has the same shape as the equation presented in (Harris and Mecrow, 1993) but with the calculation of the flux factor considers several aspects that were previously neglected. Also, the cosine of the angle between the MMF and the q-axis of the rotor $\cos(\phi)$, ϕ is the phase advance angle, appears in (4.10).

If the magnets are wider than the teeth, the fringing flux in the axial direction is actually producing torque, Figure 4.3. To estimate the active length of the C-core in the axial direction we can use the results reported by Markovic et al. (2005) in which the permeance of a tooth to tooth structure is calculated. Considering a 2D model of a C-core tooth against the core-back, the permeance per unit length can be estimated as

$$\Lambda = \mu_0 \frac{l_{core}}{g_z}\Big(1 + 0.384\frac{g_z}{l_{core}}\Big), \tag{4.11}$$

where l_{core} the C-core head width, Figure 4.3. In the previous deduction of the torque equation it was assumed that the field is constant in the perpendicular direction (two-dimensional approximation). Considering a magnetic potential difference Θ between the tooth and the core-back, the flux per unit length is given by

$$\Phi_t = \Theta\Lambda. \tag{4.12}$$

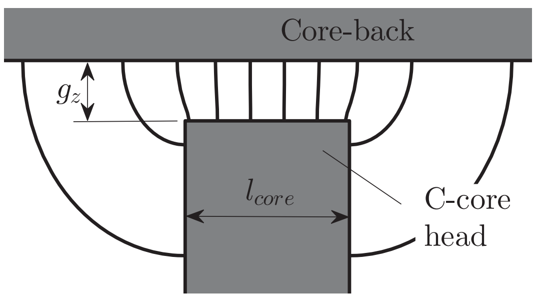

FIGURE 4.3: Fringing around the C-core head, axial geometry considered to obtain the equivalent length.

Therefore we can define an equivalent axial length, L_{eq}, as

$$\Phi_t = B_t L_{eq}, \tag{4.13}$$

where $B_t = \mu_0\Theta/g_z$. The flux per unit length is equal to that obtained using the permeance (4.11). Therefore the equivalent length is given by

$$L_{eq} \approx l_{core}\Big(1 + 0.384\frac{g_z}{l_{core}}\Big). \tag{4.14}$$

This equivalent length takes into account that the fringing flux is actually producing torque when the magnets are longer than the C-core head, l_{core}, and therefore this value should be used in (4.9). However, when the magnet length, L_{mag}, is not longer than l_{core} not all the fringing flux is effectively producing torque; in this case the equivalent length should be the magnet length.

4.3 Flux Factor

The flux-factor is the term in (4.10) that has all the information about the electro-mechanical interaction that takes place in the air-gap and determines how much of the total flux is effectively producing torque. This coefficient depends only on the complex permeance function that includes the information about the geometry and the waveform of the MMF. In this chapter two different MMF cases are considered: square wave MMF and sinusoidal MMF.

4.3.1 Flux Factor of a Single Current Loop

This section derives an expression for the flux factor at an arbitrary distance δ to the coreback. The geometry considered for the calculation is shown in Figure 4.2. The calculation of the magnetic field distribution in the air-gap is described in chapter 3. The expression of the radial component of the magnetic field distribution is shown in (4.26).

Solving the integral from (4.4), considering that the square-wave MMF, the expression of the flux-factor is the following:

$$K_B(\delta) = \frac{4}{\pi}\overline{\lambda}_r\Big[\gamma_1(\delta) - \frac{\gamma_3(\delta)}{3}\frac{\cos(3\phi)}{\cos(\phi)} + \frac{\gamma_5(\delta)}{5}\frac{\cos(5\phi)}{\cos(\phi)} - \dots\Big]. \tag{4.15}$$

It is important to remember that this is the expression for one layer and that to evaluate the integral for the total flux factor $\overline{\lambda}_r$ and $\gamma_n(\delta)$ vary with r_δ.

If the MMF of the winding is a sinusoidal function in synchronism with the rotation of the machine, then the instantaneous magnetic field is expressed as follows:

$$B_s(t) = B_{so}\cos(\omega t + \phi), \tag{4.16}$$

with

$$B_{so} = \frac{\mu_0\hat{F}}{g_z}, \tag{4.17}$$

where $\hat{F}$ is the peak value of the MMF. Accordingly, according to chapter 3, the magnetic field distribution can be expressed as

$$B_r(\theta,\delta) = B_{so}\lambda_{\log}(\delta)\cos(\theta+\phi)\,\overline{\lambda}_r\Big[1+\sum_{n=1}^{\infty}\gamma_n(\delta)\cos(n\,\theta)\Big], \tag{4.18}$$

where ϕ is the phase advance angle of the MMF. In this situation when we substitute (4.18) into (4.4) we obtain the expression of the flux factor for sine-wave MMF:

$$K_B(\delta) = \overline{\lambda}_r\gamma_1(\delta). \tag{4.19}$$

4.3.2 Total Flux Factor

The total flux factor that takes into account all the magnet thickness is obtained by evaluating the integral from (4.9). Because the magnetisation of the PM is constant, the integration over d_m is just to obtain the average value of the amplitude of the harmonics. Accordingly, the expression of the total flux factor for square-wave and sinusoidal waveforms respectively is

$$K_B^{Total} = \frac{4}{\pi}\overline{\lambda}_r\Big[\gamma_1^{av} - \frac{\gamma_3^{av}}{3}\frac{\cos(3\phi)}{\cos(\phi)} + \frac{\gamma_5^{av}}{5}\frac{\cos(5\phi)}{\cos(\phi)} - \dots\Big], \tag{4.20}$$

$$K_B^{Total} = \overline{\lambda}_r\gamma_1^{av}, \tag{4.21}$$

where γ_n^{av} is the average value of the n harmonic over the magnet thickness calculated as follows

$$\gamma_n^{av} = \frac{1}{d_m}\int_0^{d_m}\gamma_n(\delta)\,d\delta. \tag{4.22}$$

Having the value of K_B^{Total} the torque produced by the machine can be readily estimated by simply evaluating (4.10). However, K_B^{Total} depends on the magnetic field distribution in the air-gap and obtaining this function is normally complicated as discussed in chapter 3. Still, because of the formulation of the torque equation the flux factor depends only on the geometry of the air-gap.

4.4 Virtual Mutual Inductance Approach

The flux linkage in the stator windings of PM machines is normally obtained after calculating the PMs' magnetic field distribution in the air-gap and integrating the flux density over the coils surfaces.

In the virtual mutual inductance approach the magnets are replaced with equivalent current sheets (Boules, 1985). Figure 4.4 shows schematically the air-gap of the TFM with a radially magnetised PM with its equivalent current sheets. In this context, when the rotor moves the relative position of the stator windings and the equivalent current sheets changes. These current sheets can be thought of as several current loops in series.

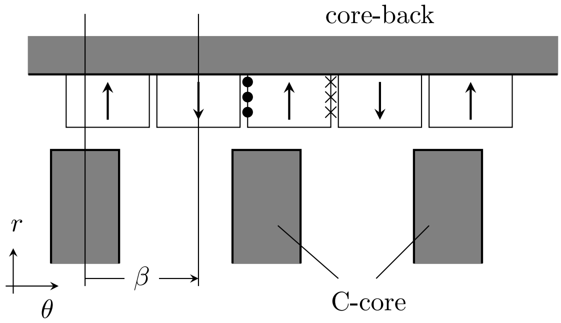

FIGURE 4.4: Schematic view of the air-gap of the TFM under study with the equivalent current loops at a particular position of the rotor, β.

The reciprocity theorem states that for any two circuits the value of the mutual inductances is the same, this is $\mathfrak{M}_{12} = \mathfrak{M}_{21}$, regardless of the geometry (Purcell, 2008; Feynman et al., 2010). Therefore, if the stator's magnetic field distribution in the air-gap of the TFM under study is known, then flux linking the equivalent current sheets due to the stator's MMF can be directly calculated as

$$\lambda_{PM} = \int_{PM} N_{PM} \vec{B}(\theta, r) \cdot d\vec{a} = \mathfrak{M}(\beta) \cdot I_S, \tag{4.23}$$

where $\vec{B}(\theta, r)$ is the magnetic field distribution produced by the stator's windings, N_{PM} is the number of turns of the equivalent current loop which is 1, I_S the stator's current and $\mathfrak{M}(\beta)$ the virtual mutual inductance between the stator windings and the equivalent current sheets, at a particular rotor position β. Based on the reciprocity theorem, the flux linkage of the stator windings due to the PMs can be calculated as

$$\lambda_S = \mathfrak{M}(\beta) \cdot I_{PM}, \tag{4.24}$$

where I_{PM} is the equivalent current of the PMs

$$I_{PM} = \mathcal{M} \cdot d_m, \tag{4.25}$$

where $\mathcal{M}$ is the magnetisation and d_m the magnet's thickness.

4.4.1 Calculation of the Virtual Mutual Inductance

The total virtual mutual inductance, $\mathfrak{M}(\beta)$, is calculated as the average of the virtual mutual inductance of single coils, $\mathfrak{M}_{sc}(\beta, r)$, along the magnet thickness.

Let us consider two consecutive permanent magnets of a TFM. Figure 4.5 shows a single equivalent coil in the relative position β in the air-gap.

Using the complex permeance function defined in (Anglada and Sharkh, 2016a) and in chapter 3, the magnetic field distribution in the air-gap produced by the stator can be expressed in polar

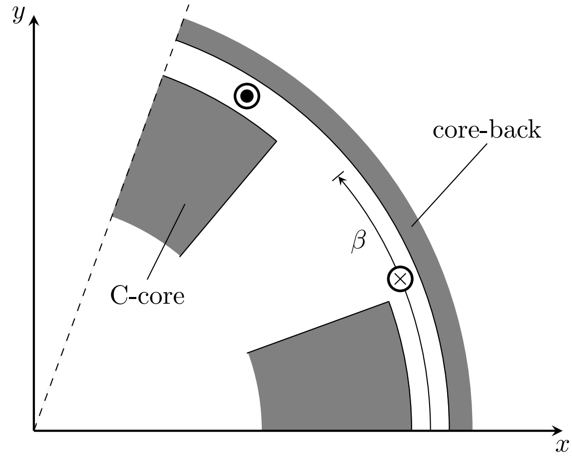

FIGURE 4.5: Schematic view of a single coil in the air-gap at the position β.

coordinates (θ is the electrical angle in radians) as

$$\vec{B}(\theta, r) = B_s \frac{R_g}{r}\Big[\overline{\lambda}_r\{1 + \sum_1^{\infty} \gamma_n(r)\cos(n\theta)\}\vec{u}_r + \sum_1^{\infty} \lambda_{\theta n}(r)\sin(n\theta)\vec{u}_\theta\Big], \tag{4.26}$$

where

$$B_s = \frac{\mu_{eq}\mu_0 F}{g_z}. \tag{4.27}$$

F is the MMF across the air-gap of value $F = N_w I_S/2$ and N_w the number of turns; μ_{eq} is the equivalent permeability, which depends on the relative permeability of the PMs (μ_r) and the magnet thickness to effective air-gap ratio. It is calculated as follows:

$$\mu_{eq} = \frac{\mu_r d_m + c_g}{g_z}. \tag{4.28}$$

The total flux linkage through the circuit that corresponds to one pair of poles is the contribution of two loops in series: the first one is positive and the second one is negative according to the direction of magnetisation of the magnets. The expression of the flux linkage over N_c pairs of poles taking into account that each C-core has two heads is therefore given by

$$\lambda_{PM}(\beta, r) = 2N_c\left[\int_{\beta-\frac{\pi}{2}}^{\beta+\frac{\pi}{2}} B_r(\theta, r)\frac{Lr}{N_c}d\theta - \int_{\beta+\frac{\pi}{2}}^{\beta+\frac{3\pi}{2}} B_r(\theta, r)\frac{Lr}{N_c}d\theta\right], \tag{4.29}$$

where L is the equivalent length of the magnets in the axial direction and N_c the number of C-cores.

The final expression of the flux linkage of a single coil is

$$\lambda_{PM}(\beta, r) = 8LR_g B_s \overline{\lambda}_r\Big[\frac{\gamma_1(r)}{1}\cos(\beta) - \frac{\gamma_3(r)}{3}\cos(3\beta) + \frac{\gamma_5(r)}{5}\cos(5\beta) - \dots\Big]. \tag{4.30}$$

Now that the total flux linking with the equivalent currents of the PMs is known, the expression of the virtual mutual inductance of a single current loop becomes

$$\lambda_{PM}(\beta, r) = \mathfrak{M}_{sc}(\beta, r) I_S \Rightarrow \mathfrak{M}_{sc}(\beta, r) = \lambda_{PM}(\beta, r) \frac{\mu_{eq}\mu_0 N_w}{2 g_z B_s}. \tag{4.31}$$

The final expression of the virtual mutual inductance between a coil at a distance r and position β can be shown to be given by:

$$\mathfrak{M}_{sc}(\beta, r) = 4\mu_{eq}\mu_0 \frac{R_g L N_w}{g_z} \overline{\lambda}_r \sum_{1,3,5...}^{\infty} \frac{\gamma_n(r)}{n} \cos(n\beta)(-1)^{\frac{n-1}{2}}. \tag{4.32}$$

The virtual mutual inductance for the distributed equivalent current of the magnets with thickness d_m can be calculated as follows

$$\mathfrak{M}(\beta) = \frac{1}{d_m} \int_0^{d_m} \mathfrak{M}_{sc}(\beta, \delta) d\delta, \tag{4.33}$$

where δ is the distance to the core-back:

$$\delta = R_g + \frac{g_z}{2} - r. \tag{4.34}$$

The final expression of the virtual mutual inductance will then be given by

$$\mathfrak{M}(\beta) = 4\mu_{eq}\mu_0 \frac{R_g L N_w}{g_z} \overline{\lambda}_r \sum_{1,3,5...}^{\infty} \frac{\gamma_n^{av}}{n} \cos(n\beta)(-1)^{\frac{n-1}{2}}, \tag{4.35}$$

where γ_n^{av} is the average value of $\gamma_n(r)$ along the magnet thickness.

4.5 Circuit Parameters and Performance

4.5.1 Back EMF and Torque Constants

The instantaneous back EMF of each phase can be obtained directly using Faraday's Law. Therefore,

$$\mathcal{E}_S(t) = -\frac{d\lambda_S(\omega t)}{dt} = -I_{PM} \frac{d\mathfrak{M}(\omega t)}{dt}, \tag{4.36}$$

which can be rewritten as

$$\mathcal{E}_S(t) = 4\mu_{eq}\mu_0 N_w \frac{R_g L}{g_z} \overline{\lambda}_r I_{PM} \omega \sum_{1,3,5...}^{\infty} \frac{\gamma_n^{av}}{n} \sin(n\omega t)(-1)^{\frac{n-1}{2}}. \tag{4.37}$$

The RMS value of the fundamental harmonic when the machine is operating in steady state at constant speed is expressed as

$$E_{RMS} = \frac{4\mu_{eq}\mu_0}{\sqrt{2}} N_w \frac{R_g L}{g_z} \overline{\lambda}_r I_{PM} \gamma_1^{av} \omega, \tag{4.38}$$

which can be expressed using the back EMF constant, k_E, (Hendershot and Miller, 2010) as

$$E_{RMS} = k_E \Omega, \tag{4.39}$$

where $\Omega = N_c \cdot \omega$ is the mechanical speed of the rotor. This gives the following expression for the back EMF constant

$$k_E = N_w N_c \frac{4\mu_{eq}\mu_0}{\sqrt{2}} \frac{R_g L}{g_z} F_m \overline{\lambda}_r \gamma_1^{av}. \tag{4.40}$$

On the other hand, the average torque per phase can be obtained using the torque equation in (Anglada and Sharkh, 2017b). The average torque per phase when the current is sinusoidal is given by

$$T_{ph} = \frac{4\mu_{eq}\mu_0}{\sqrt{2}} N_w N_c \frac{R_g L}{g_z} \overline{\lambda}_r I_{PM} \gamma_1^{av} I_{RMS}, \tag{4.41}$$

which can be rewritten as

$$T_{ph} = k_T I_{RMS}, \tag{4.42}$$

where k_T is the torque constant (Hendershot and Miller, 2010) calculated as follows

$$k_T = N_w N_c \frac{4\mu_{eq}\mu_0}{\sqrt{2}} \frac{R_g L}{g_z} F_m \overline{\lambda}_r \gamma_1^{av}. \tag{4.43}$$

As expected the expressions of (4.40) and (4.43) are exactly the same, with the only particularity that for TFMs the back EMF constant is equal to the torque constant per phase.

4.5.2 Phase Inductance

The reactance is due to the self-inductance of the coils; it can be separated into two different terms one due to the flux that crosses the air-gap, L_g, and one due to the leakage in the axial direction, L_l.

The value of L_g can be estimated using the expression of the magnetic field distribution in the air-gap to obtain the flux. For a given current i the inductance is calculated as follows

$$L_g = N_c \frac{N_w \Phi_{core}}{i}, \tag{4.44}$$

where Φ_{core} is the total flux passing through one C-core across the air-gap. The parameter $\overline{\lambda}_r$ from the complex permeance function in (4.26) can be used to obtain the total flux crossing the air-gap as follows

$$\Phi_{core} = \hat{B}\overline{\lambda}_r L \frac{2\pi R_g}{N_c}, \tag{4.45}$$

with

$$\hat{B} = \frac{\mu_{eq}\mu_0 N_w i}{2g_z}, \tag{4.46}$$

therefore, the final expression of the air-gap inductance is

$$L_g = \mu_{eq}\mu_0 N_w^2 L \frac{\pi R_g \overline{\lambda}_r}{g_z}, \tag{4.47}$$

The leakage flux in the axial direction can be estimated using the expression for the slot leakage can be found in (Say, 1965):

$$L_l = \mu_0 N_c N_w^2 l_{core}\Big(\frac{h_c - h_{co}}{3w_s} + \frac{h_{co}}{w_s}\Big), \tag{4.48}$$

where h_c is the slot depth, h_{co} is the difference between the slot depth and the coil depth, w_s the slot width, and l_{core} the C-core axial length as shown in Figure 1.10 in the introduction. The total reactance X is calculated as follows

$$X = \omega(L_g + L_l). \tag{4.49}$$

4.5.3 Power Factor

The back EMF can be calculated using (4.39) and the inductance according to (4.49). Therefore, the power factor can be directly calculated. TFMs tend to have a low power factor; in (Harris et al., 1997b) this topic is studied in detail. The conclusion is that besides the leakage, which is relatively high in these machines, the main cause is the *ineffective use of magnetic flux* (Anglada and Sharkh, 2016b). This can be easily seen in the fact that during the calculation of the virtual mutual inductance one of the equivalent current loops has a strong positive flux linking while the flux linking with the other current loop is in the opposite direction. However, still many publications state that the low power factor is due to leakage in the classical way (Mueller and Polinder, 2013; Lu et al., 2003, 2011; Kremers et al., 2014, 2015). Leakage has been defined traditionally as the part of the flux that is not crossing the air-gap (Say, 1965; Kundur, 1993; Fitzgerald et al., 2003; Matsch, 1972); the negative flux mentioned earlier is actually crossing the air-gap but in the opposite direction[1].

To operate in the maximum torque condition the current, I, has to be in phase with the back EMF, E; this means that current only has a q-axis component I_q. The phasor diagram is shown in Figure 4.6.

[1]Prof. Martyn Harris considered the leakage flux as the flux that is not effectively producing torque rather than the flux that is not crossing the air-gap. Using this definition of leakage it is true that the low power factor is due to the high leakage flux. However, in this Thesis we will use the classical definition of leakage according to (Say, 1965; Kundur, 1993; Fitzgerald et al., 2003; Matsch, 1972).

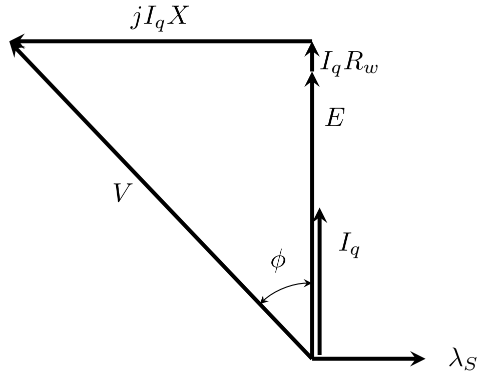

FIGURE 4.6: Phasor diagram with current only in the quadrature axis.

At high frequencies the value of X is much greater than the value of the resistance of the windings, R_w. Therefore, the angle ϕ in Figure 4.6 can be approximated as

$$\phi \approx \tan^{-1}\left(\frac{I_qX}{E}\right). \tag{4.50}$$

According to the phasor diagram shown in Figure 4.6, when the resistance of the windings is low the power factor can be calculated as follows:

$$\cos(\phi) \approx \frac{E}{\sqrt{(I_qX)^2 + E^2}}. \tag{4.51}$$

According to (4.40), the back EMF constant is proportional to $\overline{\lambda}_r\gamma_1^{av}$; which is the flux factor when operating with a sinusoidal current. Therefore, the back EMF is proportional to the flux factor:

$$E \propto K_B. \tag{4.52}$$

On the other hand, based on the torque equation:

$$T \propto N_cK_BI_q. \tag{4.53}$$

If I_q and N_c remain constant but K_B reduces, then the power factor and the torque will reduce. Therefore, the torque and the power factor are closely related through the flux factor, K_B. In the following section this concept is illustrated with a case study.

The value of the back EMF can be calculated from the flux linkage equation shown in (4.39). Since both the back EMF and the phase inductance are proportional to the frequency, the power factor at full load is independent of the frequency.

4.6 Case Study

The method described in the previous sections was applied to the geometry of the TFM built at the University of Southampton (Harris and Mecrow, 1993; Harris and Pajooman, 1995; Harris et al., 1997a, 1996; Pajooman, 1997).

The windings of the machine have $N_t = 230$ turns in the configuration analysed in this chapter and the rated current I is 10 A. The MMF across the gap under each C-core head is calculated as follows

$$F = \frac{1}{2} N_t I = 1150\,\mathrm{A}, \tag{4.54}$$

therefore the magnetic field as defined by Harris *et al.*

$$B_s = \frac{\mu_0 F}{g_z} = \frac{4\pi \cdot 10^{-7} \cdot 1150}{5.5 \cdot 10^{-3}} \approx 0.263\,\mathrm{T}. \tag{4.55}$$

The permanent magnets are made of the neodymium-iron-boron type with $B_r = 1.05$ T and $\mu_{rec} \approx 1$, which is the relative permeability of the PM. The equivalent current:

$$F_m = \mathcal{M} d_m = \frac{1.05}{4\pi \cdot 10^{-7}} \cdot 4.5 \cdot 10^{-3} \approx 3760\,\mathrm{A}. \tag{4.56}$$

The active C-core length is calculated as it is described in section 4.2 considering that the magnet width is 21 mm, which is higher than the C-core head width, l_{core}, that is 15 mm. Therefore, the equivalent length is calculated as follows

$$L_{eq} \approx l_{core} + 0.384 g_z \approx 17.11\,\mathrm{mm} \tag{4.57}$$

This methodology was implemented in Matlab. Using the CP function method, as described in chapter 3, the value of the flux factor for a square-wave current is

$$K_B^{Total} \approx 0.3105. \tag{4.58}$$

Figure 4.7 shows the average torque of one phase of the TFM obtained from the generalised torque equation presented in this chapter, Harris' torque equation (Harris and Mecrow, 1993), the value measured in the actual device and 3D FEA calculations. The method proposed in this chapter has a good agreement with FEA and experimental data in the linear region below saturation.

The results obtained from the torque equation can be compared with the studies presented in (Harris and Mecrow, 1993; Harris and Pajooman, 1995). The calculation of the flux factor proposed in (Harris and Mecrow, 1993) considers the magnets to be represented by point currents (in the 2D section) at the inner bore of the rotor core-back. Then, the amplitude of the magnetic field harmonics can be obtained from (Freeman, 1962) to calculate K_B to be 0.275, which corresponds to the torque equation - Harris line in Figure 4.7. However, it is mentioned in (Harris and Mecrow, 1993) that the equivalent current is distributed along the air-gap which the authors from (Harris and Mecrow, 1993) suggested could increase K_B to 0.334 without providing details of the calculation. This value is an overestimate compared to the value of K_B^{Total} in (4.58).

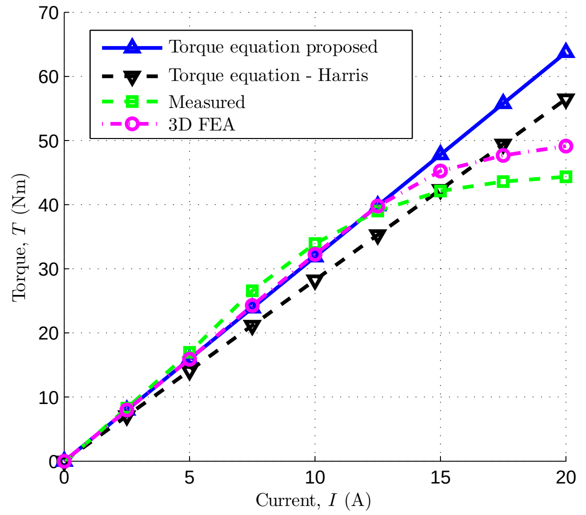

FIGURE 4.7: Average torque of the TFM obtained with the torque equation presented this chapter, Harris *et al.* torque equation, the value measured in the lab and 3D FEA (Harris and Mecrow, 1993; Harris and Pajooman, 1995).

Figure 4.8 shows the real part of the CP function, $\mathrm{Re}\{\lambda_{SC}\}$, for $\delta = 0$ mm (over the core-back), $\delta = d_m/2$ (middle of the magnet width) and $\delta = d_m$ (over the surface of the magnet). It can be appreciated that the amplitude of the harmonics increases as δ increases. Since the flux factor depends on the amplitude of the harmonics, considering only the top of the core-back will underestimate the average torque. Harris *et al.* (Harris and Mecrow, 1993; Harris and Pajooman, 1995) mentioned this effect but it was not calculated exactly. The proposed methodology considers this effect accurately when calculating the flux factor.

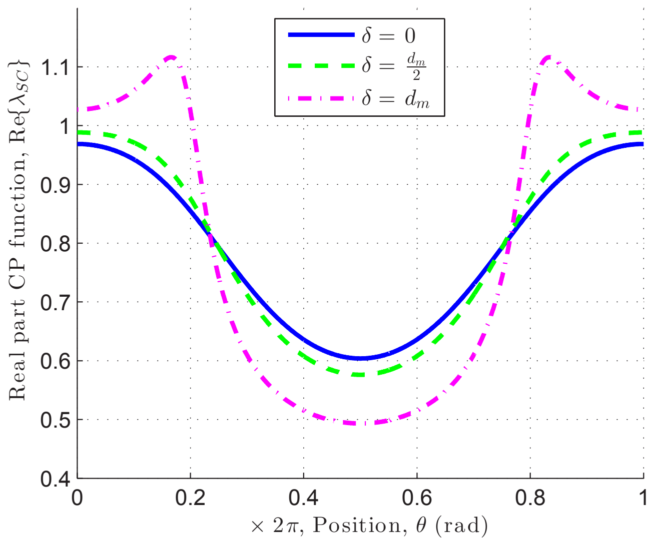

FIGURE 4.8: Real part of the CP function associated to the SC transformation, $\mathrm{Re}\{\lambda_{SC}\}$, as a function of the position, θ, for three different lengths, δ.

Regarding the virtual mutual inductance approach: the results of the analytical model are compared with experimental data and 3D FEA. The flux linkage of the stator winding was measured using a flux meter while manually rotating the rotor over 18 mechanical degrees, which corresponds to 360 electrical degrees. These measurements were reported in (Pajooman, 1997).

Figure 4.9 shows a quarter model of the TFM under study with the magnetic field passing through one C-core. The 3D model was simulated using magnetostatic FEA for several rotor positions. The flux linkage is calculated by integrating the magnetic field through the C-core back.

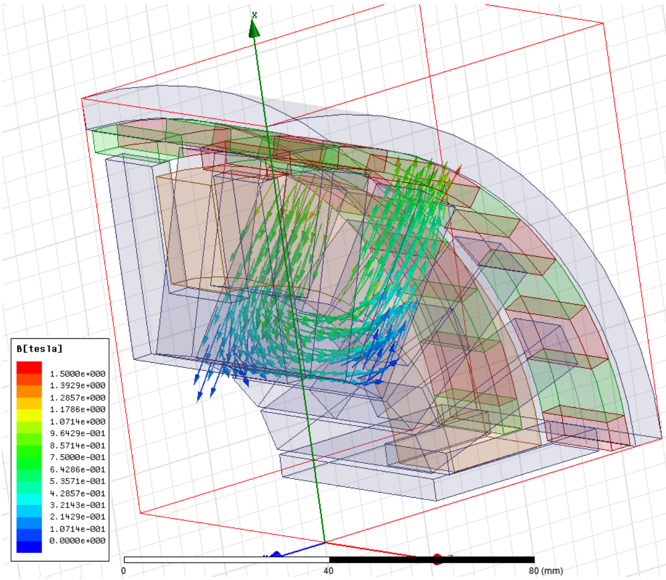

FIGURE 4.9: Magnetic field passing through a C-core, 3D FEA model.

Figure 4.10 shows the flux linkage obtained analytically, the experimental data and the 3D FEA data. It can be appreciated that the analytical method underestimates the amplitude of the flux linkage. This is probably due to the 3-dimensional interaction of the field around the C-core head, which is only partly taken into account by using the equivalent length, L.

4.6.1 Electrical Parameters of the Machine

TABLE 4.1: Electrical parameters of the TFM

Quantity	Symbol	Value
Rated current	I	10 A
Back emf constant	k_E	3.54 V/(rad/s)
Torque constant	k_T	3.54 Nm/A
Air-gap inductance	L_g	40.5 mH
Leakage inductance	L_l	5.9 mH
Phase resistance	R_w	1.57 Ω
Power factor	$\cos(\phi)$	0.35

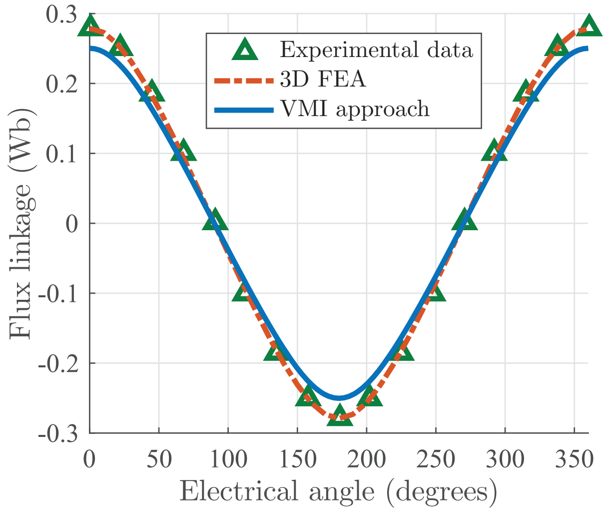

FIGURE 4.10: The measured flux linkage and the one obtained with the flux linkage equation proposed using the virtual mutual inductance (VMI) approach.

4.6.2 Study of the current design

Taking as a starting point the machine described in chapter 1 let us show how to choose the number of C-cores, which is also the number of pole pairs. Assuming that the radius of the machine, the magnet thickness d_m, the clearance gap c_g and the tooth-pitch ratio t/τ_p remain constant. The pole pitch is calculated as follows

$$\tau_p = \frac{2\pi R_g}{N_c}. \tag{4.59}$$

With these constraints it is possible to calculate the parameters of the machine (average torque, back EMF and power factor at full load) starting from $N_c = 1$ until $N_c = 35$. Also, the *maximum power factor* is calculated; which corresponds to the power factor assuming that there is no leakage ($L_l = 0$ H). The purpose of this is to show that while leakage affects the power factor it is not the main cause of the low power factor in TFMs.

Figure 4.11 shows the average torque per phase, calculated using (4.42), in blue with the scale on the left hand side of the graph. As the number of C-cores increases the average torque also increases until it reaches a maximum point, which corresponds to $N_c = 24$ C-cores.

The power factor at full load and the maximum power factor are shown in Figure 4.11 with the scale on the right hand side of the graph. It can be easily appreciated that the maximum power factor is higher than the actual power factor but it follows the same strictly decreasing trend. This shows that the low power factor of TFMs is not due to leakage but due to the low back EMF constant, which is strongly affected by the *ineffective use of the magnetic flux* as it was mentioned earlier in this chapter and discussed in (Harris et al., 1997b; Anglada and Sharkh, 2016b).

The decrease in the power factor can be caused by three reasons, based on (4.51): an increase of the rated current, an increase of the phase inductance and/or a decrease in the back EMF.

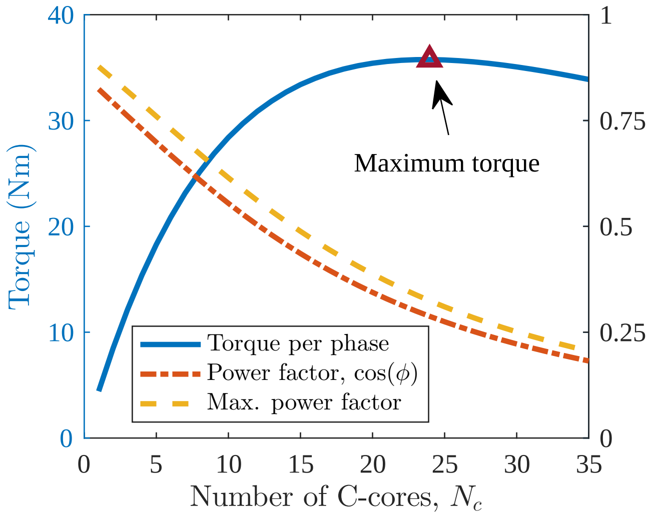

FIGURE 4.11: Average torque per phase and power factor as a function of the number of C-cores.

In this case study the rated current remains constant and therefore this is not the cause. It was proved in section 4.5.3 that the back EMF is affected directly by the flux factor; therefore, it is necessary to study if this is the dominant effect. Figure 4.12 shows the air-gap inductance, L_g, and the leakage inductance, L_l, as a function of the number of C-cores with the axis on the left hand side of the graph. The flux factor, K_B, is shown with the axis in per unit in the right hand side of the graph. It can appreciated that the air-gap inductance increases gradually but the leakage inductance remains constant. This means that there is more flux crossing the air-gap; however, not all of this flux is effectively producing torque because the flux factor is decreasing rapidly. Therefore, the low power factor is not due to an increase of the leakage flux but due to the *ineffective use of the flux* that actually crosses the air-gap.

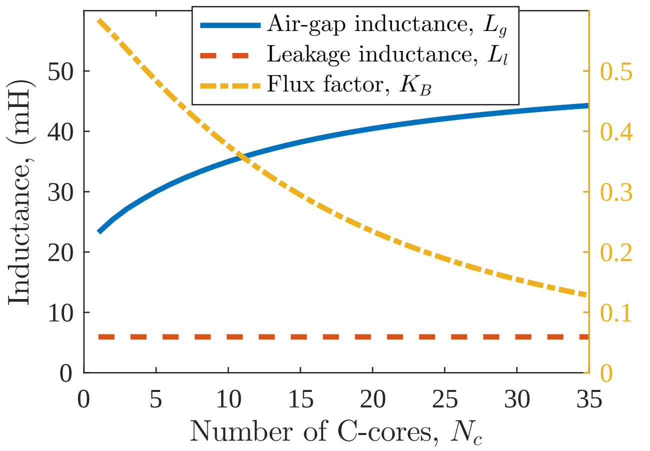

FIGURE 4.12: Air-gap inductance, L_g, and leakage inductance, L_l, as a function of the number of C-cores with the axis on the left hand side of the graph. Flux factor, K_B, with the axis in per unit on the right hand side of the graph.

If the design optimisation is done only considering torque, as many authors propose (Lu et al., 2011; Kremers et al., 2014, 2015), the optimal machine would have $N_c = 24$ C-cores. However, this number of C-cores yields a very low power factor (< 0.3). Near $N_c = 24$ C-cores the slope of the torque curve is very low and the slope of the power factor curve is steep, which means that for small improvements of torque for each C-core added there is a strong penalty in terms of power factor. Therefore, during the design process it is essential to have a happy compromise between torque density and power factor.

4.7 Conclusions

This chapter presents a comprehensive analysis of TFMs including the calculation of torque, back EMF, phase inductance and power factor using the magnetic field distribution obtained with the complex permeance function shown in chapter 3.

The torque equation presented in section 4.2 can be directly used to calculate the average torque of TFMs. This method has been validated using FEA and experimental data, Figure 4.7. The torque equation is valid when the magnetic circuit saturation is negligible.

The virtual mutual inductance approach can be used to calculate the flux linkage, back EMF and power factor. The results were contrasted with FEA and experimental data as shown in Figure 4.10.

The torque equation and the virtual mutual inductance were used to show the relationship between torque and power factor. The flux factor, which affects both the torque and the back EMF, measures the *ineffective use of the magnetic flux*. This effect is the reason of the low power factor in TFMs and not the leakage flux.

Chapter 5

Calculation of Rotor Losses in Transverse-Flux Machines

5.1 Introduction

Transverse flux machines (TFMs) tend to have large eddy currents induced in the rotor because of the presence of many asynchronous harmonics in the air-gap produced by the structures that modulate the field. In many cases the flux passing through the rotor follows a three-dimensional path and the iron cannot be laminated; in these cases the rotor has to be made of soft magnetic composites (Baker et al., 2012; Washington et al., 2012; Deodhar et al., 2015; Washington et al., 2016; Liu et al., 2015; Doering et al., 2015). Therefore, accurate estimates of rotor losses is essential to avoid designing a machine that may fail due to rotor overheating, when the rotor yoke is not made of soft magnetic iron powder composites iron or laminations.

The calculation of eddy currents in 3D geometries tends to be time consuming because the mesh has to be very refined in the conducting regions. The typical approach of *at least three elements per skin depth length* normally implies an extremely large number of elements in 3D problems (Lowther and Silvester, 1986). Analytical methods provide a *low cost* alternative in terms of computational time to 3D FEA at the initial design stages.

Previous studies have successfully calculated the rotor losses in inner rotor PM machines using the well-known current sheet model (Lawrenson et al., 1966; Stoll and Sykulski, 1992; Irenji, 1998; Zhu et al., 2004; Qazalbash et al., 2015). However, this approach has a major drawback: as the number of regions in the model increases, the complexity of the problem increases in a very significant way. This is because it is necessary to invert a matrix, which increases in size with the number of layers considered, to solve the linear system of equations resulting from applying the boundary conditions (Irenji, 1998; Qazalbash et al., 2014a,b, 2015; Anglada et al., 2016).

In this chapter we propose an analytical method that is also based on the current sheet model. However, instead of solving the linear system of equations directly we obtain a transfer matrix between layers. This implies that the only matrix that has to be inverted is of order two. A similar approach has been used in the past to obtain the eddy currents in geometries with several rectangular regions (Pipes, 1956; Greig and Freeman, 1967; Freeman, 1968). Kirtley applied a surface coefficient in a similar way in cylindrical coordinates but assuming that the eddy currents are resistance limited (solving Laplace's equation), which means that it is applicable for thin regions only (Kirtley, 1975). We have generalised the concept of the transfer matrix to cylindrical coordinates and conductive/non-conductive regions and formulated it in a systematic form.

The methodology proposed in this chapter can be applied to any number of cylindrical regions, conductive or non-conductive, excited by a cylindrical current sheet at an arbitrary position. In this chapter we use a TFM as a case study but this methodology is particularly useful for the calculation of rotor losses in high speed PM machines (Anglada et al., 2016) in which the frequencies involved are high. This approach can be used to analyse inner rotor PM machines, outer rotor PM machines, magnetic brakes, etc. To the knowledge of the author this is the first time that the current sheet model is applied for the calculation of rotor losses in TFMs or outer rotor machines.

5.2 Calculation of Rotor Losses: the Traditional Approach

In this chapter, we study the rotor loss of a non-salient outer rotor TFM. From the rotor reference frame the slots change position with time and this variation of permeance produces a variation of the magnetic field seen by the rotor, which induces eddy currents (Lawrenson et al., 1966; Stoll and Sykulski, 1992). In addition to the tooth-ripple (or slot permeance) losses there might be eddy currents induced by the stator's magnetic field distribution, which may contain asynchronous harmonics. The calculation of the asynchronous harmonics due to tooth permeance variation is done by calculating the magnetic field distribution in different rotor positions spanning one pole-pitch.

The rotor eddy-current power loss is calculated analytically using a cylindrical multilayer model in which each asynchronous harmonic is represented by a current sheet at the stator bore of an equivalent slotless configuration of the machine; this is represented schematically for 4 layers in Figure 5.1. The non-segmented magnet is modelled as a conducting region with no magnetization.

The current sheet density that represents an asynchronous harmonic of space order q and time order k can be expressed as

$$J_{qk} = \hat{J}_{qk}\cos(q\theta + k\omega t) = \mathrm{Re}\left(\hat{J}_{qk}e^{jq\theta}e^{jk\omega t}\right). \tag{5.1}$$

Maxwell's field equations for this case, based on (Irenji, 1998), can be expressed as follows:

$$\nabla \times \vec{E} = -\tfrac{\partial \vec{B}}{\partial t}, \tag{5.2}$$

$$\nabla \times \vec{H} = \vec{J}, \tag{5.3}$$

$$\vec{B} = \mu\vec{H}, \tag{5.4}$$

$$\vec{J} = \sigma\vec{E}, \tag{5.5}$$

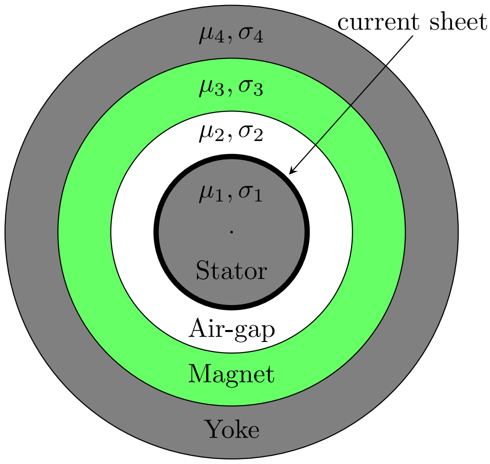

FIGURE 5.1: Cylindrical current sheet model of an outer rotor PM machine with the corresponding current sheet at the stator slotless surface.

where $\vec{E}$ is the electric field intensity, $\vec{B}$ the magnetic field, $\vec{H}$ the magnetic field intensity, $\vec{J}$ the current density, μ is the magnetic permeability and σ the electric conductivity.

The magnetic vector potential, $\vec{A}$, is defined as:

$$\nabla \times \vec{A} = \vec{B}. \tag{5.6}$$

Thus, we can obtain the relationship between the electric field and the magnetic vector potential:

$$\vec{E} = -\frac{\partial \vec{A}}{\partial t}. \tag{5.7}$$

Combining the previous equations:

$$\nabla \times \vec{H} = \nabla \times \left(\frac{\vec{B}}{\mu}\right) = \frac{1}{\mu}\nabla \times (\nabla \times \vec{A}) = -\frac{1}{\mu}\nabla^2 \vec{A}, \tag{5.8}$$

$$\nabla \times \vec{H} = \vec{J} = \sigma \vec{E} = -\sigma \frac{\partial \vec{A}}{\partial t}. \tag{5.9}$$

In the previous expression it is assumed that the permeability does not depend on the magnetic field and does not vary in time. The derivation of equation (5.8) is based on the following identities:

$$\nabla \times \nabla \times \vec{A} = \nabla(\nabla \cdot \vec{A}) - \nabla^2 \vec{A}, \tag{5.10}$$
$$\nabla \cdot \vec{A} = 0. \tag{5.11}$$

Therefore, combining equations (5.8) and (5.9) the following relation is obtained:

$$\nabla^2 \vec{A} = \mu\sigma \frac{\partial \vec{A}}{\partial t}. \tag{5.12}$$

The objective is to calculate the magnetic vector potential in the cylindrical multilayer domain shown in Figure 5.1. In cylindrical coordinates the Laplacian of $\vec{A}$ assuming no variation in the

z direction, $\vec{A} = (0, 0, A)$, is expressed as follows:

$$\nabla^2 A = \frac{1}{r}\frac{\partial}{\partial r}\Big(r\frac{\partial A}{\partial r}\Big) + \frac{1}{r^2}\frac{\partial^2 A}{\partial \theta^2}. \tag{5.13}$$

Since the applied current sheet is sinusoidal in space and time, the magnetic vector potential can be expressed as a phasor by separating the variables as

$$A(\theta, r, t) = R(r)e^{jq\theta}e^{jk\omega t}, \tag{5.14}$$

accordingly, in steady state the Laplacian can be expressed as

$$\nabla^2 A = jk\omega\mu\sigma A. \tag{5.15}$$

Substituting (5.14) into (5.15) and re-arranging the terms we obtain

$$\frac{d^2R(r)}{dr^2} + \frac{1}{r}\frac{dR(r)}{dr} - \Big(jk\omega\mu\sigma + \frac{q^2}{r^2}\Big)R(r) = 0, \tag{5.16}$$

which is a modified Bessel differential equation whose general solution is given by

$$R(\kappa r) = CI_q(\kappa r) + DK_q(\kappa r), \tag{5.17}$$

in which $\kappa^2 = jk\omega\mu\sigma$, C and D are constants that are determined by applying the boundary conditions, and I_q and K_q are the modified Bessel functions of the first and second kinds of order q, respectively. The radial and tangential components of the magnetic field distribution are calculated as follows:

$$B_r(\theta, r, t) = \frac{1}{r}\frac{\partial A}{\partial \theta} = \frac{1}{r}jq\big[CI_q(\kappa r) + DK_q(\kappa r)\big]e^{jq\theta}e^{jk\omega t}, \tag{5.18}$$

$$B_\theta(\theta, r, t) = -\frac{\partial A}{\partial r} = -\kappa\big[CI'_q(\kappa r) + DK'_q(\kappa r)\big]e^{jq\theta}e^{jk\omega t}. \tag{5.19}$$

The constants C and D for each layer (1 stator iron, 2 air-gap, 3 magnet and 4 rotor hub) are obtained after applying the following boundary conditions[1]:

1. B_r and B_θ are finite as r approaches zero ($D_1 = 0$);
2. B_r is zero at the outer radius of the rotor;
3. the radial flux density, B_r, is continuous at all interfaces;
4. at the current sheet ($r = R_1$) there is a discontinuity in the tangential field intensity, H_θ, by the amount of the current sheet;
5. the tangential field intensity, H_θ, is continuous at $r = R_2$ and $r = R_3$.

[1] Assuming that the permeability of the iron infinite.

These boundary conditions are expressed mathematically as follows

$$\frac{1}{R_1} jq\big[C_1 I_q(\kappa_1 R_1)\big] = \frac{1}{R_1} jq\big[C_2 I_q(\kappa_2 R_1) + D_2 K_q(\kappa_2 R_1)\big], \tag{5.20}$$

$$\frac{1}{R_2} jq\big[C_2 I_q(\kappa_2 R_2) + D_2 K_q(\kappa_2 R_2)\big] = \frac{1}{R_2} jq\big[C_3 I_q(\kappa_3 R_2) + D_3 K_q(\kappa_3 R_2)\big], \tag{5.21}$$

$$\frac{1}{R_3} jq\big[C_3 I_q(\kappa_3 R_3) + D_3 K_q(\kappa_3 R_3)\big] = \frac{1}{R_3} jq\big[C_4 I_q(\kappa_4 R_3) + D_4 K_q(\kappa_4 R_3)\big], \tag{5.22}$$

$$\frac{1}{R_4} jq\big[C_4 I_q(\kappa_4 R_4) + D_4 K_q(\kappa_4 R_4)\big] = 0, \tag{5.23}$$

$$-\frac{\kappa_1}{\mu_1}\big[C_1 I_q'(\kappa_1 R_1)\big] = -\frac{\kappa_2}{\mu_2}\big[C_2 I_q'(\kappa_2 R_1) + D_2 K_q'(\kappa_2 R_1)\big] + \hat{J}_{qk}, \tag{5.24}$$

$$-\frac{\kappa_2}{\mu_2}\big[C_2 I_q'(\kappa_2 R_2) + D_2 K_q'(\kappa_2 R_2)\big] = -\frac{\kappa_3}{\mu_3}\big[C_3 I_q'(\kappa_3 R_2) + D_3 K_q'(\kappa_3 R_2)\big], \tag{5.25}$$

$$-\frac{\kappa_3}{\mu_3}\big[C_3 I_q'(\kappa_3 R_3) + D_3 K_q'(\kappa_3 R_3)\big] = -\frac{\kappa_4}{\mu_4}\big[C_4 I_q'(\kappa_4 R_3) + D_4 K_q'(\kappa_4 R_3)\big]. \tag{5.26}$$

This is a linear system with 7 equations and 7 unknowns (C_1, C_2, D_2, C_3, D_3, C_4 and D_4)[2]. Once the constants are calculated the magnetic vector potential is known in all the domain and the currents induced in the axial direction are calculated as follows:

$$J_{axial} = -\sigma \frac{\partial A}{\partial t}, \tag{5.27}$$

were σ is the conductivity of the material. The total rotor losses can be obtained by integrating J_{axial}^2/σ in all the domain or using the Poynting vector (Qazalbash et al., 2014a,b; Zhu et al., 2004).

The amplitude of the current sheet that corresponds to each asynchronous harmonic, $\hat{J}_{qk}$, is effectively set to produce the same normal flux density on the surface of the magnet $\hat{B}_{qk}$ (Qazalbash et al., 2014a,b, 2015). In practice, the problem is solved by setting $\hat{J}_{qk} = 1$ and calculating the corresponding losses P_{qk1} from the solution of the diffusion equation in the current sheet model. In addition, the Laplace equation (no eddy currents) is solved to find the corresponding $\hat{B}_{qk1}$ when $\hat{J}_{qk} = 1$. Finally, the actual losses for a given $\hat{B}_{qk}$ (obtained from harmonic analysis using conformal mapping in this case) are calculated as

$$P_{qk} = \Big(\frac{\hat{B}_{qk}}{\hat{B}_{qk1}}\Big)^2 P_{qk1}. \tag{5.28}$$

[2] In theory this system of linear equations is well defined. However, there can be numerical problems because it is necessary to evaluate Bessel functions with large complex arguments, which may produce that the matrix is badly scaled and close to singular. Therefore, it is important to be careful in this stage.

5.2.1 Solution without Eddy Currents

To obtain the value of $\hat{B}_{qk1}$ in order to calculate the rotor loss using (5.28) it is necessary to solve the same problem as before but without eddy currents. Equation (5.16) can be rewritten assuming that the conductivity in all regions is zero as:

$$\frac{d^2R(r)}{dr^2} + \frac{1}{r}\frac{dR(r)}{dr} - \frac{q^2}{r^2}R(r) = 0, \tag{5.29}$$

which is an ordinary differential equation whose general solution is given by

$$R(\kappa r) = Cr^q + Dr^{-q}. \tag{5.30}$$

Therefore, the radial and tangential components of the magnetic field distribution are calculated as follows:

$$B_r(\theta, r, t) = \frac{1}{r}\frac{\partial A}{\partial \theta} = \frac{1}{r}jq\big[Cr^q + Dr^{-q}\big]e^{jq\theta}e^{jk\omega t}, \tag{5.31}$$

$$B_\theta(\theta, r, t) = -\frac{\partial A}{\partial r} = -\frac{1}{r}\big[Cr^q - Dr^{-q}\big]e^{jq\theta}e^{jk\omega t}. \tag{5.32}$$

The boundary conditions are the same as that in the previous case and the solution of the system is simpler because in this case there are not Bessel functions in the system.

5.2.2 Calculation of Power using the Poynting Vector

The Poynting vector[3] gives the power density of an arbitrary electromagnetic field. Let us define as $\mathcal{U}$ the energy density of an electromagnetic field. The rate of change of $\mathcal{U}$ can be expressed as follows:

$$\frac{\partial \mathcal{U}}{\partial t} = \varepsilon \frac{\partial \vec{E}}{\partial t} \cdot \vec{E} + \frac{1}{\mu}\frac{\partial \vec{B}}{\partial t} \cdot \vec{B}. \tag{5.33}$$

Accordingly, the Poynting vector, $\vec{S}$, is defined by

$$\vec{S} = \vec{E} \times \vec{H}. \tag{5.34}$$

We can then rewrite (5.33) using the Poynting vector as follows:

$$-\frac{\partial \mathcal{U}}{\partial t} - \vec{J}_f \cdot \vec{E} = \nabla \cdot \vec{S}, \tag{5.35}$$

where $\vec{J}_f$ is the free current density corresponding to the movement of charge. Expanding the previous expression we obtain the most common form in electrical engineering of the derivation

[3] Named after John Henry Poynting; surprisingly, the name of this expression is phonetically accurate keeping in mind that the Poynting vector gives the energy flow in a *directional way*.

of the Poynting vector, which has some similarities with the continuity equation:

$$\nabla \cdot \vec{S} + \varepsilon \frac{\partial \vec{E}}{\partial t} \cdot \vec{E} + \frac{1}{\mu} \frac{\partial \vec{B}}{\partial t} \cdot \vec{B} + \vec{J} \cdot \vec{E} = 0. \tag{5.36}$$

For a sinusoidal electromagnetic field in steady state, using the complex number notation used in this Thesis, the average power (in W/m^2) transmitted through a surface can be expressed as:

$$P_s = \frac{1}{2} \operatorname{Re} \left(E_z \cdot H_\theta^* \right), \tag{5.37}$$

where E_z is the amplitude of the electric field intensity in the z-direction and H_θ^* is the complex conjugate of the amplitude of the tangential magnetic field intensity over the surface. To obtain the total power transmitted through the surface it is necessary to integrate (5.37) over the surface. In our case, the surfaces are simply cylinders and because of the nature of the fields their amplitude is constant for a given radius. Therefore, the total power flow, P_n, through an arbitrary cylindrical surface S_n is calculated as follows:

$$P_n = \frac{1}{2} \operatorname{Re} \left(E_z|_{r=R_n} \cdot H_\theta^*|_{r=R_n} \right) \cdot S_n, \tag{5.38}$$

with:

$$S_n = 2\pi R_n L, \tag{5.39}$$

where R_n is the radius of the cylinder and L is the axial length.

The electric field intensity in the z direction can be directly calculated using the vector potential from (5.14) as follows:

$$E_z = -\frac{\partial A}{\partial t} = -jk\omega \left[C I_q(\kappa r) + D K_q(\kappa r) \right] e^{jq\theta} e^{jk\omega t}, \tag{5.40}$$

which can be rewritten as:

$$E_z = -\frac{k r \omega}{q} B_r. \tag{5.41}$$

5.2.3 The problem with the traditional approach

The above methodology has been successfully applied in many occasions (Irenji, 1998; Qazalbash et al., 2014a,b, 2015). However, the solution of the system of linear equations to obtain the coefficients in the solution of the problem with eddy currents, equations (5.20) to (5.26), can be problematic. This is because we are dealing with modified Bessel functions with large complex arguments. To avoid the numerical problems the matrix has to be inverted analytically and this can be a very slow process as the size of the matrix increases.

The other major problem of this method is that as the number of cylindrical regions (or layers) increases, the complexity of the problem increases in a very significant way. For example, in the topology shown in Figure 5.2 there are 4 regions, which meant that the system of the boundary conditions is 7 by 7. For example, if we want to study the effect of the conductivity of a retaining sleeve now we have 5 regions, which means that the system of the boundary conditions is 9 by 9. This additional complexity can hinder the application of the method from the practical point of view.

5.3 Calculation of Rotor Losses using Transfer Matrices

This section presents a general methodology to solve the eddy currents problem of a current sheet with an arbitrary number of conductive or non-conductive cylindrical regions. The basic idea is to use a transfer matrix between regions instead of solving the whole system of boundary conditions. Similar ideas have been presented in (Pipes, 1956; Greig and Freeman, 1967; Freeman, 1968; Kirtley, 1975). However, these methodologies are not widely used today probably because they are old and unknown to most of the active researchers on this field. The main advantage of the transfer matrix concept is that to obtain the quantities (B and H), it is necessary to invert a 2 by 2 matrix, which reduces the complexity of the problem. The aim of this section is to provide a systematic method to solve the problem using this approach.

Let us assume that we have a cylindrical geometry with N regions, each of them has a conductivity σ_n and a permeability μ_n, as shown schematically in Figure 5.2. There is a current sheet of time order k and space order q in between regions $h-1$ and h, which can be expressed as:

$$J_{qk} = \hat{J}_{qk}\cos(q\theta + k\omega t) = \mathrm{Re}\left(\hat{J}_{qk}e^{jq\theta}e^{jk\omega t}\right). \tag{5.42}$$

Figure 5.2 shows a simplified representation of the geometry of the problem. Only some of the regions are shown and the current sheet in between regions $h-1$ and h is shown with a thicker line.

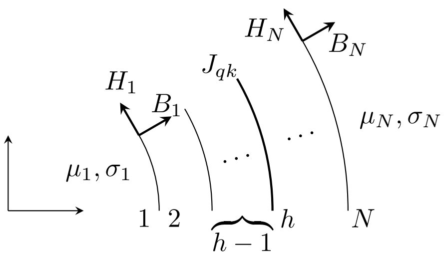

FIGURE 5.2: General model with current sheet on boundary the h.

The differential equations that govern the field in these regions are the same as in section 5.2 and the fields have the same shape. Therefore, the radial and tangential components of the magnetic field distribution for a conductive region ($\sigma \neq 0$) are expressed as follows:

$$B_r(\theta, r, t) = \frac{1}{r}\frac{\partial A}{\partial \theta} = \frac{1}{r} jq\big[CI_q(\kappa r) + DK_q(\kappa r)\big]e^{jq\theta}e^{jk\omega t}, \tag{5.43}$$

$$B_\theta(\theta, r, t) = -\frac{\partial A}{\partial r} = -\kappa\big[CI_q'(\kappa r) + DK_q'(\kappa r)\big]e^{jq\theta}e^{jk\omega t}. \tag{5.44}$$

Similarly, the components of the magnetic field for a non-conductive region ($\sigma = 0$) are expressed as follows:

$$B_r(\theta, r, t) = \frac{1}{r}\frac{\partial A}{\partial \theta} = \frac{1}{r} jq\big[Cr^q + Dr^{-q}\big]e^{jq\theta}e^{jk\omega t}, \tag{5.45}$$

$$B_\theta(\theta, r, t) = -\frac{\partial A}{\partial r} = -\frac{1}{r}\big[Cr^q - Dr^{-q}\big]e^{jq\theta}e^{jk\omega t}. \tag{5.46}$$

The only boundary condition is that there is no flux escaping from the last layer, which is the same as saying that $B_r = 0$ in layer N. In all the interfaces the radial component of the magnetic field, B_r, is continuous. The tangential field intensity, H_θ, is continuous in all interfaces except layer h in which there is a discontinuity by the amount of the current sheet amplitude.

To reduce the complexity of the problem, a transfer matrix approach is used to deal with the boundary conditions at the interfaces between layers. The objective is to obtain a transfer matrix, $[\mathbf{T}_n]$, that relates the radial component of the magnetic field, B_r, and the tangential component of the field intensity, H_θ, at the boundaries of region n. This can expressed as follows:

$$\begin{bmatrix} B_n \\ H_n \end{bmatrix} = \big[\mathbf{T}_n\big] \begin{bmatrix} B_{n-1} \\ H_{n-1} \end{bmatrix}, \tag{5.47}$$

where B_n is the radial component of the magnetic field at layer n and H_n is the tangential component of the field intensity at layer n. The transfer matrix can be obtained for each region based on the geometry and its properties. The calculation of this matrix for conductive regions and non-conductive regions is shown in sections 5.3.1 and 5.3.2, respectively.

Therefore, we can use the transfer matrix of each region to write the following equations:

$$\begin{bmatrix} B_N \\ H_N \end{bmatrix} = \big[\mathbf{T}_N\big]\big[\mathbf{T}_{N-1}\big]\dots\big[\mathbf{T}_{h+1}\big] \begin{bmatrix} B_h \\ H_h + \hat{J}_{qk} \end{bmatrix}, \tag{5.48}$$

$$\begin{bmatrix} B_h \\ H_h \end{bmatrix} = \big[\mathbf{T}_h\big]\big[\mathbf{T}_{h-1}\big]\dots\big[\mathbf{T}_2\big] \begin{bmatrix} B_1 \\ H_1 \end{bmatrix}. \tag{5.49}$$

To solve this system it is necessary to apply the boundary condition, which is simply that $B_N = 0$. Additionally, the magnetic field has to be finite in the origin. Therefore, we can write

$$H_1 = \beta_1 B_1, \tag{5.50}$$

where

$$\beta_1 = \frac{j\kappa_1 R_1}{\mu_1 q}\frac{I_q'(\kappa_1 R_1)}{I_q(\kappa_1 R_1)}, \tag{5.51}$$

when $\sigma_1 \neq 0$ and

$$\beta_1 = \frac{j}{\mu_1 q}, \tag{5.52}$$

when $\sigma_1 = 0$.

Using the previous expression we can obtain the values of B_1 and H_N as follows:

$$\begin{bmatrix} B_1 \\ H_N \end{bmatrix} = \left[\mathbf{D}\right]^{-1} \left[\mathbf{T}_N\right] \left[\mathbf{T}_{N-1}\right] \dots \left[\mathbf{T}_{h+1}\right] \begin{bmatrix} 0 \\ \hat{J}_{qk} \end{bmatrix}, \tag{5.53}$$

with

$$\left[\mathbf{D}\right] = \begin{bmatrix} 0 & 0 \\ 0 & 1 \end{bmatrix} - \left[\mathbf{T}_N\right] \left[\mathbf{T}_{N-1}\right] \dots \left[\mathbf{T}_2\right] \begin{bmatrix} 1 & 0 \\ \beta_1 & 0 \end{bmatrix}. \tag{5.54}$$

Once the values of B_1 and H_N are known, they can be used to obtain all the rest using the transfer matrices, as shown in (5.48) an (5.49).

5.3.1 Transfer matrix for a conductive region

The transfer matrix, $[\mathbf{T}_n]$, directly relates the magnetic fields at the two boundaries of a given region n. Figure 5.3 shows a schematic representation of a generic region. H_{n-1} and B_{n-1} are the tangential component of the field intensity and the radial component of the magnetic field at the inner boundary of region n, respectively.

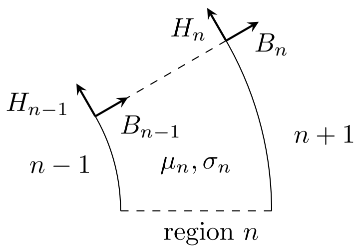

FIGURE 5.3: Simplified representation of a given region, n.

The expression of the magnetic field distribution is shown in (5.43) and (5.44). Therefore, for a region n:

$$\begin{bmatrix} B_{n-1} \\ H_{n-1} \end{bmatrix} = \begin{bmatrix} \frac{jq}{R_{n-1}} I_q(\kappa_n R_{n-1}) & \frac{jq}{R_{n-1}} K_q(\kappa_n R_{n-1}) \\ -\frac{\kappa_n}{\mu_n} I_q'(\kappa_n R_{n-1}) & -\frac{\kappa_n}{\mu_n} K_q'(\kappa_n R_{n-1}) \end{bmatrix} \begin{bmatrix} C_n \\ D_n \end{bmatrix}, \tag{5.55}$$

hence, re-arranging the terms:

$$\begin{bmatrix} C_n \\ D_n \end{bmatrix} = \frac{1}{F_n} \left[\mathbf{M}_n\right] \begin{bmatrix} B_{n-1} \\ H_{n-1} \end{bmatrix}, \tag{5.56}$$

with

$$\left[\mathbf{M}_n\right] = \begin{bmatrix} -\frac{\kappa_n}{\mu_n} K_q'(\kappa_n R_{n-1}) & -\frac{jq}{R_{n-1}} K_q(\kappa_n R_{n-1}) \\ \frac{\kappa_n}{\mu_n} I_q'(\kappa_n R_{n-1}) & \frac{jq}{R_{n-1}} I_q(\kappa_n R_{n-1}) \end{bmatrix}, \tag{5.57}$$

and

$$F_n = \frac{jq\kappa_n}{\mu_n R_{n-1}} \big[K_q(\kappa_n R_{n-1}) I_q'(\kappa_n R_{n-1}) - I_q(\kappa_n R_{n-1}) K_q'(\kappa_n R_{n-1}) \big]. \tag{5.58}$$

On the other hand we have that

$$\begin{bmatrix} B_n \\ H_n \end{bmatrix} = \big[\mathbf{N}_n \big] \begin{bmatrix} C_n \\ D_n \end{bmatrix}, \tag{5.59}$$

with

$$\big[\mathbf{N}_n \big] = \begin{bmatrix} \frac{jq}{R_n} I_q(\kappa_n R_n) & \frac{jq}{R_n} K_q(\kappa_n R_n) \\ -\frac{\kappa_n}{\mu_n} I_q'(\kappa_n R_n) & -\frac{\kappa_n}{\mu_n} K_q'(\kappa_n R_n) \end{bmatrix}. \tag{5.60}$$

Therefore, the transfer matrix is simply expressed as:

$$\big[\mathbf{T}_n \big] = \frac{1}{F_n} \big[\mathbf{N}_n \big] \big[\mathbf{M}_n \big]. \tag{5.61}$$

5.3.2 Transfer matrix for a non-conductive region

The methodology is exactly the same as in the case of a conductive region but the expression of the magnetic field distribution is shown in (5.45) and (5.46). Therefore, for a region n:

$$\begin{bmatrix} B_{n-1} \\ H_{n-1} \end{bmatrix} = \begin{bmatrix} jqR_{n-1}^{q-1} & jqR_{n-1}^{-q-1} \\ -\frac{1}{\mu_n} R_{n-1}^{q-1} & \frac{1}{\mu_n} R_{n-1}^{-q-1} \end{bmatrix} \begin{bmatrix} C_n \\ D_n \end{bmatrix}, \tag{5.62}$$

hence, re-arranging the terms:

$$\begin{bmatrix} C_n \\ D_n \end{bmatrix} = \frac{1}{F_n} \big[\mathbf{M}_n \big] \begin{bmatrix} B_{n-1} \\ H_{n-1} \end{bmatrix}, \tag{5.63}$$

with

$$\big[\mathbf{M}_n \big] = \begin{bmatrix} \frac{1}{\mu_n} R_{n-1}^{-q-1} & -jqR_{n-1}^{-q-1} \\ \frac{1}{\mu_n} R_{n-1}^{q-1} & jqR_{n-1}^{q-1} \end{bmatrix}, \tag{5.64}$$

and

$$F_n = \frac{2jq}{\mu_n R_{n-1}^2}. \tag{5.65}$$

On the other hand we have that

$$\begin{bmatrix} B_n \\ H_n \end{bmatrix} = \big[\mathbf{N}_n \big] \begin{bmatrix} C_n \\ D_n \end{bmatrix}, \tag{5.66}$$

with

$$\left[\mathbf{N}_n\right] = \begin{bmatrix} jqR_n^{q-1} & jqR_n^{-q-1} \\ -\frac{1}{\mu_n}R_n^{q-1} & \frac{1}{\mu_n}R_n^{-q-1} \end{bmatrix}. \tag{5.67}$$

Therefore, the transfer matrix is simply expressed as:

$$\left[\mathbf{T}_n\right] = \frac{1}{F_n}\left[\mathbf{N}_n\right]\left[\mathbf{M}_n\right]. \tag{5.68}$$

5.3.3 Calculation of losses

The losses can be calculated using the Poynting vector as described in section 5.2.2. For the case of the TFM under study there are 4 layers, which correspond to stator iron, permanent magnet material and rotor hub, as shown in Figure 5.1. Therefore, the total rotor losses, P_{tot}, correspond to the power flow through the cylinder of radius R_2:

$$P_{tot} = P_2 = \frac{1}{2}\,\mathrm{Re}\left(E_z|_{r=R_2} \cdot H_\theta^*|_{r=R_2}\right) \cdot S_2, \tag{5.69}$$

and the losses in the rotor hub are calculated as follows:

$$P_{hub} = P_3 = \frac{1}{2}\,\mathrm{Re}\left(E_z|_{r=R_3} \cdot H_\theta^*|_{r=R_3}\right) \cdot S_3. \tag{5.70}$$

Finally, the losses in the magnets are simply calculated as:

$$P_{mag} = P_2 - P_3 = P_{tot} - P_{hub}. \tag{5.71}$$

The same philosophy can be applied to any number of layers.

5.3.4 Reduction of the complexity of the problem

In many cases it might be useful to have a quick estimation of rotor losses without performing very complicated calculations. The only *problem* or inconvenience with the methodology proposed in this chapter is that for the calculation of the transfer matrix of a conductive region, see section 5.3.1, it is necessary to evaluate modified Bessel functions. This can be done easily in mathematical software packages such as MATLAB. However, in pure programming languages such as C or Python it is necessary to rely on external libraries. Therefore, the aim of this section is to show how to calculate the transfer matrix in a simplified way.

The methodology presented previously showed how to apply the transfer matrix to estimate the rotor losses Figure 5.3 assuming N regions. In fact, the only restriction is that each region has constant properties (μ_n and σ_n). Therefore, we can divide each region in many sub-regions and the method will still be valid. The advantage of dividing each of the regions in many subregions is that if the thickness of the region is very small compared to its radius the transfer matrix can be approximated using the results obtained for rectangular regions (Pipes, 1956; Greig and Freeman, 1967; Freeman, 1968).

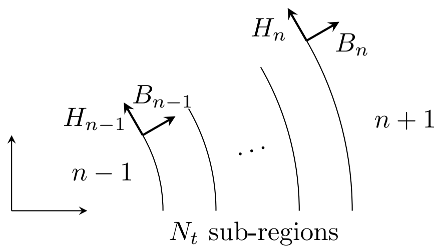

FIGURE 5.4: Region n is divided into N_t sub-regions.

If the original region n is divided into N_t sub-regions of the same thickness. The thickness of each sub-region is then calculated as follows

$$s_t = \frac{s_n}{N_t} = \frac{R_n - R_{n-1}}{N_t}. \tag{5.72}$$

The transfer matrix can be calculated directly applying the methodology presented in (Greig and Freeman, 1967; Freeman, 1968). In this Thesis the full deduction of the expression is omitted but it follows the same underlaying principle as sections 5.3.1 and 5.3.2. Therefore, the expression of the transfer matrix of a sub-region t is

$$\left[\mathbf{T}_t\right] = \begin{bmatrix} \cosh(\gamma_t s_t) & \frac{1}{\beta_t}\sinh(\gamma_t s_t) \\ \beta_t \sinh(\gamma_t s_t) & \cosh(\gamma_t s_t) \end{bmatrix}, \tag{5.73}$$

where

$$\gamma_t = \sqrt{k_t^2 + j\sigma_t \mu_t \omega}, \tag{5.74}$$

$$k_t = \frac{q}{R_t}, \tag{5.75}$$

$$\beta_t = \frac{\gamma_t}{j\mu_t k_t}. \tag{5.76}$$

The transfer matrix of region n is simply the product of the transfer matrix of all sub-regions. One reasonable approach can be to assume that the radius of all the sub-regions is the same:

$$R_t = \frac{R_n + R_{n-1}}{2}. \tag{5.77}$$

Therefore, the transfer matrix of all the sub-regions is the same and the transfer matrix can be calculated as follows:

$$\left[\mathbf{T}_n\right] = \left[\mathbf{T}_t\right]^{N_t}. \tag{5.78}$$

At this point we can calculate the transfer matrices without having to evaluate the Bessel functions. However, there are hyperbolic functions. If the thickness of the sub-region is sufficiently small we can do one last simplification:

$$[\mathbf{T}_t] = \lim_{s_t \to 0} \begin{bmatrix} \cosh(\gamma_t s_t) & \frac{1}{\beta_t}\sinh(\gamma_t s_t) \\ \beta_t \sinh(\gamma_t s_t) & \cosh(\gamma_t s_t) \end{bmatrix} = \begin{bmatrix} 1 & \frac{\gamma_t s_t}{\beta_t} \\ \beta_t \gamma_t s_t & 1 \end{bmatrix}. \tag{5.79}$$

This matrix is easy to compute and is *well behaved* in general terms. Therefore, it can be very useful to get a quick estimation of the order of magnitude of the rotor losses. However, it is important to note that the above approximations must be used with care.

5.4 3D Effects

The methodologies presented in previous sections are formulated in two-dimensions (assuming that the eddy currents are only in the z direction) and they can be used in any kind of machine not only TFMs. This approach is commonly used and it is effective when the machine studied is long in the axial direction. However, TFMs tend to have short magnets; which makes the influence of the 3D effects important.

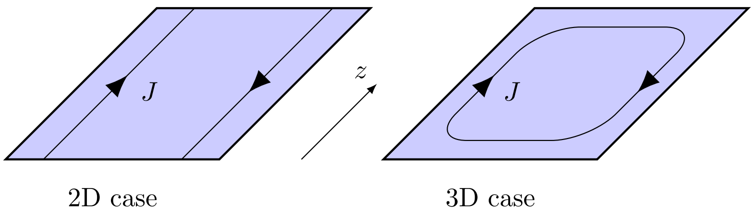

FIGURE 5.5: Paths of the eddy currents for the 2D and 3D cases.

When a machine is very long axially the magnetic fields *inside* are almost 2D and the end effects not very important. Figure 5.5 shows schematically the difference between the 2D case and the 3D case. It can be appreciated in the right hand side of Figure 5.5 that the path of the eddy currents has components that are not in the z axis. Therefore, it is important to consider this effect in machines that are short in the axial direction.

Russell and Norsworthy (1958) studied the end effect on the eddy currents induced in thin cans. Their approach was to solve the 2D problem ignoring the reaction field of the eddy currents, i. e., consider a resistance limited problem. Next, they solved the same problem but considering the end effects. If P_0 is the total power loss in the 2D case, then the power in the 3D case is $P = P_0 K_S$, where K_S is a coefficient that depends only on the geometry and the properties of the materials.

In this section we present the background theory of Russell and Norsworthy's approach and the details of the calculation of K_S. Furthermore, we show how to apply this theory in the context of the rotor losses in TFMs.

It is important to point out that this methodology is used to account for the 3D effects that appear in TFMs and complement the methodologies presented in the previous sections. All this section is based on (Russell and Norsworthy, 1958).

5.4.1 2D Case

The 2D case is simply a topology in which the axial length can be considered infinite[4]. The thin can is subject to a radial magnetic field. Since the can is thin it can be developed without loosing any generality as shown in Figure 5.6, with the appropriate Cartesian axes. The length in the x direction is $2l$, in the y direction is $2b$ with $b = \pi r$ and the thickness of the can is h.

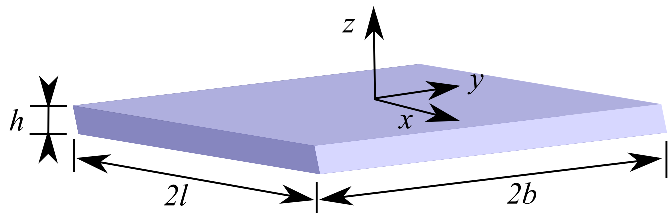

FIGURE 5.6: Schematic representation of the developed model of the thin can with the appropriate axes. This is the geometry considered for the 2D case.

The radial magnetic field, using the same notation as Figure 5.6 can be written as:

$$B_z = B_m \cos\left(\frac{\pi}{b} q y + \omega t\right), \tag{5.80}$$

where q is the harmonic order.

Assuming that the reaction field of the induced currents can be neglected, the electromotive force can be deduced from Lorentz's equation, $\vec{E} = \vec{v} \times \vec{B}$, where $\vec{v}$ is the relative speed; which has a radial component only $v = b\omega/q$. Therefore, the electric field is

$$E_x = \left(\frac{r\omega}{q}\right) B_m \cos\left(\frac{\pi}{b} q y - \omega t\right). \tag{5.81}$$

Accordingly, the current density can be written as

$$J_x = \left(\frac{\sigma r\omega}{q}\right) B_m \cos\left(\frac{\pi}{b} q y - \omega t\right). \tag{5.82}$$

The power loss per unit volume can be calculated using the values of the electric field and the current density as:

$$P_{vol} = \vec{J} \cdot \vec{E}. \tag{5.83}$$

The total loss is simply obtained by integrating the previous expression in all the domain:

$$P_0 = \iiint \vec{J} \cdot \vec{E}\, dV, \tag{5.84}$$

[4]In (Russell and Norsworthy, 1958) they refer to this case as *Conducting Shell with Zero Overhang and Zero Resistance End-Rings* because they are the same case.

which in this case is straightforward to evaluate because there are only x components. Thus, the total eddy current loss in the thin can is

$$P_0 = \frac{2\sigma h \omega^2 b^3 B_m^2 l}{\pi^2 q^2}. \tag{5.85}$$

5.4.2 3D Case

The 3D case considered in this section is the same thin can as in the previous case but with an overhang of αl (to make the case more general) and considering that that eddy currents can have components in the x and y axes, as shown in Figure 5.6.

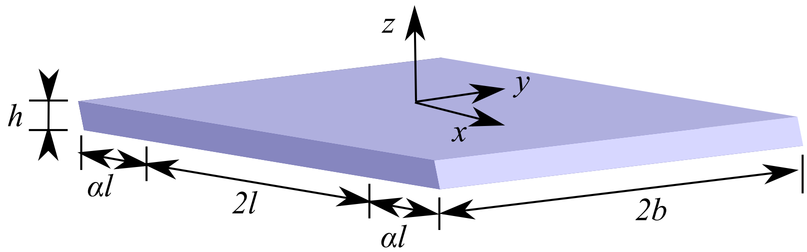

FIGURE 5.7: Schematic representation of the developed model of the thin can with the appropriate axes. This is the geometry considered for the 3D case with end effects and overhang.

The principle is similar to the previous case but the formulation is slightly different. Based on Maxwell's equations, the differential form of Faraday's law of induction can be expressed as:

$$\vec{\nabla} \times \vec{E} = -\frac{\partial \vec{B}}{\partial t}, \tag{5.86}$$

considering that the external magnetic field has component in the z axis:

$$\frac{\partial E_y}{\partial x} - \frac{\partial E_x}{\partial y} = -\frac{\partial B_z}{\partial t}. \tag{5.87}$$

This expression is equivalent to equation (10) in (Russell and Norsworthy, 1958)[5]. The current density can be directly related to the electric field in each direction:

$$J_x = \sigma_x E_x, \tag{5.88}$$

$$J_y = \sigma_y E_y. \tag{5.89}$$

Therefore, combining (5.87), (5.88) and (5.89):

$$\frac{1}{\sigma_y}\frac{\partial J_y}{\partial x} - \frac{1}{\sigma_x}\frac{\partial J_x}{\partial y} = -\frac{\partial B_z}{\partial t}. \tag{5.90}$$

[5]There is a typographical error in equation (10) in (Russell and Norsworthy, 1958). The correct expression is:

$$E_x dx + \left(E_y + \frac{\partial E_y}{\partial x} dx\right) dy - \left(E_x + \frac{\partial E_x}{\partial y} dy\right) dx - E_y dy = -\frac{\partial B_z}{\partial t} dx dy.$$

However, this error does not affect the final result because its deduction, equation (12), is correct.

In addition, we have Kirchoff's law expressed in differential form:

$$\frac{\partial J_x}{\partial x} + \frac{\partial J_y}{\partial y} = 0. \tag{5.91}$$

We can re-write (5.90) and (5.91) in a convenient form as a system of partial differential equations (PDEs):

$$\frac{1}{\sigma_y}\frac{\partial^2 J_x}{\partial x^2} + \frac{1}{\sigma_x}\frac{\partial^2 J_x}{\partial y^2} = -\frac{\partial^2 B_z}{\partial y \partial t}, \tag{5.92}$$

$$\frac{1}{\sigma_y}\frac{\partial^2 J_y}{\partial x^2} + \frac{1}{\sigma_x}\frac{\partial^2 J_y}{\partial y^2} = -\frac{\partial^2 B_z}{\partial x \partial t}. \tag{5.93}$$

In our case the external magnetic field is applied only in the central region ($|x| \leq l$). Therefore, the PDEs that govern the central region are:

$$\frac{1}{\sigma_y}\frac{\partial^2 J_x}{\partial x^2} + \frac{1}{\sigma_x}\frac{\partial^2 J_x}{\partial y^2} = -\left(\frac{\omega\pi q B_m}{b}\right)\cos\left(\frac{\pi}{b}qy + \omega t\right), \tag{5.94}$$

$$\frac{1}{\sigma_y}\frac{\partial^2 J_y}{\partial x^2} + \frac{1}{\sigma_x}\frac{\partial^2 J_y}{\partial y^2} = 0. \tag{5.95}$$

In the overhang region there is no external field. Therefore, the PDEs are expressed simply as:

$$\frac{1}{\sigma_y}\frac{\partial^2 J_x}{\partial x^2} + \frac{1}{\sigma_x}\frac{\partial^2 J_x}{\partial y^2} = 0, \tag{5.96}$$

$$\frac{1}{\sigma_y}\frac{\partial^2 J_y}{\partial x^2} + \frac{1}{\sigma_x}\frac{\partial^2 J_y}{\partial y^2} = 0. \tag{5.97}$$

The boundary conditions between the two regions are that the tangential component of the electrostatic field, E_y, is continuous and that the current satisfies Kirchoff's law. The solution of this system of PDEs is shown in detail in (Russell and Norsworthy, 1958) but for the sake of simplicity and readability of this Thesis only the final results are shown.

The following intermediate variable is defined to express the solution in a compact way[6]:

$$\xi = \tanh\left(\frac{\pi}{b}q\alpha l\sqrt{\frac{\sigma_y}{\sigma_x}}\right)\tanh\left(\frac{\pi}{b}ql\sqrt{\frac{\sigma_y}{\sigma_x}}\right). \tag{5.98}$$

The expression of the current densities in the central region is:

$$J_x = \left(\frac{\omega\sigma_x b B_m}{\pi q}\right)\cos\left(\frac{\pi}{b}qy + \omega t\right)\left[1 - \frac{\cosh\left(\frac{\pi}{b}q\sqrt{\frac{\sigma_y}{\sigma_x}}x\right)}{(1+\xi)\cosh\left(\frac{\pi}{b}q\sqrt{\frac{\sigma_y}{\sigma_x}}\right)}\right], \tag{5.99}$$

[6] This variable is called λ in Russell and Norsworthy's paper but in this Thesis the symbol of λ is used for the complex permeance function.

$$J_y = \sqrt{\frac{\sigma_y}{\sigma_x}}\Big(\frac{\omega\sigma_x bB_m}{\pi q}\Big)\sin\Big(\frac{\pi}{b}qy+\omega t\Big)\left[\frac{\sinh\Big(\frac{\pi}{b}q\sqrt{\frac{\sigma_y}{\sigma_x}}x\Big)}{(1+\xi)\cosh\Big(\frac{\pi}{b}q\sqrt{\frac{\sigma_y}{\sigma_x}}\Big)}\right]. \tag{5.100}$$

Analogously, the expression of the current densities for the overhang regions is:

$$J_x = -\Big(\frac{\omega\sigma_x bB_m}{\pi q}\Big)\cos\Big(\frac{\pi}{b}qy+\omega t\Big)\left[1-\frac{\sinh\Big(\frac{\pi}{b}q\sqrt{\frac{\sigma_y}{\sigma_x}}[x-(1+\alpha)l]\Big)}{(1+\frac{1}{\xi})\sinh\Big(\frac{\pi}{b}q\alpha\sqrt{\frac{\sigma_y}{\sigma_x}}\Big)}\right], \tag{5.101}$$

$$J_y = \sqrt{\frac{\sigma_y}{\sigma_x}}\Big(\frac{\omega\sigma_x bB_m}{\pi q}\Big)\sin\Big(\frac{\pi}{b}qy+\omega t\Big)\left[\frac{\cosh\Big(\frac{\pi}{b}q\sqrt{\frac{\sigma_y}{\sigma_x}}[x-(1+\alpha)l]\Big)}{(1+\frac{1}{\xi})\sinh\Big(\frac{\pi}{b}q\alpha\sqrt{\frac{\sigma_y}{\sigma_x}}\Big)}\right]. \tag{5.102}$$

The calculation of the power for the 3D case is similar to the 2D one but it is slightly more complicated. The power per unit volume is:

$$P_{vol} = \vec{J}\cdot\vec{E}, \tag{5.103}$$

taking into account that $\vec{E} = \vec{v}\times\vec{B}$ we can re-write the specific power as

$$P_{vol} = (\vec{v}\times\vec{B})\cdot\vec{J} = \begin{vmatrix} 0 & \frac{\omega b}{q\pi} & 0 \\ 0 & 0 & B_m\cos\Big(\frac{\pi}{b}qy+\omega t\Big) \\ J_x & J_y & 0 \end{vmatrix}. \tag{5.104}$$

The total losses are calculated by integrating the specific power all over the thin can:

$$P = \iiint (\vec{v}\times\vec{B})\cdot\vec{J}\,dV. \tag{5.105}$$

It can be shown that the expression of the total losses can be expressed as:

$$P = P_0\left[1-\frac{\tanh\Big(\frac{\pi}{b}q\sqrt{\frac{\sigma_y}{\sigma_x}}l\Big)}{\frac{\pi q}{b}\sqrt{\frac{\sigma_y}{\sigma_x}}(1+\xi)l}\right] = P_0K_S, \tag{5.106}$$

where P_0 are the total losses of the 2D case shown in the previous section. The coefficient K_S can be readily used to modify, calculate and assess the influence of the 3D effects on the eddy currents induced in a thin can.

5.4.3 Application to TFMs

The coefficient K_S deduced in the previous section is interesting because it can be used to complement the two-dimensional methodologies described in this chapter. Even though, the assumptions of Russell and Northsworthy's are based on thin cans and ignore the reaction field of the eddy currents, the coefficient can be used as a link between the 2D and the 3D models.

Furthermore, this approach is particularly well suited to complement the methodology presented in section 5.3.4 because dividing each region in many thin layers is the same as having many thin cans. Therefore, the value of K_S and the 2D losses, P_0, can be readily calculated for each thin layer. Then, the total losses are simply the sum of all the thin layers. The interaction between the field of different layers is not considered in this methodology but it remains as a useful first approximation.

From the practical point of view, the aim of this section is to relate directly equations (5.98) and (5.106) to the geometry of the TFM studied in this Thesis. The previous formulation considered the possibility of anisotropy ($\sigma_x \neq \sigma_y$); the permanent magnet material is isotropic ($\sigma_x = \sigma_y$), which simplifies the expressions.

The geometrical variables of section 5.4.2 are related to geometry of the TFM shown in chapter 1 as follows:

$$l = \frac{l_{core}}{2}, \tag{5.107}$$

$$b = \pi r, \tag{5.108}$$

$$\alpha = \frac{L_{mag} - l_{core}}{2}. \tag{5.109}$$

Thus, the practical expressions that should be used to calculate the coefficient K_S for the analysis of the single-sided TFM considered in this Thesis can be written as:

$$\nu = \frac{q l_{core}}{2r}, \tag{5.110}$$

$$\xi = \tanh(\alpha\nu) \cdot \tanh(\nu), \tag{5.111}$$

$$K_S = \left[1 - \frac{\tanh(\nu)}{\nu(1+\xi)}\right]. \tag{5.112}$$

The value of K_S does not vary in a significant way all through the magnet thickness; which is where most of the eddy currents are induced.

TABLE 5.1: Value of K_S for the TFM

Space order	q	$r = R_m$ K_S [%]	$r = R_r$ K_S [%]
1	20	24.09	24.07
3	60	24.61	24.56
5	100	25.11	25.04
7	140	25.61	25.51
9	180	26.10	25.98

Table 5.1 shows the value of Russell's coefficient at the rotor hub ($r = R_r$) and on top of the magnets ($r = R_m$) for the first even harmonics. It can be appreciated that there is not

a significant difference in the value of K_S all through the magnet thickness. Therefore, one reasonable approach is to apply the average value of the coefficient to multiply the total losses instead of applying it in each layer.

It is important to point out that the approach presented in this section is not an exact solution of the field equations in three dimensions. The solution is obtained using a 2D model and later Russell's coefficient, K_S, is used to account for the end effects. Since TFMs are intrinsically three-dimensional devices it is important to remember that this approach is useful as a first step in the analysis and should be complemented with 3D modelling techniques.

5.5 Asynchronous Harmonics

The asynchronous harmonics are produced by the interaction between the permeance function due to slotting and the rotor's magnets (no load magnetic field distribution). In addition, there are asynchronous harmonics produced by the stator's MMF.

5.5.1 No-Load Magnetic Field Distribution

The no-load magnetic field distribution in the air-gap of the slotless configuration using the rotor's reference frame can be expressed using complex number notation as

$$B_{sl}(\theta, r) = \sum_{n=1,3,5}^{\infty} K_n(r)\cos(np\theta) + j\sum_{n=1,3,5}^{\infty} D_n(r)\sin(np\theta), \tag{5.113}$$

where the coefficients $K_n(r)$ and $D_n(r)$ are calculated according to (Zhu et al., 2002) and $j = \sqrt{-1}$ is the imaginary unit. The complex permeance (CP) function using the rotor's reference frame is

$$\lambda(\theta, r, t) = \lambda_{a0} + \sum_{m=1,2,3}^{\infty} \lambda_{am}(r)\cos\big(mQ_s(\theta - \omega_m t)\big) + j\sum_{m=1,2,3}^{\infty} \lambda_{bm}(r)\sin\big(mQ_s(\theta - \omega_m t)\big), \tag{5.114}$$

where the coefficients λ_{a0}, $\lambda_{am}(r)$ and $\lambda_{bm}(r)$ are calculated using conformal mapping, as shown in chapter 3, $\omega_m = \omega/p$ is the mechanical speed of the rotor and Q_s is the number of slots of the machine. Therefore, the magnetic field distribution of the slotted geometry is

$$B_{nl}(\theta, r, t) = B_{sl}(\theta, r)\cdot\lambda^*(\theta, r, t). \tag{5.115}$$

For the calculation of rotor losses we are interested in the amplitude of the asynchronous harmonics of the radial component of the magnetic field, as discussed in section 5.3. Therefore, combining (5.113), (5.114) and (5.115) we obtain:

$$\mathrm{Re}\Big(B_{nl}(\theta,r,t)\Big) = \sum_{n=1,3,5}^{\infty} K_n(r)\cos(np\theta)\left[\lambda_{a0} + \sum_{m=1,2,3}^{\infty} \lambda_{am}(r)\cos\big(mQ_s(\theta-\omega_m t)\big)\right]$$
$$+\sum_{n=1,3,5}^{\infty} D_n(r)\sin(np\theta)\left[\sum_{m=1,2,3}^{\infty} \lambda_{bm}(r)\sin\big(mQ_s(\theta-\omega_m t)\big)\right]. \quad (5.116)$$

For a particular m, which means a time order $k = mQ_s/p$, we can re-arrange (5.116) to express explicitly each asynchronous harmonic. For each particular n we have two asynchronous harmonics whose space order, q, and amplitude, B_{qk}, are calculated as follows

$$\begin{cases} q = k+n, & \text{and } B_{qk} = K_n(r)\frac{\lambda_{am}}{2} - D_n(r)\frac{\lambda_{bm}}{2} \\ q = k-n, & \text{and } B_{qk} = K_n(r)\frac{\lambda_{am}}{2} + D_n(r)\frac{\lambda_{bm}}{2} \end{cases} \quad (5.117)$$

The machine studied in this Thesis has $Q_s = 20$ slots and $p = 20$ pole pairs. Therefore, the time orders are 1,2,3... Accordingly, the most important asynchronous harmonics are for $n = 1$, which is the fundamental waveform of the slotless solution. This means that the most important asynchronous harmonics for time order 1 have space order 0 and 2; for time order 2 have space order 1 and 3; for time order 3 have space order 2 and 4; and so forth.

5.5.2 Stator's Magnetic Field Distribution

The stator's magnetic field distribution was calculated in chapter 3. The radial component of the magnetic field can be expressed in the rotor's reference frame as follows:

$$B_{stator}(\theta,r,t) = B_s(t)\frac{R_g}{r}\overline{\lambda}_r\Big[1+\sum_{m=1,2,3}^{\infty}\gamma_m\cos\big(mQ_s(\theta-\omega_m t)\big)\Big]. \quad (5.118)$$

Assuming that the current is sinusoidal, $B_s(t)$ can be written as:

$$B_s(t) = \hat{B}_s\cos(\omega t). \quad (5.119)$$

Taking into account that $\omega_m = \omega/p$ is the mechanical speed and operating with (5.118) and (5.119) it can be proven that:

$$B_{stator}(\theta,r,t) = \hat{B}_s\frac{R_g}{r}\overline{\lambda}_r\left[\cos(\omega t) + \sum_{m=1,2,3}^{\infty}\frac{\gamma_m}{2}\Big\{\cos\big(\omega t(1-\frac{mQ_s}{p}) + mQ_s\theta\big) + \right.$$
$$\left.\cos\big(\omega t(1+\frac{mQ_s}{p}) - mQ_s\theta\big)\Big\}\right]. \quad (5.120)$$

Analogously to the no-load case, for a particular m, we can re-arrange (5.120) to express explicitly each asynchronous harmonic. For each particular m we have two asynchronous harmonics whose space order is $q = mQ_s/p$, and the amplitude, B_{qk}, are calculated as follows:

$$B_{qk} = \hat{B}_s \overline{\lambda}_r \frac{R_g}{r} \frac{\gamma_m}{2}. \tag{5.121}$$

One has a time order $k = 1 - mQ_s/p$ and the other one $k = 1 + mQ_s/p$.

Therefore, the most important asynchronous harmonic is with $m = 1$ which means a time order two[7] and a space order one.

However, it is important to note that the first term of (5.120) is an *asynchronous harmonic* with space order 0. This is because the field produced by the stator windings in the TFM studied in this Thesis is homopolar. The current formulation of the current sheet model is not able to obtain these losses and further work is required in this topic.

5.6 Limitations of the complex permeance and current sheet model

The current sheet model provides more than reasonable results, as shown in the next section, for the calculation of eddy currents as long as the amplitudes of the asynchronous harmonics are accurate. However, there are several simplifying assumptions.

First, the current sheet model is two-dimensional. Therefore, the end effects and the influence of the return path of the eddy currents induced is neglected. The model does not cater for peripheral magnet segmentation, which can significantly affect the eddy currents since the segmentation blocks the path of the induced currents.

In machines with relatively small active length to diameter ratios, it is necessary to use 3D FEA because the end effects can be significant (Hendershot and Miller, 2010). To minimise the weight of this issue we have implemented the methodology developed by Russell and Norsworthy (1958), shown in section 5.4. Nevertheless, the qualitative information and the insight provided by the current sheet model in these case can be helpful to a machine designer.

The properties of the materials are assumed to be linear and isotropic. Accordingly, the methodology presented in this paper does not take into account the saturation. Significant saturation, particularly of the tooth tip can result in significant under estimation of the magnitudes of the asynchronous harmonics and corresponding losses (Qazalbash et al., 2014a,b, 2015).

There is one particular limitation of the current sheet model that is particularly important for the case of TFMs: the losses of a homopolar components of the field, i.e. space order 0, cannot be calculated. This is related to the assumption that the harmonic can be represented with an equivalent current sheet.

Finally, the effect of the induced eddy currents on the traveling flux harmonics is neglected, the eddy currents generate travelling harmonics that interact with the slotting, which is not taken into account in the slotless current sheet model. However, this effect is expected to be negligible due to the large air-gap and the relatively weak magnetic field of the eddy currents (Irenji, 1998).

[7] The other harmonic has time order 0, which means that it is synchronous with the rotor.

5.7 Results

For the purpose of validating the methodology presented, a two-dimensional finite elements model was built. The model is made of cylindrical bodies, similar to the geometry shown in Figure 5.1, with the same properties as the TFM described in chapter 1. The current density in the Ansys model was set to produce an alternating field with an amplitude of 1 T. The model was fully parametrised to allow for a given frequency, time order and space order. Figure 5.8 shows an example of the eddy currents induced and the ohmic losses in the rotor.

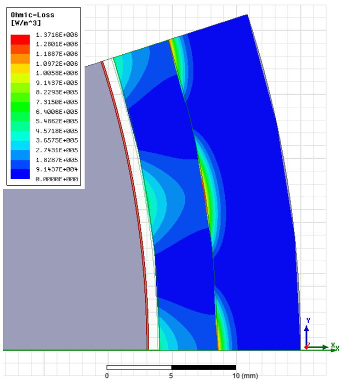

(a) Space order $q = p$.

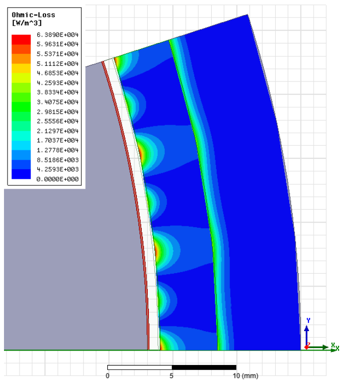

(b) Space order $q = 3p$.

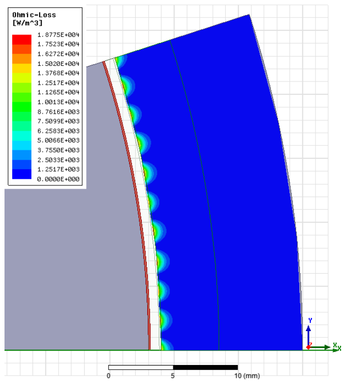

(c) Space order $q = 5p$.

FIGURE 5.8: Rotor losses in the TFM obtained using FEA at 50 Hz, $\hat{B}_{qk} = 1$ T.

A summary of the results from the simulations is shown in table 5.2. The total rotor losses were calculated for several space orders for the case of an electrical frequency of 50 Hz and 500 Hz. The value obtained using transfer matrices, P_{TM}, and the value obtained using FEA, P_{FEA}, are expressed in watt.

TABLE 5.2: Rotor losses in the TFM for a field of 1 T

q	$\hat{B}_{qk}$ [T]	f [Hz]	P_{TM} [W]	P_{FEA} [W]
p	1	50	14.7	14.84
$2p$	1	50	1.01	1.223
$3p$	1	50	0.222	0.261
$4p$	1	50	0.0802	0.108
$5p$	1	50	0.0359	0.0488
p	1	500	1057.8	1081.2
$2p$	1	500	91.83	111.48
$3p$	1	500	21.9	25.34
$4p$	1	500	8.01	10.8
$5p$	1	500	3.59	4.92

It can be appreciated that the proposed methodology presents a reasonable level of accuracy, particularly for the space order $q = p$. The larger difference between the proposed analytical method and FEA for the space orders $q = 3p$ and $q = 5p$ is probably due to the numerical errors in FEA. This is because the absolute value of the losses for the high order harmonics decrease significantly, which makes the calculation of the losses inaccurate.

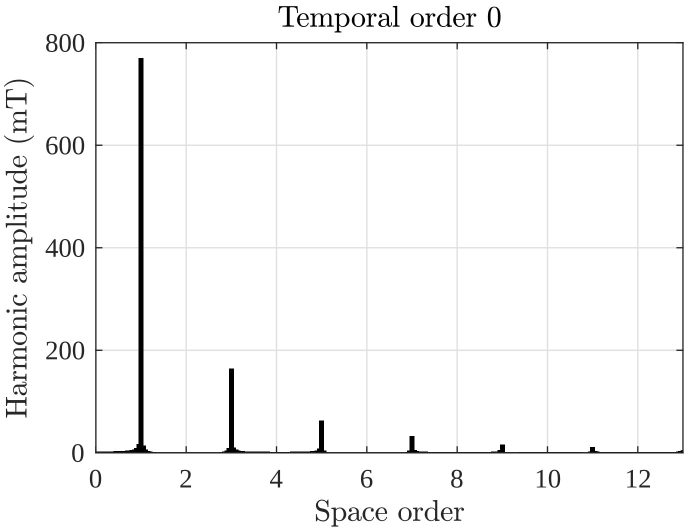

(a) Time order 0.

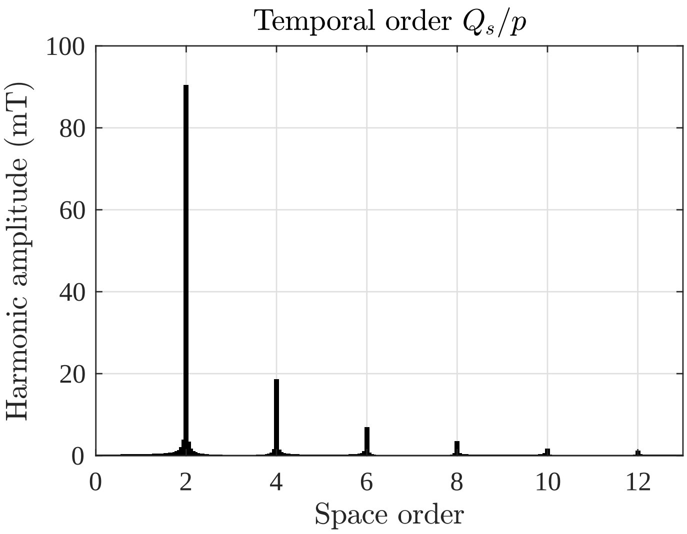

(b) Time order 1.

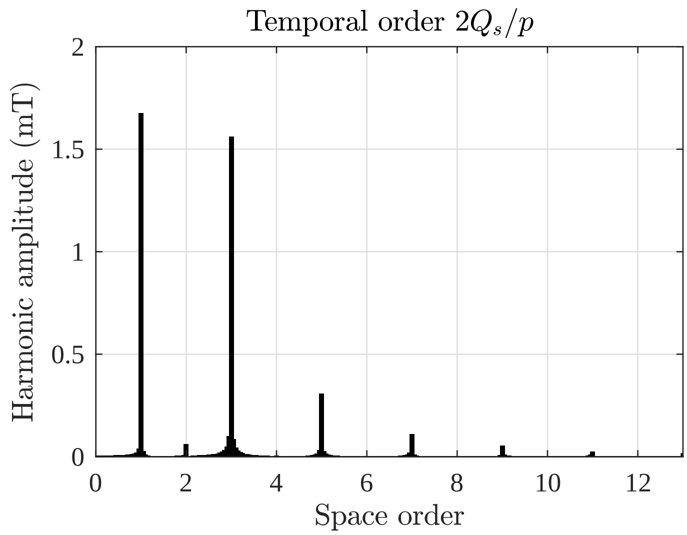

(c) Time order 2.

FIGURE 5.9: No-load asynchronous harmonics of the TFM.

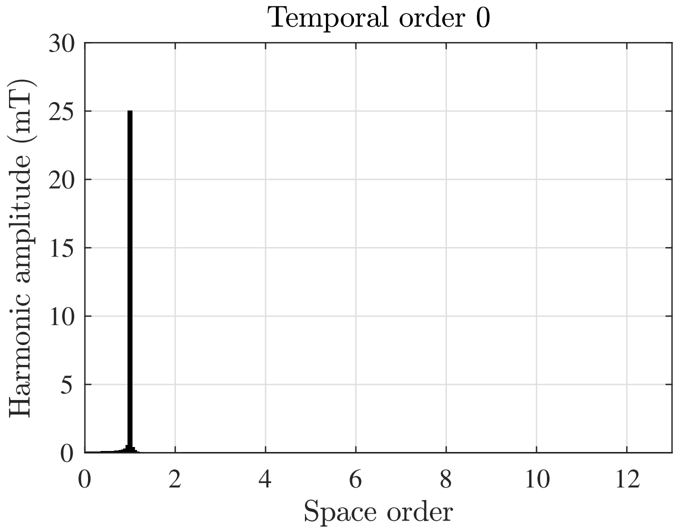

(a) Time order 0.

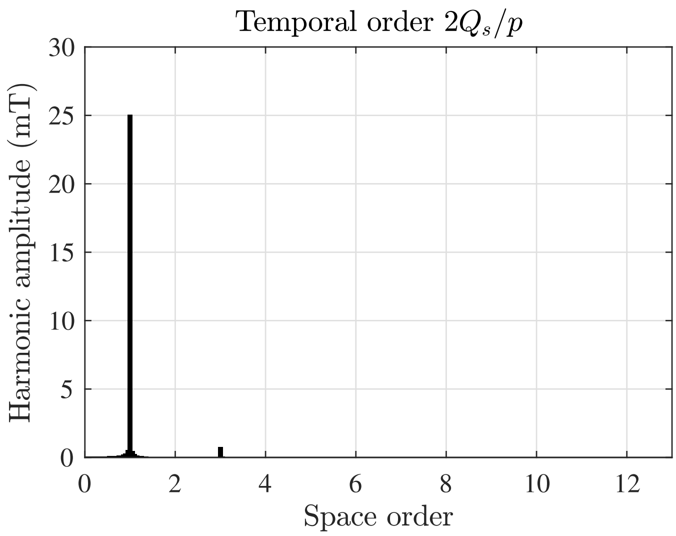

(b) Time order 2.

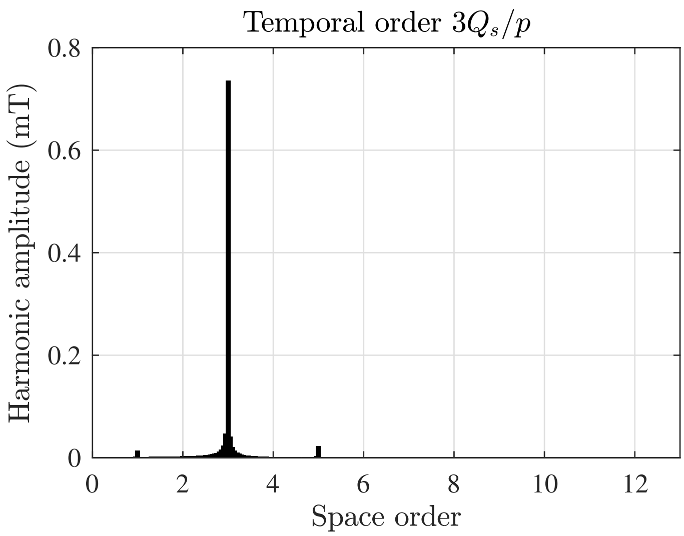

(c) Time order 3.

FIGURE 5.10: Stator's asynchronous harmonics of the TFM.

Figure 5.9 shows the no-load asynchronous harmonics of the TFM under study obtained using the CP method. The most significant asynchronous harmonic has a temporal order 1 and a space order 2 with an amplitude of $\hat{B}_{qk} = 90.4$ mT.

Figure 5.10 shows the asynchronous harmonics of the TFM under study produced by the stator windings obtained using the CP method. The most significant asynchronous harmonic has a temporal order 2 and a space order 1 with an amplitude of $\hat{B}_{qk} = 25.04$ mT.

The no load rotor losses per asynchronous harmonic when the machine is running at 1500 rpm are shown in table 5.3. The on load losses are shown in table 5.4, it can be appreciated that the most important harmonic has a space order of 1 and it is produced by the stator windings. In the following tables q is the space order, k the time order, $\hat{B}_{qk}$ the harmonic amplitude, f the electrical frequency, Ω the mechanical speed of the rotor and P the power loss.

Table 5.3: No-load rotor losses in the TFM under study

q	k	$\hat{B}_{qk}$ [mT]	f [Hz]	Ω [rpm]	P [W]
p	2	1.675	500	1500	0.011
$2p$	1	90.37	500	1500	0.75
$3p$	2	1.561	500	1500	0
$4p$	1	18.56	500	1500	0
				$P_{tot} =$	0.7614

Table 5.4: On load rotor losses in the TFM under study

q	k	$\hat{B}_{qk}$ [mT]	f [Hz]	Ω [rpm]	P [W]
p	1	25.4	500	1500	2.48
p	2	1.675	500	1500	0.011
$2p$	1	90.37	500	1500	0.75
$3p$	2	1.561	500	1500	0
$4p$	1	18.56	500	1500	0
				$P_{tot} =$	3.241

The rotor losses, no load and on load, as a function of the mechanical speed of the rotor are shown in Figure 5.11. The asynchronous harmonics considered in this figure are taken from tables 5.3 and 5.4. These values might seem low but it is important to remember that they are produced by the asynchronous harmonics and the homopolar components are not taken into consideration.

5.8 Summary

A novel analytical methodology for the calculation of rotor losses was presented in this chapter. The proposed methodology is based on the current sheet model and uses transfer matrices to reduce the complexity of the problem.

The case study is an outer rotor TFM but it is important to mention that this methodology can be applied to other machines and it is particularly useful for the analysis high speed PM machines.

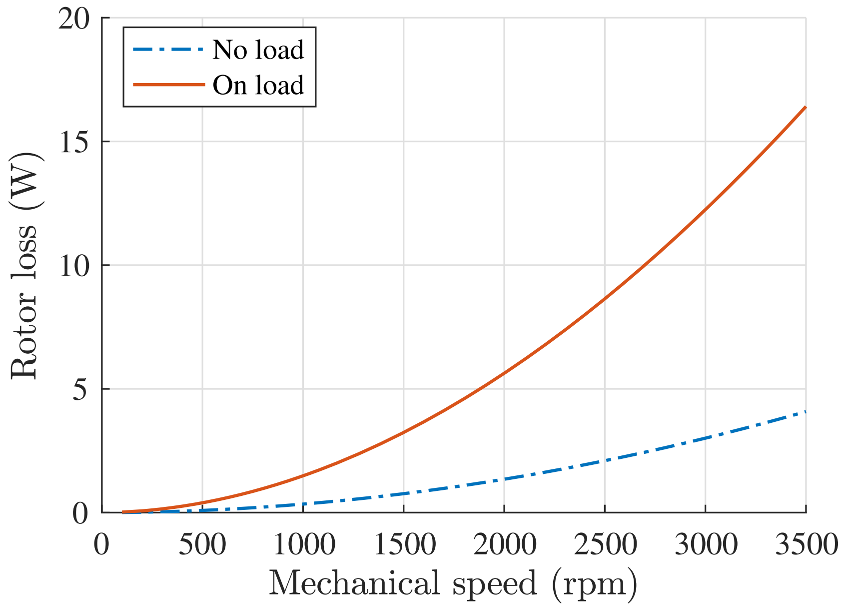

FIGURE 5.11: Rotor losses as a function of the mechanical speed of the rotor.

Chapter 6

Design and Optimisation of a TFM for Tidal Power Generation

Overview

This chapter illustrates the optimisation of a TFM for tidal power generation. The aim is to show how to use the methodologies developed in the previous chapters to intuitively design (or to do the so-called *scaling*) of a TFM. There might be some repetition in this chapter but the objective is to present a self-contained example that does not require the reader to *jump back* to the previous chapters.

The machine presented here is the same as the TFM described in chapter 1 but with three phases. This might not be the best type of TFM in terms of power density but it has a simple topology. However, the key point of this chapter is the design process itself, which can be applied to any kind of TFM.

6.1 Introduction

The design of brushless permanent magnet (PM) machines is a complex iterative process in which many factors have to be taken into account. However, when designing traditional PM machines there are several analytical expressions to obtain a quick estimation of the performance of these devices before refining the final design with more complicated methods such as FEA (Hendershot and Miller, 2010; Tapia et al., 2013). Because of the three-dimensional nature of TFMs, the number of free geometrical parameters is high; which means that the approach that uses genetic algorithms combined with 3D FEA may not be feasible (Zhang et al., 2016; Oh and Kwon, 2016). Furthermore, the simple analytical expressions derived for traditional PM machines are not always suitable for the analysis of TFMs because of their different topology and principle of operation.

The aim of this chapter is to present an intuitive TFM design optimisation philosophy based on simple analytical methods; which can complement 3D FEA in the design process. Expressions for torque and back emf constants are obtained by replacing the permanent magnets (PMs) with equivalent current sheets as shown in (Anglada and Sharkh, 2017a,b,c) and in chapter 4. These compact expressions are used to obtain a set of normalised curves that can be readily used to determine the optimal proportions and dimensions of a machine to maximise its torque density. Equivalent circuit models are used to assess the performance of the machine.

The chapter also discusses the issue of the inherent low power factor of transverse flux machines, which is fundamentally linked to its principle of operation. Maximizing torque density inherently reduces the power factor (Anglada and Sharkh, 2017c). However, the chapter will show that it is possible to improve the power factor significantly at the expense of a small reduction in the machine's torque capability. Accordingly, the chapter proposes a design optimisation procedure with the combined objective of achieving high torque density and good power factor, which will help to unlock the potential of these types of machine.

6.2 Machine Topology

To help to illustrate the design optimisation philosophy proposed in this chapter, we use the tidal turbine generator shown in Figure 6.1 as an example. The current product uses an outer rotor surface PM machine, which will provide a bench mark for the new TFM machine presented in this chapter, which will be designed to fit within the constraints of the available space. The type of TFM is the same as the one presented in chapter 1 but with 3 phases.

FIGURE 6.1: Picture of the tidal turbine developed at the University of Southampton.

There is a large number of TFM topologies from simple single-sided ones (Harris and Mecrow, 1993; Harris and Pajooman, 1995; Harris et al., 1996) to more complicated flux concentrating design (Kang and Weh, 2008; Baker et al., 2012; Washington et al., 2012; Deodhar et al., 2015; Doering et al., 2015; Washington et al., 2016; Keller et al., 2016). All of them share some similarities with claw-pole machines. In this chapter, the topology considered is a three-phase single-sided TFM with an outer rotor as shown in Figure 6.2. This topology was chosen because it has an outer rotor configuration that is required in this case. In addition, it is fairly simple and easy to manufacture. It has been studied extensively before and its simplicity makes it a good machine for illustrating the design optimisation procedure, which can be readily applied to other topologies.

Each phase in the machine in Figure 6.2 has a circular coil, linking and magnetising the N_c laminated C-cores which modulate the armature's magnetic field to produce a fundamental heteropolar harmonic in the radial direction. The number of C-cores and their width has to be carefully selected to have a tradeoff between the torque density and the power factor (Anglada and Sharkh, 2017c).

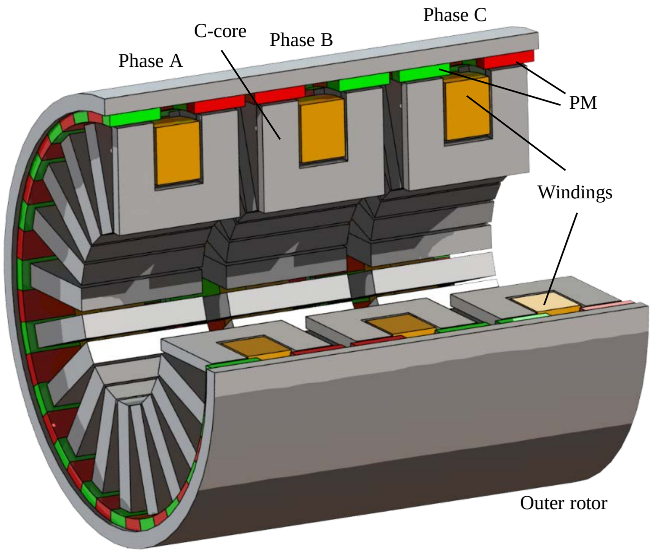

FIGURE 6.2: 3D model of the TFM topology considered for this chapter.

The outer rotor comprises a cylindrical yoke with 6 arrays of $2N_c$ heteropolar magnets each, glued to the inside surface. Each phase is associated with two arrays of magnets: one array positioned over the left-hand C-core legs and the other array, which is spatially anti-phase with the first, is positioned over the right-hand C-core legs. The three sets of magnet arrays corresponding to the three phases are spatial shifted by 120 electrical degrees (alternatively, the three sets of C-cores could be spatially shifted by 120 electrical degrees). The radial heterpolar flux harmonic interacts with the magnets to produce useful torque. The aligned position is defined as the position of the rotor in which the flux passing through the C-cores is maximum.

The key geometrical parameters of this device are shown in table 6.1, which also defines the symbols used. The value of g_z is calculated as

$$g_z = d_m + c_g. \tag{6.1}$$

The magnets' axial length is greater than the teeth's axial length because the fringing flux in the axial direction crosses the air-gap and produces additional torque (Anglada and Sharkh, 2017b). To estimate the effective active length of the C-core in the axial direction we can use results from (Markovic et al., 2005) to estimate the tooth-to-yoke permeance of the C-core head. Using this value of the permeance, the total flux in a tooth can be directly calculated. This enables the calculation of an effective axial length of a tooth, L, or model depth of an equivalent

TABLE 6.1: Symbols of the TFM

Quantity	Symbol
Stator radius	R_s
Rotor radius	R_r
Clearance gap	c_g
Magnet thickness	d_m
Magnet axial length	L_{mag}
C-core head width	l_{core}
C-core axial length	w_s
C-core height	h_s
C-core slot width	w_c
C-core slot height	h_c
Winding clearance	h_{co}
Pole pitch	θ_τ
Tooth pitch	θ_t
Slot pitch	θ_s
Number of C-cores	N_c
Number of turns	N_w
Number of phases	q
Magnetisation	$\mathcal{M}$

2 dimensional radial model of the machine. Accordingly, the effective length of a tooth, L, as defined in chapter 4 takes into account the fringing flux and is calculated as follows:

$$L \approx l_{core}\Big(1 + 0.384\frac{g_z}{l_{core}}\Big). \tag{6.2}$$

The previous expression can also be applied to estimate the value of the magnets' axial length, L_{mag}, during the design process.

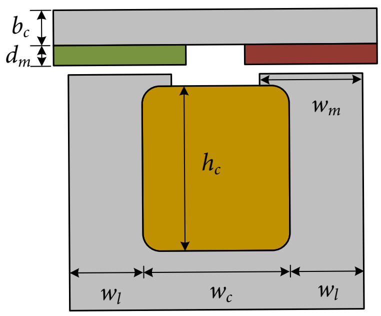

FIGURE 6.3: Dimensions of the C-core in detail.

The tidal turbine should operate over a wide range of frequencies due to the variable nature of tidal streams. Therefore, it is assumed in this chapter that the machine is driven by a fully rated power electronic converter with an active front end. This converter is back-to-back with the converter that is connected to the AC grid as shown schematically in Figure 6.4.

The control strategy of the converter is based on maximum torque scheme; which means that the current has component only in the q-axis ($i_d = 0$).

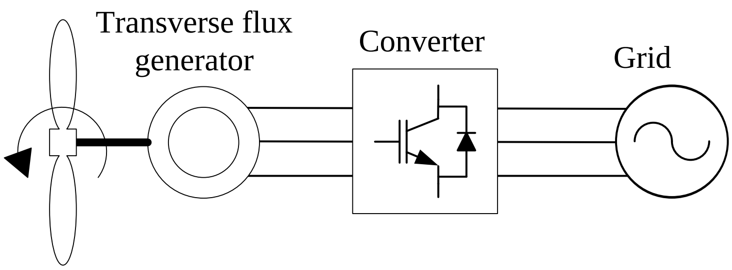

FIGURE 6.4: Topology of the tidal generation system.

An important part of this chapter is the issue of the low power factor of TFMs. This power factor refers to the side of the generator and not to the side of the grid. A low power factor of the machine would imply a converter that has to be over-rated in terms of reactive power. Therefore, improving the power factor in the machine means that the cost of the converter should be lower.

6.3 Theory

The methods to calculate torque and induced voltage are based on the idea of replacing the PMs with equivalent current sheets (Anglada and Sharkh, 2017a,b,c). The advantage of this approach is that we can obtain the torque and back emf constants by only calculating the stator's magnetic field distribution in the air-gap. This approach was described in detail in chapter 4.

The magnetic field distribution in the air-gap can be calculated analytically using a complex permeance function (Anglada and Sharkh, 2016a), which was described in chapter 3. Therefore, the magnetic field distribution in the air-gap is expressed as:

$$\vec{B}(\theta, r) = B_s \frac{R_g}{r} \Big[\overline{\lambda}_r \{ 1 + \sum_{1}^{\infty} \gamma_n(r) \cos(n\theta) \} \vec{u}_r + \sum_{1}^{\infty} \lambda_{\theta n}(r) \sin(n\theta) \vec{u}_\theta \Big], \tag{6.3}$$

where

$$B_s = \frac{\mu_{eq} \mu_0 F}{g_z}. \tag{6.4}$$

F is the MMF across the air-gap of value $F = N_w I_S/2$ and N_w is the number of turns, μ_{eq} is the equivalent permeability, which depends on the relative permeability of the PMs (μ_r) and the magnet thickness to effective air-gap ratio. It is calculated as follows

$$\mu_{eq} = \frac{\mu_r d_m + c_g}{g_z}. \tag{6.5}$$

The calculation of the coefficients of the permeance function applied to TFMs is shown in (Anglada and Sharkh, 2016a). This method was used in the current chapter to obtain the stator's magnetic field distribution in the air-gap.

6.3.1 Torque

The torque equation presented in (Anglada and Sharkh, 2017b) and in section 4.2 is based on the BiL principle. However, in this case B is the stator's magnetic field and i the equivalent current of the PMs. Therefore, the average torque per phase of a TFM can be expressed as

$$T_{ph} = k_T I_{RMS}, \tag{6.6}$$

where I_{RMS} is the stator's current and k_T is the torque constant (Hendershot and Miller, 2010) calculated as follows

$$k_T = N_w N_c \frac{4\mu_{eq}\mu_0}{\sqrt{2}} \frac{R_g L}{g_z} F_m K_B. \tag{6.7}$$

where R_g is air-gap's radius, $F_m = \mathcal{M} d_m$ is the permanent magnets' MMF and K_B is the flux factor; which is calculated as follows:

$$K_B = \overline{\lambda}_r \gamma_1^{av}. \tag{6.8}$$

6.3.2 Back emf

The flux linkage is calculated using a virtual mutual inductance approach described in section 4.4 and in (Anglada and Sharkh, 2017a). Therefore, the RMS value of the fundamental harmonic when the machine is operating in steady state at constant speed is expressed as

$$E_{RMS} = \frac{4\mu_{eq}\mu_0}{\sqrt{2}} N_w \frac{R_g L}{g_z} F_m K_B \, \omega, \tag{6.9}$$

which can be expressed using the back emf constant, k_E, (Hendershot and Miller, 2010) as

$$E_{RMS} = k_E \Omega, \tag{6.10}$$

where $\Omega = \omega / N_c$ is the mechanical speed of the rotor. This gives the following expression for the back emf constant

$$k_E = N_w N_c \frac{4\mu_{eq}\mu_0}{\sqrt{2}} \frac{R_g L}{g_z} F_m K_B. \tag{6.11}$$

6.3.3 Phase inductance

The reactance is due to the self-inductance of the coils, it can be separated into two different terms one due to the flux that crosses the air-gap, L_g, and one due to the leakage in the axial direction, L_l.

The value of L_g can be estimated using the expression of the magnetic field distribution in the air-gap to obtain the flux. For a given current i the inductance is calculated as follows

$$L_g = N_c \frac{N_w \Phi_{core}}{i}, \tag{6.12}$$

where Φ_{core} is the total flux passing through one C-core across the air-gap. The parameter $\overline{\lambda}_r$ from the complex permeance function in (6.3) can be used to obtain the total flux crossing the air-gap as follows

$$\Phi_{core} = \hat{B}\overline{\lambda}_r L \frac{2\pi R_g}{N_c}, \tag{6.13}$$

where L is the axial length and with

$$\hat{B} = \frac{\mu_{eq}\mu_0 N_w i}{2g_z}, \tag{6.14}$$

therefore, the final expression of the air-gap inductance is

$$L_g = \mu_{eq}\mu_0 N_w^2 L \frac{\pi R_g \overline{\lambda}_r}{g_z}, \tag{6.15}$$

The leakage flux in the axial direction can be estimated using the expression for the slot leakage can be found in (Say, 1965):

$$L_l = \mu_0 N_c N_w^2 l_{core}\Big(\frac{h_c - h_{co}}{3w_s} + \frac{h_{co}}{w_s}\Big), \tag{6.16}$$

where h_c is the slot depth, h_{co} is the difference between the slot depth and the coil depth, w_s the slot width, and l_{core} the C-core axial length as shown in Figure 6.3. The total reactance X is calculated as follows

$$X = \omega(L_g + L_l). \tag{6.17}$$

6.3.4 Power factor

To operate in maximum torque condition the current, I, has to be in phase with the back emf, E; this means that the current only has a q-axis component I_q. The phasor diagram is shown in Figure 6.5.

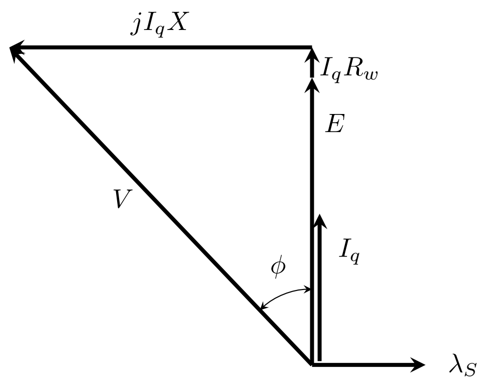

FIGURE 6.5: Phasor diagram with current only in the quadrature axis.

At high frequencies the value of X is much greater than the value of the resistance of the windings, R_w. Therefore, the angle ϕ in Figure 6.5 can be approximated as

$$\phi \approx \tan^{-1}\left(\frac{I_q X}{E}\right). \tag{6.18}$$

The value of the back emf can be calculated from the flux linkage equation shown in (6.10). Since both the back emf and the phase inductance are proportional to the frequency, the power factor at full load is independent of the frequency.

6.4 Optimisation Philosophy

The optimisation procedure presented in this chapter is based on the theory described in the previous section. The aim is to obtain a set of generic curves that can be used for the optimisation of any TFM while providing an insight into the behaviour of the system.

The flux factor, K_B, is a coefficient that measures how much of the total flux is actually producing torque (Anglada and Sharkh, 2017c). The advantage is that the flux factor depends only on the geometrical parameters of the air-gap. Therefore, it is possible to calculate the flux factor as a function of the normalised parameters of the air-gap, as shown in (6.8).

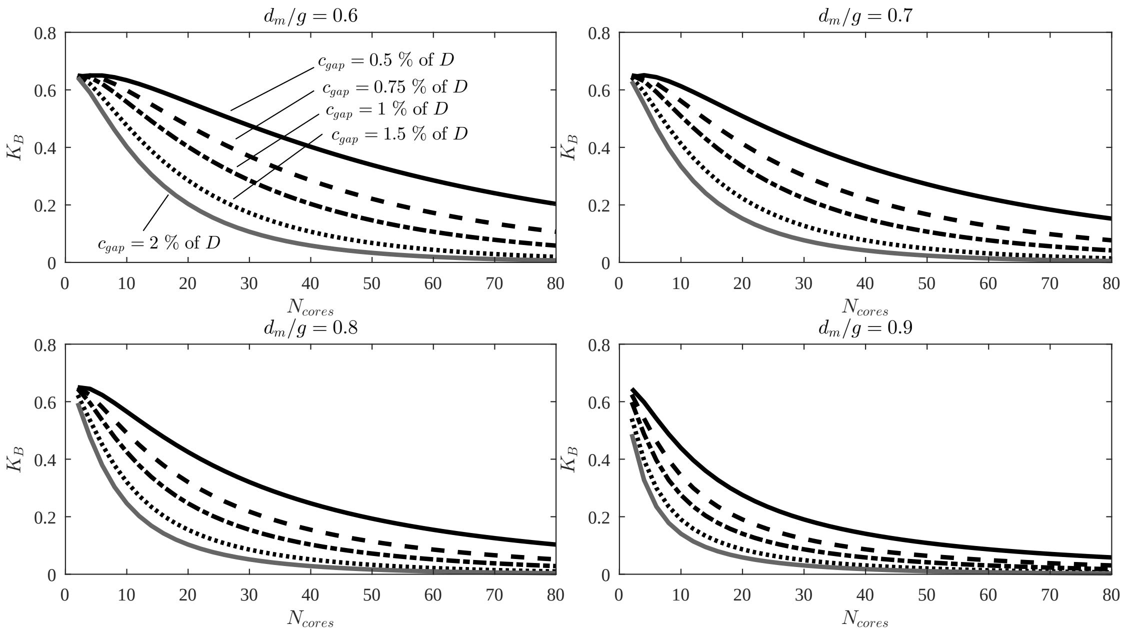

FIGURE 6.6: The flux factor, K_B, as a function of the number of C-cores for four values of d_m/g.

The flux factor was calculated for four values of the magnet thickness, d_m/g, covering most of the cases found in practice. Several curves were obtained for each value of d_m/g, each of them corresponds to a different clearance gap length. The clearance gap is expressed as a percentage of the diameter of the air-gap to make these curves as general as possible. In this case the tooth-pitch, t/τ, was kept constant as 0.3[1]; which is common in this type of machines and in the

[1]At the end of the chapter the graphs for several tooth-pitches are shown.

stepping motor design (Kenjo and Sugawara, 1995) because the optimum value of t/τ is between 0.25 and 0.4. The value of t/τ can be *tuned* at the end and it is not critical in the design process as it will be discussed later in the chapter.

Figure 6.6 shows the value of K_B obtained analytically. It can be appreciated in the four subfigures that as the number of C-cores, N_c, increases, the value of K_B is strictly decreasing. This is because if there are more C-cores they are closer together and the flux is not being used effectively as it is discussed in (Anglada and Sharkh, 2017c). However, when designing a TFM we are interested in the torque produced by the machine. Combining (6.6) and (6.7), the average torque per phase can be expressed as follows:

$$T_{ph} = I_{RMS} N_w \mathcal{M} \frac{4\mu_{eq}\mu_0}{\sqrt{2}} R_g L \frac{d_m}{g_z} N_c K_B. \tag{6.19}$$

The parameters R_g and L are the air-gap radius and the effective axial length of the C-core head. $I_{RMS}N_w$ is the electrical loading, μ_{eq} is the equivalent permeability and $\mathcal{M}$ is the magnetisation of the PMs. Equation (6.19) can be conveniently re-written as:

$$T_{ph} = I_{RMS} N_w \mathcal{M} \frac{4\mu_{eq}\mu_0}{\sqrt{2}} R_g L f_{opt}, \tag{6.20}$$

with

$$f_{opt} = \frac{d_m}{g_z} N_c K_B. \tag{6.21}$$

The function f_{opt} depends only on the geometrical parameters of the air-gap, which can be normalised to obtain a set of generic curves similar to those shown in Figure 6.6 for the flux factor. Assuming that the diameter, the axial length and the electric loading are fixed, the value of f_{opt} will determine the torque as a function of the number of C-cores. Therefore, f_{opt} can be used for the optimisation of torque.

The value of f_{opt} was calculated for the same range of the normalised parameters as the flux factor; the results are shown in Figure 6.7. All curves shown in Figure 6.7 follow the same trend: at the beginning as the number of C-cores increases there is a substantial increase in the value of f_{opt} until a maximum value is reached, this is the maximum torque design. After this point the value of f_{opt} is strictly decreasing. This behaviour can be easily understood by studying (6.21) in detail. As the number of C-cores increases the value of the flux factor, K_B, decreases. However, at the beginning this effect is compensated because f_{opt} is proportional to the product of K_B and N_c. The maximum torque design corresponds to the point in which the improvement in torque for each additional C-core is compensated by the decrease of the value of K_B.

The generic curves of f_{opt} as a function of the normalised parameters can be used to optimise a TFM for each particular case maximising the torque produced. However, the torque and power factor are very closely related and in simple terms a flux factor, K_B, implies a low power factor (Anglada and Sharkh, 2017c). Therefore, it is important to have a happy compromise between the torque and the power factor. This issue is addressed in section 6.5.

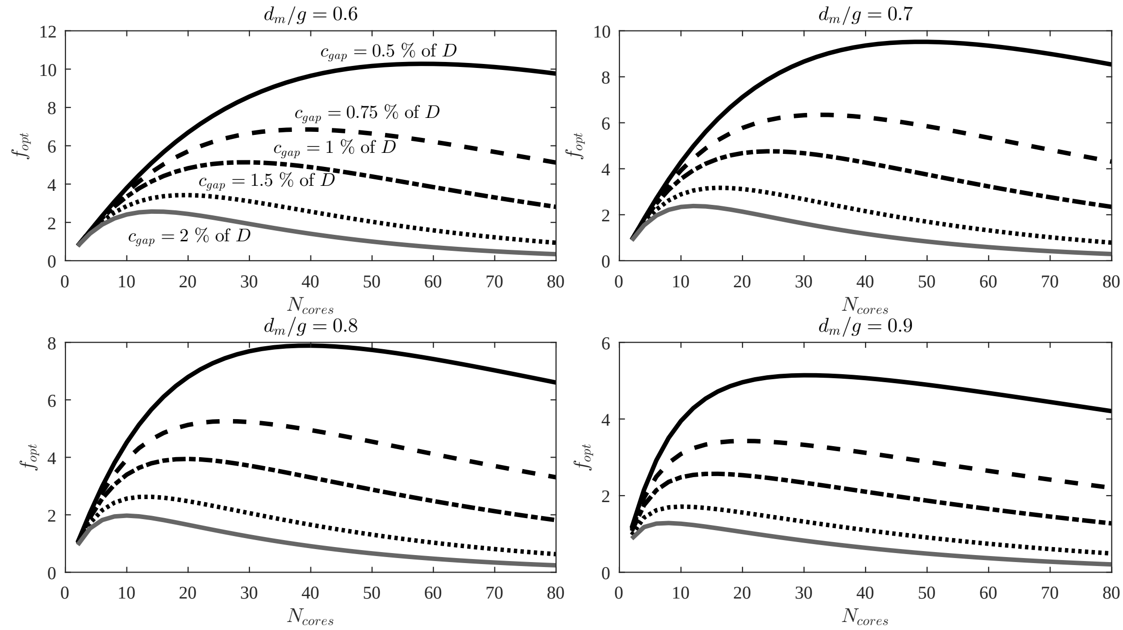

FIGURE 6.7: The torque optimisation function, f_{opt}, as a function of the number of C-cores for four values of d_m/g.

6.4.1 Optimisation of the C-core shape

Once the number of C-cores is chosen the next step is to dimension the C-core itself. For a given clearance gap and magnet thickness, the space available is a rectangle of width w_s and height h_s as shown in Figure 6.3. Based on the BiL principle described in section 6.3.1, it can be deduced that the torque is proportional to the stators magnetic field and the axial length (which is directly related to the C-core head length, w_m). Therefore, the torque is expressed as follows

$$T \propto B_s w_m, \tag{6.22}$$

where B_s is calculated according to (6.4). The dimensions are chosen for the maximum load conditions. Therefore, the maximum MMF is calculated as follows:

$$F = \frac{1}{2} w_c h_c J_{max} S_{fg}, \tag{6.23}$$

where w_c and h_c are the width and height of the windings slot as shown in Figure 6.3, respectively. J_{max} is the maximum current density and S_{fg} is the slot-fill factor. The values of w_c and h_c are constrained by the size of the C-core *window*. These constraints are expressed as follows:

$$h_s = h_t + h_c + h_b, \tag{6.24}$$

$$w_s = w_c + 2w_l. \tag{6.25}$$

Normally, the back of the C-core is slightly thicker than the legs because of the slot leakage flux. Therefore, it is reasonable to say that $h_b = k_l w_l$, with k_l = 1-1.2 normally[2].

[2]Section 6.4.1.1 comments on this topic and the C-core shape in general.

Based on the following equations we can define a function, f_{core}, which is proportional to torque:

$$f_{core} = (w_s - 2w_l)(h_s - h_t - h_b)w_m. \tag{6.26}$$

The optimum dimensions of the C-core are given after maximising f_{core} subject to the following constraints:

$$w_m \leq k_m w_l, \text{ with } k_m = \text{1-1.2}, \tag{6.27}$$

$$w_l \leq w_m, \tag{6.28}$$

$$B_{cm} + B_{cs} \leq B_{c-max}, \tag{6.29}$$

where B_{cm} and B_{cs} are the maximum values of the magnetic field in the C-core leg, which are calculated as follows:

$$B_{cm} = B_{PM} \frac{d_m}{g_z} \frac{w_m}{w_l} \left(1 + 0.384 \frac{g_z}{w_m}\right) k_t, \tag{6.30}$$

where B_{PM} is the remanent field of the PM. The term $(1 + 0.384 g_z/w_m)$ is to consider the flux from the overhang of the PMs in the axial direction and the term $1 \leq k_t$ to consider the the overhang of the PMs in the radial direction (this is because normally $t < \tau/2$, therefore there is *additional flux* from the PMs). It is important to point out that this is a preliminary design of the C-core shape that later has to be refined using more detailed models.

On the other hand,

$$B_{cs} = B_s \frac{w_m}{w_l}. \tag{6.31}$$

The value of B_{c-max} is based on the properties of the material and the level of saturation at full load that is tolerated in the design.

6.4.1.1 Some remarks about the C-core shape

The previous section showed how to optimise the C-core shape based on the current density and MMF of the PMs. Two coefficients were introduced in the process to consider that the back of the C-core should be slightly thicker than the legs and to limit the tooth-tips.

The coefficient k_l is introduced to make sure that the back of the C-core is thicker than the C-core legs. The back should be thicker because there is some slot leakage flux; therefore, the total flux in the back is higher. The coefficient k_l should be estimated based on this leakage flux to make sure that the saturation in the back iron is within reasonable limits.

On the other hand, the coefficient k_m limits the tooth-tips. For example, $k_m = 1$ means no tooth-tips at all, $k_m = 1.1$ means that the tooth-tips should not exceed by 10 % the C-core leg and so forth. The tooth-tips are interesting because they can help to improve the torque capability of the TFM. However, they can complicate the winding process; which can be an issue because one of the advantages of this TFM is the simplicity of the winding. Furthermore, the tooth-tip shape has to be designed to avoid saturation.

Finally, in general terms it is important to have a trade-off between the total MMF from the stator and the slot-leakage flux. For example, if the slots are deep and narrow the leakage flux can reduce the power factor (L_l increases). As a general rule of thumb it can be said that if the winding window is close to a square ($w_s \approx h_s$) the slot leakage will not be significant.

6.4.2 Losses

In addition to the frictional losses in the shaft's bearings there are losses in the C-cores (due to eddy currents and hysteresis), eddy currents in the rotor (in the PMs and in the rotor hub) and copper losses in the stator windings. The rotor losses due to eddy currents were calculated in chapter 5 and these results can be directly applied to this case. The copper losses can be directly calculated using Joule's Law, I^2R, once the current and the winding geometry are known. Therefore, in this section we are going to deal with the core losses in the C-cores.

The C-cores are made of laminated magnetic steel in a very similar way of a transformer. Accordingly, the core loss per unit mass can be obtained using Steinmetz's equation (Hendershot and Miller, 2010). Thus, the core losses are:

$$W_c = C_h f \hat{B}^n + C_e f^2 \hat{B}^2; \text{ in W/kg,} \tag{6.32}$$

where f is the frequency and $\hat{B}$ is the peak value of the magnetic field; which in this case is the same as B_{c-max} from the previous section. The coefficients C_h, C_e and the exponent n depend on the properties of the material. The first term in (6.32) is related to the hysteresis losses and the second one to the eddy current losses.

The values of the coefficients can be obtained from a set of curves of core-loss vs. frequency. This curve can be provided by the supplier of the material or obtained in the lab experimentally. A comprehensive study about this topic is presented in (Ionel et al., 2007). For the following analysis it is assumed that the material has been fully characterised.

6.5 Work-flow of the Process

It has been pointed out earlier that if the design is done only to maximise torque it will yield a low power factor because of the ineffective use of the magnetic flux, or what is the same: the low flux factor. Therefore, it is important to have a trade-off between torque density and power factor. This can be achieved by combining Figure 6.7 with simple iterative process. Figure 6.8 shows the work-flow of this process. This work-flow is done for a particular t/τ but including this variable to the optimisation process is straight-forward.

These are the steps of the design process:

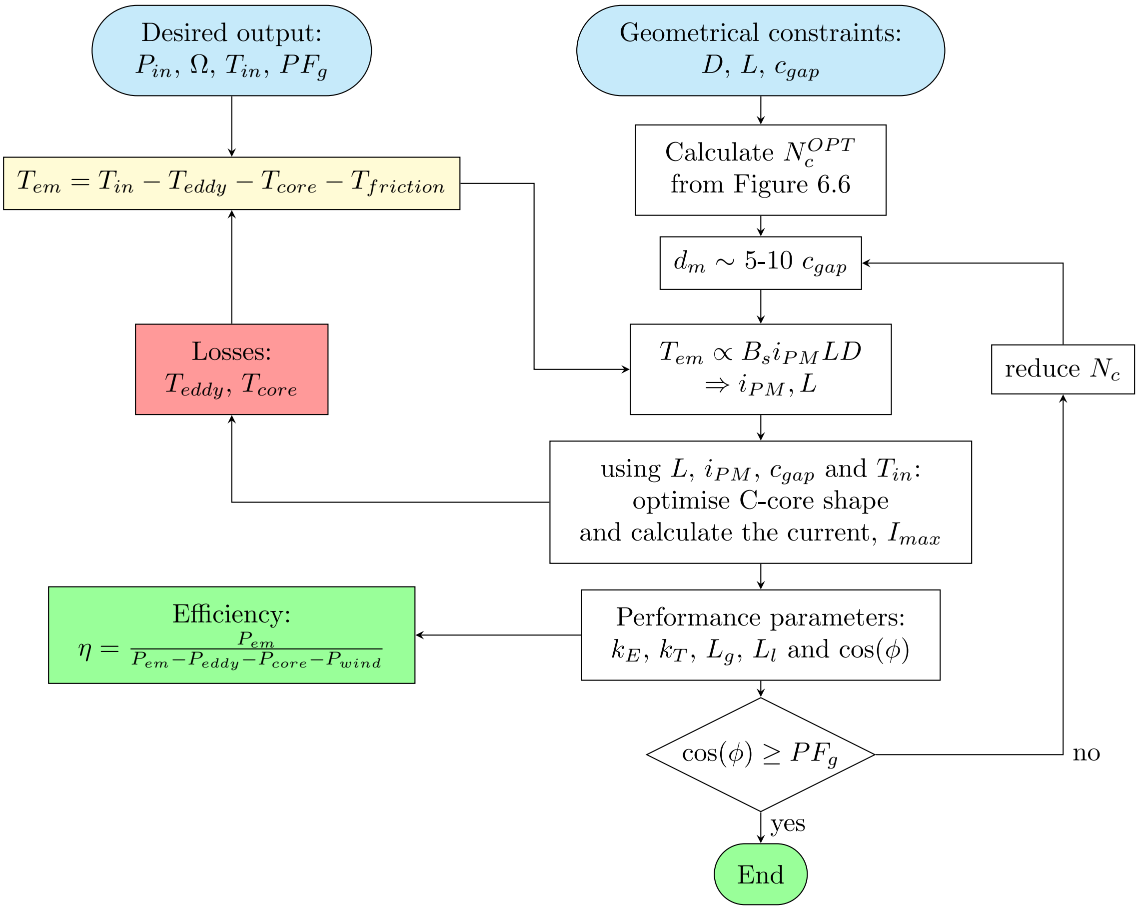

FIGURE 6.8: Simplified work-flow of the design optimisation process proposed.

1. Identify the desired output of the machines (P_{in}, Ω, T_{in} and the power factor at full load PF_g) and the geometrical constraints (D, L and c_{gap}).

2. Calculate the number of C-cores that maximises torque for the given clearance gap, c_{gap}. Normally the minimum clearance gap is related to mechanical constraints and it is common to express it as a percentage of the diameter.

3. Estimate the magnet thickness. Typical values of the magnet thickness are 5 to 10 times the clearance gap. The important point here is to make sure that the PM won't demagnetise.

4. Based on the torque required, the MMF of the PMs (i_{PM}) and the clearance gap obtain the C-core shape based on section 6.4.1.

5. Calculate the performance parameters such as torque constant, back emf constant, phase inductance, power factor at full load and losses. At this point the efficiency can be calculated.

6. Iterate with using the torque due to losses to make sure that the output torque meets the specification.

7. Check if the power factor at full load is within the acceptable levels. If the power factor is too low, then reduce N_c and repeat the optimisation process.

8. Iterate until the desired value of the power factor is achieved.

6.6 Case Study

The aim of this section is to illustrate how to design a TFM for a particular application. In this case study the machine is designed to suit a tidal turbine that was designed and built at the University of Southampton, also described in chapter 1. The design specifications are shown in table 6.2. These constraints are based on the current radial PM machine that was actually built.

TABLE 6.2: Design specifications

Quantity	Symbol	Value
Rated power	P_{em}	10 kW
Rated speed	n_{rpm}	150 rpm
Rated torque	T	670 Nm
Outer diameter	D_{out}	450 mm
Axial length	L_{max}	160 mm
Clearance gap	c_{gap}	2 mm
Current density	J_{max}	10 A/mm^2

To simplify the design process it was assumed that $d_m/g = 0.8$ and $t/\tau = 0.3$. These two parameters are important but they can be included in the design process later.

Two designs are going to be studied in this section. The so-called Machine A is done by only maximising torque and Machine B was designed including the iterative loop to correct the power factor as shown in Figure 6.8.

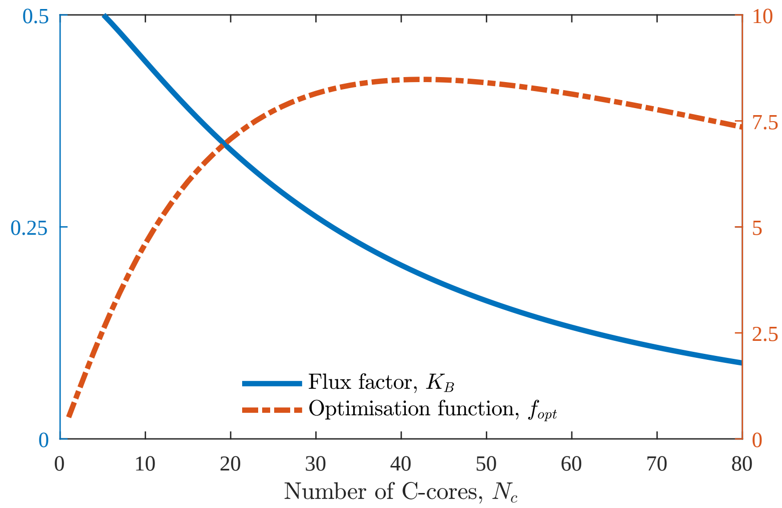

FIGURE 6.9: Flux factor, K_B, and optimisation function, f_{opt}, for the tidal turbine under study.

Figure 6.9 shows the flux factor, K_B, with the axis in the left side of the graph and the optimisation function, f_{opt}, with the axis in the right side of the graph. It can be appreciated that the maximum value of f_{opt} corresponds to $N_c = 42$ C-cores. This means that Machine A has 42 C-cores (or pole pairs).

$$f_{opt}|_{\mathrm{A}} \approx 8.478. \tag{6.33}$$

However, the value of the flux factor for $N_c = 42$ is very low:

$$K_B|_{\mathrm{A}} \approx 0.1954. \tag{6.34}$$

A low flux factor suggests a low power factor as it was pointed out in chapter 4. The power factor of machine A at full load is calculated as follows

$$\cos(\phi_{\mathrm{A}}) \approx 0.345. \tag{6.35}$$

Machine B is designed to have $N_c = 30$ C-cores, for example. Therefore, the values of the optimisation function and the flux factor are the following:

$$f_{opt}|_{\mathrm{B}} \approx 8.147, \tag{6.36}$$

$$K_B|_{\mathrm{B}} \approx 0.262. \tag{6.37}$$

Finally, the power factor of machine B is:

$$\cos(\phi_{\mathrm{B}}) \approx 0.456. \tag{6.38}$$

It can be appreciated that reducing the value of f_{opt} by a 3.9 % means an improvement of 34.10 % in terms of flux factor. Machine B has a power factor at full load that is around 32.17 % higher than machine A[3].

TABLE 6.3: Parameters of the Machines

Machine		A	B
Rated speed	n_{rpm}	150 rpm	150 rpm
Rated torque	T_{em}	670 Nm	670 Nm
Number of C-cores	N_c	42	30
Stator radius	R_s	205 mm	205 mm
Core-back radius	R_r	215 mm	215 mm
Clearance gap	c_g	2 mm	2 mm
Magnet thickness	d_m	8 mm	8 mm
Magnet axial length	L_{mag}	17 mm	17.2 mm
C-core head width	l_{core}	13.00 mm	13.25 mm
C-core axial length	w_s	46.23 mm	46.98 mm
C-core height	h_s	46.23 mm	46.98 mm
C-core slot width	w_c	20.24 mm	20.47 mm
C-core slot height	h_c	31.93 mm	32.40 mm
Total mass	M	29.90 kg	30.75 kg
Total cost[4](euro)	C	447.02	457.25

[3]All the values in percentage were calculated as follows:

$$\Delta K \text{ in } \% = \left|\frac{K_A - K_B}{K_A}\right| \times 100.$$

[4]Cost of materials:
Neodymium magnets: 45 euro/kg
Copper: 12.4 euro/kg
Magnetic steel: 3.5 euro/kg

The geometrical parameters of machine A and B are shown in table 6.3. It can be appreciated that the geometrical parameters are similar in value with the exception of the number of C-cores. The dimensions of the C-cores of machine B are slightly larger to compensate for the lower value of f_{opt}. Both machines were designed to be able to achieve the rated torque (~ 670 Nm), therefore machine B is slightly heavier and the specific torque is lower.

Table 6.4: Performance Comparison

Machine		A	B
Rated power	P_n	10.5 kW	10.1 kW
Electrical frequency	f	105 Hz	75 Hz
Rated current	I_n	16.16 A	16.58 A
Rated voltage	V	627.17 V	462.56 V
Back emf	E	216.56 V	210.74 V
Number of turns	N_w	200	200
Apparent power	S_n	30.40 kVA	23.00 kVA
Power factor	$\cos(\phi)$	0.345	0.456
Flux factor	K_B	0.1954	0.262
Specific torque	T_M	22.35 Nm/kg	21.70 Nm/kg
Specific torque	T_C	1.499 Nm/euro	1.466 Nm/euro

Table 6.4 shows the performance parameters of machine A and B. It can be appreciated that the power factor at full load of machine A is much lower than machine B making the apparent power, S_n, of machine A considerably higher (30.40 kVA compared to 23.00 kVA). Machine B has a lower specific torque in terms of Nm/kg and Nm/euro because it is slightly larger. However, the penalty in terms of specific torque is small (22.35 Nm/kg compared to 21.70 Nm/kg) compared to the improvement in power factor (0.345 compared to 0.456).

Table 6.5 shows the characteristics of several motors used in the automotive industry (Popescu et al., 2015). It can be appreciated that the specific torque (in terms of Nm/kg) of the TFM designed in this section is higher than any of the machines shown in table 6.5. It is important to note that all the machines shown in table 6.5 are liquid cooled and that it is important to consider the cooling method (and current density of the windings) to do a more detailed comparison.

Table 6.5: Some examples from the automotive industry, data from (Popescu et al., 2015)

Motor	motor type	rated torque [Nm]	total mass [kg]	T_M [Nm/kg]
YASA 400	axial PM	360	24	15
Tesla S	induction	430	90	4.77
Nissan Leaf	interior PM	300	46	6.52
Toyota Prius 2004	interior PM	400	51	7.84

In summary, this section shows two TFMs that could be used as a direct drive generator for a given tidal turbine. One was designed by maximising the torque and it results in a machine with a very low power factor. On the other hand, machine B considers that by reducing slightly the specific torque (by reducing the number of C-cores) there is a significant improvement in terms of power factor. These machines are just an example but they illustrate the design trade-offs when dealing with TFMs.

6.7 Summary

This chapter presents the design optimisation process of a TFM for tidal power generation. The electrical generator was designed to suit a particular tidal turbine developed at the University of Southampton.

The optimisation procedure uses the theory developed in chapters 3, 4 and 5. The proposed methodology is based on two sets of graphs, the flux factor K_B and the optimisation function f_{opt}, which were obtained as a function of the number of C-cores. Therefore, with these two sets of graphs a preliminary design can be obtained without incurring in a long iterative process.

The case study emphasises the strong relationship between torque and power factor. It is shown that a machine that is designed directly maximising torque will have a low power factor. To solve this issue a correction loop in the work-flow has been introduced.

The comparison between machine A and machine B in section 6.6 illustrates how to deal with the torque-power factor trade-offs.

Optimisation Graphs

Figures 6.10 to 6.13 show the optimisation graphs for several values d_m/g and t/τ. The aim is to show an example of a small database that could be used to do a more detailed optimisation of this particular TFM topology.

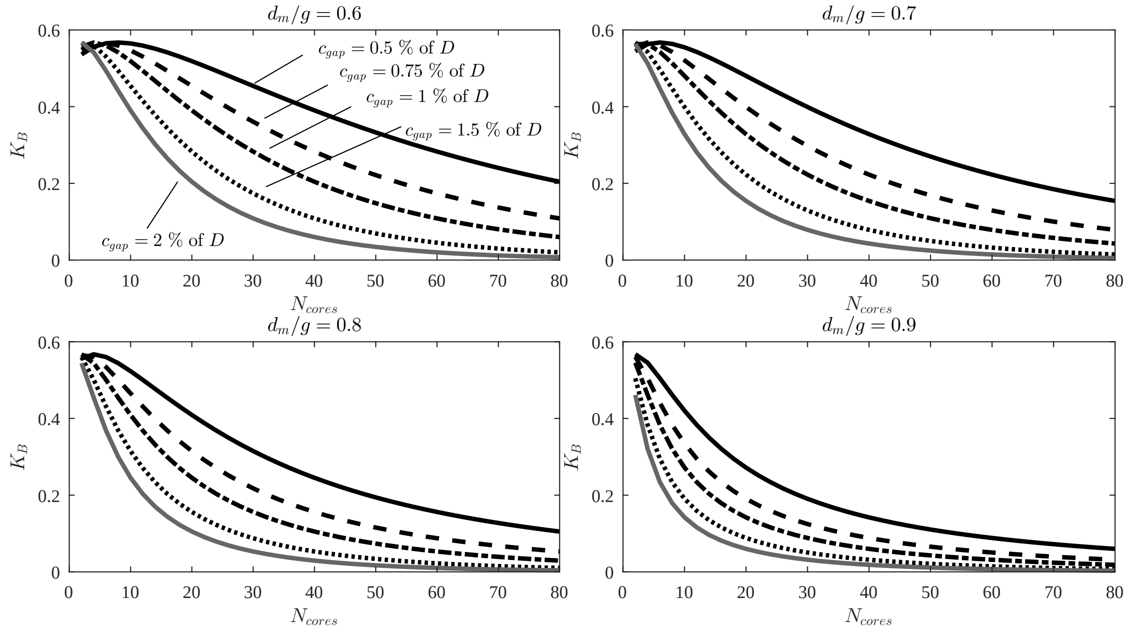

(a) Flux factor, K_B.

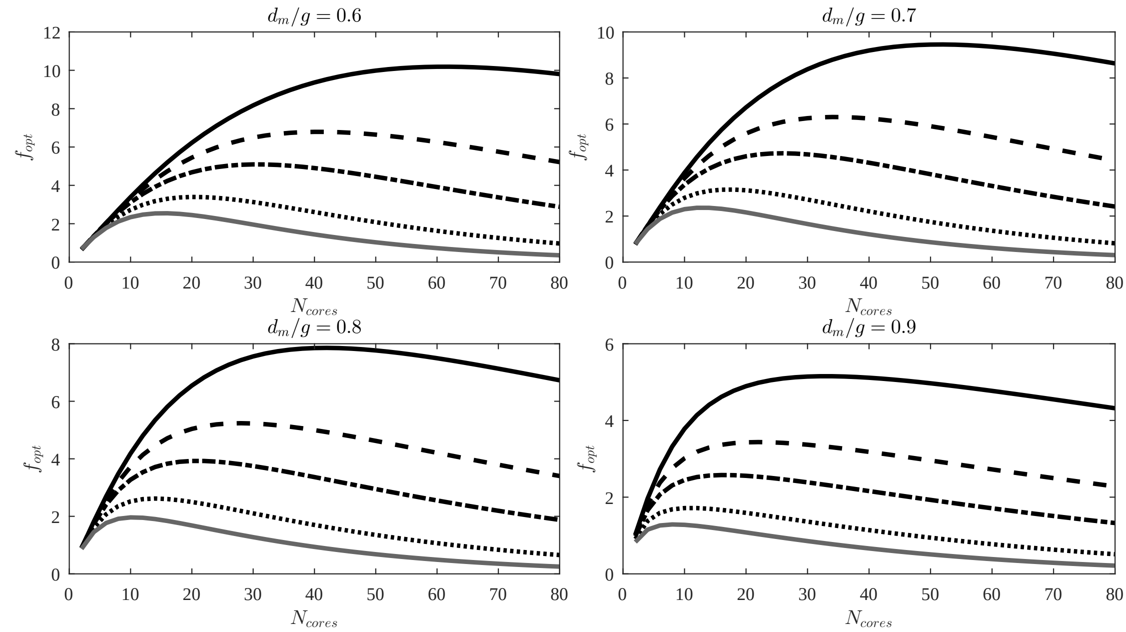

(b) Torque optimisation function, f_{opt}.

FIGURE 6.10: The flux factor, K_B, and the torque optimisation function as a function of the number of C-cores for four values of d_m/g for $t/\tau = 0.25$.

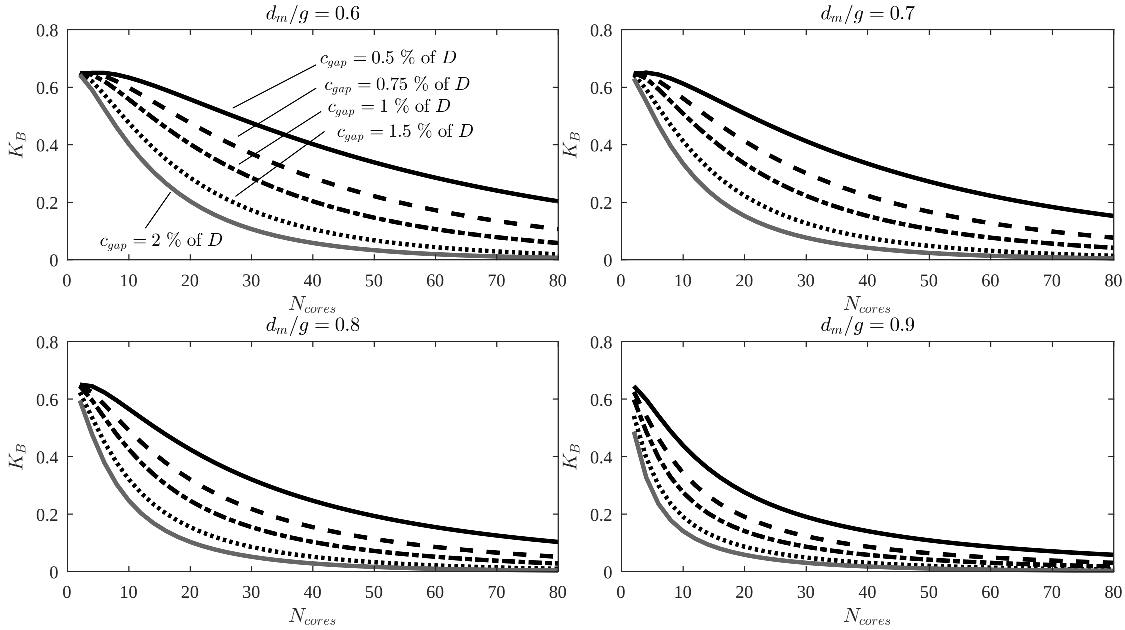

(a) Flux factor, K_B.

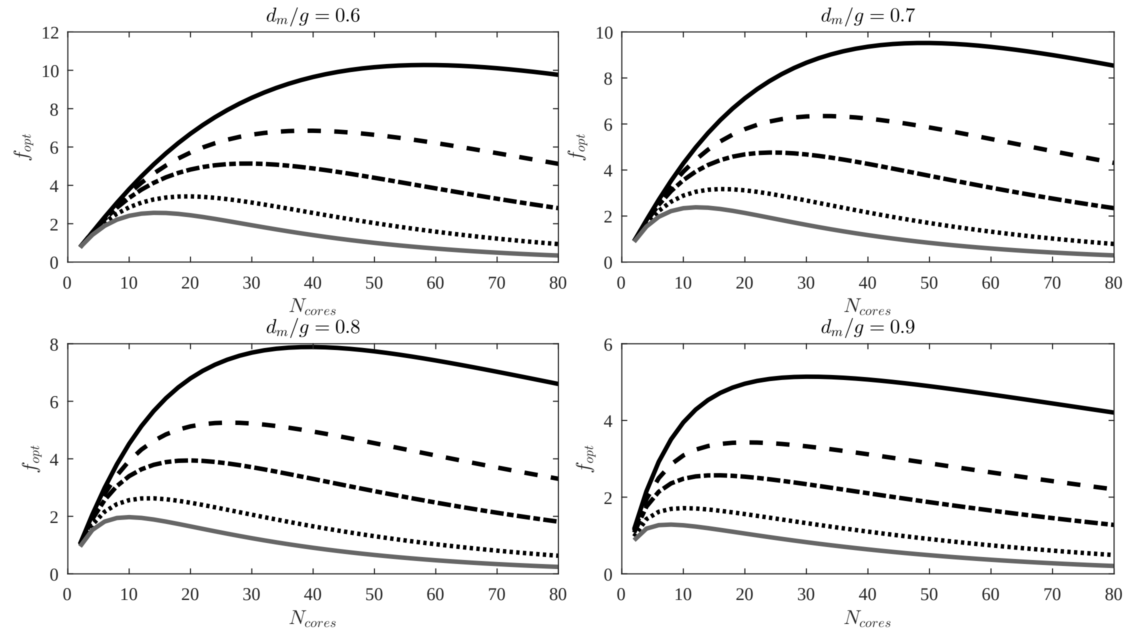

(b) Torque optimisation function, f_{opt}.

FIGURE 6.11: The flux factor, K_B, and the torque optimisation function as a function of the number of C-cores for four values of d_m/g for $t/\tau = 0.3$.

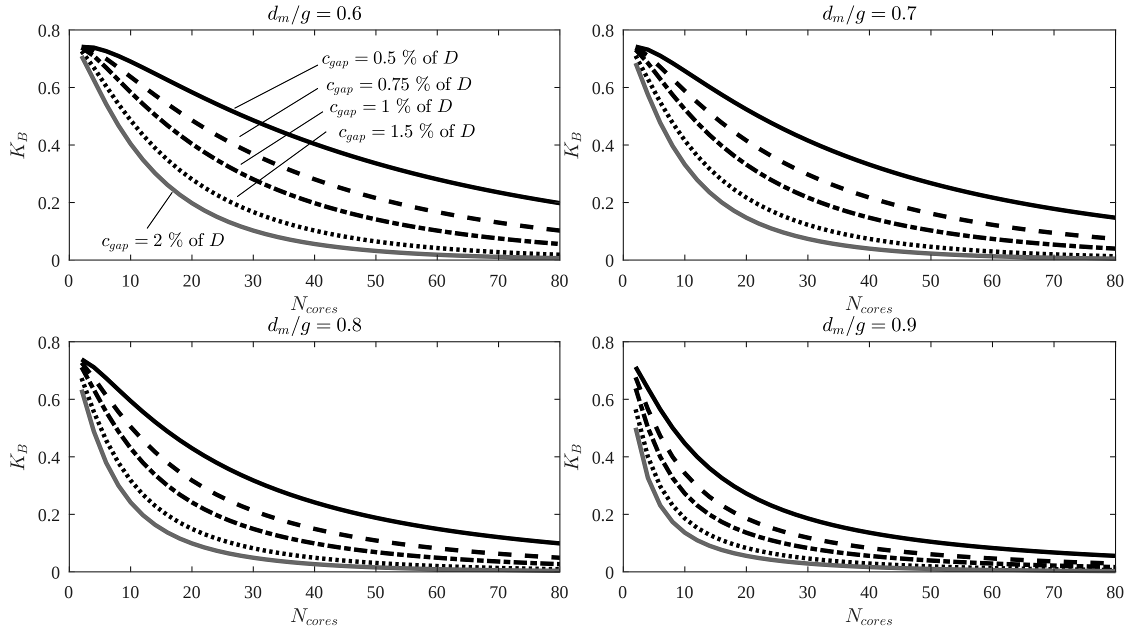

(a) Flux factor, K_B.

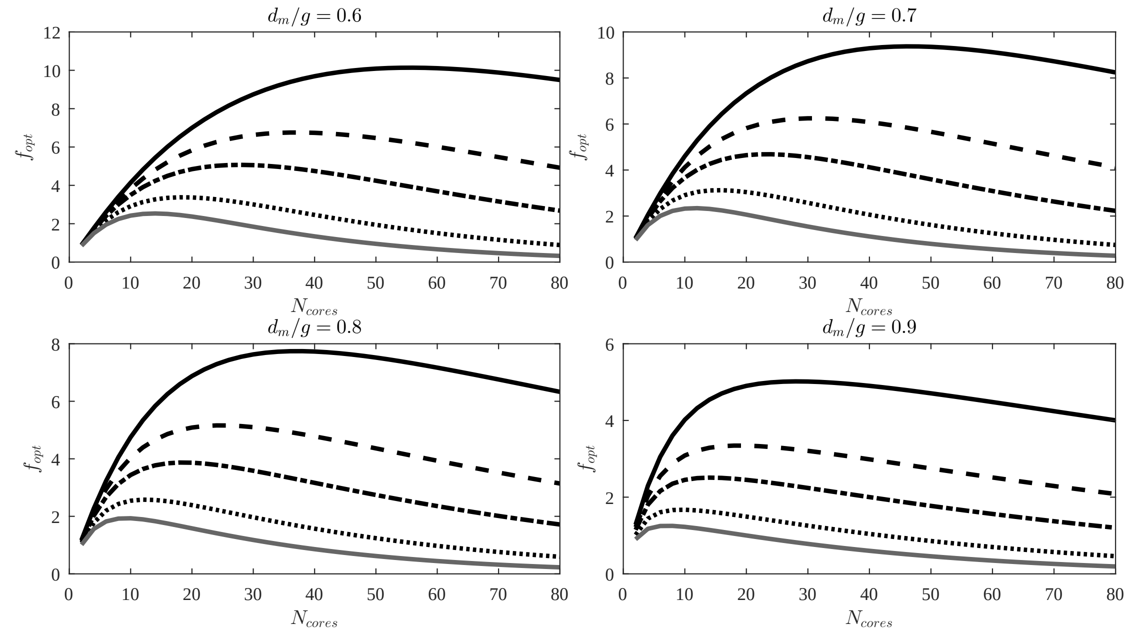

(b) Torque optimisation function, f_{opt}.

FIGURE 6.12: The flux factor, K_B, and the torque optimisation function as a function of the number of C-cores for four values of d_m/g for $t/\tau = 0.35$.

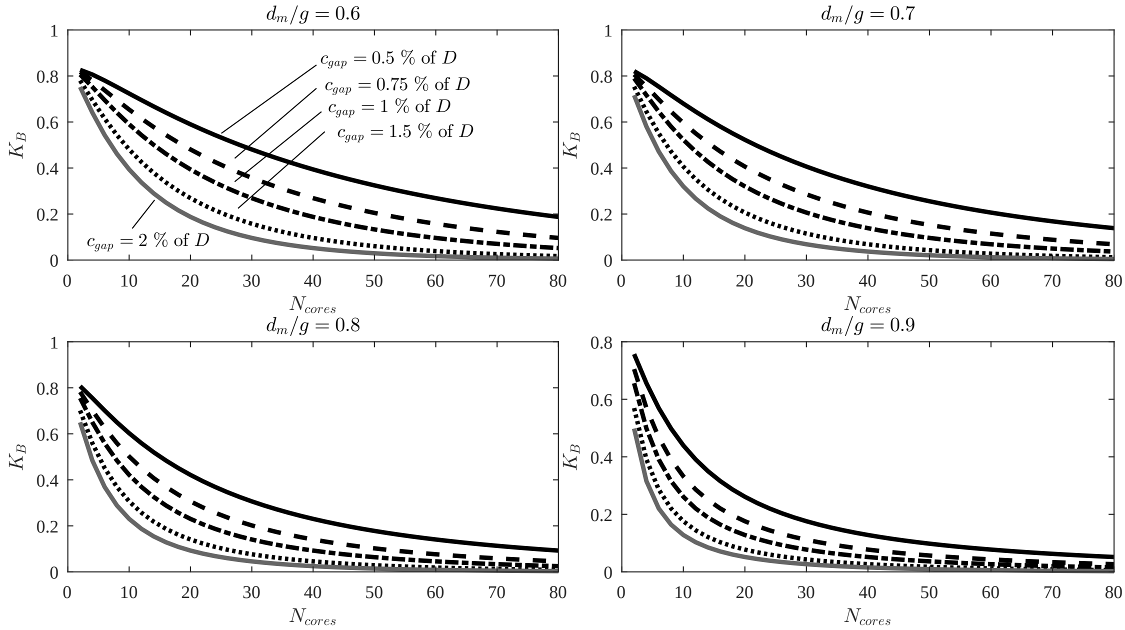

(a) Flux factor, K_B.

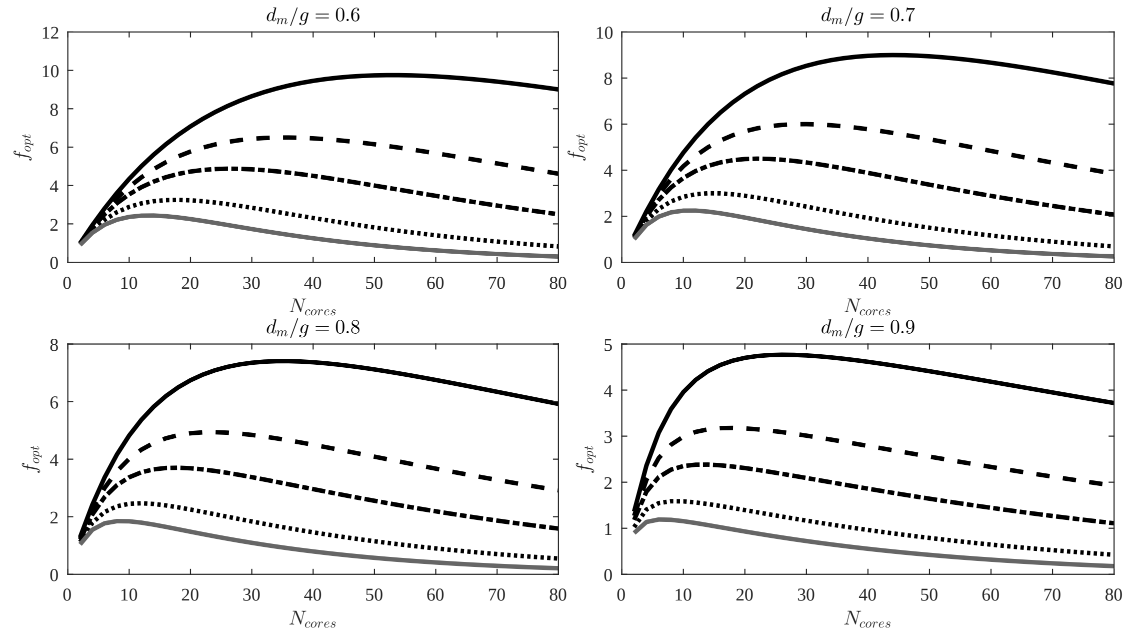

(b) Torque optimisation function, f_{opt}.

FIGURE 6.13: The flux factor, K_B, and the torque optimisation function as a function of the number of C-cores for four values of d_m/g for $t/\tau = 0.4$.

Chapter 7

Conclusions and Future Work

The novel contributions presented in this Thesis can be summarised as follows:

- The complex permeance framework has been formulated in such a way that it can be used for the analysis of transverse flux machines. Furthermore, an algorithm for the efficient calculation of the coefficients of the harmonics of the permeance function has been successfully developed.
- A generalisation of Harris *et al.*'s torque equation has been carried out. The torque equation developed effectively takes into account the fact that the force is distributed all through the magnet thickness, the effect of curvature, any shape of the mmf waveform and the phase advance angle.
- A novel methodology for the calculation of flux linkage in permanent magnet machines, i.e. the virtual mutual inductance approach, has been proposed and validated in this Thesis.
- The relationship between torque and power factor has been studied using the torque equation and the virtual mutual inductance approach showing that they are closely interlinked.
- The current sheet model has been reformulated using transfer matrices for the calculation of eddy current power losses in cylindrical geometries reducing the complexity of the problem.
- All the previous methodologies have been applied in a case study, which is the design of a transverse flux generator for a tidal turbine.

7.1 Conclusions

The aim of this work, in broad terms, has been to develop fundamental theory suitable for modelling of transverse flux machines. The theories developed are general, but they are particularly tailored for the analysis of transverse flux machines.

Firstly, the complex permeance framework was adapted for the case of TFMs using a scalar potential formulation. It was successfully implemented in Matlab using a proportional logarithmic transformation to account for curvature and the Schwarz-Christoffel Toolbox to account for slotting. The curvature coefficient defined in section 3.4 tells us when the effect of curvature is going to be significant. In simple terms, it was deduced that when the length of the magnetic gap is large compared with the air-gap radius (the ratio R_g/g_z) the effect of curvature is strong[1]. As a *rule of thumb* could be said that when the ratio R_g/g_z is below 6 the effect of curvature will be significant. In a similar way, a criterion to choose between the single-slot and multiple-slots models was obtained using the mathematical properties of the conformal transformation.

The results show that the complex permeance framework combined with the algorithm proposed for the estimation of the coefficients of the harmonics provide accurate results in unsaturated load conditions. An algorithm for the estimation of the coefficients of the complex permeance function has been deduced. This algorithm allows us to obtain the permeance function in all the air-gap evaluating the function in a limited number of points, therefore reducing the computational time. It has been demonstrated that if the set of points is generated randomly, the robustness of the algorithm improves significantly.

The torque equation proposed by Harris *et al.* is particularly useful because it relates the torque produced by a machine to its magnetic and electric loadings. However, in Harris *et al.*'s approach the permanent magnets are assumed to be current points at the rotor hub and the amplitude of the flux density harmonics was obtained from lookup tables. The generalization of the torque equation presented in this Thesis uses the complex permeance framework to obtain the magnetic field distribution in the air-gap and the force is integrated all through the magnet thickness. Furthermore, the formulation allows for the calculation of the flux factor, K_B, for any kind of mmf waveform and any phase advance angle. For the particular case study presented in chapter 4 it is shown that the flux factor calculated considering the magnets as current points is $K_B = 0.275$ while the value obtained using the proposed methodology is $K_B = 0.311$.

The virtual mutual inductance approach is based on the fact that if the permanent magnets can be replaced with equivalent current sheets, then there is a mutual inductance between these equivalent currents and the stator windings. This virtual mutual inductance can be easily calculated using the complex permeance function. Therefore, based on the reciprocity theorem ($\mathfrak{M}_{12} = \mathfrak{M}_{21}$) we can readily obtain the flux linking with the stator windings due to the permanent magnets. The analytical results have been validated using 3D FEA and experimental data for the transverse flux machine under study. Therefore, the virtual mutual inductance approach can be used for the design optimisation of transverse flux machines.

The torque equation and the virtual mutual inductance approach have been used to study the design optimisation process of transverse flux machines with special interest in the relationship between torque and power factor. This Thesis shows that if the design of a transverse flux machine is done only to maximise torque, then the power factor will tend to be low. Therefore, it is important to have a trade-off between torque and power factor particularly because small improvements of torque can produce strong penalties in terms of power factor. Furthermore, it has been demonstrated that the low power factor of these machines is not due to leakage in the classical way but due to the nature of the electromagnetic interaction that takes place.

The current sheet model has been reformulated using transfer matrices. The proposed approach reduces the mathematical complexity particularly as the number of layers increases because

[1] This effect is particularly important for the calculation of rotor losses in machines with large effective gaps such as high speed machines with retaining sleeves.

instead of solving a large linear system of equations it is necessary to invert a matrix of order 2. Therefore, the proposed methodology could be used to study machines with any number of layers, in principle. Furthermore, to reduce even more the complexity of the problem we have obtained the transfer matrices for thin layers (which can be considered rectangular regions) to avoid having to deal with Bessel functions. This could facilitate the implementation of the proposed methodology in pure programming languages such as Python or C. Special care has to be taken when applying the current sheet model to machines that are short axially, which is the case of TFMs. Therefore, a coefficient has been used to account for the 3D effects.

The case study, the optimisation of a transverse flux generator for tidal power generation, illustrates how to deal with the relationship between torque and power factor. The machine that was designed only maximising torque has a very low power factor (and an over-rated power converter hypothetically) while the other machine (with the power factor correction loop) has a slightly lower specific torque but a much higher power factor. Therefore, understanding this relationship is essential to achieve a good design.

7.2 Future Work

Some of the work done in this Thesis requires further work to reach it's full potential. The author of this Thesis believes that there are interesting research lines based on some *preliminary ideas* presented in this Thesis.

Firstly, it was discussed in section 3.6.2 that random sampling improves the reliability of the algorithm developed for the estimation of the coefficients of the complex permeance function. This can be understood intuitively because the variable *spacing* of the samples prevents from not picking up a harmonic with a wavelength similar in length. However, a more *formal* derivation of a proof of this would be necessary. Furthermore, a similar philosophy could be used for signal processing and it would be interesting to determine if a random sampling scheme is practical.

The torque equation and the virtual mutual inductance approach have been used to analyse particular transverse flux machines in this Thesis. However, both principles are completely general and are valid for any kind of permanent magnet machine. Therefore, it would be interesting to use these equations to study radial permanent magnet machines, magnetic actuators, other kinds of transverse flux machines, etc... The author believes that the torque equation could be particularly useful for the study of magnetic gears. Currently, most of the publications dealing with magnetic gears use directly FEA for the analysis and optimisation. Therefore, a torque equation for magnetic gears analogous to that presented in chapter 4 could provide an insight into the behaviour of these devices.

The main advantage of the formulation of the current sheet model for the calculation of eddy current losses presented in chapter 5 is that topologies with many layers can be studied without increasing the complexity of the problem in a significant way. This fact is particularly important for the case of high speed machines with conducting sleeves because the eddy currents in the sleeve could be readily calculated. Furthermore, a more detailed analysis of the transfer matrices and its properties could provide a better insight into the *energy flows* which could help to better understand the loss mechanisms and how to reduce them.

The current sheet model has been used successfully to calculate the losses for each harmonic (with a given time and space order). However, it cannot model the losses produced by the homopolar field components. Hence, it is necessary to develop some new ideas to deal with this limitation.

Some validation studies were presented in chapter 5. However, it would be interesting to perform a deeper analysis using 3D FEA to study the eddy currents in the rotor. Furthermore, it is necessary to study the accuracy and validity of Russell and Northsworthy's coefficient for many different cases.

Finally, in chapter 6 a simple design optimisation of a generator was presented. This approach could be used to optimise a real machine considering all the aspects of the design process, including the manufacture of a prototype.

References

Ahmed, N., Washington, J., Atkinson, G. J., and Baker, N. J. (2014). Reduction of cogging torque and torque ripple in modulated pole machines by geometrical changes. In *Power Electronics, Machines and Drives (PEMD 2014), 7th IET International Conference on*, pages 1–6.

Alger, P. L. and Arnold, R. E. (1976). The history of induction motors in america. *Proceedings of the IEEE*, 64(9):1380–1383.

Allan, G. J., Lecca, P., Mcgregor, P. G., and Swales, J. K. (2014). The economic impacts of marine energy developments: A case study from Scotland. *Marine Policy*, 43:122–131.

Alstom (2017). Alstom (now GE Renewable Energy). `https://www.gerenewableenergy.com/innovative-solutions/tidal-energy.html` [Accessed: 28/05/2017].

Amrhein, M. and Krein, P. T. (2009a). 3-D Magnetic equivalent circuit framework for modeling electromechanical devices. *IEEE Transactions on Energy Conversion*, 24(2):397–405.

Amrhein, M. and Krein, P. T. (2009b). Force calculation in 3-D magnetic equivalent circuit networks with a Maxwell stress tensor. *IEEE Transactions on Energy Conversion*, 24(3):587–593.

Amrhein, M. and Krein, P. T. (2010). Induction machine modeling approach based on 3-D magnetic equivalent circuit framework. *IEEE Transactions on Energy Conversion*, 25(2):339–347.

Andritz Hydro Hammerfest (2017). Andritz Hydro. `http://www.emec.org.uk/about-us/our-tidal-clients/andritz-hydro-hammerfest/` [Accessed: 28/05/2017].

Anglada, J. R. and Sharkh, S. (2017a). Analysis of transverse flux machines using a virtual mutual inductance approach. *IEEE Transactions on Energy Conversion*, PP(99):1–1.

Anglada, J. R. and Sharkh, S. M. (2016a). Analytical calculation of air-gap magnetic field distribution in transverse-flux machines. In *2016 IEEE 25th International Symposium on Industrial Electronics (ISIE)*, pages 141–146.

Anglada, J. R. and Sharkh, S. M. (2016b). An insight into torque production and power factor in transverse-flux machines. In *2016 XXII International Conference on Electrical Machines (ICEM)*, pages 120–125.

Anglada, J. R. and Sharkh, S. M. (2017b). Analytical calculation of the torque produced by transverse flux machines. *IET Electric Power Applications*, 11(7):1298–1305.

Anglada, J. R. and Sharkh, S. M. (2017c). An insight into torque production and power factor in transverse-flux machines. *IEEE Transactions on Industry Applications*, 53(3):1971–1977.

Anglada, J. R., Sharkh, S. M., and Qazalbash, A. A. (2016). Analysis of slotting models for the calculation of no-load rotor losses in pm machines. In *2016 XXII International Conference on Electrical Machines (ICEM)*, pages 1325–1331.

Anglada, J. R., Sharkh, S. M., and Qazalbash, A. A. (2017). Influence of curvature on air-gap magnetic field distribution and rotor losses in pm electric machines. *COMPEL - The international journal for computation and mathematics in electrical and electronic engineering*, 36(4):871–891.

Aquamarine Power (2015). Aquamarine Power. `http://www.emec.org.uk/about-us/wave-clients/aquamarine-power/` [Accessed: 28/05/2017].

Arabian-Hoseynabadi, H., Tavner, P. J., and Oraee, H. (2009). Reliability comparison of direct-drive and geared-drive wind turbine concepts. *Wind Energy*, 13(July 2009):62–73.

Baker, N. J., Atkinson, G. J., Washington, J. G., Mecrow, B. C., Nord, G., and Sjoberg, L. (2012). Design of high torque traction motors for automotive applications using modulated pole smc machines. In *Power Electronics, Machines and Drives (PEMD 2012), 6th IET International Conference on*, pages 1–6.

Baker, N. J., Cawthorne, S., Hodge, E., and Spooner, E. (2014). 3d modelling of the generator for openhydro's tidal energy system. In *Power Electronics, Machines and Drives (PEMD 2014), 7th IET International Conference on*, pages 1–6.

Bang, D. and Polinder, H. (2008). Review of generator systems for direct-drive wind turbines. In *European Wind Energy Conference*, pages 1–11.

Bang, D. J., Polinder, H., Shrestha, G., and Ferreira, J. A. (2008). Promising direct-drive generator system for large wind turbines. *EPE Journal (European Power Electronics and Drives Journal)*, 18:7–13.

Bathe, K. J. (1996). *Finite Element Procedures*. Prentice Hall.

Blissenbach, R. and Viorel, I.-A. (2003). On the Single-Sided Transverse Flux Machine Design. *Electric Power Components and Systems*, 31(2):109–128.

Boughrara, K., Chikouche, B. L., Ibtiouen, R., Zarko, D., and Touhami, O. (2009a). Analytical model of slotted air-gap surface mounted permanent-magnet synchronous motor with magnet bars magnetized in the shifting direction. *IEEE Transactions on Magnetics*, 45(2):747–758.

Boughrara, K., Lubin, T., and Ibtiouen, R. (2013). General subdomain model for predicting magnetic field in internal and external rotor multiphase flux-switching machines topologies. *IEEE Transactions on Magnetics*, 49(10):5310–5325.

Boughrara, K., Zarko, D., Ibtiouen, R., Touhami, O., and Rezzoug, A. (2009b). Magnetic field analysis of inset and surface-mounted permanent-magnet synchronous motors using schwarz-christoffel transformation. *IEEE Transactions on Magnetics*, 45(8):3166–3178.

Boules, N. (1985). Prediction of no-load flux density distribution in permanent magnet machines. *IEEE Transactions on Industry Applications*, IA-21(3):633–643.

Bull, S. R. (2001). Renewable energy today and tomorrow. *Proceedings of the IEEE*, 89(8):1216–1226.

BWE: German Wind Energy Association (2014). Yearbook wind energy 2014. Technical report.

Cabrera, B. (1982). First results from a superconductive detector for moving magnetic monopoles. *Phys. Rev. Lett.*, 48:1378–1381.

Carpenter, C. (1968). Magnetic equivalent circuits. *Proceedings of the Institution of Electrical Engineers*, 115:1503.

Carroll, J., McDonald, A., and McMillan, D. (2015). Reliability comparison of wind turbines with dfig and pmg drive trains. *IEEE Transactions on Energy Conversion*, 30(2):663–670.

Carter, F. W. (1900). Note on air-gap and interpolar induction. *Electrical Engineers, Journal of the Institution of*, 29(146):925–933.

Carter, F. W. (1926). The magnetic field of the dynamo-electric machine. *Electrical Engineers, Journal of the Institution of*, 64(359):1115–1138.

Chari, M., Csendes, Z., Silvester, P., Konrad, A., and Palmo, M. (1981). Three-dimensional Magnetostatic Field Analysis of Electrical Machinery by the Finite-element Method. *IEEE Transactions on Power Apparatus and Systems*, (8).

Chari, M. and Silvester, P. (1971). Analysis of Turboalternator Magnetic Fields by Finite Elements. *IEEE Transactions on Power Apparatus and Systems*, 90:454–464.

Clements, B. J., Coady, D., Fabrizio, S., Shang, B., Villafuerte, M., Singh, S., Kangur, A., Nozaki, M., and Josz, C. (2013). *Energy Subsidy Reform: Lessons and Implications.* International Monetary Fund, Publication Services.

Colli, V. D., Stefano, R. D., and Scarano, M. (2005). A tubular generator for marine energy direct drive applications. In *IEEE International Conference on Electric Machines and Drives, 2005.*, pages 1473–1478.

Comission to the European Parliament (2013). Renewable energy progress report. Technical report.

Deodhar, R. P., Pride, A., and Bremner, J. J. (2015). Design method and experimental verification of a novel technique for torque ripple reduction in stator claw-pole pm machines. *IEEE Transactions on Industry Applications*, 51(5):3743–3750.

Dirac, P. A. M. (1931). Quantised singularities in the electromagnetic field. *Proceedings of the Royal Society of London A: Mathematical, Physical and Engineering Sciences*, 133(821):60–72.

Dobzhanskyi, O. and Gouws, R. (2016). Performance analysis of a permanent magnet transverse flux generator with double coil. *IEEE Transactions on Magnetics*, 52(1):1–11.

Doering, J., Steinborn, G., and Hofmann, W. (2015). Torque, power, losses, and heat calculation of a transverse flux reluctance machine with soft magnetic composite materials and disk-shaped rotor. *IEEE Transactions on Industry Applications*, 51(2):1494–1504.

Dogan, H., Garbuio, L., Nguyen-Xuan, H., Delinchant, B., Foggia, a., and Wurtz, F. (2013). Multistatic reluctance network modeling for the design of permanent-magnet synchronous machines. *IEEE Transactions on Magnetics*, 49(5):2347–2350.

Douglas, C. a., Harrison, G. P., and Chick, J. P. (2008). Life cycle assessment of the Seagen marine current turbine. *Proceedings of the Institution of Mechanical Engineers, Part M: Journal of Engineering for the Maritime Environment*, 222:1–12.

Driscoll, T. A. (2005). *Schwarz-Christoffel Toolbox User's Guide: Version 2.3.* Newark, DE: Dept. Math. Sci., Univ. Delaware.

Driscoll, T. A. and Trefethen, L. N. (2002). *Schwarz-Christoffel Mapping.* Cambridge ; New York : Cambridge University Press, 2002.

Dubas, F. and Espanet, C. (2009). Analytical solution of the magnetic field in permanent-magnet motors taking into account slotting effect: No-load vector potential and flux density calculation. *IEEE Transactions on Magnetics*, 45(5):2097–2109.

Dwight, H. (1947). *Tables of Integrals and Other Mathematical Data.* Macmillan.

Echavarria, E., Hahn, B., van Bussel, G. J. W., and Tomiyama, T. (2008). Reliability of Wind Turbine Technology Through Time. *Journal of Solar Energy Engineering*, 130(August 2008):031005.

European Comission (2014). Eu energy in figures: Statistical pocketbook. Technical report.

European Comission (2015). Europe 2020. Technical report.

European Marine Energy Centre (EMEC) Ltd (2017). EMEC. `http://www.emec.org.uk/` [Accessed: 28/05/2017].

Feynman, R. P., Leighton, R. B., and Sands, M. (2010). *The Feynman Lectures on Physics, Volume II.* Basic Books.

Fitzgerald, A. E., Kingsley, C. J., and Umans, S. D. (2003). *Electric Machinery, Sixth Edition.* McGraw-Hill Education.

Freeman, E. M. (1962). The calculation of harmonics, due to slotting, in the flux-density waveform of a dynamo-electric machine. *Proceedings of the IEE - Part C: Monographs*, 109(16):581–588.

Freeman, E. M. (1968). Travelling waves in induction machines: input impedance and equivalent circuits. *Electrical Engineers, Proceedings of the Institution of*, 115(12):1772–1776.

French, C. D., Hodge, C., and Husband, M. (2002). Optimised torque control of marine transverse-flux propulsion machines. In *2002 International Conference on Power Electronics, Machines and Drives (Conf. Publ. No. 487)*, pages 1–6.

Gibbs, W. J. (1958). *Conformal Transformations in Electrical Engineering.* Chapman and Hall.

Gieras, J. F. (2005). Performance characteristics of a transverse flux generator. In *IEEE International Conference on Electric Machines and Drives, 2005.*, pages 1293–1299.

Grauers, A. (1996). *Design of Direct-driven Permanent-magnet Generators for Wind Turbines.* PhD Thesis, Chalmers University of Technology.

Greig, J. and Freeman, E. M. (1967). Travelling-wave problem in electrical machines. *Electrical Engineers, Proceedings of the Institution of*, 114(11):1681–1683.

Guo, Y., Zhu, J. G., Watterson, P. A., and Wu, W. (2006). Development of a PM Transverse Flux Motor With Soft Magnetic Composite Core. *IEEE Transactions on Energy Conversion*, 21(2):426–434.

Hague, B. (1917). The mathematical treatment of the magnetomotive force of armature windings. *Electrical Engineers, Journal of the Institution of*, 55(268):489–514.

Halbach, K. (1968). Application of conformal mapping to evaluation and design of magnets containing iron with nonlinear b(h) characteristics. *Nuclear Instruments and Methods*, 64(3):278 – 284.

Halbach, K. (1990). Understanding modern magnets through conformal mapping. *International Journal of Modern Physics B*, 04(06):1201–1222.

Hammond, P. (1982). Use of potentials in calculation of electromagnetic fields. *IEE Proceedings A - Physical Science, Measurement and Instrumentation, Management and Education - Reviews*, 129(2):106–112.

Hammond, P. (1999). The role of the potentials in electromagnetism. *COMPEL - The international journal for computation and mathematics in electrical and electronic engineering*, 18(2):103–119.

Hansen, A. D. and Hansen, L. H. (2007). Wind turbine concept market penetration over 10 years (1995-2004). *Wind Energy*, 10(November 2006):81–97.

Harris, M. R. and Mecrow, B. C. (1993). Variable reluctance permanent magnet motors for high specific output. In *Electrical Machines and Drives, 1993. Sixth International Conference on (Conf. Publ. No. 376)*, pages 437–442.

Harris, M. R. and Pajooman, G. H. (1995). Electric motors with heteropolar permanent magnets and homopolar windings: computational study of performance limits. In *1995 Seventh International Conference on Electrical Machines and Drives (Conf. Publ. No. 412)*, pages 237–241.

Harris, M. R., Pajooman, G. H., and Sharkh, S. M. A. (1996). Performance and design optimisation of electric motors with heteropolar surface magnets and homopolar windings. *IEE Proceedings - Electric Power Applications*, 143(6):429–436.

Harris, M. R., Pajooman, G. H., and Sharkh, S. M. A. (1997a). Comparison of alternative topologies for vrpm (transverse-flux) electrical machines. In *IEE Colloquium on New Topologies for Permanent Magnet Machines (Digest No: 1997/090)*, pages 2/1–2/7.

Harris, M. R., Pajooman, G. H., and Sharkh, S. M. A. (1997b). The problem of power factor in vrpm (transverse-flux) machines. In *Electrical Machines and Drives, 1997 Eighth International Conference on (Conf. Publ. No. 444)*, pages 386–390.

Hendershot, J. R. and Miller, T. J. E. (2010). *Design of Brushless Permanent-Magnet Motors*. Motor Design Books LLC.

Henneberger, G. and Bork, M. (1997). Development of a new transverse flux motor. In *IEE Colloquium on New Topologies for Permanent Magnet Machines (Digest No: 1997/090)*, pages 1/1–1/6.

Hodgins, N., Mcdonald, A., Shek, J., Keysan, O., and Mueller, M. (2009). Current and future developments of the c-gen lightweight direct drive generator for wave & tidal energy. In *Proceedings of the 8th European Wave and Tidal Energy Conference, Uppsala, Sweden*, pages 2/1–2/7.

Ibala, A., Masmoudi, A., Atkinson, G., and Jack, A. G. (2011). On the modeling of a tfpm by reluctance network including the saturation effect with emphasis on the leakage fluxes. *COMPEL - The international journal for computation and mathematics in electrical and electronic engineering*, 30(1):151–171.

Ifedi, C. J., Mecrow, B. C., Brockway, S. T. M., Boast, G. S., Atkinson, G. J., and Kostic-Perovic, D. (2013). Fault-tolerant in-wheel motor topologies for high-performance electric vehicles. *IEEE Transactions on Industry Applications*, 49(3):1249–1257.

International Energy Agency (2013a). Energy technology perspectives 2014. Technical report.

International Energy Agency (2013b). Renewable energy outlook. Technical report.

International Energy Agency (2013c). Tracking clean energy progress 2013: Iea input to the clean energy ministerial. Technical report.

International Energy Agency (2014). Key world energy statistics. Technical report.

Ionel, D. M., Popescu, M., McGilp, M. I., Miller, T. J. E., Dellinger, S. J., and Heideman, R. J. (2007). Computation of core losses in electrical machines using improved models for laminated steel. *IEEE Transactions on Industry Applications*, 43(6):1554–1564.

Irenji, N. T. (1998). *Calculation of Electromagnetic Rotor Losses in High-Speed Permanent Magnet Machines*. PhD Thesis, University of Southampton.

Janning, J. and Schwery, A. (2009). Next generation variable speed pump-storage power stations. In *2009 13th European Conference on Power Electronics and Applications*, pages 1–10.

Jeffrey, H., Jay, B., and Winskel, M. (2013). Accelerating the development of marine energy: Exploring the prospects , benefits and challenges. *Technological Forecasting & Social Change*, 80(7):1306–1316.

Kang, D., Chun, Y., and Weh, H. (2003). Analysis and optimal design of transverse flux linear motor with PM excitation for railway traction. *IEE Proceedings - Electric Power Applications*, 150(4):493.

Kang, D. H. and Weh, H. (2008). 3D-FEM Analysis Versus Test Results for Three Transversal Flux Linear Motor Topologies. *Electric Power Components and Systems*, 36(4):345–358.

Kastinger, G. (2002). Design of a novel transverse flux machine. In *2002 International Conference on Electrical Machines (ICEM)*.

Keller, M., Muller, S., and Parspour, N. (2016). Design of a permanent magnetic excited transverse flux machine for robotic applications. In *2016 XXII International Conference on Electrical Machines (ICEM)*, pages 1520–1525.

Kenjo, T. and Sugawara, A. (1995). *Stepping motors and their microprocessor controls, Second Edition*. Clarendon Press, Monographs in Electrical and Electronic Engineering.

Keysan, O., McDonald, A. S., and Mueller, M. (2011). A direct drive permanent magnet generator design for a tidal current turbine(seagen). In *2011 IEEE International Electric Machines Drives Conference (IEMDC)*, pages 224–229.

Keysan, O., Mueller, M., McDonald, A., Hodgins, N., and Shek, J. (2012). Designing the c-gen lightweight direct drive generator for wave and tidal energy. *Renewable Power Generation, IET*, 6(3):161–170.

Kirtley, J. (2003). *Electric Machines*. Massachusetts Institute of Technology: Class Notes.

Kirtley, J. L. (1975). Surface coefficient for multipole magnetic field boundary condition problems. *IEEE Transactions on Power Apparatus and Systems*, 94(3):934–938.

Krause, P., Wasynczuk, O., Sudhoff, S., and Pekarek, S. (2013). *Appendix B: Carter's Coefficient*, pages 626–628. John Wiley & Sons, Inc.

Kremers, M. F. J., Paulides, J. J. H., Janssen, J. L. G., and Lomonova, E. A. (2014). Analytical flux linkage and emf calculation of a transverse flux machine. In *Electrical Machines (ICEM), 2014 International Conference on*, pages 2668–2673.

Kremers, M. F. J., Paulides, J. J. H., and Lomonova, E. A. (2015). Toward accurate design of a transverse flux machine using an analytical 3-d magnetic charge model. *IEEE Transactions on Magnetics*, 51(11):1–4.

Kreyszig, E. (2011). *Advanced Engineering Mathematics, 10th Edition*. John Wiley & Sons, Inc.

Krop, D. C. J., Lomonova, E. a., and Vandenput, a. J. a. (2008). Application of schwarz-christoffel mapping to permanent-magnet linear motor analysis. *IEEE Transactions on Magnetics*, 44(3):352–359.

Kundur, P. (1993). *Power System Stability and Control*. McGraw-Hill Professional.

Laithwaite, E. R. (1967). Magnetic equivalent circuits for electrical machines. *Electrical Engineers, Proceedings of the Institution of*, 114(11):1805–1809.

Lawrence, J., Sedgwick, J., Jeffrey, H., and Bryden, I. (2013). An overview of the u.k. marine energy sector. *Proceedings of the IEEE*, 101(4):876–890.

Lawrenson, P. J., Reece, P., and Ralph, M. C. (1966). Tooth-ripple losses in solid poles. *Electrical Engineers, Proceedings of the Institution of*, 113(4):657–662.

Lewis, C. (2002). The advanced induction motor. In *IEEE Power Engineering Society Summer Meeting,*, volume 1, pages 250–253 vol.1.

Liu, C., Zhu, J., Wang, Y., Guo, Y., Lei, G., and Liu, X. (2015). Development of a low-cost double rotor axial flux motor with soft magnetic composite and ferrite permanent magnet materials. *Journal of Applied Physics*, 117(17).

Liu, Z. J. and Li, J. T. (2007). Analytical solution of air-gap field in permanent-magnet motors taking into account the effect of pole transition over slots. *IEEE Transactions on Magnetics*, 43(10):3872–3883.

Liu, Z. J., Li, J. T., and Jiang, Q. (2008). An improved analytical solution for predicting magnetic forces in permanent magnet motors. *Journal of Applied Physics*, 103(2008):2006–2009.

Lovatt, H. C. (2005). Analytical model of a classical switched-reluctance motor. *IEE Proceedings - Electric Power Applications*, 152(2):352–358.

Lowther, D. and Silvester, P. (1986). *Computer-Aided Design in Magnetics*. Springer-Verlag New York Inc.

Lu, K., Rasmussen, P. O., and Ritchie, E. (2011). Design considerations of permanent magnet transverse flux machines. *IEEE Transactions on Magnetics*, 47(10):2804–2807.

Lu, K. Y., Ritchie, E., Rasmussem, P. O., and Sandholdt, P. (2003). Modeling and power factor analysis of a single phase surface mounted permanent magnet transverse flux machine. In *Power Electronics and Drive Systems, 2003. PEDS 2003. The Fifth International Conference on*, volume 2, pages 1609–1613 Vol.2.

Lubin, T., Mezani, S., and Rezzoug, A. (2013). Development of a 2-D Analytical Model for the Electromagnetic Computation of Axial-Field Magnetic Gears. *IEEE Transactions on Magnetics*, 49(11):5507–5521.

Magallanes Renovables, S.L. (2017). Proyecto Magallanes. `http://www.magallanesrenovables.com/en/proyecto` [Accessed: 28/05/2017].

Marine Current Turbines LTD (2017). SeaGen. `http://www.marineturbines.com/Seagen-Technology/` [Accessed: 28/05/2017].

Markovic, M. (2004). *Magnetic field analysis in electric motors using conformal mapping*. PhD Thesis, Ecole Polytechnique Federale de Lausanne EPFL.

Markovic, M., Jufer, M., and Perriard, Y. (2004). Analyzing an Electromechanical Actuator by Schwarz-Christoffel Mapping. *IEEE Transactions on Magnetics*, 40(4):1858–1863.

Markovic, M., Jufer, M., and Perriard, Y. (2005). An exact formula for "Tooth-to-Tooth" permeance. *IEEE Transactions on Magnetics*, 41(7):2295–2299.

MathWorks (2017). Simulink. `https://uk.mathworks.com/products/simulink.html` [Accessed: 04/11/2017].

Matsch, L. W. (1972). *Electromagnetic and Electromechanical Machines*. Intext Educational Publishers.

McMillan, D. and Ault, G. W. (2010). Techno-economic comparison of operational aspects for direct drive and gearbox-driven wind turbines. *IEEE Transactions on Energy Conversion*, 25(1):191–198.

Mueller, M. and Polinder, H. (2013). *Electrical Drives for Direct Drive Renewable Energy Systems, 1st Edition*. Woodhead Publishing.

Mueller, M. A., Polinder, H., and Baker, N. (2007). Current and novel electrical generator technology for wave energy converters. In *2007 IEEE International Electric Machines Drives Conference*, volume 2, pages 1401–1406.

National Renewable Energy Laboratory (2003). Alternative design study report : Windpact advanced wind turbine drive train designs study. Technical report.

National Renewable Energy Laboratory (2004). Northern power systems windpact drive train alternative design study report northern power systems windpact drive train alternative design study report. Technical report.

National Renewable Energy Laboratory (2010). Comparative Assessment of Direct Drive High Temperature Superconducting Generators in Multi-Megawatt Class Wind Turbines. Technical report.

National Renewable Energy Laboratory (2014). Offshore Wind Market and Economic Analysis. Technical report.

National Renewable Energy Laboratory (2015). 2014-2015 Offshore Wind Technologies Market Report. Technical report.

Neville, S. (1967). Use of carter's coefficient with narrow teeth. *Electrical Engineers, Proceedings of the Institution of*, 114(9):1245–1250.

O'Connell, T. C. and Krein, P. T. (2009). A SchwarzChristoffel-Based Analytical Method for Electric Machine Field Analysis. *IEEE Transactions on Energy Conversion*, 24(3):565–577.

Oh, J. H. and Kwon, B. I. (2016). Design, optimization, and prototyping of a transverse flux-type-switched reluctance generator with an integrated rotor. *IEEE Transactions on Energy Conversion*, 31(4):1521–1529.

OpenHydro Group Limited (2017). OpenHydro. `http://www.openhydro.com/` [Accessed: 28/05/2017].

Ostovic, V. (1986). A method for evaluation of transient and steady state performance in saturated squirrel cage induction machines. *IEEE Transactions on Energy Conversion*, EC-1(3):190–197.

Ostovic, V. (1987). Computation of saturated permanent-magnet ac motor performance by means of magnetic circuits. *IEEE Transactions on Industry Applications*, IA-23(5):836–841.

Ostovic, V. (1988). A simplified approach to magnetic equivalent-circuit modeling of induction machines. *IEEE Transactions on Industry Applications*, 24(2):308–316.

Ostovic, V. (1989). A novel method for evaluation of transient states in saturated electric machines. *IEEE Transactions on Industry Applications*, 25(1):96–100.

Pajooman, G. H. (1997). *Performance assessment and design optimisation of VRPM (transverse flux) machines by finite element computation.* PhD Thesis, University of Southampton.

Pannatier, Y., Kawkabani, B., Nicolet, C., Simond, J. J., Schwery, A., and Allenbach, P. (2010). Investigation of control strategies for variable-speed pump-turbine units by using a simplified model of the converters. *IEEE Transactions on Industrial Electronics*, 57(9):3039–3049.

Pelamis Wave Power (2015). Pelamis Wave Power. `http://www.emec.org.uk/about-us/wave-clients/pelamis-wave-power/` [Accessed: 28/05/2017].

Pfister, P. D., Yin, X., and Fang, Y. (2016). Slotted permanent-magnet machines: General analytical model of magnetic fields, torque, eddy currents, and permanent-magnet power losses including the diffusion effect. *IEEE Transactions on Magnetics*, 52(5):1–13.

Pipes, L. A. (1956). Matrix theory of skin effect in laminations. *Journal of the Franklin Institute*, 262(2):127 – 138.

Polinder, H., Bang, D., van Rooij, R. P. J. O. M., McDonald, A. S., and Mueller, M. A. (2007). 10 mw wind turbine direct-drive generator design with pitch or active speed stall control. In *2007 IEEE International Electric Machines Drives Conference*, volume 2, pages 1390–1395.

Polinder, H., Ferreira, J. A., Jensen, B. B., Abrahamsen, A. B., Atallah, K., and McMahon, R. A. (2013). Trends in wind turbine generator systems. *IEEE Journal of Emerging and Selected Topics in Power Electronics*, 1(3):174–185.

Polinder, H., Mecrow, B. C., Jack, A. G., Dickinson, P., and Mueller, M. A. (2003). Linear generators for direct-drive wave energy conversion. In *Electric Machines and Drives Conference, 2003. IEMDC'03. IEEE International*, volume 2, pages 798–804 vol.2.

Polinder, H., Mecrow, B. C., Jack, A. G., Dickinson, P. G., and Mueller, M. a. (2005). Conventional and TFPM linear generators for direct-drive wave energy conversion. *IEEE Transactions on Energy Conversion*, 20(2):260–267.

Polinder, H., van der Pijl, F. F. A., de Vilder, G. J., and Tavner, P. J. (2006). Comparison of direct-drive and geared generator concepts for wind turbines. *IEEE Transactions on Energy Conversion*, 21(3):725–733.

Pompermaier, C., Sjberg, L., and Nord, G. (2012). Design and optimization of a permanent magnet transverse flux machine. In *2012 XXth International Conference on Electrical Machines*, pages 606–611.

Popescu, M., Foley, I., Staton, D. A., and Goss, J. E. (2015). Multi-physics analysis of a high torque density motor for electric racing cars. In *2015 IEEE Energy Conversion Congress and Exposition (ECCE)*, pages 6537–6544.

Potgieter, J. H. J. and Kamper, M. J. (2012). Optimum design and technology evaluation of slip permanent magnet generators for wind energy applications. In *2012 IEEE Energy Conversion Congress and Exposition (ECCE)*, pages 2342–2349.

Purcell, E. (2008). *Electricity and Magnetism, third edition.* Cambridge.

Qazalbash, A. A., Sharkh, S. M., Irenji, N. T., Wills, R. G., and Abusara, M. A. (2014a). Calculation of no-load rotor eddy-current power loss in pm synchronous machines. *IEEE Transactions on Magnetics*, 50(9):1–8.

Qazalbash, A. A., Sharkh, S. M., Irenji, N. T., Wills, R. G., and Abusara, M. A. (2014b). Rotor eddy current power loss in permanent magnet synchronous generators feeding uncontrolled rectifier loads. *IEEE Transactions on Magnetics*, 50(6):1–9.

Qazalbash, A. A., Sharkh, S. M., Irenji, N. T., Wills, R. G., and Abusara, M. A. (2015). Rotor eddy loss in high-speed permanent magnet synchronous generators. *IET Electric Power Applications*, 9(5):370–376.

Rabinovici, R. (1996). Magnetic field analysis of permanent magnet motors. *IEEE Transactions on Magnetics*, (1):265–269.

Rahman, K. M., Patel, N. R., Ward, T. G., Nagashima, J. M., Caricchi, F., and Crescimbini, F. (2006). Application of direct-drive wheel motor for fuel cell electric and hybrid electric vehicle propulsion system. *IEEE Transactions on Industry Applications*, 42(5):1185–1192.

Rajantie, A. (2016). The search for magnetic monopoles. *Physics Today*, 69.

Ran, L., Mueller, M. A., Ng, C., Tavner, P. J., Zhao, H., Baker, N. J., Mcdonald, S., and Mckeever, P. (2011). Power conversion and control for a linear direct drive permanent magnet generator for wave energy. *IET Renewable Power Generation*, 5(1):1–9.

Rasmussen, F., Thomsen, K., and Larsen, T. (2004). The gearbox problem revisited. *RisøFact Sheet*, AED-RB-17(March).

Russell, R. L. and Norsworthy, K. H. (1958). Eddy currents and wall losses in screened-rotor induction motors. *Proceedings of the IEE - Part A: Power Engineering*, 105(20):163–175.

Say, M. G. (1965). *The Performance and Design of Alternating Current Machines*. Sir Isaac Pitman & Sons Ltd.

Schmidt, E., Ertl, J., Preiss, A., Zensch, R., Schrhuber, R., and Hell, J. (2011). Simulation of steady-state and transient operational behaviour of variable-speed motor-generators of hydro power plants. In *2011 IEEE International Electric Machines Drives Conference (IEMDC)*, pages 607–611.

Semken, R. S., Polikarpova, M., Roytta, P., Alexandrova, J., Pyrhonen, J., Nerg, J., Mikkola, A., and Backman, J. (2012). Direct-drive permanent magnet generators for high-power wind turbines: benefits and limiting factors. *IET Renewable Power Generation*, 6(1):1–8.

Sharkh, S. M. A., Lai, S. H., and Turnock, S. R. (2004). Structurally integrated brushless pm motor for miniature propeller thrusters. *IEE Proceedings - Electric Power Applications*, 151(5):513–519.

Silvester, P. and Chari, M. (1970). Finite Element Solution of Saturable Magnetic Field Problems. *IEEE Transactions on Power Apparatus and Systems*, PAS-89:1642–1651.

Sopanen, J., Ruuskanen, V., Nerg, J., and Pyrhonen, J. (2011). Dynamic torque analysis of a wind turbine drive train including a direct-driven permanent-magnet generator. *IEEE Transactions on Industrial Electronics*, 58(9):3859–3867.

Spinato, F., Tavner, P. J., Bussel, G. J. W. V., and Koutoulakos, E. (2009). Reliability of wind turbine subassemblies. *IET Renewable Power Generation*, 3(4):387–401.

Spooner, E. and Dunne, P. (2011). Hydroelectric Turbine Having a Magnetic Bearing. *United Sates Patent Application Publication*.

Spooner, E., Gordon, P., Bumby, J. R., and French, C. D. (2005). Lightweight ironless-stator pm generators for direct-drive wind turbines. *IEE Proceedings - Electric Power Applications*, 152(1):17–26.

Steinmetz, C. P. (1894). Theory of the synchronous motor. *Transactions of the American Institute of Electrical Engineers*, XI:763–782.

Steinmetz, C. P. (1897). The alternating current induction motor. *Transactions of the American Institute of Electrical Engineers*, XIV(1):183–217.

Stern, N. (2007). *The Economics of Climate Change*. Cambridge University Press.

Stoll, R. (2011). *Low-Frequency Applications of Electromagnetics*. Lulu.

Stoll, R. and Sykulski, J. (1992). Modelling tooth ripple losses in the solid pole faces of synchronous machines. *COMPEL - The international journal for computation and mathematics in electrical and electronic engineering*, 11(1):105–108.

Subiabre, E. E. and Mueller, M. A. (2011). Efficiency estimation of an air-cored permanent magnet synchronous generator using finite elements and equivalent circuit modelling. In *2011 IEEE International Electric Machines Drives Conference (IEMDC)*, pages 377–382.

Tapia, J. A., Pyrhonen, J., Puranen, J., Lindh, P., and Nyman, S. (2013). Optimal design of large permanent magnet synchronous generators. *IEEE Transactions on Magnetics*, 49(1):642–650.

Tavner, P. J., Bussel, G. J. W. V., and Spinato, F. (2006). Machine and converter reliabilities in wind turbines. In *2006 3rd IET International Conference on Power Electronics, Machines and Drives - PEMD 2006*, pages 127–130.

Tesla, N. (1888a). Dynamo electric machine. US Patent 390,721.

Tesla, N. (1888b). Electro magnetic motor. US Patent 382,279.

Tesla, N. (1888c). A new system of alternate current motors and transformers. *Transactions of the American Institute of Electrical Engineers*, V(10):308–327.

Tesla, N. (1896). Alternating motor. US Patent 555,190.

Ueda, Y., Takahashi, H., Akiba, T., and Yoshida, M. (2013). Fundamental design of a consequent-pole transverse-flux motor for direct-drive systems. *IEEE Transactions on Magnetics*, 49(7):4096–4099.

U.K. Government (2008). Climate change act, tso, london. Technical report.

United Nations Framework Convention on Climate Change (2016). Paris agreement. Technical report.

U.S. Department of Energy (2013). 2012 wind technologies market report summary. Technical report.

Villegas, C. and Cawthorne, S. (2013). Hardware-in-the-loop testing for tidal energy power conversion systems. In *IEEE PES ISGT Europe 2013*, pages 1–4.

Wan, Z., Ahmed, A., Husain, I., and Muljadi, E. (2015). A novel transverse flux machine for vehicle traction aplications. In *2015 IEEE Power Energy Society General Meeting*, pages 1–5.

Washington, J. G., Atkinson, G. J., and Baker, N. J. (2016). Reduction of cogging torque and emf harmonics in modulated pole machines. *IEEE Transactions on Energy Conversion*, 31(2):759–768.

Washington, J. G., Atkinson, G. J., Baker, N. J., Jack, A. G., Mecrow, B. C., Jensen, B. B., Pennander, L., Nord, G., and Sjoberg, L. (2012). An improved torque density modulated pole machine for low speed high torque applications. In *Power Electronics, Machines and Drives (PEMD 2012), 6th IET International Conference on*, pages 1–6.

Weh, H. and May, H. (1986). Achievable force densities for permanent magnet excited machines in new configurations. In *Electrical Machines (ICEM), 1986 International Conference on*.

Weh, H. and Mayer, R. (1984). Synchronous machine with permanent magnet excitation as a flexible propulsion motor with high efficiency. In *Electrical Machines (ICEM), 1984 International Conference on*.

Wello OY (2017). Wello OY. http://www.emec.org.uk/about-us/wave-clients/wello-oy/.

Windpower Monthly (2005). The gearbox challenge. *Windpower Monthly*, (November).

Woodson, H. H. and Melcher, R. J. (1968). *Electromechanical Dynamics*. John Wiley & Sons.

Wu, L. J., Zhu, Z. Q., Staton, D., Popescu, M., and Hawkins, D. (2010a). Combined complex permeance and sub-domain model for analytical predicting electromagnetic performance of surface-mounted pm machines. In *5th IET International Conference on Power Electronics, Machines and Drives (PEMD 2010)*, pages 1–6.

Wu, L. J., Zhu, Z. Q., Staton, D., Popescu, M., and Hawkins, D. (2010b). Comparison of analytical models for predicting electromagnetic performance in surface-mounted permanent magnet machines. In *2010 IEEE Vehicle Power and Propulsion Conference*, pages 1–6.

Wu, L. J., Zhu, Z. Q., Staton, D., Popescu, M., and Hawkins, D. (2011). An Improved Subdomain Model for Predicting Magnetic Field of Surface-Mounted Permanent Magnet Machines Accounting for Tooth-Tips. *IEEE Transactions on Magnetics*, 47(6):1693–1704.

Wu, L. J., Zhu, Z. Q., Staton, D., Popescu, M., and Hawkins, D. (2012a). Analytical Model of Eddy Current Loss in Windings of Permanent-Magnet Machines Accounting for Load. *IEEE Transactions on Magnetics*, 48(7):2138–2151.

Wu, L. J., Zhu, Z. Q., Staton, D. A., Popescu, M., and Hawkins, D. (2012b). Comparison of Analytical Models of Cogging Torque in Surface-Mounted PM Machines. *IEEE Transactions on Industrial Electronics*, 59(6):2414–2425.

Yan, J., Lin, H., Huang, Y., Liu, H., and Zhu, Z. Q. (2009). Magnetic field analysis of a novel flux switching transverse flux permanent magnet wind generator with 3-d fem. In *2009 International Conference on Power Electronics and Drive Systems (PEDS)*, pages 332–335.

Yang, G., Cheng, D., Zhang, H., and Kou, B. (2012). Bidirectional Crosslinking Transverse Flux Permanent Magnet Synchronous Motor. *IEEE Transactions on Magnetics*, 49(3):1–1.

Zarko, D., Ban, D., and Lipo, T. A. (2006). Analytical calculation of magnetic field distribution in the slotted air gap of a surface permanent-magnet motor using complex relative air-gap permeance. *IEEE Transactions on Magnetics*, 42(7):1828–1837.

Zarko, D., Ban, D., and Lipo, T. A. (2009). Analytical solution for electromagnetic torque in surface permanent-magnet motors using conformal mapping. *IEEE Transactions on Magnetics*, 45(7):2943–2954.

Zavvos, A., Mcdonald, A., and Mueller, M. (2013). Optimisation tools for large permanent magnet generators for direct drive wind turbines. *IET Renewable Power Generation*, 7(2):163–171.

Zhang, B., Wang, A., and Doppelbauer, M. (2016). Multi-objective optimization of a transverse flux machine with claw-pole and flux-concentrating structure. *IEEE Transactions on Magnetics*, 52(8):1–10.

Zhang, H., Kou, B., Zhao, W., and Yang, G. (2014). Design and analysis of a bidirectional cross-linking transverse flux permanent magnet synchronous motor. In *2014 17th International Symposium on Electromagnetic Launch Technology*, pages 1–6.

Zhu, Z. and Hu, J. (2012a). Electrical machines and power-electronic systems for highpower wind energy generation applications: Part i market penetration, current technology and advanced machine systems. *COMPEL - The international journal for computation and mathematics in electrical and electronic engineering*, 32(1):7–33.

Zhu, Z. and Hu, J. (2012b). Electrical machines and power-electronic systems for highpower wind energy generation applications: Part ii power electronics and control systems. *COMPEL - The international journal for computation and mathematics in electrical and electronic engineering*, 32(1):34–71.

Zhu, Z., Wu, L., and Xia, Z. (2010). An Accurate Subdomain Model for Magnetic Field Computation in Slotted Surface-Mounted Permanent-Magnet Machines. *IEEE Transactions on Magnetics*, 46(4):1100–1115.

Zhu, Z. Q. and Howe, D. (1993a). Instantaneous magnetic field distribution in brushless permanent magnet dc motors. ii. armature-reaction field. *IEEE Transactions on Magnetics*, 29(1):136–142.

Zhu, Z. Q. and Howe, D. (1993b). Instantaneous magnetic field distribution in brushless permanent magnet dc motors. iii. effect of stator slotting. *IEEE Transactions on Magnetics*, 29(1):143–151.

Zhu, Z. Q. and Howe, D. (1993c). Instantaneous magnetic field distribution in permanent magnet brushless dc motors. iv. magnetic field on load. *IEEE Transactions on Magnetics*, 29(1):152–158.

Zhu, Z. Q., Howe, D., Bolte, E., and Ackermann, B. (1993). Instantaneous magnetic field distribution in brushless permanent magnet dc motors. i. open-circuit field. *IEEE Transactions on Magnetics*, 29(1):124–135.

Zhu, Z. Q., Howe, D., and Chan, C. C. (2002). Improved analytical model for predicting the magnetic field distribution in brushless permanent-magnet machines. *IEEE Transactions on Magnetics*, 38(1):229–238.

Zhu, Z. Q., Ng, K., Schofield, N., and Howe, D. (2004). Improved analytical modelling of rotor eddy current loss in brushless machines equipped with surface-mounted permanent magnets. *IEE Proceedings - Electric Power Applications*, 151(6):641–650.

Appendix A

Rotor Losses in High Speed PM Machines

The current sheet model applied for the calculation of rotor losses was presented in chapter 5. In that chapter it was applied for the analysis of a TFM, which is probably not the best example to illustrate the usefulness of the proposed methodology. This is because most of the rotor losses in TFMs are produced by the homopolar components of the magnetic field, which cannot be accurately represented using the current sheet model.

On the other hand, the current sheet model is particularly useful for the calculation of rotor losses in high speed PM machines. In fact, the methods developed by the author of this Thesis shown in chapter 5 were developed for this kind of machine (Anglada et al., 2016, 2017).

This appendix shows the application of the current sheet model for the case of high speed PM machines. The aim is to show the influence of the slotting models and the effect of curvature on no-load rotor losses.

Section A.1 is based on (Anglada et al., 2016) and section A.2 is based on (Anglada et al., 2017).

A.1 Analysis of Slotting Models for the Calculation of No-Load Rotor Losses in PM Machines

Figure A.1 shows a quarter of the cross-section of a high speed (the rated speed, $n_{rpm} \approx 60$ krpm) PM generator with a non-conductive rotor sleeve to hold the magnets, making the effective air-gap even larger (Qazalbash et al., 2014b). The parameters of this machine are shown in table A.1.

Taking into account that the permeability of the magnets and the sleeve is close to μ_0 the effective air-gap length:

$$g = h_m + t_{sl} + h_g = 9.4\text{mm}. \tag{A.1}$$

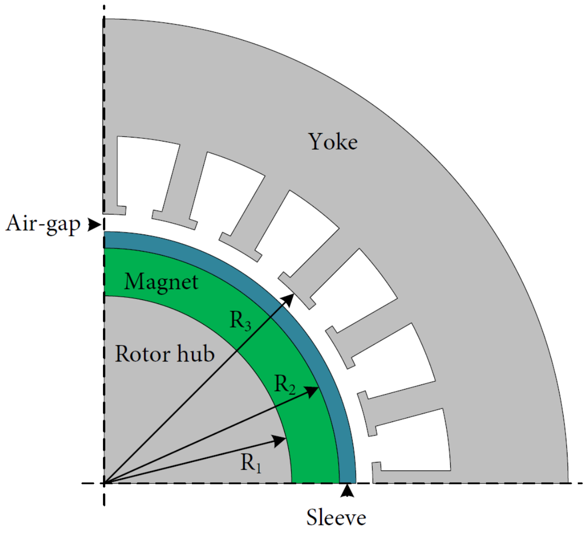

FIGURE A.1: Quarter model of the PM synchronous generator under study.

TABLE A.1: Parameters of the Machine

Quantity	Symbol	Value
Number of poles	$2p$	4
Number of slots	Q_s	24
Core length	L	125 mm
Rotor radius	R_1	21.6 mm
Magnet outer radius	R_2	27.1 mm
Stator radius	R_3	31 mm
Magnet thickness	h_m	5.5 mm
Sleeve thickness	t_{sl}	2 mm
Clearance gap	h_g	1.9 mm
Slot opening	b_o	3 mm
Rotor hub permeability	μ_r	750
Rotor hub conductivity	σ_r	$6.7 \cdot 10^6$ S/m
Magnet conductivity	σ_m	$0.77 \cdot 10^6$ S/m
Magnet material	-	NdFeB
Magnet remanence	B_r	1.07 T
Magnet coercivity	H_c	851 kA/m

In the developed model of the machine $t = 3.492$mm and $s = 3.394$mm, therefore

$$\frac{g}{s} \approx 2.770, \tag{A.2}$$

$$\frac{t}{s} \approx 1.029. \tag{A.3}$$

Clearly the machine is in the region where only the multiple-slots model should be used, as discussed in section 2.6.3. To study the limitations of the single-slot model the CP function is obtained for a multiple-slots and single-slot configuration for comparison. Both methodologies include a first conformal transformation to model the effect of curvature (Rabinovici, 1996).

The no-load magnetic field distribution in the air-gap of the slotless configuration using the rotor's reference frame can be expressed using complex number notation as

$$B_{sl}(\theta, r) = \sum_{n=1,3,5}^{\infty} K_n(r)\cos(np\theta) + j\sum_{n=1,3,5}^{\infty} D_n(r)\sin(np\theta), \tag{A.4}$$

where the coefficients $K_n(r)$ and $D_n(r)$ are calculated according to (Zhu et al., 2002) and $j = \sqrt{-1}$ is the pure imaginary part. The CP function (both for the multiple-slots and single-slot models) using the rotor's reference frame is

$$\lambda(\theta, r, t) = \lambda_{a0} + \sum_{m=1,2,3}^{\infty} \lambda_{am}(r)\cos\big(mQ_s(\theta - \omega t)\big) + j\sum_{m=1,2,3}^{\infty} \lambda_{bm}(r)\sin\big(mQ_s(\theta - \omega t)\big), \tag{A.5}$$

where the coefficients λ_{a0}, $\lambda_{am}(r)$ and $\lambda_{bm}(r)$ are calculated using conformal mapping. Therefore, according to (Zarko et al., 2006) the magnetic field distribution of the slotted geometry is

$$B(\theta, r, t) = B_{sl}(\theta, r) \cdot \lambda^*(\theta, r, t). \tag{A.6}$$

The radial and tangential components of the CP function on the surface of the magnets are shown in Figure A.2. It can be appreciated that there are similarities in waveform but the single-slot model is ignoring the effect of the neighbouring slots that is expressed mathematically as the boundary conditions on the middle of the teeth: (a) derivative of the radial component is zero and (b) the tangential component is zero. These two conditions are not satisfied by the waveform obtained with the single-slot model.

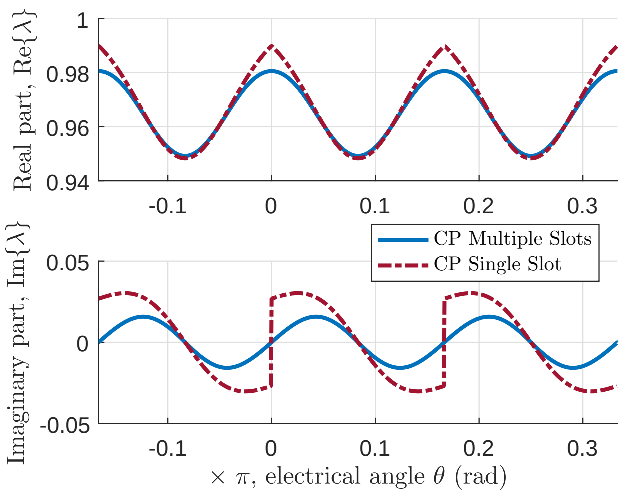

Figure A.2: Complex permeance function obtained with the multiple-slots and single-slot models; radial and tangential components.

Figure A.3 shows the waveform of the radial component of the no-load magnetic field distribution on the surface of the magnet at a particular rotor position using two-dimensional static FEA, multiple-slots model and single-slot model. It can be appreciated that the waveforms look very similar in Figure A.3. However, the amplitudes of the asynchronous harmonics have some significant differences because of the singularities and discontinuities of the single-slot CP function shown in Figure A.2. The amplitude of the most significant asynchronous harmonics is shown in

Figure A.4. The single-slot model overestimates significantly the amplitude of the asynchronous harmonics.

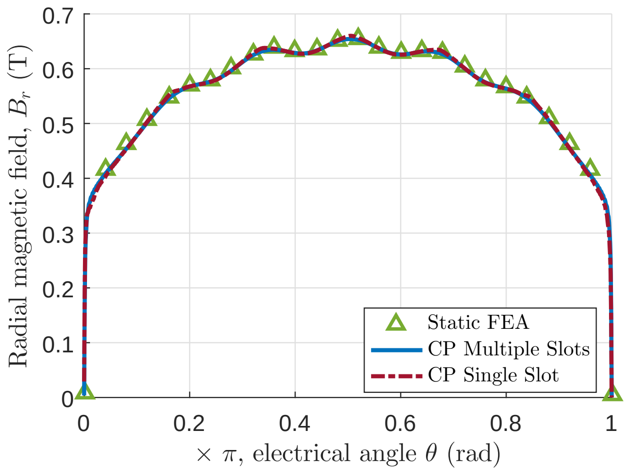

FIGURE A.3: Magnetic field distribution in the air-gap obtained using two-dimensional static FEA and the CP function.

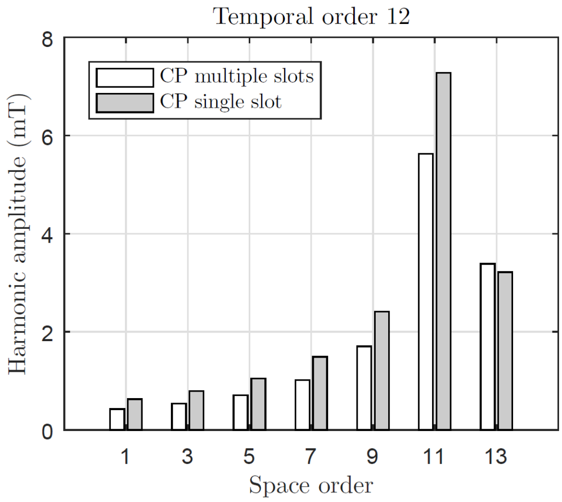

FIGURE A.4: No-load amplitude of the significant magnetic induction space harmonics of time order 12 at 90 000 rpm.

Table A.2 shows a comparison of the no-load losses obtained with the linear transient FEA calculations, the multiple-slots CP function and the single-slot CP function for the machine under study at running at 90 000 rpm.

TABLE A.2: No-load rotor power loss

Transient FEA	$\approx$ 11.2 W
Multiple-slots model	$\approx$ 15.5 W
Single-slot model	$\approx$ 29.4 W

The rotor losses obtained with the single-slot CP function are significantly higher than the result obtained with FEA. On the other hand, the value obtained with the multiple-slots CP function has a good agreement (around 4 W error) compared to the single-slot model (around 18 W error) which could in some cases make the difference as far as the feasibility of a design variant.

The complex permeance function used in this Thesis assumes rectangular slots without tooth-tips, which is valid if there is not saturation in the tooth-tips as discussed in (Zarko et al., 2006; Qazalbash et al., 2014a).

A.1.1 Conclusion

The case study presented here of a high speed PM motor illustrates the importance of using the appropriate model. Ignoring the effect of the adjacent slots, i. e., using a single-slot model, produces a significant error in the calculation of rotor losses because the machine is clearly in the region of multiple-slots method. Using the multiple-slots model improves the accuracy considerably.

A.2 Effect of Curvature on Rotor Losses

Figure A.5 shows a quarter cross-section of a high speed PM machine, which requires a sleeve to hold the magnets, making the effective air-gap relatively large. Machine B is the same as Machine A but scaled 2:1 keeping the air-gap parameters (magnet thickness, sleeve thickness, clearance gap and slot opening) constant. The parameters of these machines are shown in Table A.3. The slots of the machines shown in Figure A.5 have tooth tips, but as long as the teeth tips are not saturated, which is the case in these machines, the rectangular slot model shown in Figure 3.3 remains valid (Zarko et al., 2006; Qazalbash et al., 2014a).

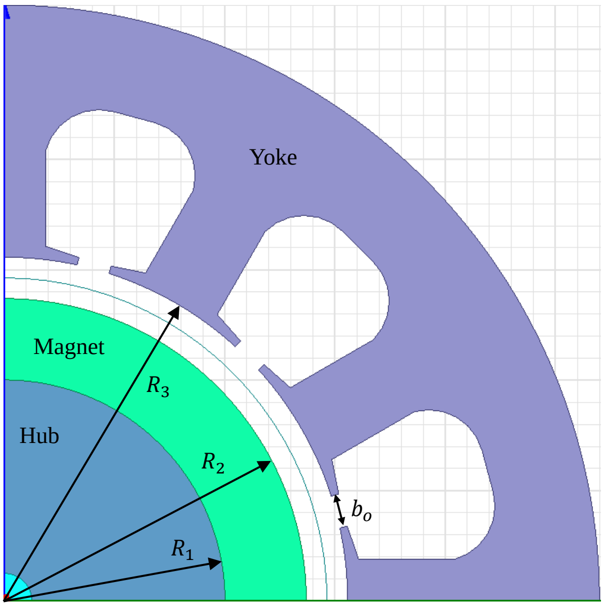

FIGURE A.5: Quarter model of the PM synchronous machines under study.

Taking into account that the permeability of the magnets and the sleeve is close to μ_0 the effective air-gap length as defined in Figure 3.3 is:

$$g_z = h_m + t_{sl} + h_g = 11.12 \text{ mm}, \tag{A.7}$$

Table A.3: Parameters of the Machines

Machine		A	B
Rated speed	n_{rpm}	65 krpm	32.5 krpm
Number of poles	$2p$	4	4
Number of slots	Q_s	12	12
Core length	L	109 mm	218 mm
Rotor hub radius	R_1	20 mm	47.43 mm
Magnet outer radius	R_2	27.4 mm	54.8 mm
Stator radius	R_3	31.15 mm	58.55 mm
Magnet's thickness	h_m	7.37 mm	7.37 mm
Sleeve's thickness	t_{sl}	2.95 mm	2.95 mm
Clearance gap	h_g	0.8 mm	0.8 mm
Slot opening	b_o	3 mm	3 mm
Rotor hub permeability	μ_{r1}	750	750
Rotor hub conductivity	σ_r	$6.7 \cdot 10^6$ S/m	$6.7 \cdot 10^6$ S/m
Magnet conductivity	σ_m	$0.77 \cdot 10^6$ S/m	$0.77 \cdot 10^6$ S/m
Magnet material	-	NdFeB	NdFeB
Magnet permeability	μ_{r2}	1.07	1.07
Magnet remanence	B_r	1.05 T	1.05 T
Magnet coercivity	H_c	781 kA/m	781 kA/m

where h_m is the magnet's thickness, t_{sl} the sleeve's thickness and h_g the clearance gap as shown in Table A.3.

The no-load magnetic field distribution in the air-gap of the slotless configuration in the rotor's reference frame can be expressed using complex number notation as

$$B_{sl}(\theta, r) = \sum_{n=1,3,5}^{\infty} K_n(r)\cos(np\theta) + j \sum_{n=1,3,5}^{\infty} D_n(r)\sin(np\theta), \tag{A.8}$$

where the coefficients $K_n(r)$ and $D_n(r)$ are calculated according to (Zhu et al., 2002) and $j = \sqrt{-1}$ is the imaginary unit. The complex permeance (CP) function using the rotor's reference frame is

$$\lambda(\theta, r, t) = \lambda_{a0} + \sum_{m=1,2,3}^{\infty} \lambda_{am}(r)\cos\big(mQ_s(\theta - \omega_m t)\big) + j \sum_{m=1,2,3}^{\infty} \lambda_{bm}(r)\sin\big(mQ_s(\theta - \omega_m t)\big) \tag{A.9}$$

where the coefficients λ_{a0}, $\lambda_{am}(r)$ and $\lambda_{bm}(r)$ are calculated using conformal mapping and $\omega_m = \omega/p$ is the mechanical speed of the rotor. Therefore, the magnetic field distribution in the slotted geometry is

$$B(\theta, r, t) = B_{sl}(\theta, r) \cdot \lambda^*(\theta, r, t). \tag{A.10}$$

For the calculation of rotor losses we are interested in the amplitude of the asynchronous harmonics of the radial component of the magnetic field, as it discussed later in chapter 5. Therefore, combining (A.8), (A.9) and (A.10) we obtain:

$$\begin{aligned}\mathrm{Re}\Big(B(\theta,r,t)\Big) = \sum_{n=1,3,5}^{\infty} K_n(r)\cos(np\theta)\left[\lambda_{a0} + \sum_{m=1,2,3}^{\infty}\lambda_{am}(r)\cos\big(mQ_s(\theta-\omega_m t)\big)\right] \\ + \sum_{n=1,3,5}^{\infty} D_n(r)\sin(np\theta)\left[\sum_{m=1,2,3}^{\infty}\lambda_{bm}(r)\sin\big(mQ_s(\theta-\omega_m t)\big)\right]. \quad \text{(A.11)}\end{aligned}$$

For a particular m_o, which means a time order $k = m_o Q_s/p$, we can re-arrange (A.11) to express explicitly each asynchronous harmonic. For each particular n_o we have two asynchronous harmonics whose space orders, q_1 and q_2, and amplitudes, $B_{q_1 k}$ and $B_{q_2 k}$, are calculated as follows

$$\begin{cases} q_1 = k + n_o, & \text{and } B_{q_1 k} = K_{n_o}(r)\frac{\lambda_{am_o}}{2} - D_{n_o}(r)\frac{\lambda_{bm_o}}{2} \\ q_2 = k - n_o, & \text{and } B_{q_2 k} = K_{n_o}(r)\frac{\lambda_{am_o}}{2} + D_{n_o}(r)\frac{\lambda_{bm_o}}{2} \end{cases} \quad \text{(A.12)}$$

The two machines studied in this appendix have $Q_s = 12$ slots and $p = 2$ pole pairs. Therefore, the time orders are 6, 12, 18...

The radial and tangential components of the CP function on the surface of the magnets are shown in Figure A.6. In this case the value of the coefficient K_J is

$$K_J = \begin{cases} 1.6\,\%, & \text{for machine A} \\ 0.37\,\%, & \text{for machine B,} \end{cases} \quad \text{(A.13)}$$

which according to Figure 3.5 places Machine A in the region where strong effect of the curvature is expected. Machine B is in the region of Figure 3.5 where the effect of curvature is expected to be small. This is confirmed by Figure A.6, which shows the permeance functions of both machines with and without taking curvature into account.

A.2.1 Transient FEA

Transient FEA was used to calculate rotor losses directly. A constant mechanical speed was assigned to the rotor without any other excitation besides the PM magnetisation. In this case, the element size was determined such that there are at least 3 elements per skin depth. The model had around 100 thousand elements. for accurate calculation of eddy currents. The time step was set to 0.5 μs such that there are at least 10 time steps per slot opening so that the slotting permeance variation is captured at a high resolution. Mesh size and time step independence were also confirmed.

Figure A.7 shows the eddy current density obtained from the transient FEA simulation. It can be appreciated that most of the rotor losses are concentrated in the magnets.

A.2.2 Results and Discussion

Figure A.8 shows the waveform of the radial component of the no-load magnetic field distribution on the surface of the magnet at a particular rotor position using two-dimensional static FEA,

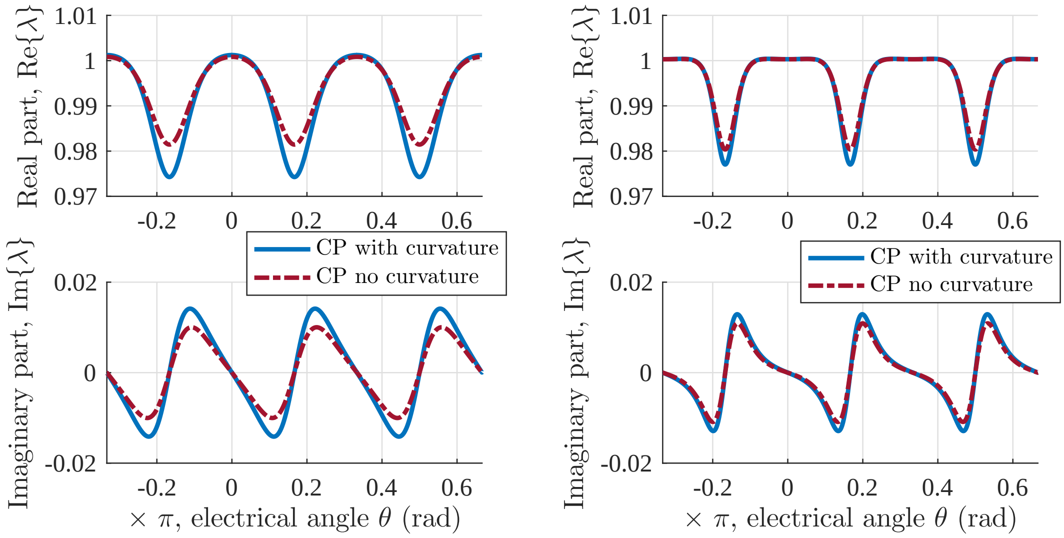

(a) Machine A.

(b) Machine B.

FIGURE A.6: Complex permeance function obtained with and without curvature; radial and tangential components.

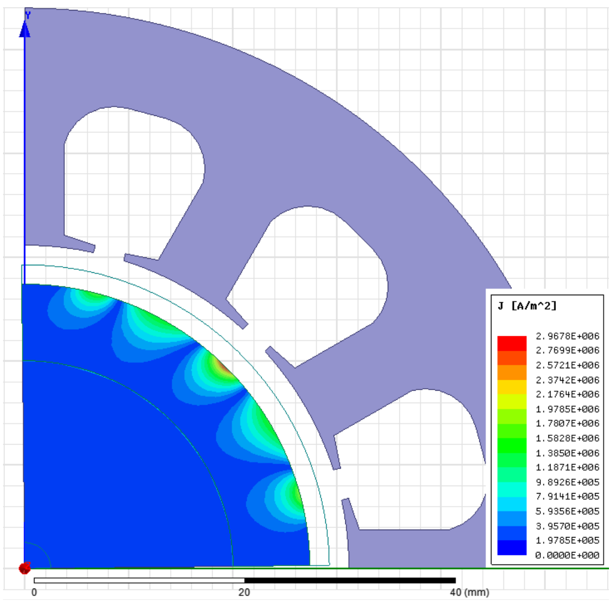

FIGURE A.7: Eddy current density at a particular instant of time obtained using transient FEA, Machine A shown as an example.

CP function with curvature and CP function without curvature. It can be appreciated in Figure A.8 that in machine A the CP function without curvature underestimates the amplitude of the tooth-ripple harmonics. On the other hand, in the case of machine B; which has smaller K_J, this effect is less significant.

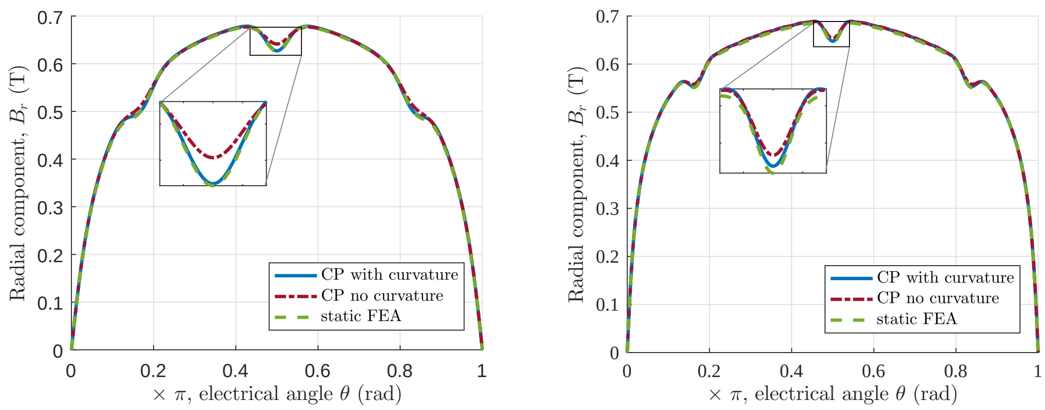

(a) Machine A.

(b) Machine B.

FIGURE A.8: Magnetic field distribution in the air-gap obtained using two-dimensional static FEA and the CP function with and without curvature.

Ignoring the effect of curvature underestimates the amplitude of the asynchronous harmonics in both cases as shown in Figure A.9. However, in Machine A this effect is more significant.

The no-load rotor losses obtained using transient FEA are shown in Figure A.10. Table A.4 shows a comparison of the average no-load rotor losses obtained with the linear transient FEA, the CP function taking into account the effect of curvature and the CP function neglecting the effect of curvature for the machines under study running at rated speed. The no-load rotor losses were calculated using the current sheet model described in section 5.3.

TABLE A.4: No-load rotor power loss

Machine		A	B
Transient FEA	$\approx$	25.4 W	76.2 W
Model with curvature	$\approx$	22.7 W	87.0 W
Model without curvature	$\approx$	12.7 W	67.0 W

The no-load rotor losses obtained using the CP function without curvature are significantly lower than the result obtained using FEA. On the other hand, the value obtained when the effect of curvature is taken into account agrees reasonably well with FEA. In Machine A, the model with curvature underestimates the losses by a factor of 0.89 compared to the model without curvature, which underestimates losses by a factor of 0.5. In machine B, the model with curvature overestimates the losses by a factor of 1.14 and in the model without curvature underestimates the losses by a factor of 0.88. This is consistent with the fact that the curvature coefficient is higher in Machine A than in Machine B and as expected the discrepancy between the results neglecting curvature and FEA is greater in Machine A.

The difference between FEA and the model with curvature may be explained to be due to numerical errors as well as the assumptions made in the current sheet model.

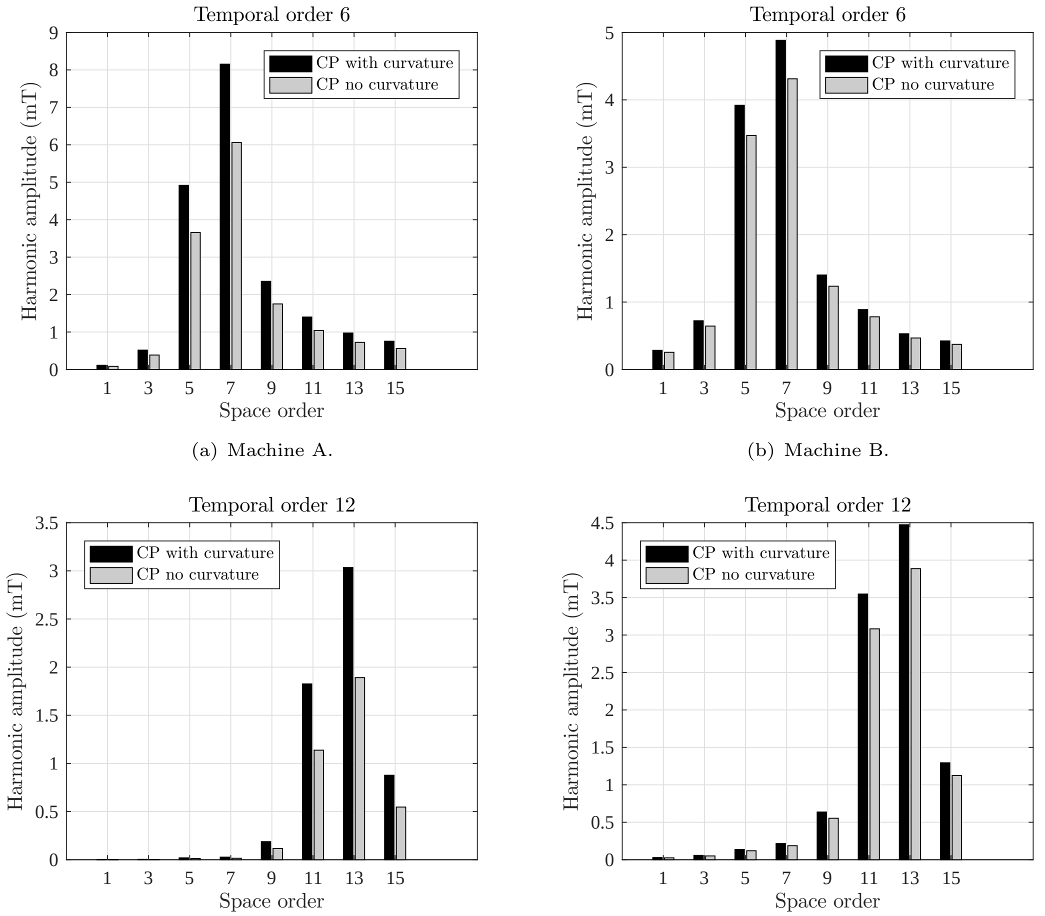

(a) Machine A. (b) Machine B.

(c) Machine A. (d) Machine B.

FIGURE A.9: Amplitudes of significant magnetic induction space harmonics, Machine A is running at 65 000 rpm and Machine B is running at 32 500 rpm.

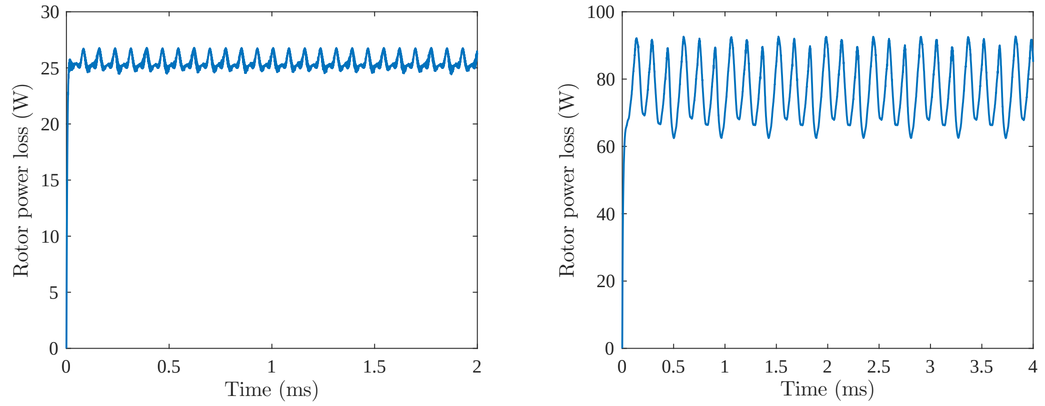

(a) Machine A. (b) Machine B.

FIGURE A.10: No-load rotor power loss at rated speeds calculated using transient FEA.

A.2.3 Conclusions

The value of the curvature coefficient, K_J which is the ratio of the air-gaps in the rectangular and cylindrical models in the w and z-planes, respectively, tends to be small. However, this small change of the air-gap length in the w-plane has a significant influence in the amplitude of the asynchronous harmonics of the magnetic field distribution as shown in Figure A.9.

The case study presented in section A.2 illustrates how strong the effect of curvature can be in machines with a large effective air-gap, particularly on rotor losses. Ignoring the effect of curvature grossly underestimates the no-load eddy current losses in the rotor in Machine A with large ratio of air-gap length to radius ratio. On the other hand, the effect of curvature is less significant in Machine B as anticipated from the smaller value of K_J.

Appendix B

Simulation of Electro-mechanical Systems

The equations proposed in sections 4.2 and 4.4 can be used to simulate the response of the electro-mechanical system. We can consider the electro-mechanical energy conversion system a *black box* with two terminals, one that corresponds to the *mechanical world* and the other one to the *electrical world* as shown in Figure B.1. This method is usually referred as the Conservation of Energy Method (Woodson and Melcher, 1968).

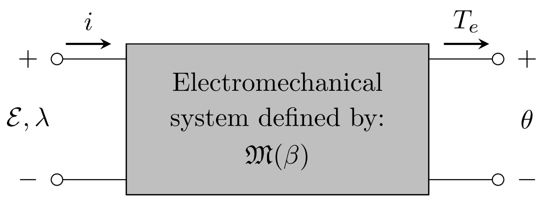

FIGURE B.1: Schematic electromechanical energy conversion system.

The mechanical terminal has two variables, T_e and θ that are the electromagnetic torque and the rotor position. The electrical terminal has also two variables, $\mathcal{E}$ and i that are the voltage and current respectively. The induced voltage is the derivative of the flux linkage, which in this context is usually called λ:

$$\mathcal{E} = -\frac{d\lambda}{dt}, \tag{B.1}$$

were λ is obtained using the virtual mutual inductance approach. On the other hand, the mechanical system is ruled by the following equation:

$$J\frac{d\Omega(t)}{dt} = T_m - T_d - T_e + T_{cog}, \tag{B.2}$$

where J is the inertia of the shaft, $\Omega = N_c \cdot \omega$ the angular speed, N_c is the number of C-cores, T_e the electromagnetic torque, T_m the mechanical torque (load in a motor for example), $T_{cog}(\theta)$ is the cogging torque and T_d a damping torque.

Figure B.2 shows a simplified block diagram that implements the proposed methodology. It shows that the instantaneous electromagnetic torque can be obtained from the torque equation described in section 4.2 and that the back emf (through the flux linkage) using the virtual mutual inductance approach from section 4.4.

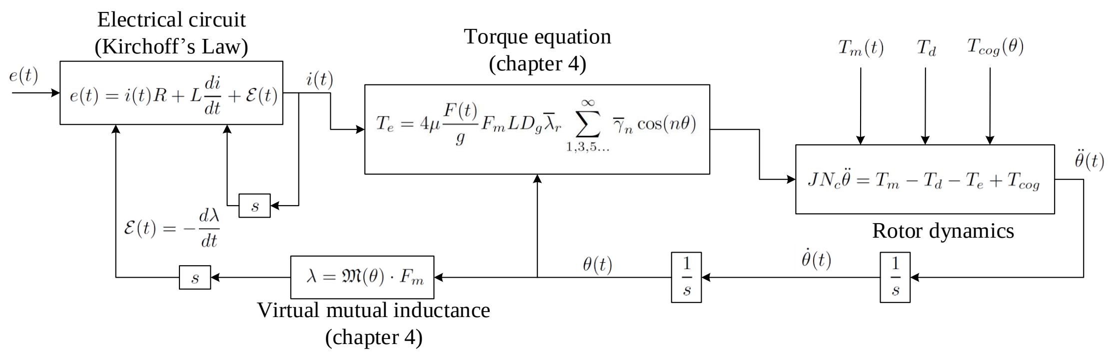

FIGURE B.2: Schematic representation of the simulation philosophy.

From the practical point of view, this simulation philosophy is particularly well suited to be implemented in Matlab+Simulink (MathWorks, 2017). One particularly attractive option is to combine this idea with the SimPowerSystems. Each of the phases of the machine can be represented with an inductance, a resistance and a controlled voltage source whose values come from the flux linkage obtained using the virtual mutual inductance approach.

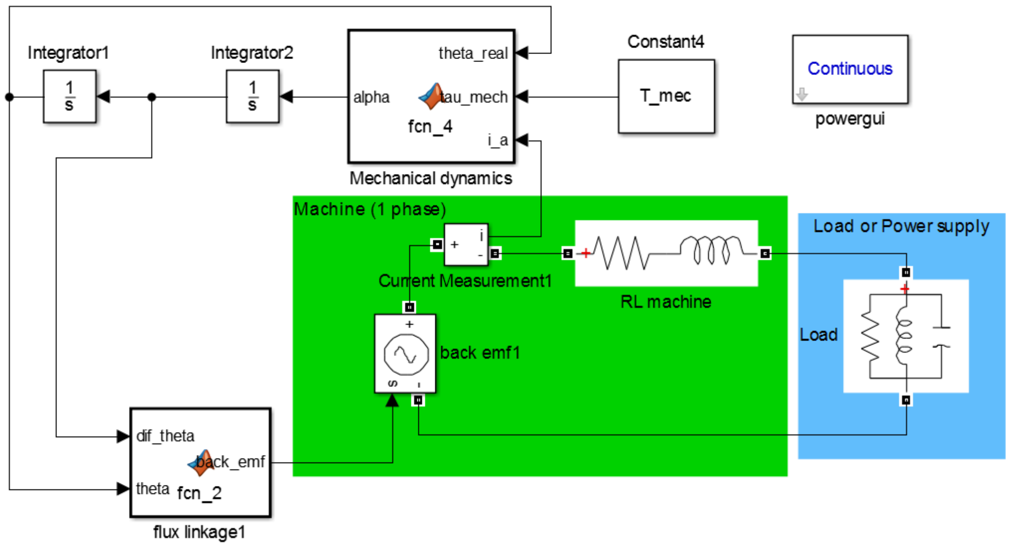

FIGURE B.3: One phase of the machine implemented in Simulink SimPowerSystems.

Figure B.3 shows the implementation of the proposed methodology in Matlab/Simulink. In this particular case, one phase of the machine connected to a load (or power supply) is shown in a simplified way. One block (a S-function) deals with the mechanical dynamics and the other one calculates the back emf that goes to the controlled power supply.

Appendix C

Software Developed in Matlab

C.1 Complex permeance function

```
function [ output_args ] = cp_func_renedo( Rm,Rs,Rr,bo,Qs,R,dslot )
%Calculates the CP according to Renedo.
%   It uses the SC toolbox developed by Driscoll.

mu0=4*pi*1e-7;

Rg=(Rr+Rs)/2;
N_points=1000;

% Parameters of the machine:

alpha_s=bo/Rs;
alpha_t=2*pi/Qs-alpha_s;


t=Rg*alpha_t;
s=Rg*alpha_s;
d=4*dslot;
delta=R-Rr;
g2=Rs-Rr;

theta_lambda=alpha_t+alpha_s;
theta_points=(0:(N_points))*theta_lambda/N_points;

% Coordinates of the problem:
s_dom= [Rr Rs Rs*(cos(alpha_t/2)+j*sin(alpha_t/2)) (Rs+d)*(cos(alpha_t/2)+j*sin(alpha_t/2)) (
    Rs+d)*(cos(alpha_t/2+alpha_s)+j*sin(alpha_t/2+alpha_s)) (Rs)*(cos(alpha_t/2+alpha_s)+j*
    sin(alpha_t/2+alpha_s)) (Rs)*(cos(alpha_t+alpha_s)+j*sin(alpha_t+alpha_s)) (Rr)*(cos(
    alpha_t+alpha_s)+j*sin(alpha_t+alpha_s))];
s_points=(Rr+delta)*(cos((0:N_points)*theta_lambda/N_points)+j*sin((0:N_points)*theta_lambda/
    N_points));

z_dom=log(s_dom);
z_points=log(s_points);

p=polygon(z_dom);
% Indicates the right angles in the Canonical Domain:
alpha=[0.5 0.5 1 1 1 1 0.5 0.5];

% Remember that acording to this criteria X is the plane with the toothed
% member and w is the plane with the canonical rectangle.

% Define the Canonical Domain:
```

```
f=crrectmap(p,alpha);

% Vertices of the canonical rectangle:
vc1=evalinv(f,z_dom(1));
vc2=evalinv(f,z_dom(2));
vc7=evalinv(f,z_dom(7));
vc8=evalinv(f,z_dom(8));
% figure
% plot([vc1 vc2 vc7 vc8])

g_poly=vc1-vc2;

l_poly=abs(vc1-vc8);
% Modified rectangle:

vc1_m=real(vc1)*log(Rr/Rs)/g_poly+j*imag(vc1)*theta_lambda/l_poly+log(Rr);
vc2_m=real(vc2)*log(Rr/Rs)/g_poly+j*imag(vc2)*theta_lambda/l_poly+log(Rr);
vc7_m=real(vc7)*log(Rr/Rs)/g_poly+j*imag(vc7)*theta_lambda/l_poly+log(Rr);
vc8_m=real(vc8)*log(Rr/Rs)/g_poly+j*imag(vc8)*theta_lambda/l_poly+log(Rr);

tp_points=evalinv(f,z_points);
for k=2:(N_points)
    %SC_derivative(k)=evaldiff(f,evalinv(f,z_points(k)));
    SC_derivative(k)=(evaldiff(f,tp_points(k)))^-1;
end
SC_derivative(1)=(evaldiff(f,evalinv(f,z_points(2))))^-1;
SC_derivative(N_points+1)=(evaldiff(f,evalinv(f,z_points(N_points-1))))^-1;

d_tz=real(SC_derivative)*log(Rr/Rs)/g_poly+j*imag(SC_derivative)*log(Rr/Rs)/g_poly;
t_points=real(tp_points)*log(Rr/Rs)/g_poly+j*imag(tp_points)*theta_lambda/l_poly+log(Rr);
k_points=exp(t_points);

for k=1:(N_points+1)
    d_ks(k)=k_points(k)*d_tz(k)/s_points(k);
end
cp_func=conj(d_ks);
output_args=[theta_points; cp_func];
end
```

C.2 Calculation of the no-load asynchronous harmonics

```

% Generic machine (inner rotor):
% Calculation of the space and time harmonics.

clc
clear all


%% Parameters:

mu_0=4*pi*10^-7; % [m kg s^-2 A^-2]

R_r=58.5*10^-3; % [m] rotor radius
R_s=70*10^-3; % [m] stator radius
R_m=66.5*10^-3; % [m] magnet radius
bo=3e-3; % [m] slot opening width

p=2; % pole pairs
alpha_p=1; % pole-arc to pitch ratio
Qs=48; % number of slots

c_gap=R_s-R_m; % [m] clearance gap
dslot=25e-3; %slot depth
```

```
B_r=1.05; % [T] magnet remanence CHECK THIS WITH SULEIMAN
H_c=B_r/mu_0; % A/m
mu_r=1.05; % relative permeability


N_harm=1551; % maximum harmonic order, has to be even
N_points=1000; % number of points for the waveform

r=R_m+0.01*10^-3; % [m] radius where we want to calculate the waveform
R_wave=r;

N_pos=350;

%% Calculation of the coefficientsof magnetisation:

M_vec=zeros(1,N_harm);

for count=1:2:N_harm
    n=count;
    A1(count)=sin((n*p+1)*alpha_p*pi/2/p)/((n*p+1)*alpha_p*pi/2/p);
    A2(count)=sin((n*p-1)*alpha_p*pi/2/p)/((n*p-1)*alpha_p*pi/2/p);

    Mr_vec(count)=(B_r/mu_0)*alpha_p*(A1(count)+A2(count));
    Mt_vec(count)=(B_r/mu_0)*alpha_p*(A1(count)-A2(count));

    M_vec(count)=Mr_vec(count)+n*p*Mt_vec(count);

    A3(count)=(n*p-1/n/p)*Mr_vec(count)/M_vec(count)+1/n/p;
end

%% Calculate waveform for a given r>Rm:
% In the air-gap.

if R_m<r
    % eq. (34) and (35) in Zhu's paper 1993:

    theta=(0:N_points)*pi/p/(N_points)-pi/2/p;
    % Calculation of the coeficients:

    for count=1:2:N_harm
        n=count;
        KB=mu_0*M_vec(count)/mu_r*n*p/((n*p)^2-1)*((A3(count)-1)+2*(R_r/R_m)^(n*p+1)-(A3(count)+1)*(R_r/R_m)^(2*n*p))/((mu_r+1)/mu_r*(1-(R_r/R_s)^(2*n*p))-(mu_r-1)/mu_r*((R_m/R_s)^(2*n*p)-(R_r/R_m)^(2*n*p))); % checked
        f_Br=(r/R_s)^(n*p-1)*(R_m/R_s)^(n*p+1)+(R_m/r)^(n*p+1);
        f_Bt=-(r/R_s)^(n*p-1)*(R_m/R_s)^(n*p+1)+(R_m/r)^(n*p+1);

        coefs_radial(count)=KB*f_Br;
        coefs_tan(count)=KB*f_Bt;
    end

    B_rI=zeros(1,length(theta));
    B_tI=zeros(1,length(theta));
    for count=1:N_harm
        n=count;
        B_rI=B_rI+coefs_radial(count)*cos(n*p*theta);
        B_tI=B_tI+coefs_tan(count)*sin(n*p*theta);

    end
    B_r=B_rI;
    B_t=B_tI;

end

%% Calculate waveform for a given r<=Rm
% In the magnets.
```

```
if R_m>=r

    % eq. (36) and (37) in Zhu's paper 1993:

    theta=(0:N_points)*pi/p/(N_points)+pi/2/p/2;

    % Calculation of the coeficients:

    for count=1:2:N_harm
        n=count;
        C2=((A3(count)-1/mu_r)*(R_m/R_s)^(2*n*p)+(1+1/mu_r)*(R_r/R_m)^(n*p+1)*(R_m/R_s)^(2*n*
    p)-(A3(count)+1/mu_r)-(1-1/mu_r)*(R_r/R_m)^(n*p+1))/((mu_r+1)/mu_r*(1-(R_r/R_s)^(2*n*p))
    -(mu_r-1)/mu_r*((R_m/R_s)^(2*n*p)-(R_r/R_m)^(2*n*p)));

        C1=mu_0*M_vec(count)*n*p/((n*p)^2-1)*C2*((r/R_m)^(n*p-1)+(R_r/R_m)^(n*p-1)*(R_r/r)^(n
    *p+1));

        C1s=mu_0*M_vec(count)*n*p/((n*p)^2-1)*C2*((r/R_m)^(n*p-1)-(R_r/R_m)^(n*p-1)*(R_r/r)^(
    n*p+1));

        B1=mu_0*M_vec(count)*n*p/((n*p)^2-1)*(R_r/r)^(n*p+1);

        D1=mu_0*M_vec(count)*n*p/((n*p)^2-1)*A3(count);
        D1s=mu_0*M_vec(count)/((n*p)^2-1)*A3(count);

        coefs_radial(count)=C1+B1+D1;
        coefs_tan(count)=-C1s+B1-D1s;


    end

    B_rII=zeros(1,length(theta));
    B_tII=zeros(1,length(theta));
    for count=1:N_harm
        n=count;
        B_rII=B_rII+coefs_radial(count)*cos(n*p*theta);
        B_tII=B_tII+coefs_tan(count)*sin(n*p*theta);

    end

    B_r=B_rII;
    B_t=B_tII;

end


theta_p=(0:N_points)*2*pi/p/(N_points); % electrical angle




Br_slotless=B_r;
Bt_slotless=B_t;
theta=theta_p; % electrical angle


%% Complex permeance:
temp2=cp_func_renedo( R_m,R_s,R_r,bo,Qs,R_wave,dslot );
cp_func=temp2(2,:);
theta_points=temp2(1,:); % mechanical angle


% Calculate the coeffs of the fourier series multiple slots:

f1_t=imag(cp_func);
f1_r=real(cp_func);

```

```
theta_integration=theta_points*Qs; % to make it up to 2*pi

a_0=1/2/pi*trapz(theta_integration,f1_r);
a_1=1/pi*trapz(theta_integration,f1_r.*cos(1*theta_integration));
a_2=1/pi*trapz(theta_integration,f1_r.*cos(2*theta_integration));
a_3=1/pi*trapz(theta_integration,f1_r.*cos(3*theta_integration));
a_4=1/pi*trapz(theta_integration,f1_r.*cos(4*theta_integration));
a_5=1/pi*trapz(theta_integration,f1_r.*cos(5*theta_integration));
a_6=1/pi*trapz(theta_integration,f1_r.*cos(6*theta_integration));
a_7=1/pi*trapz(theta_integration,f1_r.*cos(7*theta_integration));

b_1=1/pi*trapz(theta_integration,f1_t.*sin(1*theta_integration));
b_2=1/pi*trapz(theta_integration,f1_t.*sin(2*theta_integration));
b_3=1/pi*trapz(theta_integration,f1_t.*sin(3*theta_integration));
b_4=1/pi*trapz(theta_integration,f1_t.*sin(4*theta_integration));
b_5=1/pi*trapz(theta_integration,f1_t.*sin(5*theta_integration));
b_6=1/pi*trapz(theta_integration,f1_t.*sin(6*theta_integration));
b_7=1/pi*trapz(theta_integration,f1_t.*sin(7*theta_integration));

% make sure the phase is right.
alpha=0;
theta_temp=Qs*(theta/p+alpha);
f_tempr=a_0+a_1*cos(theta_temp)+a_2*cos(2*theta_temp)+a_3*cos(3*theta_temp)+a_4*cos(4*theta_temp)+a_5*cos(5*theta_temp)+a_6*cos(6*theta_temp)+a_7*cos(7*theta_temp);
f_tempt=b_1*sin(theta_temp)+b_2*sin(2*theta_temp)+b_3*sin(3*theta_temp)+b_4*sin(4*theta_temp)+b_5*sin(5*theta_temp)+b_6*sin(6*theta_temp)+b_7*sin(7*theta_temp);

% Apply the complex permeance:

B_slotless_complex=Br_slotless+i*Bt_slotless;
cp_func_adapted=conj(f_tempr+i*f_tempt);

cp_func_adapted=(f_tempr+i*f_tempt);

Bcp_complex=B_slotless_complex.*cp_func_adapted;
Bcp_r=real(Bcp_complex);
Bcp_t=imag(Bcp_complex);

%% Several rotor positions:

clear theta theta_temp
% make sure the phase is right.

alpha_vec=(0:N_pos)/(N_pos)*2*pi/Qs; % mechanical

theta=(0:N_points)*pi/(N_points); % electrical
alpha=0;


count=1;

x_ms=zeros(length(theta),length(alpha_vec));
y_ms=zeros(length(theta),length(alpha_vec));


for alpha=alpha_vec;
    theta_temp=Qs*(theta/p+alpha); % to make it up to 2*pi
    f_tempr=a_0+a_1*cos(theta_temp)+a_2*cos(2*theta_temp)+a_3*cos(3*theta_temp)+a_4*cos(4*theta_temp)+a_5*cos(5*theta_temp)+a_6*cos(6*theta_temp)+a_7*cos(7*theta_temp);
    f_tempt=b_1*sin(theta_temp)+b_2*sin(2*theta_temp)+b_3*sin(3*theta_temp)+b_4*sin(4*theta_temp)+b_5*sin(5*theta_temp)+b_6*sin(6*theta_temp)+b_7*sin(7*theta_temp);
    % Apply the complex permeance:

    B_slotless_complex=Br_slotless+i*Bt_slotless;
    cp_func_adapted=conj(f_tempr+i*f_tempt);

    Bcp_complex=B_slotless_complex.*cp_func_adapted;
    Bcp_r=real(Bcp_complex);
```

```
    Bcp_t=imag(Bcp_complex);

    x_ms(:,count)=Bcp_r;
    y_ms(:,count)=Bcp_t;
    count=count+1;
end
time=transpose(theta/pi*180);

%% Calculate FFT

% Multiple slots:

[m1,n1]=size(x_ms);
%Matrix manipulation
%Data for N-pole Xn
%
x1=(x_ms(1,:)-x_ms(m1,:))/2;
x1n=x_ms(2:m1-1,:);
Xn=[x1;x1n];
%Generating points for S-pole, data for S-pole is the negative of data for N-pole
Xs=-Xn;
%
Xns=[Xn;Xs];
time2 = linspace(0,time(end)*2,size(Xns,1));

[m,n]=size(Xns);
Xnsfft2=fft2(Xns);
Xnsabs=abs(Xnsfft2)/(m*n);
%Matrix manipulation
X=Xnsabs;
if rem(m,2)==0,
    X1m0=X(2:(m/2),1);
    X2m0=X(m/2+2:m,1);
    X2m0=flipud(X2m0);
    Xm0=X1m0+X2m0;
    %
    X13=X(2:m/2,2:n);
    X24=X(m/2+2:m,2:n);
    X24=flipud(fliplr(X24));
    X1234=X13+X24;
    Y=zeros(m/2,n);
    Y(1,:)=X(1,:);
    Y(2:m/2,1)=Xm0;
    Y(2:m/2,2:n)=X1234;
else
    X1m0=X(2:m/2+0.5,1);
    X2m0=X(m/2+1:m,1);
    X2m0=flipud(X2m0);
    Xm0=X1m0+X2m0;
    %
    X13=X(2:m/2+0.5,2:n);
    X24=X(m/2+1:m,2:n);
    X24=flipud(fliplr(X24));
    X1234=X13+X24;
    %
    Y=zeros(m/2+0.5,n);
    Y(1,:)=X(1,:);
    Y(2:m/2+0.5,1)=Xm0;
    Y(2:m/2+0.5,2:n)=X1234;
end
% if Y is partitioned from the middle column, then the first part represent the forward
    rotating waves and second part the backward rotating waves.
Xfft2=Y;
%Mat_to_write = Y(2:2:20,1:6);
Mat_to_write = Y;
%xlswrite('multiple_slots_mat',Mat_to_write)

Mat_multiple_slots=Y(1:70,1:70);
```

```

for k1=1:length(Y(:,1))
    %Y_n(k1,:)=Y(k1,:);
    for k2=1:length(Y(1,:))
        Y_n(k1,k2)=Y(k1,length(Y(1,:))-k2+1);
    end
end
Mat_multiple_slots_n=Y_n(1:70,1:70);
```

C.3 Class that defines a TFM

```
classdef tfm_class < handle
% airgap_screen: represents the airgap of the VRPM machine with
% superconducting screens to clock the magnetic field. Considering the
% effect of curvature. It is based on SC Toolbox developed by driscoll
% Jaime Renedo Anglada, University of Southampton

    properties
        s_self
        t_self
        g_self
        d_self
        gnew_self
        Rg_self
        n_cores

        polygon_self
        map_self
        h_canonical

        coeffs_pf
    end
    methods
        %% Definition of the object:

        function obj = airgapVRPM_no_screen_curvature (input_s, input_t, input_g, input_d, input_Rg,n_cores)
            obj.s_self = input_s;
            obj.t_self = input_t;
            obj.g_self = input_g;
            obj.Rg_self = input_Rg;
            obj.d_self = input_d;
            obj.n_cores=n_cores;
        end

        %% Building the conformal map from the SC toolbox

        function obj = build_map (obj)
            s=obj.s_self;
            t=obj.t_self;
            g=obj.g_self;
            Rg=obj.Rg_self;
            d=obj.d_self;

            gnew=Rg*log((Rg+g/2)/(Rg-g/2));
            obj.gnew_self=gnew;

            % Polygon for SC toolbox (Driscoll)
            path(path,'C:\Users\jra1c13\Documents\MATLAB\sc')
            % Geometric operations for the map:
            % Generate a polygon with the geometry of the problem:
            v=[d*i t/2+d*i t/2 t/2+s t/2+s+d*i t+s+d*i t+s+(d+gnew)*i (d+gnew)*i];
            v1=v(1);
            v2=v(2);
```

```
            v3=v(3);
            v4=v(4);
            v5=v(5);
            v6=v(6);
            v7=v(7);
            v8=v(8);

            p=polygon(v);
            obj.polygon_self=p;

            % Indicates the right angles in the Canonical Domain:
            alpha=[0.5 1 1 1 1 0.5 0.5 0.5];

            % Remember that acording to this criteria X is the plane with the toothed
            % member and w is the plane with the canonical rectangle.

            % Define the Canonical Domain:

            f=crrectmap(p,alpha);
            obj.map_self=f;

            % Vertices of the canonical rectangle:
            vc1=evalinv(f,v1);
            vc6=evalinv(f,v6);
            vc7=evalinv(f,v7);
            vc8=evalinv(f,v8);

            obj.h_canonical=abs(vc1-vc8); % height of the canonical rectangle.

        end
        %% Magnetic field waveform
        % delta is the distance to the coreback, V is the MMF and n_points
        % is the number of points evaluated. In case we want to plot it.

        function result = B_func (obj,delta,V,n_points)

            s=obj.s_self;
            t=obj.t_self;
            g=obj.g_self;
            d=obj.d_self;
            gnew=obj.gnew_self;
            Rg=obj.Rg_self;

            f=obj.map_self;

            result=zeros(3,2*n_points-1);


            B_w=V/obj.h_canonical;

            l_ag_line=n_points;
            Br=zeros(l_ag_line,1);
            Bt=zeros(l_ag_line,1);

            Ri=Rg+g/2-delta;
            delta_SC=Rg*log((Rg+g/2)/(Rg+g/2-delta)); %distance in the w plane

            ag_line=(gnew-delta_SC+d)*i+(s+t)/2*(0:n_points)/n_points;
            x=real(ag_line);

            for count=2:(l_ag_line-1)
                dif=evaldiff(obj.map_self,evalinv(f,ag_line(count)));
                B_temp=B_w/conj(dif)*Rg/Ri;

                Br(count)=real(B_temp);
                Bt(count)=imag(B_temp);

            end
```

```
            Br(1)=Br(2);
            Bt(1)=0;

            count=l_ag_line;
            Br(count)=Br(count-1);
            Bt(count)=0;

            for count=1:n_points
                result(1,count)=Br(count);
                result(2,count)=Bt(count);
                result(3,count)=x(count);

                if count<n_points
                    result(1,2*n_points-count)=Br(count);
                    result(2,2*n_points-count)=-Bt(count);
                    result(3,2*n_points-count)=s+t-x(count);
                end

            end

        end


        %% Evaluation of lambda(theta,r) at one point
        % delta is the distance to the coreback, V is the MMF and n_points
        % is the number of points evaluated. In case we want to plot it.

        function result = eval_lambda (obj,theta_in,r_in)

            s=obj.s_self;
            t=obj.t_self;
            g=obj.g_self;
            d=obj.d_self;
            gnew=obj.gnew_self;
            Rg=obj.Rg_self;

            f=obj.map_self;
            V=g;
            B_w=V/obj.h_canonical;
            Ri=r_in;
            delta=Rg+g/2-Ri;
            delta_SC=Rg*log((Rg+g/2)/(Rg+g/2-delta)); %distance in the w plane
            point=(gnew-delta_SC+d)*i+(s+t)/(2*pi)*theta_in;

            dif=evaldiff(obj.map_self,evalinv(f,point));
            B_temp=B_w/conj(dif)*Rg/Ri;
            result=B_temp;

        end


        %% Evaluation of lambda(theta,r) at one point
        % delta is the distance to the coreback, V is the MMF and n_points
        % is the number of points evaluated. In case we want to plot it.

        function result = gen_vec_points(obj,N_points,dm)
            g=obj.g_self;
            Rg=obj.Rg_self;

            for k=1:N_points
                result(k,:)=[(0.01+0.98*rand(1,1))*2*pi Rg+g/2-(0.01+0.98*rand(1,1))*dm ];
            end


        end


        %% Evaluation of lambda(theta,r) at one point
```

```
        % delta is the distance to the coreback, V is the MMF and n_points
        % is the number of points evaluated. In case we want to plot it.

        function result = eval_coeffs_lambdar (obj,vec_points,N_harmonics,N_poly)

            s=obj.s_self;
            t=obj.t_self;
            g=obj.g_self;
            d=obj.d_self;
            gnew=obj.gnew_self;
            Rg=obj.Rg_self;

            f=obj.map_self;

            result=zeros(N_harmonics+1,N_poly+1);
            lambda_sol=zeros(1,length(vec_points(:,1)));
            delta_temp=zeros(1,length(vec_points(:,1)));

            for count1=1:length(vec_points(:,1))
%                 Rg+g/2-vec_points(count1,2)
                lambda_sol(count1)=real(obj.eval_lambda(vec_points(count1,1),vec_points(count1,2)))*vec_points(count1,2)/Rg;
                delta_temp(count1)=Rg+g/2-vec_points(count1,2);
                theta_temp(count1)=vec_points(count1,1);
            end

            Delta=zeros(length(vec_points(:,1)),1+N_harmonics*(N_poly+1));

            Delta(:,1)=Delta(:,1)+1;

            for count1=1:length(vec_points(:,1))
                control_count=0;
                control_count2=1;
                for count2=2:(N_harmonics*(N_poly+1)+1)
                    Delta(count1,count2)=delta_temp(count1)^control_count*cos(control_count2*theta_temp(count1));
                    if control_count==N_poly
                        control_count=0;
                        control_count2=control_count2+1;
                    else
                        control_count=control_count+1;
                    end
                end
            end


            Gamma=(inv(transpose(Delta)*Delta)*transpose(Delta))*transpose(lambda_sol);

            result(1,1)=Gamma(1);
            count_aux=2;
            for count1=2:(N_harmonics+1)

                for count2=1:(N_poly+1)
                    result(count1,count2)=Gamma(count_aux)/Gamma(1);
                    count_aux=count_aux+1;
                end
            end
            obj.coeffs_pf=result;
        end


         %% Evaluation of lambda(theta,r) at one point
        % delta is the distance to the coreback, V is the MMF and n_points
        % is the number of points evaluated. In case we want to plot it.

        function result = pflux_linkage (obj,dm)

            coeffs_func=obj.coeffs_pf;
```

```
            n_cores=obj.n_cores;

            resolution=25;

            N_terms=length(coeffs_func(1,:));
            N_harm=length(coeffs_func(:,1));

            coeffs_func(1,1)

            coeffs_mod=coeffs_func((2:N_harm),:);

            count2=1;
            for delta_c=0:(dm/resolution):dm
                for h=1:N_terms
                    temp_delta(h,1)=delta_c^(h-1);
                end

                gamma_matrix(count2,:)=coeffs_mod*temp_delta;

                count2=count2+1;
            end
%             gamma_matrix
            gamma_av1=mean(gamma_matrix(:,1))
            gamma_av3=mean(gamma_matrix(:,3))
            gamma_av5=mean(gamma_matrix(:,5))
            gamma_av7=mean(gamma_matrix(:,7))

            mu_0=4*pi*10^-7;
            Rg=obj.Rg_self
            L=0.036/2;
            Mag=1.05/(4*pi*10^-7);
            n=20;
            N_wind=115;
            g=obj.g_self

            K=4*mu_0*Rg*L/g/n_cores; % we need to check this

            beta=0:(2*pi/100):(2*pi);
            M_func=K*coeffs_func(1,1)*(gamma_av1*cos(beta)-gamma_av3*cos(3*beta)/3+gamma_av5*cos(5*beta)/5-gamma_av7*cos(7*beta)/7);
            result=M_func;

            Phi_func=n*M_func*Mag*dm*10^-3*N_wind;
%
            plot(beta,Phi_func)
%             for beta=0:(2*pi/100):(2*pi)
%
%
%             end

        end



        %% Expression of the magnetic field as Fourier Series:

        function fourier_coeffs = fourier_series(obj,delta,V,n_points)
            temp_matrix=obj.B_func (delta,V,n_points);
            lambda=obj.s_self+obj.t_self; % because we defined x of length lambda

            x=temp_matrix(3,:);
%             x(length(x))
%             lambda
            Br=temp_matrix(1,:);
            Bt=temp_matrix(2,:);


            % Using trapz fuction:
```

```
            alpha=trapz(x,Br)/lambda;
            Bm=alpha;


            F1=Br.*(cos(2*1*pi*x./lambda));
            F2=Br.*(cos(2*2*pi*x./lambda));
            F3=Br.*(cos(2*3*pi*x./lambda));
            F4=Br.*(cos(2*4*pi*x./lambda));
            F5=Br.*(cos(2*5*pi*x./lambda));

            gamma_1=trapz(x,F1)*2/(lambda*Bm);
            gamma_2=trapz(x,F2)*2/(lambda*Bm);
            gamma_3=trapz(x,F3)*2/(lambda*Bm);
            gamma_4=trapz(x,F4)*2/(lambda*Bm);
            gamma_5=trapz(x,F5)*2/(lambda*Bm);

            fourier_coeffs=[Bm gamma_1 gamma_2 gamma_3 gamma_4 gamma_5];
        end


      %% KB calculation:
        % n_int: the number of points for the integration layers

        function Kb_out = Kb_calc_square (obj,dm)
            coeffs_func=obj.coeffs_pf;
            n_cores=obj.n_cores;

            resolution=50;

            N_terms=length(coeffs_func(1,:));
            N_harm=length(coeffs_func(:,1));

            coeffs_func(1,1);

            coeffs_mod=coeffs_func((2:N_harm),:);

            count2=1;
            for delta_c=0:(dm/resolution):dm
                for h=1:N_terms
                    temp_delta(h,1)=delta_c^(h-1);
                end

                gamma_matrix(count2,:)=coeffs_mod*temp_delta;

                count2=count2+1;
            end
%             gamma_matrix
            gamma_av1=mean(gamma_matrix(:,1));
            gamma_av3=mean(gamma_matrix(:,3));
            gamma_av5=mean(gamma_matrix(:,5));
            gamma_av7=mean(gamma_matrix(:,7));
            Kb_out=4/pi*coeffs_func(1,1)*(gamma_av1-gamma_av3/3+gamma_av5/5-gamma_av7/7)

        end


      %% KB calculation:
        % n_int: the number of points for the integration layers

        function Kb_out = Kb_calc_sin (obj,dm)
            coeffs_func=obj.coeffs_pf;
            n_cores=obj.n_cores;

            resolution=50;

            N_terms=length(coeffs_func(1,:));
            N_harm=length(coeffs_func(:,1));

```

```
            coeffs_func(1,1);

            coeffs_mod=coeffs_func((2:N_harm),:);

            count2=1;
            for delta_c=0:(dm/resolution):dm
                for h=1:N_terms
                    temp_delta(h,1)=delta_c^(h-1);
                end

                gamma_matrix(count2,:)=coeffs_mod*temp_delta;

                count2=count2+1;
            end
%             gamma_matrix
            gamma_av1=mean(gamma_matrix(:,1));
            gamma_av3=mean(gamma_matrix(:,3));
            gamma_av5=mean(gamma_matrix(:,5));
            gamma_av7=mean(gamma_matrix(:,7));


            Kb_out=coeffs_func(1,1)*(gamma_av1)

        end

        %% Plot the magnetic field:
        % n_int: the number of points for the integration layers

        function result = plot_field (obj,n_pointsu,n_pointsv,V)

            g=obj.g_self;
            s=obj.s_self;
            t=obj.t_self;
            d=obj.d_self;
            Rg=obj.Rg_self;
            lambda=s+t;
            f=obj.map_self;

            B_w=V/obj.h_canonical;
            theta_lambda=lambda/Rg;
            theta_s=s/Rg;
            theta_t=t/Rg;


            Z_coord=zeros(2*n_pointsu,n_pointsv);
            B_com=zeros(2*n_pointsu,n_pointsv);
            Br=zeros(2*n_pointsu,n_pointsv);
            Bt=zeros(2*n_pointsu,n_pointsv);

            distance_g=(0:(2*n_pointsu))*g*2/n_pointsu;
            %distance_g_w=Rg*log((Rg+g/2)/(Rg+g/2-distance_g))
            theta_vec=(0:n_pointsv)*theta_lambda/n_pointsv;

            for k=1:(2*n_pointsu)
                for h=1:(n_pointsv)
                    r_temp=Rg+g/2-distance_g(k);
                    Z_coord(k,h)=r_temp*exp(i*theta_vec(h));
                    d_w=Rg*log((Rg+g/2)/r_temp);
%                     Z_coord(k,h)
                    w_temp=i*(d+g-d_w)+theta_vec(h)*Rg;
                    if r_temp>(Rg-g/2)
                        if k==1
                            r_temp=Rg-distance_g(2)+g/2;
                            d_w=Rg*log((Rg+g/2)/r_temp);
                            w_temp=i*(d+g-d_w)+theta_vec(h)*Rg+lambda/10000;
                            dif=evaldiff(obj.map_self,evalinv(f,w_temp));
                            B_temp=B_w/conj(dif)*Rg/r_temp;
                            B_com(k,h)=B_temp;
```

```
                        elseif h==1
                            w_temp=i*(d+g-d_w)+theta_vec(2)*Rg;
                            B_temp=B_w/conj(dif)*Rg/r_temp;
                            B_com(k,h)=B_temp;
                        elseif h==n_pointsv
                            w_temp=i*(d+g-d_w)+theta_vec(n_pointsv-1)*Rg;
                            B_temp=B_w/conj(dif)*Rg/r_temp;
                            B_com(k,h)=B_temp;

                        else
%                             w_temp
                            dif=evaldiff(obj.map_self,evalinv(f,w_temp));
                            B_temp=B_w/conj(dif)*Rg/r_temp;
                            B_com(k,h)=B_temp;
                        end

                    elseif theta_vec(h)>(theta_t/2) && theta_vec(h)<(theta_t/2+theta_s)
                        dif=evaldiff(obj.map_self,evalinv(f,w_temp));
                        B_temp=B_w/conj(dif)*Rg/r_temp;
                        B_com(k,h)=B_temp;
%                         B_com(k,h)=0;

                    else
                        B_com(k,h)=NaN;

                    end

                end
            end
            X=real(Z_coord);
            Y=imag(Z_coord);

            F_z=B_com;


           figure
            %VectorField2d([real(F_z), imag(F_z)], X,Y);
            contourf(X,Y,real(F_z),100,'LineStyle','none')

            figure
            %VectorField2d([real(F_z), imag(F_z)], X,Y);
            contourf(X,Y,imag(F_z),100,'LineStyle','none')


        end

    end

end
```

C.4 Example of the modelling of a TFM

```
%   This code studies the optimal number of C-cores as a function of the normalised parameters.
%   It is based in conformal mapping and uses the
%   SC-toolbox by Driscoll and a logarithmic conformal transformation.
%   Author: Jaime Renedo Anglada, University of Southampton
%   s: slot width
%   g: airgap
%   t: tooth width
%   d: slot depth
%   R_coreback: radius of the coreback of the machine
%   dm: magnet width

```

```
%% Add the path of the library and define standar variables:

clc
clear all

t_lambda=0.39;

N=11;
res_B=1000;

vec_cores=1:35;


D=151.5; % [mm]
R_g=D/2;
g=5.5; % [mm]
dm=4.51; % [mm]
c_gap=g-dm; % [mm]
F=sqrt(2)*1150; % [A]
Mag=1.05/(4*pi*10^-7);
Fm=Mag*dm*10^-3; % [A]
Leq=17.11; % [mm]
mu_0=4*pi*10^-7;
mu_r=1.05;
mu_eq=(mu_r*dm+g-dm)/g;
Bs=mu_eq*mu_0*F/g*10^3;  % [T]
N_wind=230;

count=1;
for N_cores=vec_cores
    count

    lambda=pi*D/N_cores
    t=t_lambda*lambda;
    s=lambda-t;
    d=3*lambda;

    test2_curv=tfm_class (s,t,g,d,R_g,N_cores);
    test2_curv.build_map
    points=test2_curv.gen_vec_points(1000,dm);
    N_harm=11;
    N_pol=5;
    coeffs_func=test2_curv.eval_coeffs_lambdar (points,N_harm,N_pol);
    lambda_r=coeffs_func(1,1);
    K_B=test2_curv.Kb_calc_sin(dm);
    Kb(count)=K_B;
    Ke(count)=K_B;
    Torque(count)=2*Kb(count)*N_cores*Bs*Fm*D*Leq*10^-6;

   % Inductance:
   L_ind(count)=mu_eq*mu_0*N_wind^2/g*pi*lambda_r*Leq*R_g*10^-3;
   h1=24;
   h2=2;
   ws=20;
   lambda_say=h1/3/ws+h2/ws;

   % half the value of Say because there is half the leakage. is it good?
   angle_t=t/R_g;
   L_leak(count)=N_cores*mu_0*N_wind^2*lambda_say*angle_t*(R_g-g/2)*10^-3;
   omega=2*pi*50;
   rms_emf=2*sqrt(2)*mu_0*N_wind*Fm*K_B*omega*Leq*R_g/g*10^-3;
   amp_rms=10;
   phi(count)=atand(amp_rms*(L_ind(count)+L_leak(count))*omega/rms_emf);
   phi2(count)=atand(amp_rms*(L_ind(count))*omega/rms_emf);

   power_factor(count)=cosd(phi(count));
   power_factor2(count)=cosd(phi2(count));

```

```
    count=count+1;
end


save('data_power_factor')
```

C.5 Calculation of the rotor losses in a TFM

```

%% Calculate the rotor losses:
% This is the code that uses Bessel fuctions to calculate the rotor losses.
% Author: Jaime Renedo Anglada, University of Southampton.
clc
clear all

% Modified bessel function of the first kind: I = besseli(nu,Z)
% Modified bessel function of the second kind: K = besselk(nu,Z)
% k_p=sqrt(j*omega*mu*sigma)
%



%% Parameters (TFM soton):

mu_0=4*pi*10^-7; % [m kg s^-2 A^-2]
p=20; % pairs of poles

B_given=0.09; % [T]
time_order_given=1;
space_order_given=2;


n_rpm=300; % [rpm]

f_1=n_rpm/60*p; % [Hz]
f_1=50;
omega=2*pi*f_1; % [rad/sec]
alpha_p=1;

mu_r=1.05;

R_1=73*10^-3; % [m] rotor radius
R_2=74*10^-3; % [m] magnet radius
R_3=78.5*10^-3; % [m] stator radius
R_4=85*10^-3; % [m] outer radius

R_wave=73.75e-3; % [m]

L=17*10^-3; % [m] axial length
% L=1;


sigma_1_eval=3*10^-15; % [S/m]
sigma_2_eval=3*10^-15; % [S/m]
sigma_3_eval=0.77*10^6; % [S/m]
sigma_4_eval=6.7*10^6; % [S/m]



mu_1=5000*mu_0; % [m kg s^-2 A^-2]
mu_2=mu_0; % [m kg s^-2 A^-2]
mu_3=mu_r*mu_0; % [m kg s^-2 A^-2]
mu_4=750*mu_0; % [m kg s^-2 A^-2]

```

```
delta_1=sqrt(2/(sigma_1_eval*omega*mu_1)); % Skin depth in [m]
delta_2=sqrt(2/(sigma_2_eval*omega*mu_2)); % Skin depth in [m]
delta_3=sqrt(2/(sigma_3_eval*omega*mu_3)); % Skin depth in [m]
delta_4=sqrt(2/(sigma_4_eval*omega*mu_4)); % Skin depth in [m]

N_div=1000;

%% Select only the significant harmonics:
vec_B_given=B_given; % [T]
vec_time2=time_order_given;
vec_space2=space_order_given;

%% Calculation of rotor losses forward rotating:

length_harmonics=length(vec_B_given);

P_ms_matrix=zeros(length_harmonics,1);
P_hub_matrix=zeros(length_harmonics,1);

warning=false;
vec_space_warning=[];
vec_time_warning=[];

P_ms_tot=0;
    for count=1:length_harmonics
        k_time=vec_time2(count);
        h_space=vec_space2(count);
        q_eval=p*h_space; % space order
        omega_eval=f_1*2*pi*k_time;
        B_ms_given=vec_B_given(count)
        omega=omega_eval

        %% Define the symbolic variable
        sigma_1=3*10^-15; % [S/m]
        sigma_2=3*10^-15; % [S/m]
        sigma_3=0.77*10^6; % [S/m]
        sigma_4=6.7*10^6; % [S/m]
        %% Current sheet model:
        J_kq=1;
        k_p_1=sqrt(1i*omega*mu_1*sigma_1);
        k_p_2=sqrt(1i*omega*mu_2*sigma_2);
        k_p_3=sqrt(1i*omega*mu_3*sigma_3);
        k_p_4=sqrt(1i*omega*mu_4*sigma_4);

        % New method:
        q=q_eval;

        % Region 1:
%         beta_1=1i*k_p_1*R_1*besseli_d(q,k_p_1*R_1)/besseli(q,k_p_1*R_1)/mu_1*q_eval;
        beta_1=mu_0*1i/mu_1/q;

        % choose the type of transfer matrix you need.
        % Region 2:
%         T_2=TransferMatrix_comp( R_1, R_2, mu_2, sigma_2_eval, omega, q_eval);
        T_2=TransferMatrix_medium_simp( R_1, R_2, mu_2, sigma_2_eval, omega, q_eval, N_div);
%         T_2=TransferMatrix_simp( R_1, R_2, mu_2, sigma_2_eval, omega, q_eval, N_div);
%         T_2=TransferMatrix_super_simp( R_1, R_2, mu_2, sigma_2_eval, omega, q_eval, N_div);

        % Region 3:
%         T_3=TransferMatrix_comp( R_2, R_3, mu_3, sigma_3_eval, omega, q_eval);
        T_3=TransferMatrix_medium_simp( R_2, R_3, mu_3, sigma_3_eval, omega, q_eval, N_div);
%         T_3=TransferMatrix_simp( R_2, R_3, mu_3, sigma_3_eval, omega, q_eval, N_div);
%         T_3=TransferMatrix_super_simp( R_2, R_3, mu_3, sigma_3_eval, omega, q_eval, N_div);


        % Region 4:
%         T_4=TransferMatrix_comp( R_3, R_4, mu_4, sigma_4_eval, omega, q_eval);
        T_4=TransferMatrix_medium_simp( R_3, R_4, mu_4, sigma_4_eval, omega, q_eval, N_div);
```

```
%         T_4=TransferMatrix_simp( R_3, R_4, mu_4, sigma_4_eval, omega, q_eval, N_div);
%         T_4=TransferMatrix_super_simp( R_3, R_4, mu_4, sigma_4_eval, omega, q_eval, N_div);


        %% Estimation of the coefficients
        Mat_D=[0 0; 0 1]-T_4*T_3*T_2*[1 0; beta_1 0];
%         temp_mat=inv(Mat_D);
        vec_sol=Mat_D\T_4*T_3*T_2*[0; mu_0*J_kq];

        % Get the fields:
        B_1=vec_sol(1);
        H_1=beta_1*B_1/mu_0;

        H_4=vec_sol(2)/mu_0;

        temp_2=T_2*[B_1; mu_0*(H_1+J_kq)];
        B_2=temp_2(1);
        H_2=temp_2(2)/mu_0;

        temp_3=T_3*[B_2; mu_0*H_2];
        B_3=temp_3(1);
        H_3=temp_3(2)/mu_0;


        %% Calculate the power losses for J_kq=1:
        S1=2*pi*R_1*L;
        S2=2*pi*R_2*L;
        S3=2*pi*R_3*L;

        E_1=-omega/q*R_1*B_1;
        E_2=-omega/q*R_2*B_2;
        E_3=-omega/q*R_3*B_3;

        P1_j1_temp=0.5*real(E_1*conj(H_1+J_kq))*S1;
        P2_j1_temp=0.5*real(E_2*conj(H_2))*S2;
        P3_j1_temp=0.5*real(E_3*conj(H_3))*S3;

        %% Solution with no eddy currents:

        syms q

        syms sigma_1
        syms sigma_2
        syms sigma_3
        syms sigma_4

        clear A

        syms A

        A(1,1)=R_1^q;
        A(1,2)=-R_1^q;
        A(1,3)=-R_1^(-q);

        A(2,1)=-1/mu_1*R_1^(q);
        A(2,2)=1/mu_2*R_1^(q);
        A(2,3)=-1/mu_2*R_1^(-q);

        A(3,2)=R_2^q;
        A(3,3)=R_2^(-q);
        A(3,4)=-R_2^q;
        A(3,5)=-R_2^(-q);

        A(4,2)=-1/mu_2*R_2^(q);
        A(4,3)=1/mu_2*R_2^(-q);
        A(4,4)=1/mu_3*R_2^(q);
        A(4,5)=-1/mu_3*R_2^(-q);

```

```
        A(5,4)=R_3^q;
        A(5,5)=R_3^(-q);
        A(5,6)=-R_3^q;
        A(5,7)=-R_3^(-q);

        A(6,4)=-1/mu_3*R_3^(q);
        A(6,5)=1/mu_3*R_3^(-q);
        A(6,6)=1/mu_4*R_3^(q);
        A(6,7)=-1/mu_4*R_3^(-q);

        A(7,6)=R_4^q;
        A(7,7)=R_4^(-q);


        B1=[0 J_kq*R_1/q_eval 0 0 0 0 0];
        B=transpose(B1);

        X_1=A\B;

        C10_temp=X_1(1);
        C_10=double(subs(C10_temp,q, q_eval));

        C20_temp=X_1(2);
        C_20=double(subs(C20_temp,q, q_eval));

        D20_temp=X_1(3);
        D_20=double(subs(D20_temp,q, q_eval));

        C30_temp=X_1(4);
        C_30=double(subs(C30_temp,q, q_eval));

        D30_temp=X_1(5);
        D_30=double(subs(D30_temp,q, q_eval));

        C40_temp=X_1(6);
        C_40=double(subs(C40_temp,q, q_eval));

        D40_temp=X_1(7);
        D_40=double(subs(D40_temp,q, q_eval));

        B_calculated=abs(-j*q_eval*(C_20*R_wave^(q_eval-1)+D_20*R_wave^(-q_eval-1)));


        K_B_ms=B_ms_given/B_calculated;

        if isnan(K_B_ms)
            K_B_ms=0;
            warning=true;
            vec_space_warning=[vec_space_warning h_space];
            vec_time_warning=[vec_time_warning h_space];
        end


        %% Calculate the power losses for J_kq=1:

        P1_j1=P1_j1_temp;
        P2_j1=P2_j1_temp;
        P3_j1=P3_j1_temp;

        P_j1_mag=P2_j1-P3_j1;
        P_j1_hub=P3_j1;


        %% Final estimation of the rotor losses:
        P_mag_ms=alpha_p*P_j1_mag*K_B_ms^2;
        P_hub_ms=alpha_p*P_j1_hub*K_B_ms^2;

        P_ms_matrix(count)=P_mag_ms;
```

```
        P_hub_matrix(count)=P_hub_ms;
        P_ms_tot=P_ms_tot+P_mag_ms+P_hub_ms;


    end
```

```
function [ T_mat ] = TransferMatrix_comp( R_1, R_2, mu, sigma, omega, q)
%Calculation of the transfer matrix of a region. Complete methodology.
% Author: Jaime Renedo Anglada, University of Southampton.

mu_0=4*pi*10^-7; % [m kg s^-2 A^-2]
k_p=sqrt(1i*omega*mu*sigma);

N_div=1000;
test_nan=besselk_d(q,k_p*R_1)*besseli_d(q,k_p*R_1);

if isnan(test_nan)

    S_2l=R_2-R_1;
    S_2d=S_2l/N_div;

    T_2=[1 0; 0 1];
    for count2=0:(N_div)
        delta=S_2d;
        r_2a=R_1+delta*count2+delta/2;

        k_2=q/r_2a;
        d_2=1/sqrt(sigma*mu*omega);
        gamma_2h=sqrt(k_2^2+1i/d_2^2);
        beta_2h=gamma_2h/(1i*mu*k_2);
        T_2h=[cosh(gamma_2h*S_2d) sinh(gamma_2h*S_2d)/beta_2h/mu_0; mu_0*beta_2h*sinh(
    gamma_2h*S_2d) cosh(gamma_2h*S_2d)];
        T_2=T_2*T_2h;
    end
    T_mat=T_2;

else
    F_2=mu_0*1i*k_p*q/(mu*R_1)*(besselk(q,k_p*R_1)*besseli_d(q,k_p*R_1)-besseli(q,k_p*R_1)*
    besselk_d(q,k_p*R_1));
    M_2=[-mu_0*k_p/mu*besselk_d(q,k_p*R_1) -1i*q/R_1*besselk(q,k_p*R_1); mu_0*k_p/mu*
    besseli_d(q,k_p*R_1) 1i*q/R_1*besseli(q,k_p*R_1)];
    N_2=[1i*q/R_2*besseli(q,k_p*R_2) 1i*q/R_2*besselk(q,k_p*R_2); -mu_0*k_p/mu*besseli_d(q,
    k_p*R_2) -mu_0*k_p/mu*besselk_d(q,k_p*R_2)];
    T_mat=[1 0; 0 -1]*N_2*M_2/F_2*[1 0; 0 -1];

end


end
```

```
function [ T_mat ] = TransferMatrix_medium_simp( R_1, R_2, mu, sigma, omega, q, N_div)
%Calculation of the transfer matrix of a region. Medium simplified methodology.
% Author: Jaime Renedo Anglada, University of Southampton.

mu_0=4*pi*10^-7; % [m kg s^-2 A^-2]

S_2l=R_2-R_1;
S_2d=S_2l/N_div;


T_2=[1 0; 0 1];
for count2=0:(N_div)
    delta=S_2d;
    r_2a=R_1+delta*count2+delta/2;

    k_2=q/r_2a;
    d_2=1/sqrt(sigma*mu*omega);
```

```
    gamma_2h=sqrt(k_2^2+1i/d_2^2);
    beta_2h=gamma_2h/(1i*mu*k_2);

    T_2h=[cosh(gamma_2h*S_2d) sinh(gamma_2h*S_2d)/beta_2h/mu_0; mu_0*beta_2h*sinh(gamma_2h*S_2d) cosh(gamma_2h*S_2d)];
    T_2=T_2*T_2h;
end
T_mat=T_2;
end
```

```
function [ T_mat ] = TransferMatrix_simp( R_1, R_2, mu, sigma, omega, q, N_div)
%Calculation of the transfer matrix of a region. Simplified methodology.
% Author: Jaime Renedo Anglada, University of Southampton.

mu_0=4*pi*10^-7; % [m kg s^-2 A^-2]

S_21=R_2-R_1;
S_2d=S_21/N_div;

T_2=[1 0; 0 1];
for count2=0:(N_div)
    delta=S_2d;
    r_2a=R_1+delta*count2+delta/2;

    k_2=q/r_2a;
    d_2=1/sqrt(sigma*mu*omega);
    gamma_2h=sqrt(k_2^2+1i/d_2^2);
    beta_2h=gamma_2h/(1i*mu*k_2);

    T_2h=[1 gamma_2h*S_2d/beta_2h/mu_0; mu_0*beta_2h*gamma_2h*S_2d 1];

    T_2=T_2*T_2h;
end
T_mat=T_2;
end
```

```
function [ T_mat ] = TransferMatrix_super_simp( R_1, R_2, mu, sigma, omega, q, N_div)
%Calculation of the transfer matrix of a region. Super simplified methodology.
% Author: Jaime Renedo Anglada, University of Southampton.

mu_0=4*pi*10^-7; % [m kg s^-2 A^-2]

S_21=R_2-R_1;
S_2d=S_21/N_div;

T_2=[1 0; 0 1];

delta=S_2d;
r_2a=(R_1+R_2)/2;

k_2=q/r_2a;

d_2=1/sqrt(sigma*mu*omega);
gamma_2h=sqrt(k_2^2+1i/d_2^2);
beta_2h=gamma_2h/(1i*mu*k_2);

T_2h=[1 gamma_2h*S_2d/beta_2h/mu_0; mu_0*beta_2h*gamma_2h*S_2d 1];

T_2=T_2h^N_div;

T_mat=T_2;


end
```

C.6 Optimisation of a tidal turbine

```
%% Optimisation of the shape of a C-core:
% You have a Bs_max which comes from the level of flux from the PM, see my
% own notes for more details. The constraints of the C-core are
% geometrical and the air-gap is given. Specifications of the Casimere
% tidal generator from TSL

clc
clear all

Dyoke=430; %[mm]

N_phase=3;
N_rows=1;

Length=150; % [mm]
ws_0=Length/N_phase/N_rows*0.9; % [mm]
hs_0=ws_0;


dm=8; % [mm]
c_gap=2; % [mm]
g=c_gap+dm; % [mm]

D_ccores=Dyoke-2*dm-2*c_gap; %[mm]
D_g=D_ccores+g; % [mm]
R_g=D_g/2;

J=10; % [A/mm^2]

% 150 rpm more less
n_rpm=150; % [rpm]
n_rad=n_rpm/60*2*pi; % [rad/s]

% Rated torque:
T_out=670; % [Nm]
T_out1=670/N_phase; % [Nm]

pf_given=0.4;

% rho_steel=7650; % kg/m^3

rho_steel=7.650/1000; % kg/cm^3
rho_pm=7.3/1000; % kg/cm^3
rho_cu=8.96/1000; % kg/cm^3

cost_pm=45; % [euro/kg]
cost_steel=3.5; % [euro/kg]
cost_cu=12.4; % [euro/kg]

slot_fill=0.5;



%% Calculate the torque for a given t, s, lambda...


mu_0=4*pi*10^-7;
mu_eq=1;

N=5;
res_B=500;

Mag=1.05/(4*pi*10^-7);
Fm=Mag*dm*10^-3; % [A]

```

```
N_wind=200;

t_lambda=0.3;

hs=hs_0;
ws=ws_0;

%% Choose optimum Nc
%
Nc_max=find_nc_max();
error_wanted=0.005;
vec_pf=[];
T_out_max=T_out1;
correction_factor=12;

count=1
flag=true;
while flag
    Kb_max=KB_VRPM_read(Nc_max);
    Ke=KE_VRPM_read(Nc_max);
    flag2=true;
    while flag2
        [ wm,hc,wc ] = opt_c_core( hs,ws,dm,c_gap,slot_fill*J );
        L_eq=wm*(1+0.384*g/wm);
        F=0.5*slot_fill*J*hc*wc;
        I_n=2*F/N_wind;
        Bs=mu_0*F/g*10^3;

        k_e=N_wind*Nc_max*4*mu_0*R_g*L_eq*Fm*Kb_max/sqrt(2)/g*10^-3;

        Torque_temp=k_e*I_n; % [Nm]

        if abs((T_out_max-Torque_temp)/T_out_max)<error_wanted
            flag2=false;
            Torque_calc=Torque_temp;

        elseif Torque_temp>T_out_max
            hs=0.999*hs;
            ws=0.999*ws;
        elseif Torque_temp<T_out_max
            hs=1.001*hs;
            ws=1.001*ws;
        end
    end

    N_cores=Nc_max-correction_factor;


    Kb=KB_VRPM_read(N_cores);
    Kb_old=Kb;
    Ke=KE_VRPM_read(N_cores);

    L_eq=wm*(1+0.384*g/wm);
    F=0.5*slot_fill*J*hc*wc;
    Bs=mu_0*F/g*10^3;
    I_n=2*F/N_wind;
    k_e=N_wind*N_cores*4*mu_0*R_g*L_eq*Fm*Kb/sqrt(2)/g*10^-3;
    Torque_temp=k_e*I_n; % [Nm]
    if abs((T_out1-Torque_temp)/T_out1)<error_wanted
        flag=false;
        Torque_calc=Torque_temp;
        lambda=pi*D_g/N_cores;

        t=t_lambda*lambda;
        s=lambda-t;
        d=3*lambda;
        R_g=D_g/2;

```

```
        test2_curv=airgapVRPM_no_screen_curvature (s,t,g,d,D_g/2,N_cores);
        test2_curv.build_map
        points=test2_curv.gen_vec_points(1000,dm);
        N_harm=11;
        N_pol=5;
        coeffs_func=test2_curv.eval_coeffs_lambdar (points,N_harm,N_pol);
        lambda_r=coeffs_func(1,1);

        K_B_sc=test2_curv.Kb_calc_sin(dm);
        K_B=KB_VRPM_read(N_cores);
        Kb=K_B;
        Ke=K_B
        I_n=2*F/N_wind
        k_e=N_wind*N_cores*4*mu_0*R_g*L_eq*Fm*Kb/sqrt(2)/g*10^-3;
        Torque=k_e*I_n

        % Inductance:
        L_ind=mu_eq*mu_0*N_wind^2/g*pi*lambda_r*L_eq*R_g*10^-3;
        h1=hc;
        h2=1;
        ws2=wc;
        lambda_say=h1/3/ws2+h2/ws2;
        k_e=N_wind*N_cores*4*mu_0*R_g*L_eq*Fm*K_B/sqrt(2)/g*10^-3;

        % half the value of Say because there is half the leakage. is it good?
        angle_t=t/R_g;

        L_leak=N_cores*mu_0*N_wind^2*lambda_say*angle_t*(R_g-g/2)*10^-3;

        omega_elec=N_cores*n_rad;
        rms_emf=k_e*n_rad;
        rms_emf_calc=rms_emf;
        amp_rms=2*F/N_wind;
        phi=atand(amp_rms*(L_ind+L_leak)*omega_elec/rms_emf);

        power_factor=cosd(phi)
        power_factor_calc=cosd(phi)
        vec_pf=[vec_pf power_factor];


    elseif Torque_temp<T_out1
        T_out_max=1.0001*T_out_max
    elseif Torque_temp>T_out1
        T_out_max=0.9999*T_out_max
    end
end


%% Final calculations

wl=wm;

vol_pm=2*pi*(R_g+g/2-dm/2)*wm*dm*2*N_rows*N_phase; % [mm^3]
vol_cores=N_rows*N_phase*N_cores*(hs*ws-hc*wc)*t; % [mm^3]
vol_yoke=N_rows*N_phase*ws*pi*((R_g+g/2+wl)^2-(R_g+g/2)^2); % [mm^3]
vol_cu=2*pi*(R_g-g/2-hc/2)*wc*hc*N_rows*N_phase; % [mm^3]

vol_tot=N_rows*N_phase*pi*(R_g+g/2+wl)^2*ws; % [mm^3]

mass_pm=rho_pm*vol_pm/1000; % [kg]
mass_cores=rho_steel*vol_cores/1000; % [kg]
mass_cu=slot_fill*rho_cu*vol_cu/1000; % [kg]

tot_mass=mass_pm+mass_cores+mass_cu

tot_cost_pm=cost_pm*mass_pm; % [euros]
tot_cost_cores=cost_steel*mass_cores; % [euros]
tot_cost_cu=cost_cu*mass_cu; % [euros]
```

```
tot_cost_pm;
tot_cost_cores;
tot_cost_cu;

tot_cost=tot_cost_pm+tot_cost_cores+tot_cost_cu


k_e=N_wind*N_cores*4*mu_0*R_g*L_eq*Fm*K_B/sqrt(2)/g*10^-3;

% specific torque:
T_specific=3*Torque_calc/tot_mass
T_specific_eu=3*Torque_calc/tot_cost

% electrical parameters:
I_n=2*F/N_wind
E_n=rms_emf_calc
f_elec=omega_elec/2/pi
power_factor_calc
V_n=E_n/power_factor_calc
Total_torque=3*Torque_calc
speed_rpm=n_rpm
P_n=3*I_n*E_n/1000
S_n=3*I_n*V_n/1000
```